MODELING THE NEUTRAL-ATMOSPHERIC PROPAGATION DELAY IN RADIOMETRIC SPACE TECHNIQUES

V. B. MENDES

April 1999

TECHNICAL REPORT
NO. 199

PREFACE

In order to make our extensive series of technical reports more readily available, we have scanned the old master copies and produced electronic versions in Portable Document Format. The quality of the images varies depending on the quality of the originals. The images, in this version of the report, have been converted to searchable text.

MODELING THE NEUTRAL-ATMOSPHERIC PROPAGATION DELAY IN RADIOMETRIC SPACE TECHNIQUES

V. B. Mendes

Department of Geodesy and Geomatics Engineering
University of New Brunswick
P.O. Box 4400
Fredericton, N.B.
Canada
E3B 5A3

September 1998

PREFACE

This technical report is a reproduction of a dissertation submitted in partial fulfillment of the requirements for the degree of Doctor of Philosophy in the Department of Geodesy and Geomatics Engineering, September 1998. The research was supervised by Dr. Richard B. Langley. Major funding was provided by the Programa Ciência and PRAXIS XXI of Junta Nacional de Investigação Científica e Tecnológica (Portugal).

 The citation to this work should appear as follows:

Mendes, V. B. (1999). *Modeling the neutral-atmosphere propagation delay in radiometric space techniques*. Ph.D. dissertation, Department of Geodesy and Geomatics Engineering Technical Report No. 199, University of New Brunswick, Fredericton, New Brunswick, Canada, 353 pp.

ABSTRACT

The propagation delay induced by the electrically-neutral atmosphere has been recognized as the most problematic modeling error for radiometric space geodetic techniques. A mismodeling of this propagation delay affects significantly the height component of position and constitutes therefore a matter of concern in space-geodesy applications, such as sea-level monitoring, postglacial rebound measurement, earthquake-hazard mitigation, and tectonic-plate-margin deformation studies.

The neutral-atmosphere propagation delay is commonly considered as composed of two components: a "hydrostatic" component, due essentially to the dry gases of the atmosphere, and a "non-hydrostatic" component, due to water vapor. Each one can be described as the product of the delay at the zenith and a mapping function, which models the elevation angle dependence of the propagation delay.

This dissertation discusses primarily the accuracy of zenith delay prediction models and mapping functions found in the scientific literature. This performance evaluation is based on a comparison against 32,467 benchmark values, obtained by ray tracing one-year's worth of radiosonde profiles from 50 stations distributed worldwide, and comprised different phases: ray-tracing accuracy assessment, model development, and model accuracy assessment.

We have studied the sensitivity of the ray-tracing technique to the choice of physical models, processing strategies, and radiosonde instrumentation accuracy. We have concluded that errors in ray tracing can amount to a few centimetres, under special circumstances, but they largely average out for each station's time series of profiles.

In order to optimize the performance of the models, we have established databases of the temperature-profile parameters using 50 additional sites, for a total of 100 radiosonde stations. Based on these large databases, we have developed models for lapse rate and tropopause height determination, which have improved significantly the performance of models using the information.

From our model assessment we have concluded that the hydrostatic component of the zenith delay can be predicted with sub-millimeter accuracy, using the Saastamoinen model, provided accurate measurements of surface total pressure are available. The zenith non-hydrostatic component is much more difficult to predict from surface meteorological data or site dependent parameters, and the best models show values of root-mean-square (rms) scatter about the mean of a few centimetres in the zenith direction.

Notwithstanding the large number of mapping functions we have analyzed, only a small group meet the high standards of modern space geodetic data analysis: Ifadis, Lanyi, MTT, and NMF. For the total number of radiosonde stations analyzed, none of the mapping functions revealed themselves to be superior for all elevation angles. For elevation angles above 15 degrees, Lanyi, MTT, and NMF yield identical mean biases and

the best total error performances. At lower elevation angles, Ifadis and NMF are clearly superior. As regards the rms scatter about the mean, Ifadis performs the best for all elevation angles, followed closely by Lanyi.

TABLE OF CONTENTS

LIST OF TABLES

LIST OF FIGURES

LIST OF MAJOR SYMBOLS

SYMBOL	DESIGNATION	UNITS	SECTION
d_g	geometric delay (ray bending)	m	5.3
d_{na}	neutral-atmosphere propagation delay	m	3.2
d_h^z	zenith hydrostatic delay	m	3.2
d_{na}^z	zenith total delay	m	3.2
d_{nh}^z	zenith non-hydrostatic delay	m	3.2
e	water vapor pressure	hPa	2.3
e_{si}	saturation vapor pressure over ice	hPa	2.4
e_{sw}	saturation vapor pressure over pure water	hPa	2.4
e'_{sw}	saturation vapor pressure over water (moist air)	hPa	2.4
f_w	enhancement factor	unitless	2.4
g	magnitude of acceleration due to gravity	$m\ s^{-2}$	2.5
H	height above sea level (orthometric height)	km	3.1
H	height above sea level (orthometric height)	m	3.3
$\mathscr{H}$	scale height	km	2.5
H_t	tropopause height	km	3.1
H_d^e	dry equivalent height (Hopfield)	km	3.1

H_w^e	wet equivalent height (Hopfield)	km	3.1
M_d	mean molecular weight for dry air	kg $kmol^{-1}$	2.3
M_w	molecular weight of water vapor	kg $kmol^{-1}$	2.3
m	total mapping function	unitless	3.2
m_d	mean mass of dry air	kg	2.3
m_h	hydrostatic mapping function	unitless	3.2
m_{nh}	non-hydrostatic mapping function	unitless	3.2
m_w	mass of water	kg	2.3
N	total refractivity	N-units	3.1
n	refractive index	unitless	3.1
P	total pressure	hPa	2.3
P_c	partial pressure due to carbon dioxide	hPa	3.1
P_d	partial pressure due to dry air	hPa	2.3
q	specific humidity	g kg^{-1}	2.4
R	universal gas constant	J $kmol^{-1}$ K^{-1}	2.1
R_d	mean specific gas constant for dry air	J kg^{-1} K^{-1}	2.3
R_w	specific gas constant water vapor	J kg^{-1} K^{-1}	2.3
r	mixing ratio	unitless	2.4
T	absolute temperature	K	2.3
T_m	weighted mean temperature	K	5.3
t	temperature	°C	2.3
t_{dew}	dew-point depression	°C	2.4

t_{dry}	dry-bulb temperature	°C	2.4
t_{wet}	wet-bulb temperature	°C	2.4
U	relative humidity	%	2.4
Z_d	compressibility factor for dry air	unitless	2.3
Z_w	compressibility factor for water vapor	unitless	2.3
α	temperature lapse rate	K km^{-1}	4.2
α	temperature lapse rate	K m^{-1}	3.3
δ_w	absolute humidity	g m^{-3}	2.4
ε	geometric (true) elevation angle	rad	3.2
φ	latitude	rad	3.1
λ	water vapor lapse rate parameter	unitless	3.3
θ	refracted (apparent) elevation angle	rad	3.2
ρ	total density	kg m^{-3}	2.3
ρ_d	density of dry air	kg m^{-3}	2.3
ρ_w	density of water vapor	kg m^{-3}	2.3

ACKNOWLEDGEMENTS

I wish to express my gratitude to my supervisor Dr. Richard Langley for his continuous guidance, encouragement, and support throughout these years of graduate studies. His suggestions and thorough review of the draft manuscript lead to significant improvement in the scientific quality of this dissertation.

The financial support of the Programa Ciência and PRAXIS XXI by the former Junta Nacional de Investigação Científica e Tecnológica (Portugal) is gratefully acknowledged.

I would like to express my warmest thanks to Professor Raimundo Vicente for his encouragement in pursuing an academic career and for his recommendations at the beginning of my graduate studies.

Special thanks also go to fellow graduate students for fruitful exchange of ideas (especially Marcelo Santos, Attila Komjathy, and Anthony van der Wal); to the Dixieland Dandies and the Fredericton City Band for wonderful moments of joy; and to Isabel Cavalcante, Graça and Fernando Artilheiro for bearing with me in different occasions.

Many thanks to Jim Davis, Tom Herring, and Arthur Niell, for providing the ray-tracing software and radiosonde data (Arthur Niell), to Gunnar Elgered and the Swedish Meteorological and Hydrological Institute for providing radiosonde data, to Anthea

Coster and Arthur Niell for a rewarding experience in participation in the WWAVE project.

I would like to extend my appreciation to the members of the Examining Board (Dr. R. Langley, Dr. L. Mayer, Dr. C. Bourque, Dr. A. Kleusberg, and Dr. B. Colpitts) and the External Examiner (Dr. G. Elgered) for valuable comments and suggestions made on the draft manuscript, which contributed to improving this dissertation.

I wish to thank my wife Dulce and my son Tiago for their endless love, support, and understanding.

This thesis is dedicated to my parents, Maria dos Anjos and Belarmino.

1. INTRODUCTION

1.1. Motivation

The space age brought with it new technologies that have unequivocally revolutionized geodesy and other sciences over the last three decades. The majority of these space-based techniques use radio signals that propagate through the earth's atmosphere. Both the electrically-charged region of the earth's atmosphere, the ionosphere, and the electrically-neutral region, predominantly the troposphere and the stratosphere, affect the speed and direction of travel of radio waves. While the ionosphere behaves as a dispersive medium at radio frequencies and poses no major problem to dual-frequency radiometric techniques, the non-dispersive nature of the earth's electrically-neutral atmosphere can be more problematic, requiring modeling or other techniques to reduce its impact. The neutral-atmosphere delay is divided into two components: a hydrostatic (dry) component, which is mostly due to the dry gases of the air, and a non-hydrostatic (wet) component, which is due to the water vapor in the atmosphere.

The hydrostatic component contributes more than about 90% to the total delay and varies smoothly both spatially and temporally, as the dry air is well mixed. For a sea-level location and in the zenith direction, the hydrostatic delay is ~2.3 m; its non-hydrostatic counterpart is normally less than ~0.4 m, and can be almost non-existent in polar and arid

regions. By comparison with the hydrostatic propagation delay, the non-hydrostatic component is highly variable in time and space, as the water vapor content in the atmosphere is inhomogeneous. Assuming a regionally-laterally-homogeneous atmosphere, the delay at the zenith can be related to the delay at a given elevation angle by using a mapping function. For an elevation angle of 5 degrees, the value of this "scale factor" is ~10.

The propagation delay due to the neutral atmosphere has been recognized as a major (in some cases *the* major) modeling error for many space-based electromagnetic ranging techniques, such as very long baseline interferometry, one-way and two-way satellite-based positioning systems, satellite altimetry, satellite laser ranging, radio science experiments, and planetary spacecraft tracking.

In very long baseline interferometry (VLBI), the main observables are the difference in arrival time at two earth-based antennas of radio waves emitted by an extragalactic radio source (group delay) and the rate of change of the interferometric phase delay (phase-delay rate) (for details on the VLBI technique see, e.g., Whitney et al. [1976], Clark et al. [1985], Thompson et al. [1986], Reid and Moran [1988], and Felli and Spencer [1989]). Gontier et al. [1997] admit that "*the correction of the tropospheric delay is currently the major modeling error in astrometric and geodetic VLBI*".

Although they use a different source of signals, satellite-based global positioning systems have performances that are also limited by the influence of the earth's atmosphere. These systems include the Navstar Global Positioning System (GPS), the Global Navigation

Satellite System (GLONASS), the Doppler Orbitography and Radiopositioning Integrated by Satellite (DORIS) system, and the Precise Range and Range-rate Experiment (PRARE).

GPS and GLONASS are one-way systems that primarily measure pseudoranges and carrier phases of signals transmitted by satellites in the L band of the electromagnetic spectrum. GPS satellites emit a signal composed of two carrier frequencies, which are modulated with two pseudorandom noise (PRN) codes – termed P-code (precision code) and C/A-code (coarse/acquisition code) – and referred to as L1 (1575.42 MHz) and L2 (1227.60 MHz). Those PRN codes are unique for each satellite (in the case of the P-code, they are one-week segments of the full code, which are re-initialized each week at 0 hours Sunday) and therefore used to identify unambiguously each GPS satellite. High-precision applications rely on superior accuracy of carrier phase measurements. GLONASS satellites on the other hand are identified by the frequency of the carrier signal, as the system uses a frequency division multiple access technique. All GLONASS satellites share the same PRN codes. The range of applications for these systems (in particular GPS) largely exceeds those for geodetic VLBI, due to their ease of use and relatively low cost. Details on these systems can be found in a number of monographs, like Wells et al. [1986], Seeber [1993], Hofman-Wellenhoff et al. [1997], Leick [1994], Kleusberg and Teunissen [1996], and Strang and Borre [1997]. As in VLBI, the effect of the atmosphere is seen as the major limiting error source in high-precision applications.

DORIS is a microwave one-way Doppler-tracking system that uses a set of ground beacons broadcasting at 2.2 GHz (S-band) and 401 MHz (UHF). The main observable in DORIS is the Doppler shift of the signals received on board a satellite from which the radial velocity with respect to the ground station is determined and subsequently from which range measurements are derived [Willis et al., 1990; Seeber, 1993; Cazenave et al., 1993; Dow et al., 1994].

PRARE is a spaceborne tracking system which provide two-way range and range-rate measurements to ground stations. The onboard system transmits two signals, at 2.2 GHz (S-band) and 8.5 GHz (X-band) frequencies, modulated with pseudo-random noise codes. The time delay in signal propagation provides range measurements, whereas the Doppler-shifted carrier phase provides range-rate measurements [Seeber, 1993; Francis et al., 1995; Schäfer and Schumann, 1995].

Satellite laser ranging (SLR) measures the round-trip travel time of a laser signal transmitted between a ground station and a satellite equipped with retroreflectors. A major limitation in SLR ranging accuracy is the propagation delay due to the atmosphere [Gardner, 1976; Herring and Pearlman, 1993; Degnan, 1993]. Degnan [1993] states that "*one centimeter systematic atmosphere-induced error is the dominant error source in modern day SLR measurements*". However, the optical frequencies used in SLR are almost insensitive to the ionosphere and water vapor content, and the hydrostatic component is the main cause of atmospheric error in SLR [Abshire and Gardner, 1985; Degnan, 1993]. Unlike its effect on radio waves, the neutral atmosphere is dispersive for

light waves. The problem of SLR neutral-atmosphere delay correction can therefore be overcome in the future via two-color ranging systems [Degnan, 1993; Varghese et al., 1993; Schlüter et al., 1993]. The Marini-Murray model [Marini and Murray, 1973] is generally used in SLR atmospheric correction, as the number of models developed for laser data correction is very limited (see Yan [1996] for a recently-developed mapping function for optical frequencies and Mironov [1993] for an analysis of the Marini-Murray model). Due to the peculiarity of SLR, the models used for atmospheric correction in this technique were not analyzed in our research.

The main goal of satellite altimetry is to measure the sea surface topography and to study the circulation of the oceans. The source of information is radar altimetry measurements from missions such as Seasat (see special issues of the *Journal of Geophysical Research*, Vol. 87, No. C5, 1982, and Vol. 88, No. C3, 1983), Geosat (see special issues of the *Journal of Geophysical Research*, Vol. 95, No. C3, 1990, and Vol. 95, No. C10, 1990), TOPEX/Poseidon (see special section of the *Journal of Geophysical Research*, Vol. 99, No. C12, 1994; Ruf et al. [1995]; Keihm et al. [1995]; Zieger et al. [1995]; Keihm and Ruf [1995]), and ERS-1 and ERS-2 (e.g. Albani et al. [1994]; Francis et al. [1995]; Dow et al. [1996]). A radar altimeter on board a satellite transmits electromagnetic pulses and measure the two-way travel time, from which the range measurements are derived. The pulses emitted by the satellite-born radar altimeters are affected by the earth's neutral atmosphere and have therefore to be corrected.

Radio science experiments designed to study a particular phenomenon and to conduct spacecraft tracking (e.g. Keihm and Marsh [1996]), using one- or two-way phase measurements between an earth station and a spacecraft, are among other kinds of applications for which the effect of the neutral atmosphere reveals itself as the dominant source of error.

As demonstrated by Beutler et al. [1988] for GPS networks, the effect of a differential neutral-atmosphere error, Δd_{na}^{z}, induces an amplified relative height error, Δh, which is given in a first approximation by the following rule-of-thumb:

$$\Delta h = \frac{\Delta d_{na}^{z}}{\sin \varepsilon_{min}} \tag{1.1}$$

where ε_{min} is the cut-off angle (minimum elevation angle observed); so, for a cut-off angle of 20°, a bias of 1 cm in the zenith delay introduces a height bias of ~3 cm. Even if we assume a perfect zenith delay determination, mapping the zenith delay to other elevation angles can still produce errors greater than that admissible for high-precision applications, some of which require millimetre-level vertical accuracy, such as sea-level rise monitoring [Pan and Sjöberg, 1993; Peltier, 1996], determination of vertical motion due to postglacial rebound and ice thickness variation [Tushingham, 1991; James and Lambert, 1993; Mitrovica et al., 1993; Peltier, 1995; Argus, 1996; Trupin et al., 1996], studies of regional deformation [Kroger et al., 1987; Ma et al., 1990; Lindqwister et al., 1991; Feigl et al., 1993; Jackson and Bilham, 1994; Chen et al., 1996; Dunn et al., 1996; Tabei et al., 1996], and earthquake hazard mitigation [Williams et al., 1993]. Other applications

whose success depends strongly on adequate neutral-atmosphere modeling are, for example, the establishment of reference frames [IERS, 1994; IERS, 1995; IERS, 1997a; MacMillan and Ma, 1997], studies of earth's orientation and associated variations [Carter et al., 1984; Carter et al., 1985; Herring, 1988; Freedman, 1991; Herring et al., 1991; Lindqwister et al., 1992; Li, 1994; Ray, 1996; Hefty and Gontier, 1997], monitoring plate tectonic motion [Herring et al., 1986; Ward, 1990; Argus and Gordon, 1990; Matsuzaka et al., 1991; Dixon et al., 1991; Soudarin and Cazenave, 1995; Larson et al., 1997; Reilinger et al., 1997], high-accuracy ground and airborne positioning [Shi and Cannon, 1995; Mendes et al., 1995; Collins et al., 1996; Alber et al., 1997], and time transfer [Lewandowski and Thomas, 1991; Lewandowski et al., 1992]. There is therefore a strong motivation to evaluate the accuracy of the current strategies proposed for neutral-atmosphere propagation delay modeling. This dissertation focuses primarily on the analysis of zenith delay prediction models and mapping functions.

There are essentially three methods to correct for the neutral-atmosphere delay: pure modeling, direct calibration and self-calibration (or estimation). In **pure modeling**, the zenith delay is generally predicted from surface meteorological measurements using a prediction model, and subsequently projected to the desired line of sight by a mapping function. In the **direct calibration** approach, the zenith hydrostatic component is obtained from a prediction model driven by accurate measurements of pressure and the non-hydrostatic component is directly measured by an independent technique. In the **self-calibration** approach this non-hydrostatic component is estimated from the positioning

system data along with other parameters of interest, using a least squares or Kalman filter estimation technique.

- pure modeling

Pure modeling is the least effective of the three techniques, due to the difficulties in accurately predicting the zenith non-hydrostatic delay. In most cases, this prediction is no better than a few centimetres, resulting in unacceptable errors in positioning needed for most of the space-based geodetic applications.

- direct calibration

There are a few instruments to estimate the non-hydrostatic component of the neutral-atmosphere delay (or the equivalent precipitable water) by direct calibration (see, e.g., Kuo et al. [1993]), the most used of which are the water vapor radiometers (WVRs). A WVR is a ground-based passive microwave instrument that determines the water vapor content along a given line-of-sight by measuring the brightness temperature (equivalent blackbody temperature) of the sky (for details on WVR see, e.g., Resch [1984], Davis [1986], Elgered [1993], and Solheim [1993]). The water vapor molecules in the atmosphere induce a peak in the radiation spectrum centered at 22.235 GHz, and therefore a WVR operates at a frequency close to this value. A second frequency is used to measure the highly variable background radiation level, which is mainly due to liquid water droplets and oxygen (the choice of WVR frequencies is discussed by Wu [1979], for example). The non-hydrostatic delay is obtained from the measured brightness temperatures using an adopted algorithm (see Robinson [1988], Elgered [1993], and

Johansson et al. [1993]). Different WVR types are described in the literature (e.g. Guiraud et al. [1979], Elgered et al. [1982], Janssen [1985], Hogg and Snider [1988], Bürki et al. [1992], Peiyuan [1992], Kuehn et al. [1993], and Keihm [1995]). Elgered et al. [1991] briefly describe different WVRs used in VLBI experiments. A large number of intercomparison tests between different WVRs have been performed (e.g. Rocken et al. [1991]; Kuehn et al. [1993]). Linfield et al. [1995] estimate the precision of current WVRs at the 2-3 mm level, but they can have a small bias which is dependent on the site location and season (see Solheim [1993] and Linfield et al. [1995] for discussion of WVR error sources) and are unreliable during rain.

There are a few alternatives to the WVRs in direct calibration of the non-hydrostatic delay. However, except for radiosondes, the use of these instruments is very limited. Comparisons between microwave radiometry and radiosondes are documented in Hogg et al. [1981], Elgered and Lundqvist [1984], Westwater et al. [1989], England et al. [1993], and Kuehn et al. [1993]. England et al. [1992] compare radiometers against a Raman lidar and Jackson and Gasiewski [1995] compare measurements made with the NASA Goddard Space Flight Center's Millimeter-wave Imaging Radiometer (MIR) against radiosondes and a Raman lidar; Elgered [1982] compares a microwave radiometer, an infrared spectral hygrometer and radiosonde data; Sierk et al. [1997] compare measurements from a solar spectrometer, a radiometer, and GPS. Walter and Bender [1992] present a system that measures the difference in the travel times between an optical and a microwave signal, designated as SPARC (Slant Path Atmospheric Refraction Calibrator). As the main source of dispersion between the two signals is due

to the delay induced by the water vapor in the microwave signal, the non-hydrostatic delay can be deduced.

Independent of the method used, the direct calibration is limited not only by the accuracy and precision of the instrument used to measure the non-hydrostatic delay, but also by the performance of the hydrostatic mapping function.

- self-calibration

In a first approximation, a residual neutral-atmosphere delay, Δd_{na}, is given by the following expression:

$$\Delta d_{na} \approx \frac{\Delta d_{na}^{z}}{\sin\varepsilon}, \tag{1.2}$$

where Δd_{na}^{z} is the residual neutral-atmosphere delay at the zenith and ε is the elevation angle. On the other hand, the change in the neutral-atmosphere delay, Δd_{na}^{V}, due to a change in the vertical position of a receiver, ΔV, is given approximately by [Treuhaft, 1992]:

$$\Delta d_{na}^{V} \approx \Delta V \cdot \sin\varepsilon . \tag{1.3}$$

As can be witnessed in Figure 1.1, the signatures of a station height error and of a residual neutral-atmosphere error are quite similar for a large range of elevation angles, and only the inclusion of observations taken at low elevation angles will help to separate these effects. However, the errors in the mapping functions also increase at low elevation

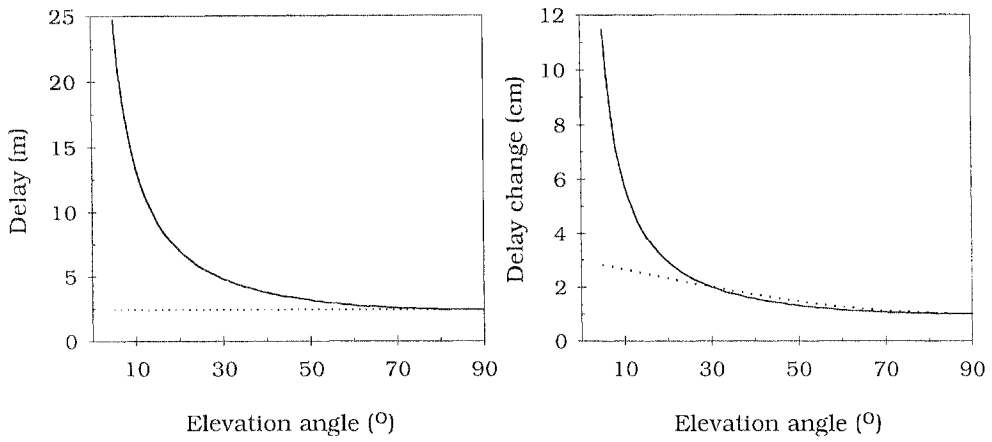

Figure 1.1 – The left plot shows the neutral-atmosphere delay signature due to a zenith delay of 2.4 m (solid line) compared with a signature due to a station height offset of 2.4 m (dotted line). The right plot shows the effect of 1-cm error in the zenith neutral-atmosphere delay (solid line), as compared with a change of –2 cm in the vertical position of a receiver combined with a clock offset equivalent to 3-cm delay (dotted line). In both cases, and especially for the second situation, the inclusion of low elevation angle observations is essential to separate both signatures (Adapted from Rogers [1990] and Treuhaft [1992]).

angles, hence the success of the method depends very much on the accuracy of the mapping functions.

There is a large variety of studies comparing the different mathematical procedures used in self-calibration of the neutral-atmosphere delay (see, e.g., Herring et al. [1990] and van der Wal [1995] for a review of the characteristics of some stochastic estimation procedures) and comparison studies of the estimates obtained using different instrumentation. Brunner and McCluskey [1991] promote the importance of estimating corrections of all sites in a network. Tralli et al. [1992] compared GPS and VLBI

estimates and obtained an agreement of 3-11 mm (rms) for four of five sites analyzed. Tralli and Lichten [1990] compared the estimates from first-order Gauss-Markov and random walk processes. They conclude that the GPS self-calibration yields a precision and accuracy in baseline determination comparable to or better than that obtained using direct calibration with WVRs. Elgered et al. [1991] compared data from different WVRs against Kalman filtering estimates from VLBI. They concluded that both methods yielded to comparable accuracies for that particular experiment. Similar conclusions were obtained by Tralli and Dixon [1988], that is, the estimation of tropospheric zenith delay parameters and WVR direct calibration result in similar levels of accuracy in baseline determinations.

Kuehn et al. [1993] have compared wet neutral-atmosphere delays from WVR, radiosondes, and VLBI. They conclude that the use of WVR data and the estimation technique are equivalent, and that the differences between WVRs, radiosonde and VLBI estimates are up to ~1 cm. Linfield et al. [1997] compared GPS and WVR measurements at Goldstone over an 82-day period and obtained an agreement in zenith delay estimates of better than 6 mm (rms). Elgered et al. [1997] obtained an agreement of 1 mm (rms) between the integrated precipitable water vapor estimates from GPS, radiosonde, and WVR, using 4 days of data acquired in different Swedish locations.

Van der Wal [1995] investigated three different estimation methods used in self-calibration of the neutral-atmosphere delay. Based on the analysis of 10 days of GPS data pertaining to 5 baselines, he concluded that the conventional weighted least squares,

the sequential weighted least squares and the Kalman filtering procedures "*perform at roughly the same level of accuracy and precision*".

All these methods are also limited by the accuracy of the surface pressure measurements used to predict the zenith hydrostatic delay, violations in the assumption of hydrostatic equilibrium [Hauser, 1989], and horizontal atmospheric gradients [MacMillan and Ma, 1997; Chen and Herring, 1997]. The azimuthal dependence of the neutral-atmosphere delay can however be included in the self-calibration technique, by introducing gradient parameters as additional unknowns.

A by-product of the self-calibration technique, especially when applied to GPS, is the estimate of the zenith non-hydrostatic delay of radio signals through the atmosphere, which provides significant information for climate modeling and weather forecasting [Bevis et al., 1992; Kuo et al., 1993; Bevis et al., 1994], and correction of synthetic aperture radar (SAR) data [Goldstein, 1995; Rignot, 1996; Tarayre and Massonnet, 1996; IERS, 1997b]. The feasibility of "GPS-meteorology" is well documented in the recent literature (e.g. Rocken et al. [1995]; Dodson and Shardlow [1995]; Dodson et al. [1996]; Nam et al., 1996; Coster et al. [1996a; 1996b]; Derks et al. [1997]; Ware et al. [1997]; Elgered et al. [1997]). The improvement of zenith non-hydrostatic delay estimates seems to be dependent upon issues related to the adopted estimation strategy, such as the elevation angle cutoff used (e.g. Bar-Sever and Kroger [1996]; Coster et al. [1996b]), and errors in both the hydrostatic and the non-hydrostatic mapping functions, which would corrupt the estimates of the zenith delay. Furthermore, the zenith non-

hydrostatic delay estimates have to be converted to values of precipitable water vapor by using a conversion factor, a problem also of concern in the context of this dissertation.

1.2. Literature review

The relevant literature involving the problematic nature of the neutral-atmosphere propagation delay correction for space geodetic systems is quite extensive, and fairly well documented in Langley et al. [1995]. This section reviews the most significant independent studies in assessing neutral-atmosphere propagation delay models (zenith delay and/or mapping functions); a review of significant literature in different key areas related to this dissertation was already presented in the previous section.

Recent work concerning the assessment of zenith delay prediction models and/or mapping functions has been reported by Janes et al. [1991], Estefan and Sovers [1994], MacMillan and Ma [1994], and Forgues [1996].

Janes et al. [1991] have assessed the performance of eight zenith delay prediction models and ten mapping functions against benchmark values obtained by ray tracing the U.S. Standard Atmosphere [NOAA/NASA/USAF, 1976] and the U.S. Standard Atmosphere Supplements, 1966 [ESSA/NASA/USAF, 1966]. They concluded that the explicit forms of the Saastamoinen zenith delay prediction models [Saastamoinen, 1973] coupled with the CfA-2.2 hydrostatic mapping function [Davis et al., 1985], and the Goad and Goodman wet mapping function [Goad and Goodman, 1974] would lead to the best overall performance under most conditions. It is important to note that this study did not

evaluate the mapping function performance per se, but rather the ensemble zenith delay prediction model plus mapping function.

MacMillan and Ma [1994] discuss the improvement in baseline length precision and accuracy using the Ifadis [Ifadis, 1986] and MTT [Herring, 1992] mapping functions as compared against the combination CfA-2.2 [Davis et al., 1985] and Chao [Chao, 1974]. The newer functions reduced the baseline length scatter by about 20%. They also concluded that baseline length repeatabilities are optimum for a cutoff angle of 7-8°.

Estefan and Sovers [1994] compared the performance of six mapping functions (and different function variations) using VLBI measurements carried out over a 5-year period. Based on the statistical analysis of the VLBI measurements, they concluded that Lanyi [1984], CfA-2.2 [Davis et al., 1985], Ifadis [1986], MTT [Herring, 1992], and NMF [Niell, 1996] mapping functions performed better than the Chao [1974] mapping function; however, among those tested they found that "*no one "best" tropospheric mapping function exists for every application and all ranges of elevation angles*".

Forgues [1996] simulated the impact of 15 mapping functions on GPS positioning, as a function of a large number of factors, such as the elevation angle, the site location, the duration of the observation session, and the estimation of tropospheric parameters. Using the MTT [Herring, 1992] function as reference, she concluded that, for the ensemble of simulations used, the functions by Davis et al. [1985], Lanyi [1984], Ifadis [1986], and Niell [1996] performed the best, both in absolute and relative mode, for short and long baselines.

1.3. Dissertation contribution

The main contributions of this dissertation can be summarized as follows:

- review and systematization of methods used in computation of water vapor pressure from different meteorological parameters;
- establishment of large databases and statistics for various meteorological parameters useful for the characterization of neutral-atmosphere refraction;
- development of models for tropopause height and temperature lapse rate determination;
- thorough evaluation of ray-tracing accuracy by analyzing the effects of different factors such as the computation of saturation vapor pressure, the choice of refractivity constants, the use of the enhancement factor, the effects of radiosonde data errors, and ray-tracing-computation strategies;
- development of models for the determination of geometric delay (ray bending);
- development and improvement of models for the computation of the mean temperature;
- comprehensive assessment of zenith delay model and mapping function performance; this dissertation constitutes the most comprehensive evaluation of zenith delay models and mapping functions, not only by the number of models evaluated, but also by the amount of benchmark data used. It reviews and analyzes the most significant models and mapping functions developed in the last three decades against ray-tracing data

from 50 stations, which constitutes the only study that has evaluated such a large number of models and under so many spatially and temporally varying climatic conditions;

- optimization of mapping function performances based on some developed models.

1.4. Dissertation outline

Chapter 1: Introduction is the chapter that outlines the directions followed in the dissertation development. It gives emphasis to the motivation for this particular research subject, reviews the most significant literature related to the topic, and remarks on the contributions of this dissertation.

Chapter 2: The Earth's Atmosphere reviews the main features of the earth's atmosphere. The chapter reviews the classifications of the earth's atmosphere as a function of its composition and vertical structure. It describes the physics of the earth's atmosphere and summarizes the variables dominantly used to express the moisture content of the atmosphere. Some forms of model atmospheres are presented.

Chapter 3: Neutral-Atmosphere Refraction introduces the main concepts used in this dissertation. The chapter reviews the concept of refractivity and describes different atmospheric refractivity models. It introduces the concepts of neutral-atmosphere propagation delay, the zenith delay prediction model, and the mapping function. It describes the models used in modeling the zenith delay and its elevation angle dependence.

Chapter 4: Data Description and Analysis describes the data used in assessing the neutral-atmosphere propagation delay models. The chapter initially describes the radiosonde instruments generally used in upper-air data collection, and discusses their precision. It follows with a full analysis of meteorological parameters additionally needed in assessing the models (the tropopause height, inversion height, and lapse rate) and a description of the methods used to build the associated databases. Finally it introduces new models for tropopause height and lapse rate determination.

Chapter 5: Ray Tracing describes the algorithms used in ray tracing the radiosonde data and builds the database of traces to be used as a "benchmark" against which the models are compared. It fully describes the effect of the processing strategies, the choice of physical models, and data precision on ray-tracing accuracy and discusses the ray-tracing limitations due to unmodeled effects, such as horizontal atmospheric gradients. The chapter also introduces the precipitable water and geometric delay databases obtained as ray-tracing by-products and presents new models to determine those parameters.

Chapter 6: Model Assessment describes the results of the comparison of zenith delay models and mapping functions against ray tracing. The chapter describes the methodology used in the assessment and discusses the influence of different processing strategies on the performance of the models. It presents full statistical analysis of the performance of the models globally and locally, for 50 selected sites.

Chapter 7: Conclusions and Recommendations remarks on the major conclusions drawn from the work documented in this dissertation, and suggests some recommendations to be followed in neutral-atmosphere propagation delay modeling.

2. THE EARTH'S ATMOSPHERE

The radio signals used by space techniques for geodetic positioning, such as very long baseline interferometry (VLBI) and the Global Positioning System (GPS), have to propagate through the earth's atmosphere. Along their paths, they are significantly affected by free electrons present in the ionosphere and by the constituents of an electrically neutral atmospheric layer, which includes the lower part of the stratosphere and the troposphere. The effects on radio signals of these two media are of different similitude. The ionosphere is a dispersive medium, that is, the free electrons of the ionosphere cause a frequency dependent phase advance or a group delay; the first-order effect can thus be almost completely removed by using dual-frequency observations. The neutral atmosphere causes a non-dispersive delay and the modeling of this effect requires the knowledge of the atmospheric properties in a tridimensional space.

The goal of this chapter is to give an overview of the main characteristics of the earth's atmosphere and to introduce the "radio meteorology" terminology. Along with the fundamentals of the composition, physics, and structure of the earth's atmosphere, a review of the different moisture variables used to express atmospheric water vapor content is also presented.

2.1. Composition

The gaseous envelope surrounding the earth's surface, bounded to it by gravitational attraction, is by definition the earth's atmosphere. It is composed of different constituents, which can be grouped under three main categories: dry air, water substance, and aerosols [Iribarne and Godson, 1973]. Other forms of classification can be found (e.g. Fleagle and Businger [1980]; Rogers and Yau [1989]), but the former leads more smoothly to the approach used in radiowave propagation, which considers the atmosphere as a mixture of two ideal gases: dry air and water vapor.

Dry air is a mixture of gases, in which nitrogen, oxygen, and argon are the major constituents and account for about 99.95% of the total volume, as shown in Table 2.1. With the exception of carbon dioxide, ozone, and other minor constituents, all the gases of this group are mixed in nearly-fixed proportions up to a height of 80-100 km. This remarkable uniformity of proportions is due to the process of mixing associated with the relative fluid motions of the air parcels. Above that limit, the influence of diffusion supersedes mixing and an increase in the proportion of lighter gases with height is observed (e.g. Iribarne and Godson [1973]; Fleagle and Businger [1980]; Barry and Chorley [1987]).

Carbon dioxide appears in variable concentration near the ground, as a result of various phenomena, such as photosynthesis, absorption and release by the oceans, industrial activities, volcanic eruptions, deforestation, and fires. Above this surface layer, it is about

Table 2.1 – Main constituents of the earth's dry atmosphere below 80 km. The values of the molecular weight (M_i) and volume fraction of each constituent (N_i) are from Lide [1997]. For the other columns: R_i represent the computed values of the specific gas constant of each constituent, that is, $R_i = R/M_i$, where R is the universal gas constant ($R = 8314.510 \pm 0.070$ J kmol^{-1} K^{-1} [Lide, 1997]); $M_i \cdot N_i$ represent the effective molecular weight of each constituent; the sum of the individual contributions yields an approximate value of 28.9644 kg kmol^{-1} for the (mean effective) molecular weight of dry air; m_i represent the mass fraction of each constituent, using the computed mean molecular weight.

Constituent		M_i (kg kmol^{-1})		R_i (J kg^{-1} K^{-1})	(kg kmol^{-1})	
Nitrogen	N_2	28.01348	0.78084	296.804	21.874	0.75520
Oxygen	O_2	31.9988	0.209476	259.838	6.7030	0.231421
Argon	Ar	39.948	0.00934	208.133	0.3731	0.0129
Carbon dioxide	CO_2	44.010	0.000314	188.923	0.0138	0.000477
Neon	Ne	20.1797	18.18 ppm	412.02	0.000367	12.67 ppm
Helium	He	4.002602	5.24 ppm	2077.28	0.000021	7.24 ppm
Krypton	Kr	83.80	1.14 ppm	99.22	0.000096	3.30 ppm
Hydrogen	H_2	2.01588	0.5 ppm	4124.5	0.000001	0.03 ppm
Ozone	O_3	47.9982	variable	173.225	-	-

0.035% by volume at present (it is increasing at about 1.5 % per year [Peixoto and Oort, 1992]), and approximately constant with height [Iribarne and Godson, 1973; Wallace and Hobbs, 1977; Ahrens, 1994].

Ozone is another of the constituents of dry air with variable concentration. The primary source of ozone is the ultraviolet solar radiation impinging on the upper layers of the atmosphere. Therefore, ozone is concentrated mainly between about 15 and 35 km

[Barry and Chorley, 1987]. Although a minor constituent of the atmosphere in respect to relative concentration, ozone plays an important role as the principal absorber and emitter of electromagnetic radiation in the earth's atmosphere. The ozone concentration is very low over the equatorial regions and increases with latitude; it varies only slightly with season in equatorial regions, but shows significant variation with season for higher latitudes, reaching maximum values in spring (see WMO [1995] for details regarding ozone variation in recent years).

Water can exist in the atmosphere in any of its three physical states: water vapor, liquid droplets and ice crystals. Water in the form of vapor is a highly variable constituent of the atmosphere, both in space and time. The main source of the atmospheric water vapor is the evaporation from bodies of water and transpiration by plants. The concentration is largest near the surface and drops to very small values at higher altitudes. On average, the quantity of water vapor above 10 km is negligible [ESSA/NASA/USAF, 1966; ISO, 1983].

The water vapor content of the atmosphere is also a function of the local geographic conditions and meteorological phenomena; its concentration is very small in the polar regions and large desert regions, with amounts of less than 1% of the volume of the air, but quite significant above tropical rain forests, reaching about 4% of the volume of the air (e.g. Lutgens and Tarbuck [1979]).

The other two forms of water are water droplets and ice crystals, of which clouds are made.

Aerosols are suspended particles of small size (such as smoke, dust, pollen, and organic matter). The presence of aerosols in the atmosphere is the result of a great number of activities, both human (e.g. industrial and urban pollution) and natural (e.g. volcanic activity and wind-raised dust).

2.2. Vertical structure

The atmosphere can be divided into a series of layers, based on the chemical composition, vertical distribution of temperature, or degree of ionization.

As regards to its chemical composition, the atmosphere is generally divided into two layers: the homosphere and the heterosphere.

The ***homosphere*** is a layer of uniform and relatively well-mixed composition, with respect to the major constituents, extending up to about 100 km (e.g. Wallace and Hobbs [1977]; Miller and Thompson [1979]; Iribarne and Cho [1980]).

The ***heterosphere*** is the layer above the homosphere, with varying composition. In this layer, molecular diffusion becomes an important process, responsible for the stratification of the gases according to their molecular weight. Positively charged particles and free electrons are a significant part of the air composition within this layer.

When the temperature distribution is used as the main property in the establishment of an atmospheric segmentation, several layers are considered.

The lowest layer of the atmosphere is the ***troposphere***. It is characterized by a general constant decrease of the temperature with increasing height of about 6.5 °C/km, on

average. The actual value of this temperature gradient varies with height and season, and geographically (see Chapter 4).

The troposphere is an unstable layer, with significant atmospheric turbulence due to vertical convection currents, particularly in the region near the earth's surface, denominated as the ***boundary layer***. The thermal structure of this layer, whose thickness can vary from tens of metres to one or two kilometres [Peixoto and Oort, 1992], is mainly controlled by the heating of the earth's surface, due to solar radiation and turbulent mixing. When the earth's surface cools, some locations may experience an abnormal increase of temperature with increasing height, especially during the night. These ***temperature inversions*** are frequent in the Arctic regions, for example, as a result of an intense radiational cooling over a snow surface. The depth of a temperature inversion is to a certain extent correlated with the length of the night and limited to ~1 km, except for the Arctic regions [Kyle, 1991].

The troposphere contains about 80% of the total molecular mass of the atmosphere (e.g. Wallace and Hobbs [1977]; Fleagle and Businger [1980]) and, as mentioned before, nearly all the water vapor and aerosols. The upper limit of the troposphere is characterized by a sudden change in the temperature gradient, a level called the ***tropopause***, which marks the transition to the stratosphere. The tropopause height is variable and depends on time and place. It typically ranges from ~7-10 km, over the polar regions, to ~16-18 km, over the tropical and equatorial regions (e.g. Cole et al. [1965]; Miller and Thompson [1979]; Iribarne and Cho [1980]; Fleagle and Businger

[1980]; Barry and Chorley [1987]). This limit varies also from season to season (higher in summer) and with the passage of air masses. The tropopause is clearly defined in the tropical regions, less well defined at mid-latitudes and can be almost absent in the polar regions, particularly in winter [Fleagle and Businger, 1980]. According to Barry and Chorley [1987], there is a correlation between the tropopause height and the sea-level temperature and pressure. Other correlations are studied in Chapter 4.

The ***stratosphere*** is the second largest layer of the atmosphere, extending upwards to ~50 km. The temperature distribution in this layer is not uniform. In the lower part (up to ~20 km) the stratosphere is approximately isothermal. Then the temperature increases gradually with the height, due to the presence of ozone, which absorbs the ultraviolet solar radiation, reaching a maximum of about 0 °C, at ~50 km [Iribarne and Cho, 1980]. The irregular distribution of ozone over the earth and its variability with the seasons leads to a variable temperature distribution. The level at which the maximum temperatures are reached is called the ***stratopause***, and it marks the transition to the next layer, the mesosphere.

The main characteristic of the ***mesosphere*** is the sharp decrease of temperature with increasing height, at a rate of approximately 3 °C/km [Miller and Thompson, 1979]. The temperature reaches a minimum of about -90 °C, at the height of ~85 km (e.g. Fleagle and Businger [1980]), the coldest point in the atmosphere. This is the level of transition to the thermosphere, called the ***mesopause***.

The ***thermosphere*** is a layer of rapidly increasing temperature, with variations associated with solar activity. The maximum temperature, reached at ~500 km, varies between about 400 °C and about 2000 °C, depending on the time of day, latitude and solar activity (e.g. Iribarne and Cho [1980]; Fleagle and Businger [1980]). Due to molecular diffusion, a high concentration of light gases can be found in this layer, making the air density very low. The process of dissociation of the molecular oxygen and other constituents is also significant in this layer; above ~130 km, most oxygen is in atomic form. The upper limit of this layer is not well defined (300 - 500 km) and is bounded by a nearly isothermal layer, the ***thermopause***.

The ***exosphere*** is defined as the region where the mean free path (average distance traveled by a molecule between two collisions) is so great that the lighter particles tend to escape from the atmosphere. The main constituents of this layer are atomic oxygen, ionized oxygen, and hydrogen atoms.

The outermost layer of the atmosphere is the ***magnetosphere***, characterized by a supremacy of the earth's magnetic field over the gravitational field in the distribution of electrons and protons. One peculiarity of this layer is the existence of the Van Allen radiation belts, which are zones of a near-permanent concentration of charged particles. Beyond this layer, the earth's atmosphere merges with that of the sun.

The ionization state of the atmosphere created by solar radiation has also been used to characterize the atmosphere.

The radiation emitted by the sun produces significant ionization in the upper atmosphere. The term ***ionosphere*** is used to designate the region of the atmosphere characterized by a strong degree of ionization, produced mainly by solar ultraviolet and corpuscular radiation. The free electrons in this layer affect significantly the propagation of the electromagnetic radiation. The ionosphere extends from ~50 km to ~1000 km, that is, it covers the region of the lower thermosphere and heterosphere.

The variability of the ionization leads to a classification of different ionospheric layers, each one with boundaries not well defined. The ionospheric boundaries and structure presented here follow Iribarne and Cho [1980].

The ***D layer*** is the ionospheric region up to ~90 km characterized by the lowest concentration of electron density (10^3–10^4 electrons/cm^3), and observed during the day only. It is composed of negative ions, positive ions and free electrons. Under normal conditions, the degree of ionization is not strong enough to interfere with the propagation of the radio waves.

The ionization on the ***E layer*** shows a high degree of correlation with the incident solar radiation, making it almost absent during the night (most of the electrons recombine with positive ions). During the day-time, the electron density is about one order of magnitude greater than that observed in the D layer (10^5 electrons/cm^3). It ranges from ~90 km to ~140 km, and is composed of positive ions and free electrons. Within this layer, a thin ionospheric layer with an augmented electron concentration is sometimes observed. Due

to its transient character, it is called ***sporadic E layer***, E_s, and is associated with quasi-periodic amplitude scintillations [Coco et al., 1995].

The highest ionospheric layer is the ***F layer***, with a lower boundary of ~140 km, which involves two regions of different characteristics. The F_1 layer is the lowest layer, which exists only during daytime. The F_2 layer is the layer within the ionosphere with the highest electron density, reaching a maximum concentration of 10^6 electrons/cm^3 at 250-500 km. Although it does not disappear during night-time, the electron density during this period decreases by about one order of magnitude. It is also very sensitive to the sunspot cycle. Further, sudden ionospheric disturbances due to coronal holes, solar flares, and magnetic disturbances can affect the behavior of this and other ionospheric layers, as a result of a significant increase in the electron density.

Below the ionosphere, the atmosphere is electrically neutral and this region is named the ***neutral atmosphere***. The neutral atmosphere includes the lower part of the stratosphere and the troposphere.

Although both the ionosphere and the neutral atmosphere affect the propagation of radio waves, the study of the resulting effects have to be addressed differently. Unlike the neutral atmosphere, the ionosphere is a dispersive medium for radio waves, and its first-order effects can be removed almost completely by using two different carrier frequencies (for discussion of residual effects see, e.g., Brunner and Gu [1991] and Bassiri and Hajj [1993]). As far as the neutral atmosphere is concerned, the effect on radio signal propagation is a function of pressure, temperature, and water vapor content. Therefore,

the profiles of these variables have to be known accurately and the underlying physics understood to properly model the effect. The following section addresses the last issue.

2.3. Equations of state

In a mixture of gases, the pressure that a particular gas would exert if it alone occupied the whole volume at the same temperature is the ***partial pressure***. If we assume that any i^{th} individual gas of the atmosphere behaves as an ideal gas, we can apply the equation of state:

$$P_i V = n_i R T, \tag{2.1}$$

where for some volume of air V, P_i is the partial pressure, T is the temperature, R is the universal gas constant (see Table 2.1), and n_i is the number of moles, for that particular constituent. As

$$n_i = \frac{m_i}{M_i},$$

where m_i is the gas mass, and M_i the corresponding molecular weight, we can express Equation (2.1) as

$$P_i V = m_i R_i T, \tag{2.2}$$

where $R_i = R/M_i$ is the specific gas constant for that particular constituent (see Table 2.1). Furthermore, if we introduce the *specific volume*, α, we get:

$$P_i \alpha = R_i T. \tag{2.3}$$

According to Dalton's law, the pressure P exerted by a mixture of k gases, each one exerting a partial pressure P_i proportional to its molecular concentration, is given by the sum of the partial pressures:

$$P = \sum_{i=1}^{k} P_i \,. \tag{2.4}$$

Consequently, for a mixture of k gases of total mass m, we have:

$$PV = mR_m T, \tag{2.5}$$

where R_m is a mean specific gas constant for the mixture. This constant is given by:

$$R_m = \frac{\sum_{i=1}^{k} m_i R_i}{m}, \tag{2.6}$$

where m_i and R_i are the mass and specific gas constant of the i^{th} component of the mixture, respectively.

Likewise, if the mean molecular weight of the mixture, M_m, given by:

$$M_m = \frac{\sum_{i=1}^{k} n_i M_i}{n} \tag{2.7}$$

is known, then

$$R_m = \frac{R}{M_m} \,. \tag{2.8}$$

If we consider dry air as a mixture of ideal gases, we can use the mean molecular weight for dry air, M_d, computed using the values given in Table 2.1 (and propagate the

uncertainties given in Lide [1997]), and obtain the (mean) specific gas constant for dry air, R_d, that is,

$$R_d = 287.06 \pm 0.01 \, J \, kg^{-1} \, K^{-1}.$$

The partial pressure due to dry air, P_d, is given by:

$$P_d = \frac{m_d R_d T}{V}, \tag{2.9}$$

where m_d is the mass of dry air. Introducing the density of the dry air, ρ_d, we obtain

$$\boxed{P_d = \rho_d R_d T}, \tag{2.10}$$

which represents the ***equation of state for dry air*** (or the ideal gas law for dry air).

The water vapor can also be treated in a first approximation as an ideal gas and, in a similar manner, using $M_w = 18.0153 \pm 0.0003$ kg kmol^{-1} for the molecular mass of water vapor [Lide, 1997], the following value for the specific gas constant for water vapor, R_w, is obtained:

$$R_w = 461.525 \pm 0.003 \, J \, kg^{-1} \, K^{-1}.$$

The partial pressure exerted by water vapor is termed the ***water vapor pressure***, e. As with the procedure used for dry air, we get:

$$e = \frac{m_w R_w T}{V}, \tag{2.11}$$

or, introducing the density of water vapor, ρ_w,

$$\boxed{e = \rho_w R_w T}, \tag{2.12}$$

which is the ***equation of state for water vapor***.

If we consider a certain volume of moist air, consisting of a mass m_d of dry air and a mass m_w of water vapor, its total density is given by:

$$\rho = \rho_d + \rho_w = \frac{m_d + m_w}{V}. \tag{2.13}$$

If the two components are well mixed, the total pressure, *P*, is:

$$P = P_d + e, \tag{2.14}$$

or, by using (2.9) and (2.11),

$$P = \left(\frac{m_d R_d + m_w R_w}{V} \right) T. \tag{2.15}$$

Substituting (2.13) in this expression,

$$P = \rho \left(\frac{m_d R_d + m_w R_w}{m_d + m_w} \right) T = \rho R_d \left[\frac{1 + \left(\frac{m_w}{m_d} \right) \cdot \left(\frac{R_w}{R_d} \right)}{1 + \left(\frac{m_w}{m_d} \right)} \right] T,$$

or

$$P = \rho R_d \left(\frac{1 + \frac{r}{\varepsilon}}{1 + r} \right) T, \tag{2.16}$$

where

$$r = \frac{m_w}{m_d} \tag{2.17}$$

is the mixing ratio (see next section), and

$$\varepsilon = \frac{R_d}{R_w} \approx 0.622 . \tag{2.18}$$

The similarity of Equation (2.16) with Equation (2.10) is well known, showing clearly that the factor in parentheses is nothing else than a correction arising from the presence of the water vapor. If we define a new variable

$$T_V = \left(\frac{1 + \frac{r}{\varepsilon}}{1 + r} \right) T , \tag{2.19}$$

we obtain the following ***equation of state for moist air***:

$$P = \rho R_d T_V . \tag{2.20}$$

The introduced variable represents the temperature that dry air would have for identical values of pressure and volume of moist air, and is denominated ***virtual temperature***.

In the physical world, neither the dry air or the water vapor are ideal gases. The departures of these mixtures of gases from ideal gas behavior are functions of the pressure and temperature and can be corrected using the compressibility factors. The inverse of the compressibility factors for dry air, Z_d^{-1}, and water vapor, Z_w^{-1}, are given by Owens [1967]:

$$Z_d^{-1} = 1 + P_d\left(57.90\times10^{-8} - \frac{9.4581\times10^{-4}}{T} + \frac{0.25844}{T^2}\right) \tag{2.21}$$

$$Z_w^{-1} = 1 + e\left(1 + 3.7\times10^{-4}\, e\right)\left(-2.37321\times10^{-3} + \frac{2.23366}{T} - \frac{710.792}{T^2} + \frac{7.75141\times10^{4}}{T^3}\right) \tag{2.22}$$

and rearranged by Thayer [1974] as:

$$Z_d^{-1} = 1 + P_d\left[57.90\times10^{-8}\left(1 + \frac{0.52}{T}\right) - 9.4611\times10^{-4}\frac{t}{T^2}\right] \tag{2.23}$$

$$Z_w^{-1} = 1 + 1650\times\left(\frac{e}{T^3}\right)\left(1 - 0.01317t + 1.75\times10^{-4}t^2 + 1.44\times10^{-6}t^3\right). \tag{2.24}$$

As before, P_d and e are respectively the partial pressures of dry air and water vapor, in hectopascals, T is the absolute air temperature, in kelvins, and the new variable t is the air temperature in degrees Celsius (T – 273.15 K; see also section 5.1.2). These units and symbols will be always assumed throughout this dissertation, unless specified. The reformulation used in Thayer [1974] allows simpler and easier computations.

2.4. Moisture variables

The determination of the amount of water vapor content in moist air is vital in many applications. In addition to the water vapor pressure, already defined in the last section, many other variables are used by meteorologists to express the water vapor content of moist air. In this section, we define some of those variables and, whenever appropriate, we establish the relations between them and the water vapor pressure, a fundamental

quantity in radio wave propagation studies. This compilation of definitions results from a comparative analysis based on different sources, namely List [1966], Fleagle and Businger [1980], Iribarne and Cho [1980], Dutton [1986], Barry and Chorley [1987], and Rogers and Yau [1989].

- **saturation vapor pressure**

For a given temperature and volume, there is a limit to the amount of water vapor this volume can hold. When this limit is reached, the water vapor will coexist in equilibrium with the condensed phase (water or ice) and the air is said to be saturated. The pressure corresponding to the state of saturation is termed ***saturation vapor pressure***. Depending on whether saturation is reached over a planar surface of water or a planar surface of ice, the saturation vapor pressure is classified respectively as over water, e_{sw}, or over ice, e_{si}. Unless specified, hereafter the saturation vapor pressure over water will be always assumed. Furthermore, hectopascal (hPa) units will always be assumed.

There is experimental evidence that the saturation vapor pressure is a function of temperature only and the functional model defining this relationship is given by the ***Clausius-Clapeyron equation*** (e.g. Iribarne and Cho [1980]; Dutton [1986]):

$$e_{sw} = e_{sw}(T) = e_{s0} \exp\left[\frac{Lv}{R_w}\left(\frac{1}{T_0} - \frac{1}{T}\right)\right], \tag{2.25}$$

where Lv is the latent heat of vaporization ($Lv \approx 2.50 \times 10^6$ J kg^{-1}, near 0 °C), e_{s0} is a reference saturation vapor pressure – usually the value of e_{sw} at 0 °C (6.11 hPa) – and T_0 is the reference temperature (273.15 K). The latent heat of vaporization is not constant,

and depends on the temperature, changing about 6% over the temperature range between –30 °C and 30 °C [Rogers and Yau, 1989].

There is a significant number of models available to compute the saturation vapor pressure, mostly based on the Clausius-Clapeyron equation. Some of the models available are analyzed in Chapter 4.

Moist air behaves differently from the ideal case of pure water vapor: the addition of water vapor to dry air results in a mixture with slightly lower average molecular weight. Therefore, for a given temperature, the saturation pressure of water vapor in moist air is different from the saturation pressure of pure water vapor. Contrary to the case of pure water vapor, the saturation vapor pressure for moist air, e'_{sw}, depends not only on the temperature but also on the pressure of the moist air. The ratio of saturation vapor pressure of moist air to that of pure water is called the ***enhancement factor***, f_w. Buck [1981] fitted several equations to the Hyland [1975] determinations of the enhancement factor; for high-accuracy applications, Buck recommends the following equation:

$$f_w = 1.00072 + 3.20 \times 10^{-6} P + 5.9 \times 10^{-10} P\, t^2 . \qquad (2.26)$$

The saturation vapor pressure of moist air can then be computed as:

$$e'_{sw} = e_{sw} f_w \qquad (2.27)$$

Figure 2.1 shows the enhancement factor for different values of pressure, and for a temperature range of [-50 °C, 50 °C], using Equation (2.26). Even for the worst scenarios of temperature extremes, and for sea-level values of pressure, the enhancement

factor is about 1.005, representing a correction to the (pure water) saturation vapor pressure of less than 0.5%. The effect of the enhancement factor in ray-tracing computations is analyzed in Chapter 5.

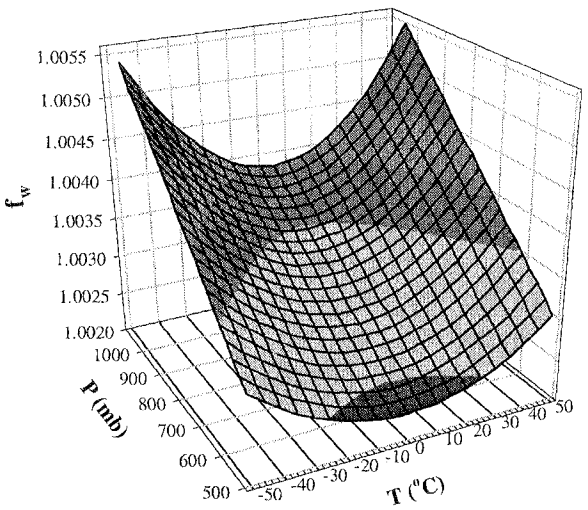

Figure 2.1 – Enhancement factor variation.

- **mixing ratio**

In a given volume of moist air, the mixing ratio, *r*, is the mass of water vapor per unit mass of dry air:

$$r = \frac{m_w}{m_d} = \frac{\rho_w}{\rho_d}. \tag{2.28}$$

We can express the mixing ratio as a function of pressure using

$$\rho_w = \frac{e}{R_w T} \tag{2.29}$$

and

$$\rho_d = \frac{P - e}{R_d T}, \tag{2.30}$$

then

$$\boxed{r = \varepsilon \frac{e}{P - e}}. \tag{2.31}$$

Since e<<P, we can approximate Equation (2.31) as

$$r \approx \varepsilon \frac{e}{P}. \tag{2.32}$$

As an example, for a total pressure of 1013.25 hPa and a water vapor pressure of 30 hPa, this approximation underestimates the mixing ratio by ~3%.

From the approximation given by Equation (2.32), we obtain:

$$\boxed{e \approx \frac{1}{\varepsilon} rP}. \tag{2.33}$$

- **specific humidity**

The ***specific humidity***, q, is defined as the mass of water vapor per unit mass of moist air:

$$q = \frac{m_w}{m} = \frac{\rho_w}{\rho}. \tag{2.34}$$

This variable can also be written as

$$q = \varepsilon \frac{e}{P - (1 - \varepsilon) e} \tag{2.35}$$

or, in a good approximation,

$$q \approx \varepsilon \frac{e}{P}. \tag{2.36}$$

For the same conditions used before, that is, $P = 1013.25\,\text{hPa}$ and $e = 30\,\text{hPa}$, this approximation underestimates q by ~1%. Using the approximate formula, we obtain:

$$\boxed{e \approx \frac{1}{\varepsilon} P q}. \tag{2.37}$$

The specific humidity is generally expressed in g/kg and has nearly the same values as the mixing ratio. They can be related with one another by the following expressions:

$$q = \frac{r}{1+r}, \tag{2.38}$$

and

$$r = \frac{q}{1-q}. \tag{2.39}$$

- **absolute humidity**

The ***absolute humidity***, δ_w, also called vapor density or water vapor concentration, is defined as the mass of water vapor per unit volume of moist air:

$$\delta_w = \frac{m_w}{V} \tag{2.40}$$

It is generally expressed in g/m^3. For these units, and using Equation (2.11), we get

$$\delta_w = \frac{e}{R_w T}, \tag{2.41}$$

that is,

$$\delta_w = 216.67\frac{e}{T}^{*}. \tag{2.42}$$

Therefore, we have:

$$\boxed{e = \frac{1}{216.67}T\delta_w}. \tag{2.43}$$

- **relative humidity**

The relative humidity, *U*, is the most widely used measure of humidity. It is defined as the ratio of the mixing ratio to the saturation mixing ratio, r_s, which is the saturation value of the mixing ratio at the same temperature and total pressure [List, 1966], and is generally expressed as a percentage:

$$U(\%) = 100\frac{r}{r_s}. \tag{2.44}$$

Since the saturation mixing ratio is a function of the temperature, the relative humidity is therefore very sensitive to temperature changes. The relative humidity can be approximated by:

$$U(\%) \approx 100\frac{e}{e_{sw}} \approx 100\frac{q}{q_s}, \tag{2.45}$$

then

---

* Conversion factor: 1 hPa J^{-1} kg = (10^2 Pa) J^{-1} (10^3 g) =10^5 (N m^{-2}) (N m)$^{-1}$ g = 10^5 g m^{-3}.

$$\boxed{e = e_{sw}\frac{U}{100}}. \tag{2.46}$$

An exact formulation is presented in Crane [1976]:

$$\boxed{e = e_{sw}\frac{U}{100}\left[1-\left(1-\frac{U}{100}\right)\frac{e_{sw}}{P}\right]^{-1}}. \tag{2.47}$$

The error committed by using the approximation (2.46) is expressed in Figure 2.2. For a standard mean sea-level value of pressure (1013.25 hPa) and for the range of temperatures of meteorological interest, the maximum percentage error occurs for high values of temperature and low values of relative humidity, reaching more than 10% (underestimation). The error is negligible for temperatures below 0 °C. The introduction of the total pressure in Equation (2.47) do not introduce any additional uncertainty in the computation of e, as this equation is insensitive to errors in total pressure.

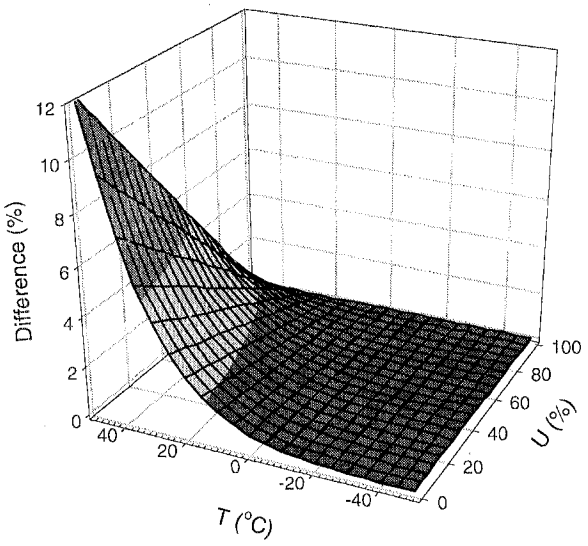

Figure 2.2 – Error surface for Equation 2.46.

- **dew-point temperature**

The dew-point temperature, T_d, of moist air, at a certain temperature, pressure, and mixing ratio, is the temperature to which the air must be cooled, keeping the pressure and mixing ratio constant, for it to reach saturation with respect to liquid water. If the saturation is reached with respect to ice, it is called ***frost-point temperature***.

Dew-point temperature can be obtained using a dew-point hygrometer [Barry and Chorley, 1987] and constitutes therefore a direct measure of the water vapor pressure, as this quantity can be defined as the saturation vapor pressure at the dew point:

$$e = e_{sw}(T_d).$$

Another method to measure the amount of water vapor in the atmosphere is via the ***dew-point depression***, t_{dew}, which is the difference between the dry-bulb temperature and wet-bulb temperature. The dry-bulb temperature, t_{dry}, is the ambient temperature of moist air, shielded from radiation, as measured by a standard thermometer. The wet-bulb temperature, t_{wet}, is the lowest temperature obtainable by ventilating a standard thermometer, whose bulb is covered with a wetted wick. At constant pressure and within a closed thermodynamic system, this happens when saturation is reached. The water vapor pressure can be computed from the wet-bulb temperature and dew-point depression using the following recommended psychrometer formula [WMO, 1987a]:

$$\boxed{e = e_{sw} - 0.000646\,(1 + 0.000944\,t_{wet})\,P\,t_{dew}}, \qquad (2.48)$$

with t_{wet} and t_{dew} in °C. This formula was used as a reference in an intercomparison test involving psychrometer formulae from several countries [WMO, 1987a].

2.5. Model atmospheres

Different approximations to the earth's atmosphere are provided by model atmospheres. Despite the limitations always involved in any type of representation, due to the actual variability of atmospheric properties, such models are nevertheless useful as references for the average properties of the earth's atmosphere. In this section we describe some such models, using a terminology based on Hess [1959].

2.5.1. Homogeneous atmosphere

The homogeneous atmosphere is a dry atmosphere for which we assume a constant density. Under this assumption, if we consider the atmosphere as a series of concentric layers of equal thickness, each of these layers will equally contribute to the total pressure at the earth's surface. However, as the surface pressure is finite, the number of layers, and thus the height of the atmosphere, has a limit called the ***scale height***, $\mathcal{H}$. To determine this height, we use the **hydrostatic equation**:

$$\mathbf{0} = -\nabla P + \rho \mathbf{g} \tag{2.49}$$

where ∇ is the gradient operator, and $\mathbf{g}$ the acceleration vector due to gravity [Dutton, 1986; Bannon et al., 1997]. Considering that all variables involved are just a function of the height component, z, we obtain the approximation

$$dP = -\rho g\, dz\,, \tag{2.50}$$

where g is the magnitude of the acceleration due to gravity and dz the differential height between two layers, separated by a differential pressure dP. As: (1) we are assuming a constant density throughout the atmosphere (we can use the sea level density, ρ_0, as a reference) and (2) we can also assume a constant acceleration of gravity (the acceleration of gravity varies only slightly with height, decreasing no more than ~1% for a height variation of ~30 km [Vanícek and Krakiwsky, 1986]), we can integrate Equation (2.50) from sea level (z=0) to $\mathcal{H}$ (top of the atmosphere), to which correspond pressures P_0 and 0, respectively, to get:

$$-\int_{P_0}^{0} dP = \int_{0}^{\mathcal{H}} \rho_0\, g\, dz \Rightarrow P_0 = \rho_0\, g\, \mathcal{H}\,, \tag{2.51}$$

or

$$\mathcal{H} = \frac{P_0}{\rho_0\, g}\,. \tag{2.52}$$

Using the equation of state for dry air, we get for the atmosphere scale height:

$$\boxed{\mathcal{H} = \frac{R_d\, T_0}{g}}\,, \tag{2.53}$$

where T_0 is the sea level temperature. For a global value of temperature (T = 273 K), the scale height is about 8 km.

The homogeneous atmosphere is physically unrealistic, as it gives a high and constant temperature lapse rate [Hess, 1959], but provides an easy way to compute the scale height, a quantity useful in radio wave propagation studies.

2.5.2. Isothermal atmosphere

An isothermal atmosphere is a dry atmosphere of constant temperature. Applying the equation of state for dry air to the hydrostatic equation, we get:

$$\frac{dP}{P} = -\frac{g}{R_d T} dz . \tag{2.54}$$

Integrating this equation from sea level to a height z, of pressure P,

$$\int_{P_0}^{P} \frac{dP}{P} = -\frac{g}{R_d T} \int_{0}^{z} dz , \tag{2.55}$$

we get

$$P = P_0 \exp\left(-\frac{gz}{R_d T} \right), \tag{2.56}$$

or, using (2.53),

$$\boxed{P = P_0 \exp\left(-\frac{z}{\mathscr{H}} \right)}. \tag{2.57}$$

This equation can therefore be used to give the profile of pressure as a function of height, which approaches zero only for $z \to \infty$. It also shows that within a region of constant g and T, pressure decreases exponentially with height.

2.5.3. Constant-lapse-rate atmosphere

A constant-lapse-rate atmosphere assumes that temperature varies linearly with height:

$$T = T_0 - \alpha z \tag{2.58}$$

where α is the temperature lapse rate, defined as the negative vertical gradient of temperature,

$$\alpha = -\frac{dT}{dz}. \tag{2.59}$$

Substituting Equation (2.10) into Equation (2.50), using Equation (2.58) for T, and integrating between sea level and a height z, we get

$$\int_{P_0}^{P} \frac{dP}{P} = -\frac{g}{R_d} \int_0^z \frac{1}{T_0 - \alpha z} dz, \tag{2.60}$$

hence

$$P = P_0 \left(\frac{T_0 - \alpha z}{T_0} \right)^{\frac{g}{R_d \alpha}} \tag{2.61}$$

or

$$\boxed{P = P_0 \left(\frac{T}{T_0} \right)^{\frac{g}{R_d \alpha}}}. \tag{2.62}$$

Since we assumed a constant lapse rate, this formula is not valid for an isothermal atmosphere, that is, for $\alpha = 0$.

2.5.4. Standard atmospheres

The atmosphere models described so far were derived under very specific assumptions and do not represent adequately the average properties of the actual atmosphere. The first attempts to develop model atmospheres closely matching those properties date from the 1920s, and are generally denominated standard atmospheres. The number of standard atmospheres now available is very broad (see, e.g., ANSI/AIAA [1990]), but not all of them fit the requisites demanded by radio wave propagation research. In order to be useful, a standard atmosphere has to provide pressure, temperature, and moisture height profiles, as well as information on latitudinal and seasonal variations of these parameters, within the neutral-atmosphere region.

A large group of standard atmospheres was developed assuming that the air is moisture-free, in hydrostatic equilibrium, and behaving as a perfect gas. The first standard atmospheres were developed in the 1920s by *ICAO* (International Civil Aviation Organization), *NACA* (National Advisory Committee for Aeronautics), and *ICAN* (International Commission for Air Navigation). Details on these atmospheres can be found in List [1966]. One of the more recent models is the *U.S. Standard Atmosphere, 1976* [NOAA/NASA/USAF, 1976], which is identical to the *ICAO Standard Atmosphere, 1964*, up to 32 km.

For this group of models, the structure of earth's atmosphere is described in terms of temperature, pressure and density profiles, usually based on certain average conditions for a specific latitude. In general, the atmosphere is divided into a series of layers, within

which a constant temperature gradient is assumed. For the height range of our interest (the neutral atmosphere, essentially up to a height of about 50 km), the atmospheres of this group differ mostly in the values of the temperature and height of the tropopause, and the value of the acceleration of gravity.

The limitations of these atmospheres are obvious: they do not provide information on the water vapor content of the atmosphere and on the seasonal and latitudinal variability of the atmospheric properties with respect to the chosen reference values. Such kinds of information is supported by the *U.S. Standard Atmosphere Supplements, 1966* [ESSA/NASA/USAF, 1966], the *U.S. AFGL Air Force Reference Atmospheres* [Cole and Kantor, 1978], and the *International Organization for Standardization (ISO) Reference Atmospheres for Aerospace Use, 1982* [ISO, 1982; 1983], hereafter designated as USSA66, AF78, and ISO82, respectively.

USSAS66 consists of a set of hydrostatically consistent supplemental atmospheres, developed for the latitudes of 15° N (tropical), 30° N (sub-tropical), 45° N (mid-latitude), 60° N (subarctic), and 75° N (arctic). The atmospheric properties are described for heights up to 120 km, except for the arctic atmospheres, which are limited to 30 km due to lack of data.

The seasonal variability is accounted for by considering regimes for January and July, except for 15° N, which is conveniently described by an annual regime, due to the small seasonal variability of the tropical atmosphere. In addition, for the subarctic and arctic atmospheres, two additional regimes are considered, to represent cold and warm

stratospheric regimes. Information on the moisture content of the atmosphere is provided by values of relative humidity.

The temperature profiles for USSA66 atmospheres (depicted in Figure 2.3), are composed of a series of layers, within which a constant temperature gradient is assumed. These profiles show the occurrence of the tropopauses, as well as the clear winter surface temperature inversions in the polar regions (see Chapter 4).

The pressure profiles are computed using the formulae of the pressure variation for an isothermal atmosphere and constant-lapse-rate atmospheres, described earlier. The surface pressure variations over the globe are very small (only a few percent), and decrease exponentially with height, at nearly the same rate in summer and winter.

For USSA66, the amount of moisture in the atmosphere is given in terms of the relative humidity, for the first 10 km.

AF78 describes seasonal, latitudinal and longitudinal variability of the atmosphere up to 90 km in a series of mean monthly atmospheric models, ranging from 0° to 90° N, with 15° interval. In the case of the North Pole, the atmosphere model is restricted to 55 km height. The longitudinal variations of temperature, pressure and density with respect to the monthly median values are described in a group of special models, restricted to 55 km height and to latitudes of 60° N and 75° N.

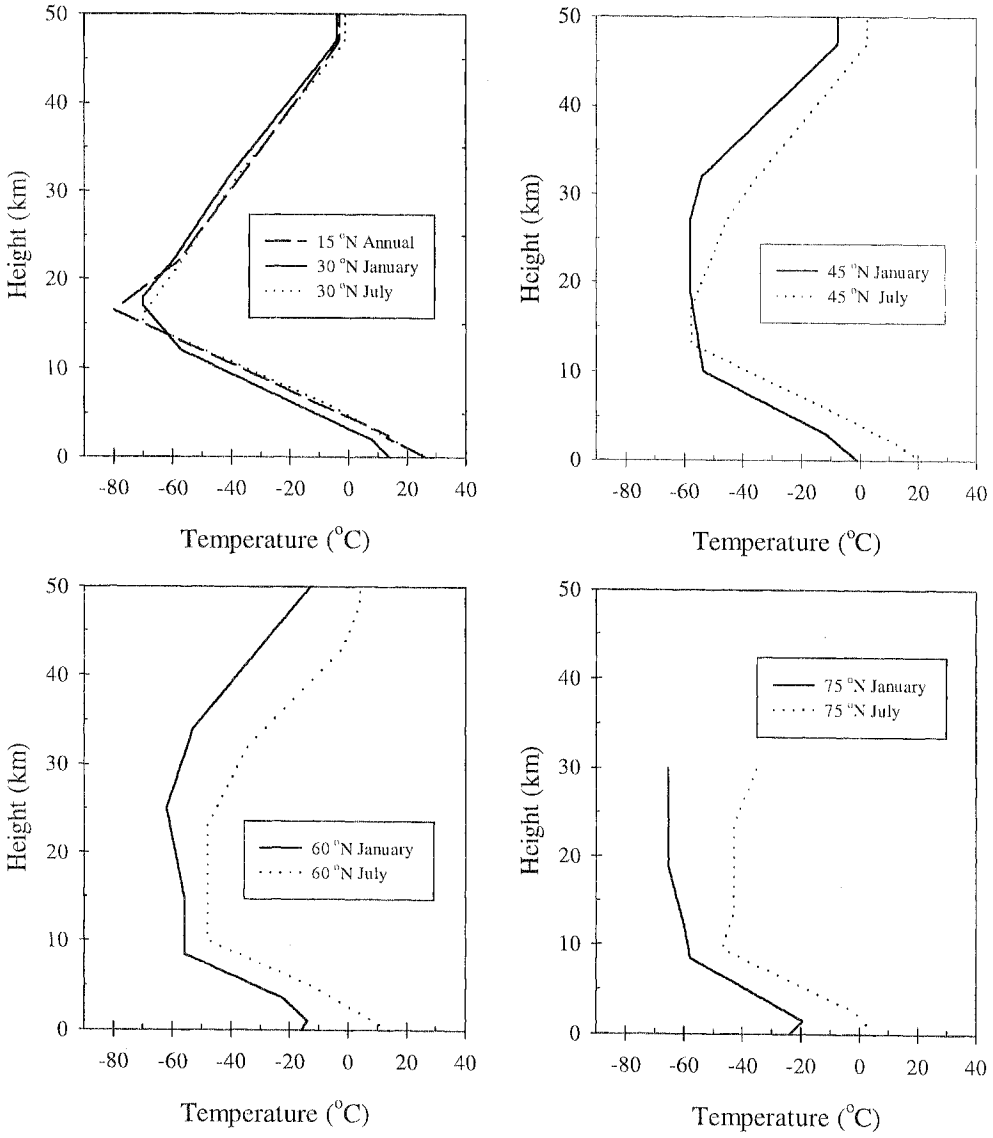

Figure 2.3 – Temperature profiles for the U.S. Standard Atmosphere Supplements, 1966, for the first 50 km.

ISO82 consists of a set of reference atmospheres, developed for latitudes of 15° N (tropical), 30° N (sub-tropical), 45° N (mid-latitude), 60° N (sub-arctic), and 80° N (sub-arctic). For all latitudes, two regimes are defined (June-July and December-January),

except for the tropical atmosphere, which has an annual regime, as in USSA66. For 60°N, reference atmospheres for cold and warm stratospheric regimes (December-January) are also presented. The pressure and temperature profiles for ISO82 are slightly different from the USSA66 profiles. As regards the moisture content, ISO82 provide values of mixing ratio, water vapor pressure (see Figure 2.4), and dew point temperature (up to the height of 10 km), for the latitudes of 10° N, 30° N, 50° N, and 70° N. The water vapor pressure is mainly concentrated in the first 2 km of the atmosphere, and shows a large latitudinal and seasonal variation.

The moist-air standard atmospheres provide a valuable source of information, and have been frequently used in a wide variety of applications, such as the development of mathematical models for propagation delay correction (e.g. Niell [1996]) and generation of reference values for assessment studies (e.g. Janes et al. [1991]). The main limitations are: (1) the fact that the atmosphere at any instant and location can behave much differently from the average conditions they represent; (2) none of them provide information for the southern hemisphere (in a first approximation it can be assumed anti-symmetrical). Even though ISO82 provides information similar to USSA66, the latitudes used to describe pressure and temperature do not match the ones used to describe the moisture content. USSA66 is therefore the most adequate and consequently most used for radiowave propagation studies, and selected in this dissertation to evaluate the ray tracing algorithm accuracy to be presented in Chapter 5.

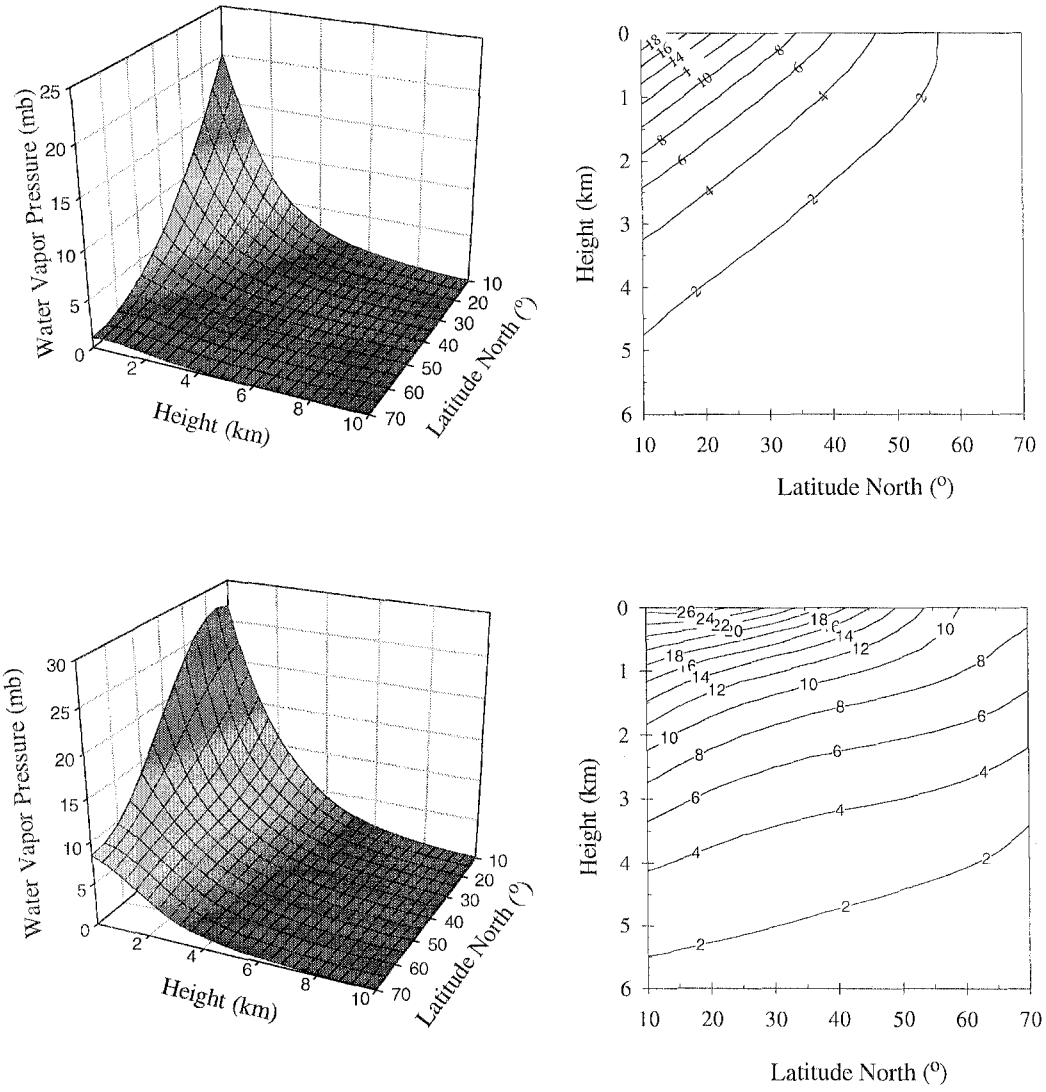

Figure 2.4 – The global distribution of water vapor pressure, as a function of latitude and height, as given by ISO82 atmospheres, for January (top plots) and July (bottom plots).

In this chapter we have presented the main features and physics of the earth's atmosphere. The variables used to describe the moisture content of the atmosphere and their relationships were reviewed, and the model atmospheres which approximate the actual earth's atmosphere were highlighted.

In the next chapter, the refraction within the neutral atmosphere will be analyzed.

3. NEUTRAL-ATMOSPHERE REFRACTION

When radio signals traverse the earth's atmosphere, they are affected significantly by the variability of the refractive index of the lower, electrically-neutral region. The refractive index is greater than unity and, consequently, it causes an excess path delay. In addition, the changes in the refractive index with varying height cause a bending of the ray. The combination of these two effects is called neutral-atmosphere refraction or propagation delay.

The neutral-atmosphere propagation delay is directly related to the refractive index (or the refractivity), as it results from its integration with respect to height. At every point of the atmosphere the refractive index of a parcel of air can be expressed as a function of atmospheric pressure, temperature, and humidity. The neutral-atmosphere propagation delay can be divided into an hydrostatic and a non-hydrostatic component and can be determined from models that approximate the atmospheric profiles.

At the zenith, and for a sea-level location, the hydrostatic component of the propagation delay is about 2.3 m and accounts for about 90% of the total delay. It can be accurately determined using surface pressure values. The wet component has a very large spatial and temporal variability and can not be accurately predicted from surface measurements of any moisture variable, as the correlation with the conditions aloft is generally very

poor. For elevation angles other than the zenith, these delays have to be projected to an arbitrary elevation angle, using a mapping function.

In this chapter, we first introduce the concept of refractivity and we review and compare models proposed for representation of refractivity profiles. Secondly, we present the ray trace equations and the terminology concerning refraction modeling. Finally, we describe a series of models used to predict the neutral-atmosphere propagation effect on radio signals.

3.1. Refractivity

The ***refractive index*** of a medium, n, is defined as the ratio of the speed of propagation of an electromagnetic wave in a vacuum, c, to the (phase) speed of propagation in the medium in question, v:

$$n = \frac{c}{v}. \tag{3.1}$$

The refractive index of a parcel of moist air is different from unity because its constituents suffer polarization induced by the electromagnetic field of the radio signals. The molecules of water vapor have a permanent dipole moment: the induced polarization produces an orientation effect, which contributes significantly to the variations of the refractive index. The dry constituents have no permanent dipole moment, but their molecules are displaced under the influence of the electromagnetic field and a dipole moment is generated. The polarization effect is related to the dielectric constant of the air, ε, which can expressed as a function of the meteorological parameters by the

following expression [Bean and Dutton, 1966]:

$$\varepsilon - 1 = K_1^* \frac{P_d^*}{T} + K_2^* \frac{e}{T}\left(A + \frac{B}{T}\right) + K_3^* \frac{P_c}{T}, \tag{3.2}$$

where K_i^* (i = 1,3), A, and B are constants, P_d^* is the partial pressure of dry gases (CO_2-free) and P_c is the partial pressure of CO_2. This formula considers the effects of non-polar gases (CO_2-free dry air), CO_2, and water vapor. If the dielectric constant is known, the refractive index can then be obtained as a function of two constants, through Maxwell's formula [Born and Wolf, 1975]:

$$n = \sqrt{\mu\varepsilon}, \tag{3.3}$$

where μ is the magnetic permeability (≈ 1, for air).

It is important to note that the refractive index is actually a complex number, the imaginary part of which corresponds to the absorption coefficient. For radio frequencies, the refraction effects are only dependent on the real part of the refractive index and, with exception of anomalous dispersion of the 22.235 GHz water vapor line and 60 GHz absorption line of oxygen, air is essentially a non-dispersive medium [Bean and Dutton, 1966; Crane, 1976]. Liebe [1985] presents a formula for refractivity that takes into account the anomalous dispersion.

As the electromagnetic waves in the atmosphere propagate just slightly slower than in a vacuum, refractive index is more conveniently expressed by another quantity, denominated ***refractivity***, *N*:

$$N = 10^6 (n - 1). \tag{3.4}$$

From Equations (3.2) and (3.3), the following expression for the refractivity can be derived [Bean and Dutton, 1966]:

$$N = K_1 \frac{P_d^*}{T} + K_2 \frac{e}{T} + K_3 \frac{e}{T^2} + K_4 \frac{P_c}{T}, \tag{3.5}$$

where K_i are constants to be determined, known as ***refractivity constants***.

Equation (3.5) can simplified to the following three-term expression by adjusting the constant K_1 determined in laboratory under CO_2-free air to include the average amount of CO_2 present in the atmosphere (see, e.g., Smith and Weintraub [1953] and Boudouris [1963]). The resulting expression is thereafter given as

$$N = K_1 \frac{P_d}{T} + K_2 \frac{e}{T} + K_3 \frac{e}{T^2}, \tag{3.6}$$

where P_d is the partial pressure due to dry gases, <u>including</u> CO_2. In fact as the partial pressure due to CO_2 is so small compared with the total pressure, the fourth term in Equation (3.5) can be just omitted, without significant influence on the accuracy of the determination of N.

If we take into account the compressibility factors to account for the non-ideal behavior of gases, we have:

$$N = K_1 \left(\frac{P_d}{T}\right) Z_d^{-1} + \left[K_2 \left(\frac{e}{T}\right) + K_3 \left(\frac{e}{T^2}\right)\right] Z_w^{-1}. \tag{3.7}$$

The first term on the right-hand side of Equation (3.7) does not depend on the water vapor content of the atmosphere and is therefore known as the ***dry component*** of the

refractivity; the terms in brackets represent the ***wet component*** of the refractivity.

The refractivity constants are determined empirically in a laboratory, by measuring the resonance frequency of a cavity into which a known quantity of gas is introduced; the obtained resonant frequency is then compared with the resonant frequency for the cavity in vacuum conditions (for details see, e.g., Boudouris [1963]; Bean and Dutton [1966]). Table 3.1 summarizes the most significant recent evaluations of the refractivity constants. In this list, some refractivity constants were converted from the original values, to be in accordance with values of pressure expressed in hectopascals. More complete tables of experimental determinations of refractivity constants can be found in Hartmann and Leitinger [1984], Hartmann [1993], and Bevis et al. [1994].

Table 3.1 – Determinations of the refractivity constants.

REFERENCE	K_1 (K hPa^{-1})	K_2 (K hPa^{-1})	K_3 (10^5 K^2 hPa^{-1})	K_2' (K hPa^{-1})
Boudouris [1963]	77.59±0.08	72±11	3.75±0.03	24±11
Smith and Weintraub [1953]	77.61±0.01	72±9	3.75±0.03	24±9
Thayer [1974]	77.60±0.01	64.79±0.08	3.776±0.004	17±10
Hill et al. [1982]	–	98±1	3.583±0.003	–
Hill [1988]	–	102±1	3.578±0.003	–

The Smith and Weintraub refractivity constants have been used extensively in radio wave propagation studies. The resulting equation for the refractivity is estimated to have an accuracy of about 0.5%, for the range of atmospheric parameters usually experienced in the earth's atmosphere and frequencies below 30 GHz [Smith and Weintraub, 1953]. For the frequency range below 20 GHz, Thayer [1974] claims an accuracy in the

determination of N ranging from ~0.02%, for dry air, to ~0.05% (extremely moist air), i.e., a significant improvement with respect to Smith and Weintraub [1953]. However, there is some controversy about Thayer's refractivity constants.

In the determination of the refractivity constants, Thayer [1974] assumed that K_2 is the same at radio and optical frequencies. Thayer claimed that this constraint results in better determination of the refractivity constants. Such hypothesis was criticized by Hill et al. [1982], who claimed that the contribution of the infrared resonances of water vapor to K_2 is ignored. In their approach, the sum of the contributions of infrared water vapor resonances is used to compute the radio refractive index. However, the calculated constants obtained differ significantly from those determined experimentally by previous researchers by several standard deviations. Although possible reasons for these discrepancies have been pointed out in their paper, this disagreement could not be satisfactorily explained and the authors recommended the use of a set of empirical refractivity constants, such as those determined by Boudouris [1963]. The values obtained by Hill [1988] showed the same disagreement as before, and the difference remains unexplained.

If we assume that the air behaves as an ideal gas, then $P_d = P - e$, and Equation (3.6) becomes:

$$N = K_1 \frac{P}{T} + (K_2 - K_1)\frac{e}{T} + K_3 \frac{e}{T^2}. \tag{3.8}$$

An additional simplification can be introduced in Equation (3.8), to give the following

two-term expression:

$$N = K_1 \frac{P}{T} + K_3^* \frac{e}{T^2}, \tag{3.9}$$

Noting that

$$K_3^* \frac{e}{T^2} = (K_2 - K_1)\frac{e}{T} + K_3 \frac{e}{T^2}, \tag{3.10}$$

we can divide both sides by (e/T) and solve for the new constant, K_3^*. We therefore obtain

$$K_3^* = T\left[(K_2 - K_1) + \frac{K_3}{T}\right]. \tag{3.11}$$

Using T = 273 K as a mean temperature value and the refractivity constants of Smith and Weintraub [1953], we get:

$$N = 77.61\frac{P}{T} + 3.73\times10^5 \frac{e}{T^2}, \tag{3.12}$$

a simplification that gives values of N within 0.02% of those obtained using the 3-term expression, for the same set of refractivity constants and temperature range of -50 °C to 40 °C [Bean and Dutton, 1966].

An alternate separation of the refractivity components was derived by Davis et al. [1985]. Using the equation of state for a non-ideal gas, we can write Equation (3.7) as:

$$N = K_1 R_d \rho_d + K_2 R_w \rho_w + K_3 \frac{e}{T^2} Z_w^{-1}. \tag{3.13}$$

Since $\rho_d = \rho - \rho_w$, Equation (3.13) may be expressed as:

$$N = K_1 R_d \rho + \rho_w \left(K_2 R_w - K_1 R_d\right) + K_3 \frac{e}{T^2} Z_w^{-1}. \tag{3.14}$$

Using the equation of state for water vapor, we have:

$$N = K_1 R_d \rho + \frac{e}{R_w T}\left(K_2 R_w - K_1 R_d\right) Z_w^{-1} + K_3 \frac{e}{T^2} Z_w^{-1}, \tag{3.15}$$

or

$$N = K_1 R_d \rho + \left[K_2 - K_1\left(\frac{R_d}{R_w}\right)\right]\frac{e}{T} Z_w^{-1} + K_3 \frac{e}{T^2} Z_w^{-1}. \tag{3.16}$$

Defining a new constant:

$$K_2' = K_2 - K_1\left(\frac{R_d}{R_w}\right) = K_2 - K_1\left(\frac{M_w}{M_d}\right), \tag{3.17}$$

we can therefore rewrite Equation (3.7) as:

$$N = K_1 R_d \rho + \left[K_2'\left(\frac{e}{T}\right) + K_3\left(\frac{e}{T^2}\right)\right] Z_w^{-1}. \tag{3.18}$$

Using the K_i values determined by Thayer [1974], and assuming independent errors in K_1 and K_2, the value for K_2' is [Davis et al., 1985]:

$$K_2' = (17 \pm 10)\ \mathrm{K\ hPa^{-1}}.$$

The high standard deviation associated with this determination, relative to the uncertainties in Thayer's values, is explained by the fact that Davis et al. [1985] used for

K_2 an uncertainty of 10 K hPa^{-1} (closer to previous experimental uncertainties) rather than the uncertainty indicated in Thayer [1974]. In Table 3.1 we present values of K_2' for the other sets of refractivity constants. The uncertainties listed for this parameter were computed using the uncertainties associated with K_1 and K_2, assuming no correlation, and exact values for the molecular weights of dry air and water vapor.

Equation (3.18) has some interesting features. Firstly, the first term of the refractivity is no longer purely "dry", as there is a contribution of the water vapor hidden in the total density; secondly, this first term became independent of the mixing ratio, a highly variable quantity; finally, the "wet component" is no longer equivalent to the wet component of the "dry/wet formalism" expressed by Equation (3.6). Although the total refractivity is equivalent in both formalisms, the different partitionings lead to different refractivity components. As opposed to "dry component", the first term of Equation (3.18) is denominated as the ***hydrostatic component*** of the refractivity, a term suggested by Davis et al. [1985] which is now widely used. The term in brackets of the Equation (3.18) is still known as "wet", as in the dry/wet formalism, which makes the term somewhat ambiguous. Therefore, we will call that term the ***non-hydrostatic component***, for the sake of clarity. Figure 3.1 shows contour plots for the non-hydrostatic component of the refractivity and for the differences between the wet component and the non-hydrostatic component, covering a wide range of temperatures and relative humidity. From this figure, it is concluded that the wet component is about 4% larger than the non-hydrostatic component.

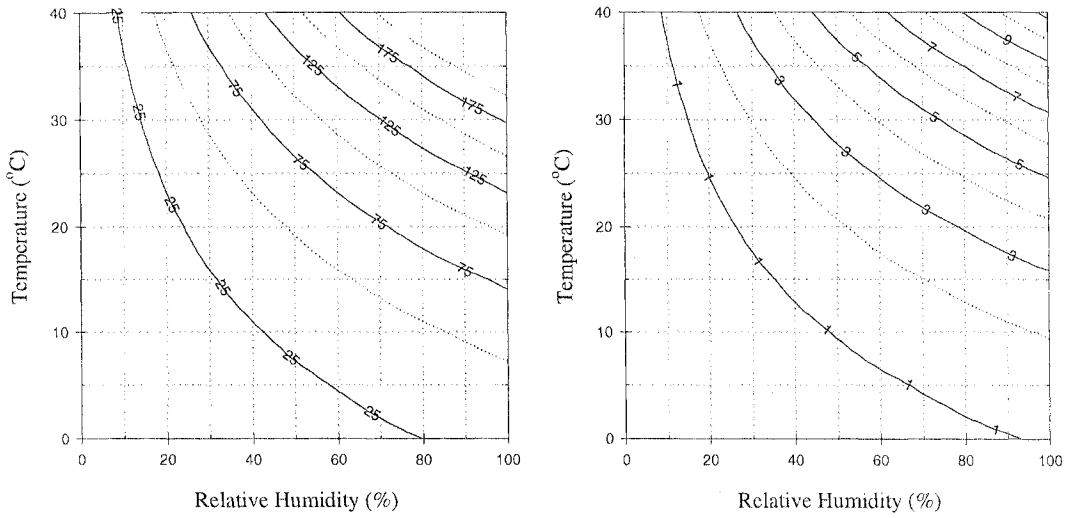

Figure 3.1 – Contour plots in refractivity units of the non-hydrostatic refractivity (left) and of the difference between the wet and the non-hydrostatic refractivities (right), for a wide range of temperature and relative humidity.

Under this new formalism, a two-term expression for the refractivity can also be derived:

$$N = K_1 R_d \rho + K_3^* \frac{e}{T^2}, \tag{3.19}$$

where K_3^*

$$K_3^* = K_2' T_m + K_3, \tag{3.20}$$

where T_m is the mean temperature (see Chapter 5). For the set of refractivity constants given by Thayer [1974], we obtain:

$$N = 77.60 R_d \rho + 3.82 \times 10^5 \frac{e}{T^2}. \tag{3.21}$$

In Chapter 5 we will investigate the implications of the choice of the different refractivity formalisms in radio wave propagation studies.

3.1.1. Refractivity models

As suggested by its dependence on the meteorological parameters, the refractivity is height dependent and different mathematical models have been proposed to represent approximately the refractivity profile. In this section, some of these models are reviewed.

The simplest model to represent the variation of N with height is the ***linear model***, also known as 4/3 earth model, proposed by Schelleng et al. [1933]. In this model, the earth is assumed to have an effective earth radius of about 4/3 of the actual earth radius (~8500 km), and allows consequently that the path of a radio ray be drawn as a straight line over such earth as opposed to curve lines over the true earth; that is, as it propagates nearly parallel to the earth's surface. Although very simple, this model describes adequately the refractivity profile in the first kilometer above the earth's surface. For higher altitudes, the refractivity gradient of the linear model is too large to adequately describe the refractivity profile.

For an average atmosphere, an accepted standard value of the vertical gradient of the refractivity, ΔN, is -39 km^{-1} [IEEE, 1990], which represents a typical median value for temperate climate regions. *The* ***Standard Radio Atmosphere*** [IEEE, 1990] is based on the linear model and is expressed as:

$$N = N_s + \Delta N(H - H_s), \tag{3.22}$$

where N_s is the (total) surface refractivity (N_s = 315, for average conditions, at sea level), H is the height above sea level, and H_s is the height above sea level of the surface point used to compute the surface refractivity (note: in this section all heights are expressed in kilometres).

At the time the analysis of refractivity profiles based on actual observations became possible, the results obtained showed that for high altitudes N decreases not linearly but approximately exponentially [Bean and Thayer, 1959; Bean and Dutton, 1966]:

$$N = N_0 \exp\left(-\frac{H}{\mathscr{H}_N}\right), \tag{3.23}$$

where N_0 is a mean sea level (total) refractivity, and $\mathscr{H}_N$ is the scale height for the (total) refractivity.

A ***single-exponential model*** was adopted, in 1958, by the IRCC (International Radio Consultative Committee) of the International Telecommunication Union as a reference atmosphere for refractivity (e.g. Bean and Thayer [1959]):

$$N = 300\exp\left(-0.139H\right). \tag{3.24}$$

This single-exponential model is still used as basis for the ***Standard Atmosphere for Refraction*** [IEEE, 1990]:

$$N = 315\exp\left(-0.136H\right). \tag{3.25}$$

The ***CRPL Reference Atmosphere, 1958*** [Bean and Thayer, 1959; Bean and Dutton, 1966] is a three-part hybrid model, which combines the linear model with the exponential

model; is based on the fact that: (1) the linear model is a very good approximation of the refractivity profile in the first km above the earth's surface; (2) the mean refractivity index gradient in the first km is inversely correlated with the surface refractivity; (3) the range of typical N values has a minimum of ~105, at the altitudes of about 8 to 9 km above sea level; (4) above this height, the refractivity profile is well described by an exponential model. The model is defined by the following set of equations:

$$N = N_s - 7.32\,\exp(0.005577\,N_s)\cdot(H - H_s) \qquad H_s \le H \le (H_s + 1\,\text{km})$$

$$N = N_1 \exp\left\{-\frac{[(H-1) - H_s]}{8 - H_s}\,\ln\left(\frac{N_1}{105}\right)\right\} \qquad (H_s + 1\,\text{km}) \le H \le 9\,\text{km} \qquad (3.26)$$

$$N = 105\exp\{-0.1424(H-9)\}\,, \qquad H \ge 9\ \text{km}$$

where N_1 is the value of the refractivity at 1 km above the surface. The profile is piece-wise continuous.

The ***CRPL Exponential Reference Atmosphere, 1958*** [Bean and Thayer, 1959] is a simplification of the above model, by considering a single exponential model, given by:

$$N = N_s \exp\left\{-\ln\left(\frac{N_s}{N_1}\right)\cdot(H - H_s)\right\}. \qquad (3.27)$$

This model gives a good representation of the refractivity for the first 3 km, but gives low values of N for higher altitudes. The profiles for a selected number of refractivity models are presented in Figure 3.2.

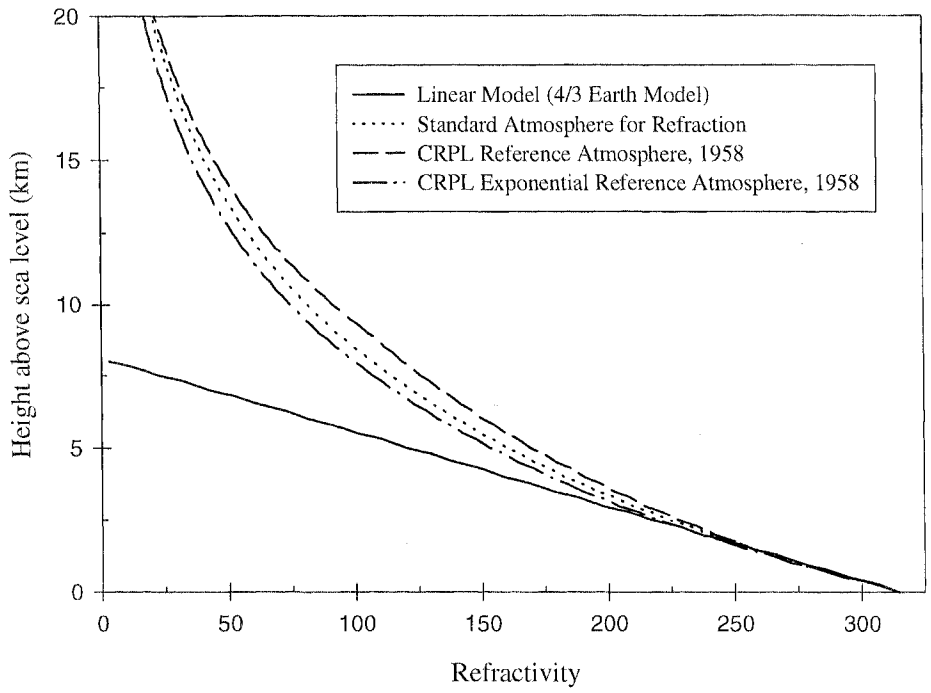

Figure 3.2 – Refractivity profile for different models, for heights below 20 km.

All these models do not separate the two components of refractivity. As the height variation of each of these components is different, a model describing the individual refractivity profiles should more accurately represent the refractivity profiles than a single exponential profile. A ***bi-exponential model*** was proposed by Bean [1961]:

$$N = N_{ds} \exp\left(-\frac{H}{\mathscr{H}_{Nd}}\right) + N_{ws} \exp\left(-\frac{H}{\mathscr{H}_{Nw}}\right), \tag{3.28}$$

where N_{ds} and N_{ws} are the dry and wet surface refractivity components, and $\mathscr{H}_{Nd}$ and $\mathscr{H}_{Nw}$ are the dry and wet scale heights, respectively. One advantage of the bi-exponential model is that it attempts to account for the different scale heights of the dry and wet

components of moist air. Bean presents some typical average values of N_{ds}, N_{ws}, $\mathscr{H}_{Nd}$ and $\mathscr{H}_{Nw}$.

In order to better accommodate the changes in lapse rate above the tropopause, Bean et al. [1966] modified the bi-exponential model and defined a ***three-exponential model***, in which two exponentials for the dry component of the refractivity are proposed: a tropospheric dry component and a stratospheric dry component. The model is expressed as:

$$N = N_{d0}\exp\left(-\frac{H}{\mathscr{H}_{Nd}}\right) + N_{w0}\exp\left(-\frac{H}{\mathscr{H}_{Nw}}\right) \qquad \text{if } H \le H_t$$

$$N = N_{d0}\exp\left(-\frac{H_t}{\mathscr{H}_{Nd1}} - \frac{H - H_t}{\mathscr{H}_{Nd2}}\right) + N_{w0}\exp\left(-\frac{H}{\mathscr{H}_{Nw}}\right), \qquad \text{if } H > H_t \quad (3.29)$$

where N_{d0} and N_{w0} are the dry and wet mean sea level refractivity components, $\mathscr{H}_{Nd1}$ is the tropospheric dry refractivity scale height, $\mathscr{H}_{Nd2}$ is the stratospheric dry refractivity scale height, and H_t is the tropopause height. All the parameters needed in the application of this model can be roughly estimated from the proposed seasonal world maps [Bean et al., 1966].

As already seen in Chapter 2, for an isothermal atmosphere (i.e. an atmosphere for a lapse rate approaching zero) the pressure decreases exponentially with height and therefore the refractivity profile approaches an exponential. Hopfield [1969] concluded that if the air temperature varies linearly with the height at a constant lapse rate, the refractivity profile

is a polynomial function of the height rather than exponential, with a degree associated with the value of the lapse rate. The general expression obtained by Hopfield is:

$$N_d = N_{ds}\left(\frac{H_d^e - H}{H_d^e}\right)^{\mu} \tag{3.30}$$

$$N_w = N_{ws}\left(\frac{H_w^e - H}{H_w^e}\right)^{\mu}, \tag{3.31}$$

where

$$\mu = \frac{g}{R_d \alpha} - 1,$$

and H_d^e and H_w^e are the dry and wet equivalent heights (defined as the height above the station at which N_d and N_w are zero, respectively; that is, $H_d^e \equiv H_d^e - H_s$ and $H_w^e \equiv H_w^e - H_s$), and g is assumed constant.

Helen Hopfield selected $\mu = 4$, which corresponds to $\alpha \approx 6.8$ K/km, a value considered "normal" in the troposphere. The quartic expression was also found to be "*a reasonably good approximation to the usual decrease of N_w with heights*" [Hopfield, 1969] and the two refractivity profiles can therefore be written as (for heights below the associated equivalent heights, otherwise $N_d = N_w = 0$):

$$N_d = N_{ds}\frac{\left(H_d^e - H\right)^4}{\left(H_d^e\right)^4} \tag{3.32}$$

and

$$N_w = N_{ws} \frac{\left(H_w^e - H\right)^4}{\left(H_w^e\right)^4}. \tag{3.33}$$

She also investigated different approaches to express the equivalent dry height and concluded [Hopfield, 1969] that H_d^e could be expressed as a function of the latitude of the station φ, according to the following relation:

$$H_d^e = 43.130 - 5.206 \sin^2 \varphi, \tag{3.34}$$

where H_d^e is given in kilometres. Based on one-year sets of radiosonde data for different locations, from Alaska to Antarctica, the equivalent dry height was later expressed as a function of the surface temperature instead [Hopfield, 1971]. The new relation is:

$$H_d^e = 40.082 + 0.14898\, t_s, \tag{3.35}$$

where t_s is the surface temperature in °C.

An improved set of coefficients was proposed in Hopfield [1972]:

$$H_d^e = 40.136 + 0.14872\, t_s. \tag{3.36}$$

Hopfield did not find a satisfactory value for the wet equivalent height and its variations were never fully understood [Hopfield, 1978; Hopfield, 1979]. In Hopfield [1969], the wet equivalent height is postulated to be 12.0 km. In Hopfield [1971], the values range from 8.6 km to 11.5 km, and a linear relation with the temperature was proposed:

$$H_w^e = 13.268 - 0.09796\, t_s. \tag{3.37}$$

3.2. Neutral-atmosphere propagation delay: a definition.

The refractive index within the neutral atmosphere plays an important role in the propagation of radio waves. On one hand, the velocity of propagation of a radio signal is reduced when approaching the earth's surface, as the refractive index is higher than unity; on the other hand, the continuous variation of the refractive index causes a deviation of its trajectory from a straight line, a direct consequence of **Fermat's principle**, or the principle of least time (see e.g. Born and Wolf [1975]).

Fermat's principle states that the travel time of light (or any electromagnetic wave) between two arbitrary points, *dt*, is stationary with respect to neighboring paths, that is:

$$\delta \int_{ray} dt = 0 , \tag{3.38}$$

where the integration is performed along the ray path. In terms of path length, we have:

$$\delta \int_{ray} c\,dt = 0 , \tag{3.39}$$

where c is the speed of light in vacuum. As

$$c\,dt = c\,\frac{ds}{v} = n\,ds , \tag{3.40}$$

where ds is a differential element of length along the ray path and v the speed of propagation of the ray in the specific propagation medium, we can also state the variational equation for Fermat's principle as:

$$\delta \int_{ray} n\,ds = 0, \tag{3.41}$$

where $n = n(s)$. In this equation, the integral

$$L = \int_{ray} n\,ds \tag{3.42}$$

is the so-called optical path length or, in more generic terms, the **electromagnetic path length**. As can be seen in Figure 3.3, the trajectory of a ray approaching the vicinity of the earth's surface will penetrate through atmospheric layers of different refractivities; consequently, it will change its direction, in order to follow a stationary path: the resulting path is curved and concave downwards, in general. Therefore, and in terms of distance, the electromagnetic path between any two points in the atmosphere is longer than the corresponding straight-line path or **geometric path**, whose length G, is defined as:

$$G = \int_{vac} ds, \tag{3.43}$$

where the integration is now performed in vacuum.

We define **neutral-atmosphere propagation delay**, d_{na}, as the difference between the electromagnetic path length and the geometric path length:

$$d_{na} = \int_{ray} n\,ds - \int_{vac} ds\,. \tag{3.44}$$

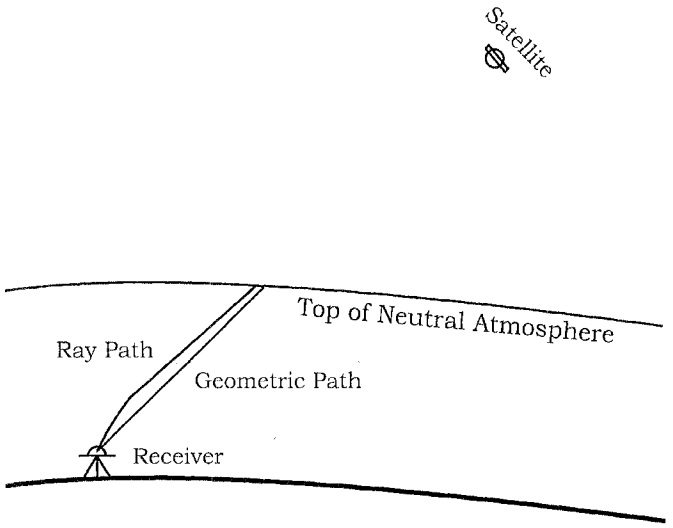

Figure 3.3 – The bending of the path of a radio wave. Due to variations in the refractive index, the ray follows a curved path.

This terminology is not universal and different terms have appeared in literature, such as atmospheric propagation delay, tropospheric (propagation) delay, tropospheric refraction, excess (propagation) path, and path delay. Some of these terms are unfortunately misleading, a fact that will be better understood if we split the two components of the delay embodied in Equation (3.44).

Let *S* be the geometric length of the electromagnetic path followed by the ray, that is:

$$S = \int_{ray} ds. \tag{3.45}$$

Using Equation (3.44) we get:

$$d_{na} = \int_{ray} n\,ds - \int_{ray} ds + \int_{ray} ds - \int_{vac} ds$$

or

$$d_{na} = \int_{ray} (n-1)\,ds + \left[\int_{ray} ds - \int_{vac} ds \right]. \qquad (3.46)$$

In this equation, the first term on the right-hand side is the excess path length due to the delay experienced by the signal, or simply **excess path delay** (also called range error), ΔL; the second term is the delay due to the bending of the ray, called **geometric delay**, ray bending or angular bending, τ. Therefore, our definition of neutral-atmosphere propagation delay encompasses both the excess path delay (although some authors use this term to include the geometric delay) and the geometric delay. The term tropospheric delay is frequently used to designate the neutral-atmosphere delay. Although not totally correct, the designation is well accepted, as the major contribution to the neutral-atmosphere propagation delay comes from the troposphere; in particular, almost all the water vapor occurs within the troposphere. Because the term refraction includes implicitly the excess path delay and the ray bending, it also works well as an alternative designation to propagation delay.

The separation of the neutral-atmosphere propagation delay into two components is advantageous, as the geometric delay is only significant for radio signals coming from low elevation angles (below about 10°); furthermore, for a horizontally stratified atmosphere, S and G are identical in the zenith direction and the geometric delay is zero.

The next logic step is to derive an expression for the neutral-atmosphere propagation delay. In order to derive such an expression, we have to assume the knowledge of the refractive index at every position in a three-dimensional atmosphere. Under this

assumption, a solution can be sought in the field of variational calculus, by solving the Euler-Lagrange equation. Integral expressions have been derived by, e.g., Wachowsky [1973] and Davis [1986], upon which the development presented in Appendix I is based. From this development we obtain the following expression:

$$d_{na} = \int_{r_s}^{r_a} \frac{(n-1)nr}{\sqrt{n^2 r^2 - n_s^2 r_s^2 \cos^2\theta_s}} dr + \int_{r_s}^{r_a} \left(\frac{nr}{\sqrt{n^2 r^2 - n_s^2 r_s^2 \cos^2\theta_s}} - \frac{r}{\sqrt{r^2 - r_s^2 \cos^2\varepsilon}} \right) dr \quad (3.47)$$

where θ is the refracted (apparent) elevation angle and ε is the geometric (true) elevation angle.

In general, the direct integration of Equation (3.47) is not possible, as the refractivity profile along the ray path is not known. Therefore it has to be numerically integrated (if discrete values of the refractivity profile are available) or approximated analytically by a model. The first solution will be studied in Chapter 5.

Before looking into the analytical approximations (modeling), let us consider the particular case for which the incoming signal arrives from the zenith direction ($\varepsilon = 90°$). In this case, as we are assuming a spherically symmetrical atmosphere, there is no ray bending and Equation (3.47) becomes:

$$d_{na}^{z} = \int_{r_s}^{r_a} (n-1) dz , \quad (3.48)$$

or

$$d_{na}^{z} = 10^{-6} \int_{r_s}^{r_a} N dz , \quad (3.49)$$

where the symbol "z" is used to denote integration in the zenith direction.

The delay just defined is named the ***neutral-atmosphere total zenith delay***, or simply the ***zenith delay***. If we consider the refractivity to be composed of a hydrostatic and a non-hydrostatic component, the zenith delay can also be split into two components, termed the ***zenith hydrostatic delay*** and ***zenith non-hydrostatic delay*** (or dry and wet, if the dry/wet formalism is used). Under this consideration, Equation (3.49) becomes:

$$d_{na}^{z} = 10^{-6} \int_{r_s}^{r_a} N_h \, dz + 10^{-6} \int_{r_s}^{r_a} N_{nh} \, dz \,, \tag{3.50}$$

or symbolically,

$$d_{na}^{z} = d_{h}^{z} + d_{nh}^{z} \,, \tag{3.51}$$

where d_h^z represents the zenith hydrostatic delay and d_{nh}^z represents the zenith non-hydrostatic delay.

Another situation for which we have no bending is when we assume a flat earth and a constant refractivity; in this case, the neutral-atmosphere propagation delay at any elevation angle can be related to the zenith delay by the following expression:

$$d_{na} = d_{na}^{z} \csc(\varepsilon) \,. \tag{3.52}$$

The propagation delay obtained using this expression, usually recognized as the "cosecant law", is obviously not very accurate, as it relies on invalid assumptions: a flat earth and constant refractivity. Nevertheless, it suggests that it is possible to express the neutral-

atmosphere propagation delay as a product of the zenith delay and a function that relates this delay to the delay at other elevation angles, that is,

$$d_{na} = d_{na}^{z}\, m(\varepsilon)\,. \tag{3.53}$$

This expression defines a ***mapping function***, $m(\varepsilon)$. This particular mapping function maps the total zenith delay. However, as the zenith delay can be expressed as the sum of the two components, mapping functions can be developed in order to map separately the hydrostatic and the non-hydrostatic component. Therefore, in general we have:

$$\boxed{d_{na} = d_{h}^{z} \cdot m_{h}(\varepsilon) + d_{nh}^{z} \cdot m_{nh}(\varepsilon)}\,, \tag{3.54}$$

where $m_h(\varepsilon)$ is a ***hydrostatic mapping function***, and $m_{nh}(\varepsilon)$ a ***non-hydrostatic mapping function***.

3.3. Neutral-atmosphere propagation delay modeling

In the previous section, it was suggested that the integral expression for the neutral-atmosphere propagation delay can be approximated by initially finding closed-form analytical models for the zenith delay and then by mapping this delay to the elevation angle of the incoming signal, using a mapping function. In this section, we review a very significant number of analytical models reported in the scientific literature in the last few decades. The formalism inherent to each model in the analysis is maintained in accordance with their original formulation.

3.3.1. Hydrostatic and dry zenith delay models

Previously, we have defined the zenith hydrostatic delay as

$$d_h^z = 10^{-6} \int_{r_s}^{r_a} N_h \, dz \,, \tag{3.55}$$

or, by using Equation (3.18),

$$d_h^z = 10^{-6} K_1 R_d \int_{r_s}^{r_a} \rho \, dz \,. \tag{3.56}$$

Using Equation (2.50), we have

$$\int_{r_s}^{r_a} \rho \, dz = \int_{r_a}^{r_s} \frac{dP}{g} dz \,, \tag{3.57}$$

or

$$\int_{r_s}^{r_a} \rho \, dz = \frac{P_s}{g_m} \,, \tag{3.58}$$

where g_m is the acceleration due to gravity at the center of mass of the vertical column of air, and P_s is the surface pressure; hence:

$$d_h^z = 10^{-6} K_1 R_d \frac{P_s}{g_m} \,. \tag{3.59}$$

The modeling of the zenith hydrostatic delay is therefore straightforward, and models can only differ due to the choice of the refractivity constant and on the modeling of the height and latitude dependence of acceleration of gravity. Models based on this theoretical

approach were developed by Saastamoinen [1973] – later modified by Davis et al. [1985] – and Baby et al. [1988], for example. Hopfield developed zenith dry models based on the quartic refractivity profile. A brief summary of these models is given below. For the sake of conciseness and intercomparison, the formulations for all models will be presented to be conformable with the following units: metres, for delay; hectopascals, for values of pressure; kelvins, for temperature; kelvins/metre, for temperature lapse rate; metres, for heights; percentage, for relative humidity. Furthermore, the subscript "s" is used to denote surface values or values relative to the station (as opposed to sea-level values).

- **Saastamoinen**

Saastamoinen [1973] found that g_m can be expressed (in ms^{-2}) as

$$g_m = 9.784(1 - 0.0026\cos 2\varphi - 0.00000028H_s), \tag{3.60}$$

where φ is the latitude of the station and H_s is the station height above sea level, in metres. Saastamoinen used the refractivity constant given by Essen and Froome. Using Equation (3.59) and simplifying the relationship for standard conditions, he obtained:

$$\boxed{d_h^z = \frac{0.002277\,P_s}{(1 - 0.0026\cos 2\varphi - 0.00000028H_s)}}. \tag{3.61}$$

- **Davis et al.**

Davis et al. [1985] used the K_1 refractivity constant given by Thayer [1974], and the "improved version" of the Saastamoinen model became:

$$\boxed{d_h^z = \frac{0.0022768\,P_s}{(1 - 0.0026\cos 2\varphi - 0.00000028\,H_s)}}. \tag{3.62}$$

- **Baby et al.**

Baby et al. [1988] suggested the acceleration of gravity be expressed as:

$$g_m = \frac{g_s}{1 + \dfrac{2}{r_s \sigma(\mu + 1)}}. \tag{3.63}$$

In this equation, g_s is the surface gravity at the station,

$$\mu = \frac{g_s}{R_d \alpha}\left(1 - \frac{2}{r_s \sigma}\right), \tag{3.64}$$

$$\sigma = \frac{\alpha}{T_s}, \tag{3.65}$$

and r_s is the mean geocentric radius of the station, in metres, that is,

$$r_s = r_0 + H_s,$$

where r_0 is the earth radius (the authors suggested r_0 = 6 378 000 m).

Combining (3.63) with (3.59), and using the K_1 refractivity constant given in Bean and Dutton [1966] they obtained:

$$\boxed{d_h^z = \frac{0.022277 P_s}{g_s}\left(1 + \frac{2}{r_s \sigma(\mu + 1)}\right)}. \tag{3.66}$$

The reader should be aware of a few typographical errors and inconsistencies in Baby et al. [1988].

- **Hopfield**

A different strategy was followed by Hopfield [1969], who assumed that the theoretical dry refractivity profile could be expressed by the quartic model:

$$N_d = N_{ds} \frac{\left(H_d^e - H\right)^4}{\left(H_d^e\right)^4}. \tag{3.67}$$

Using Equation (3.55), the integration with respect to height leads to

$$d_d^z = 10^{-6} N_{ds} \frac{H_d^e}{5}. \tag{3.68}$$

Hopfield based her models on the two-term expression given by Equation (3.9) and the refractivity constant determined by Smith and Weintraub [1953]; therefore, the final expression is given by (with the equivalent height given in metres):

$$\boxed{d_d^z = 77.6\times10^{-6} \frac{P_s}{T_s} \frac{H_d^e}{5}}. \tag{3.69}$$

Different models can therefore be obtained, depending on the choice of the expression for the dry equivalent height (see section 3.1.1).

3.3.2. Non-hydrostatic and wet zenith delay models

The approach to be followed in the development of a zenith non-hydrostatic delay model is similar to the one used in the previous paragraph. By definition, the zenith non-hydrostatic delay is given by

$$d_{nh}^{z} = 10^{-6} \int_{r_s}^{r_a} N_{nh}\, dz\,, \tag{3.70}$$

or, using Equation (3.18) and ignoring the compressibility factor,

$$d_{nh}^{z} = 10^{-6} \int_{r_s}^{r_a} K_2' \left(\frac{e}{T} \right) + K_3 \left(\frac{e}{T^2} \right) dz\,. \tag{3.71}$$

Whereas the hydrostatic component of the tropospheric delay can be determined very accurately as a function of the surface pressure, assuming the condition of hydrostatic equilibrium, the non-hydrostatic component requires a water vapor profile, which generally shows no strong dependence on the surface conditions. Due to the difficulty of handling this problem, a large number of wet and zenith non-hydrostatic delay models have been attempted, and the most important of these are described herein.

- **Hopfield**

Hopfield [1969, 1971, 1972] followed the same procedure she used to derive the dry zenith delay, and based her wet zenith delay models on the quartic atmospheric profile. In a similar fashion to the dry zenith delay approach, we get:

$$\boxed{d_w^z = 10^{-6} N_{ws} \frac{H_w^e}{5}}\,, \tag{3.72}$$

where the wet component of the surface refractivity is the second term of the Smith and Weintraub two-term expression, that is:

$$N_{ws} = 3.73 \times 10^5 \frac{e_s}{T_s^2}\,. \tag{3.73}$$

- **Saastamoinen**

Saastamoinen [1973] assumes that there is a linear decrease of temperature with height, and that the water vapor pressure decreases with height. This variation is described by the following law:

$$e = e_s \left(\frac{T}{T_s} \right)^{\frac{\nu g}{R_d \alpha}}, \tag{3.74}$$

where ν is a numerical coefficient to be determined from local observations. Under these assumptions, Saastamoinen obtained:

$$\int_{r_s}^{r_a} \frac{e}{T} \, dz = \frac{R_d}{\nu g} e_s \tag{3.75}$$

and

$$\int_{r_s}^{r_a} \frac{e}{T^2} \, dz = \frac{R_d}{\nu g - \alpha R_d} \frac{e_s}{T_s}. \tag{3.76}$$

Substituting (3.75) and (3.76) in (3.71), we get:

$$d_w^z = 10^{-6} \left[\left(K_2 - K_1 \frac{R_d}{R_w} \right) \frac{R_d}{\nu g} + \frac{K_3}{T_s} \left(\frac{R_d}{(\nu g - \alpha R_d)} \right) \right] e_s, \tag{3.77}$$

where the variables involved can be chosen to represent the local conditions.

Using the refractivity constants by Essen and Froome and for mid-latitudes and average conditions, Saastamoinen obtained the following simplified model:

$$\boxed{d_w^z = 0.002277\left(\frac{1255}{T_s}+0.05\right)e_s}. \tag{3.78}$$

- **Chao**

In 1971, Chao derived a zenith wet delay model based upon the application of the hydrostatic law to the water vapor, and the ideal gas law [Chao, 1971a]. As these assumptions lead to unreasonable results when compared against the obtained using radiosonde data, Chao replaced the ideal gas law equation of state by the adiabatic law

$$e = k^{\beta}\rho_w^{\beta},$$

where β is the specific heat ratio (~1.3 for water vapor), and obtained the following expression [Chao, 1973]:

$$\boxed{d_w^z = 4.70\times10^2\frac{e_s^{1.23}}{T_s^2}+1.71\times10^6\frac{e_s^{1.46}}{T_s^3}\alpha}. \tag{3.79}$$

This model is not very sensitive to the temperature lapse rate and the use of a mean value of α (e.g. 0.0065 K km^{-1}) has no significant implications in the accuracy of the model.

- **Callahan**

The model developed by Callahan [1973] assumes a linear temperature lapse rate and is based on an empirical exponential model of the water vapor pressure as a function of height:

$$e = e_s\exp\left(-aH-bH^2\right), \tag{3.80}$$

where a = 0.248 km^{-1} and b = 0.048 km^{-2} are nominal values (H is the height above the

surface, in kilometres). In its full form the model is very complex, but the following simplified version can be obtained for a set of nominal values:

$$\boxed{d_w^z = \frac{1035\, e_s}{T_s^{\,2}}} \tag{3.81}$$

- **Berman**

In the derivation of the several wet zenith delay models, Berman [1976] assumes that: (1) the wet refractivity is zero at the tropopause (11 km); (2) the temperature decreases at a constant rate α; (3) relative humidity is constant with altitude and equal to its value at the surface. Under these assumptions, Berman derived the "Berman 70" model:

$$\boxed{d_w^z = \frac{0.373}{\alpha\,(B - AC)}\left(1 - \frac{C}{T_s}\right)^2 e_s}, \tag{3.82}$$

where U_s is the relative humidity (%),

$$e_s = 0.061 U_s \exp\left(\frac{AT_s - B}{T_s - C}\right), \tag{3.83}$$

A = 17.1485,

B = 4684.1,

C = 38.45.

The derivation of other improved Berman models are based on the existence of a strong correlation between the ratios of the wet and zenith hydrostatic delays and the corresponding refractivities:

$$\frac{d_w^z}{d_d^z} \approx K \cdot \left(\frac{N_w}{N_d} \right), \tag{3.84}$$

where K is a constant to be determined.

These new models, named "Berman 74", "Berman (D/N)", and "Berman (TMOD)", are of the form:

$$\boxed{d_w^z = 10.946\, K \left(\frac{e_s}{T_s} \right)}. \tag{3.85}$$

The values of K for the different models are shown in Table 3.2.

In the "Berman (D/N)" model, two coefficients are determined, one to be applied to day profiles, the other to night profiles. Berman found a significant improvement of the separate day-night profile over the composite "Berman 74". The "Berman (TMOD)" profile is an attempt to moderate the systematic diurnal surface variations, producing similar results to the "Berman (D/N)" profile.

Table 3.2 – The value of K for the Berman wet zenith delay models.

	Berman 74	**Berman (D/N)**	**Berman (TMOD)**
K	0.3224	0.2896 (day) 0.3773 (night)	0.3281

- **Ifadis**

The set of models derived by Ifadis [1986] is based on the fact that there is a linear correlation between the zenith non-hydrostatic delay and the surface meteorological

parameters, although weak. A set of models dependent on the season, climate and a global model were derived. The global model is given by:

$$\boxed{d_w^z = 0.00554 - 0.880\times10^{-4}\left(P_s - 1000.0\right) + 0.272\times10^{-4}\, e_s + 2.771\left(\frac{e_s}{T_s}\right)}. \quad (3.86)$$

- **Askne and Nordius**

Askne and Nordius [1987] derived a two-parameter closed form model, which attempts to model seasonal and climatic variations of the zenith non-hydrostatic delay. They assumed that the water vapor pressure decreases with height, at a much faster rate than the total pressure, and according to the power law:

$$e = e_s\left(\frac{P}{P_s}\right)^{\lambda+1}, \quad (3.87)$$

where λ is a parameter dependent on season and latitude. Therefore, the zenith non-hydrostatic wet delay is expressed as:

$$d_{nh}^z = 10^{-6}\left(K_2' + \frac{K_3}{T_m}\right)\frac{e_s}{P_s}\int_{r_s}^{r_a}\left(\frac{P}{P_s}\right)^{\lambda}\frac{P}{T}dz. \quad (3.88)$$

The evaluation of the integral after some manipulation leads to:

$$\boxed{d_{nh}^z = 10^{-6}\left(K_2' + \frac{K_3}{T_m}\right)\frac{R_d}{(\lambda+1)g_m}e_s}, \quad (3.89)$$

where the mean temperature is expressed as

$$T_m = T_s\left(1 - \frac{\alpha R_d}{(\lambda+1)g_m}\right). \tag{3.90}$$

As pointed out in their paper, this formula agrees with the one derived by Saastamoinen, for $\alpha = 0.0062\ \mathrm{K\,m^{-1}}$ and $\lambda = 3$.

The zenith non-hydrostatic delay is especially sensitive to the variations in λ, and the authors suggested that both α and λ should be chosen to fit the location and season. As options to obtain these parameters, the authors suggested the values of λ given in Smith [1966] (see Table 3.3), whereas the values of α may be estimated from radiosonde statistics, if available (see also Chapter 4). Ifadis [1993] estimated this parameter for a number of sites for stations located mainly in the northern hemisphere and concluded that the annual variation for λ is characterized, in general, by a sinusoidal curve.

Table 3.3 – Values of the empirical coefficient λ [Smith, 1966].

φ (°N)	SEASON				Annual Mean
	Winter	Spring	Summer	Autumn	
0-10	3.37	2.85	2.80	2.64	2.91
10-20	2.99	3.02	2.70	2.93	2.91
20-30	3.60	3.00	2.98	2.93	3.12
30-40	3.04	3.11	2.92	2.94	3.00
40-50	2.70	2.95	2.77	2.71	2.78
50-60	2.52	3.07	2.67	2.93	2.79
60-70	1.76	2.69	2.61	2.61	2.41
70-80	1.60	1.67	2.24	2.63	2.03
80-90	1.11	1.44	1.94	2.02	1.62
Mean	**2.52**	**2.64**	**2.62**	**2.70**	**2.61**

- **Baby et al.**

Baby et al. [1988] used the two-term expression given by Equation (3.19) to represent the refractivity, and refractivity constants from Bean and Dutton [1966]. Two types of models were proposed by Baby et al.. The first type is based on the assumptions that the relative humidity is constant and equal to its surface value up to a height H_m, where it reduces to zero, and that the temperature is assumed to decrease with increasing height at a constant rate. They developed *ad hoc* expressions to compute the saturation pressure and proposed two zenith non-hydrostatic delay models, which differ only in the saturation pressure computation. However, they found that a semiempirical model lead to precision comparable to the theoretical model, but with improved accuracy; the semiempirical model is given by the expression:

$$\boxed{d_{nh}^{z} = 10^{-3} U_s \nu 10^{\gamma t_s}}, \tag{3.91}$$

where ν and γ are empirical coefficients, associated with seasonal and climatic variations. The coefficients were determined by fitting data from a one-year radiosonde campaign (carried out in the context of the Global Atmospheric Research Program, in 1979) and are listed in Table 3.4.

To summarize, the input parameters for the described models are given in Table 3.5.

Table 3.4 – Empirical coefficients to be used in the Baby et al. [1988] semiempirical wet zenith delay model (ν is expressed in mm·(%)$^{-1}$ and γ in °C^{-1}).

Latitude Interval min - max	CLIMATE			
	Oceanic		Continental	
	ν	γ	ν	γ
90° S - 70° S	0.6421	0.0290	0.4164	0.0193
70° S - 50° S	0.5864	0.0259	0.5593	0.0362
50° S - 30° S	0.6124	0.0247	0.5369	0.0285
30° S - 10° S	0.4729	0.0296	0.4229	0.0335
10° S - 10° N	1.0772	0.0192	0.6542	0.0269
10° N - 30° N	0.8063	0.0213	0.6626	0.0249
30° N - 50° N	0.6614	0.0241	0.7574	0.0224
50° N - 70° N	0.7075	0.0244	0.7652	0.0236
70° N - 90° N	0.7434	0.0256	0.7687	0.0257
Global	**0.7284**	**0.0236**	**0.7284**	**0.0236**

Table 3.5 – Input parameters (either directly or indirectly used) for the non-hydrostatic and wet zenith delay models.

Model and Reference	e_s	T_s	α	λ	U_s	H	other
Hopfield [1969]	✓	✓					
Hopfield [1972]	✓	✓					
Saastamoinen [1973]	✓	✓					
Chao [1973]	✓	✓	✓				
Callahan [1973]	✓	✓					
Berman 70 [Berman, 1976]	✓	✓	✓				
Berman 74 [Berman, 1976]	✓	✓					
Berman TMOD [Berman, 1976]	✓	✓					
Ifadis [1986]	✓	✓					P_s
Askne and Nordius [1987]	✓	✓	✓	✓		✓	g_m, φ
Baby et al. [1988]		✓			✓		ν, γ

3.3.3. Mapping functions

In Section 3.3, it was suggested that the elevation dependence of the neutral-atmosphere propagation delay could be related to the delay that the signal would experience at other elevation angles through the use of mapping functions, and a simple mapping function to map the total zenith delay was introduced.

In the early years of space geodesy, the zenith delay and the mapping function were not clearly separated; the propagation delay was therefore determined using a "hybrid model" that combined zenith delay model(s) and mapping function(s). The need of a complete separation between zenith delay models and mapping function(s) is a requirement of the new strategies in propagation delay modeling for high precision applications; due to the poor modeling of the wet zenith delay from surface meteorological measurements, this separation permits the zenith wet delay (or the residual delay) be estimated along with other geodetic or geophysical parameters in the data reduction process or estimated from an alternative method. In the last couple of decades, numerous hybrid models and mapping functions have been developed. For our analysis all the hybrid models were separated into their components, as a mapping function can always be defined [Davis, 1986].

The existing mapping functions can be distributed basically in three major groups. A first group of mapping functions is based on the quartic profile developed by Hopfield [1969] and include the Hopfield [1969], Yionoulis [1970], Moffett [1973], Goad and Goodman [1974], Black [1978], Black and Eisner [1984], and Santerre [1987] mapping functions.

A second group is constituted by mapping functions based on the truncated form of a continued fraction, and include the functions reported in Marini and Murray [1973], Chao [1972], Davis et al. [1985], Ifadis [1986], Herring [1992], and Niell [1996]. The mapping functions developed by Yan and Ping [1995] constitute a variant of the continued fraction, as they are based on the complementary error function. A smaller group is based on the expansion of the "cosecant law" and includes Saastamoinen [1973] and Baby et al. [1988] mapping functions. The remaining mapping functions existing in the literature do not fall directly under these categories. As a general rule, all the mapping functions assume azimuthal symmetry of the neutral atmosphere and hydrostatic equilibrium. A brief description of the main features of most extant mapping functions (by category group) follows. Mathematical models will be given for a selected number of functions, either in the text or in Appendix II. A comparative table of the mapping functions' main features is also presented at the end of this section.

- **Hopfield (*HO*)**

The two-quartic refractivity profiles, given by Equations (3.30) and (3.31), are the basis of the mapping functions derived by Hopfield [1969], even though the quartic profile for the wet component has no physical or statistical justification. The mapping functions assume therefore a constant lapse rate of ~6.8 K km^{-1} for the neutral atmosphere, azimuthal symmetry, and hydrostatic equilibrium. Moreover, ray bending is also ignored. Under these assumptions, Hopfield arrived to the following expression for the total delay (see full derivation in Wells [1974]):

$$d^{i}_{trop} = \frac{10^{-6} N_{si}}{\left(h_{tro_i}\right)^4} \int_{-h_{tro_i}}^{0} \frac{\left(r_{tro_i} + x\right) x^4}{\sqrt{\left(r_{tro_i} + x\right)^2 - \left(r_s \cos\varepsilon\right)^2}} dx, \tag{3.92}$$

where the two auxiliary variables are

$$h_{tro_i} = r_{tro_i} - r_s = H^e_i - H_s$$

and

$$x = H - H^e_i,$$

r_{tro_i} is the geocentric radius of the point at which N_i becomes negligible, r_s is the geocentric radius of the station, H_s is the station's height, H^e_i are the equivalent heights, and H is the height above sea level. In all these expressions and hereafter, i = 1, 2, denotes dry and wet components (or hydrostatic and non-hydrostatic, if applicable), respectively. The solution at the zenith is readily obtained from Equation (3.92), making $\varepsilon = 90°$:

$$d^{z}_{i} = 10^{-6} N_{si} \frac{H^e_i}{5}. \tag{3.93}$$

Therefore Equation (3.92) can be explicitly expressed as the product of a zenith delay and a mapping function:

$$d^{i}_{trop} = d^{z}_{i} \left[\frac{5}{H^e_i} \int_{-h_{tro_i}}^{0} \frac{\left(r_{tro_i} + x\right) x^4}{\sqrt{\left(r_{tro_i} + x\right)^2 - \left(r_s \cos\varepsilon\right)^2}} dx \right]. \tag{3.94}$$

The closed-form solution for the integral in Equation (3.92) obtained by Hopfield proved to be very sensitive to roundoff errors for high elevation angles, even using double precision. We have implemented the formulation in quadruple precision for a series of tests and we obtained a numerically stable solution. The values obtained agree very well with ones provided by the Yionoulis [1970] formulation and therefore we have not considered it in our analysis.

- **Yionoulis (*YI*)**

To avoid the roundoff errors for high elevation angles in the Hopfield formulation, Yionoulis [1970] proposed a series expansion form for the integrand in Equation (3.92). Due to the difficulty in finding a series expansion with a rate of convergence satisfactory for the full range of elevation angles, Yionoulis presented two series expansions, one for high elevation angles and another for lower elevation angles, with a large overlapping region of convergence. This fact allows the choice of the boundary between high and low elevation angles to be left to the user. Wells [1974] suggested this boundary to be as low as possible, in order to minimize the number of arithmetic operations. For a broad set of meteorological conditions, he found that a changeover elevation angle of 17° gives a convergence of 1 mm in the dry component, after three terms in the series summation. The same convergence is obtained for the wet component with a changeover angle of 7°, after 2 terms have been evaluated.

- **Moffett (*HM*)**

Simplified approximations of the Hopfield mapping functions are presented in Moffett [1973] and are sometimes incorrectly referred to in the literature as the Hopfield model(s) or mapping functions. These simplified mapping functions have been used extensively, as they depend on the elevation angle only:

$$\boxed{m_d(\varepsilon) = \frac{1}{\sin(\varepsilon^2 + 6.25^\circ)}} \tag{3.95}$$

$$\boxed{m_w(\varepsilon) = \frac{1}{\sin(\varepsilon^2 + 2.25^\circ)}}. \tag{3.96}$$

- **Goad and Goodman (*GG*)**

Goad and Goodman [1974] modified the Hopfield model by assuming that the temperature decreases linearly with increasing height in the troposphere, but that it remains constant in the stratosphere (two-layer atmosphere), the same assumptions used by Saastamoinen [1973] in deriving his mapping function. To accomplish that, the wet and dry components of the Saastamoinen zenith corrections are used to calibrate the equivalent heights H_d^e and H_w^e. As regards the mapping function component, the authors used a Taylor's series approximation for the integrand in Equation (3.92) and obtained a series of coefficients from direct integration. The Goad and Goodman mapping functions are sometimes referred to in the literature as Modified Hopfield. This designation should be avoided, as it may be confused with the Moffett mapping functions.

- **Santerre (*ST*)**

The mapping functions developed by Santerre [1987] are a further modification of the Goad and Goodman mapping functions, which takes into account ray bending for elevation angles below 45°.

- **Black (*BL*)**

Black [1978] mapping functions are simple analytic forms derived from the integration of a Taylor series expansion of a normalized integral obtained from geometric considerations. They are based on the quartic profiles developed by Hopfield [1969] and use the equivalent heights proposed by Hopfield [1971]. In their simpler form, the mapping functions are as follows:

$$m_i(\varepsilon) = \left(1 - \left(\frac{\cos\varepsilon}{1 + (1 - l_c)\left(\frac{H_i^e}{r_s} \right)} \right)^2 \right)^{-\frac{1}{2}}, \tag{3.97}$$

where $l_c = 0.85$. In the complete formulation (as used in our analysis), l_c is a weak function of surface temperature and elevation angle. These mapping functions were recommended for elevation angles above 5°.

- **Black and Eisner (*BE*)**

The Black and Eisner [1984] mapping function for the total delay is a further modification of Black's, and is expressed as a simple geometrical model, which depends

on the elevation angle only, with one fitted parameter:

$$m_t(\varepsilon) = \frac{1}{\sqrt{1-\left(\frac{\cos\varepsilon}{1+0.001}\right)^2}} \tag{3.98}$$

This mapping function is claimed to be valid for elevation angles greater than 7°.

- **Chao (*CH*)**

Marini [1972] showed that the elevation angle dependence of the atmospheric delay can be expressed as a continued fraction form, in the sine of the elevation angle ε:

$$m(\varepsilon) = \cfrac{1}{\sin\varepsilon + \cfrac{a}{\sin\varepsilon + \cfrac{b}{\sin\varepsilon + \cfrac{c}{\sin\varepsilon + \cdots}}}}, \tag{3.99}$$

where the coefficients a, b, c, ... are constants or linear functions.

In the case of the Chao [1972, 1974] mapping functions, the continued fraction is truncated to second order terms and the second order (sin ε) is replaced by (tan ε), to ensure that the mapping function will be unity for signals observed in the zenith direction. The mapping functions were obtained by an analytical fitting to radiosonde-derived average refractivity profiles. The coefficients a and b are fitted numeric constants:

$$m_d(\varepsilon) = \frac{1}{\sin\varepsilon + \cfrac{0.00143}{\tan\varepsilon + 0.0445}} \tag{3.100}$$

$$m_w(\varepsilon) = \frac{1}{\sin\varepsilon + \frac{0.00035}{\tan\varepsilon + 0.017}}. \qquad (3.101)$$

Estefan and Sovers [1994] also present a set of "revised" constants for the dry mapping function, as well as a set of mapping tables ("look-up tables"), which were also developed by Chao for both dry and wet components. These tables in particular (which were assessed in our study) include the effect of ray bending, and are (theoretically) valid for any elevation angle.

- **Marini and Murray (*MM*)**

The Marini and Murray [1973] mapping function (according to the explicit formulation expressed in Davis [1986]) uses a second order continued fraction, with the coefficient b set as a fitted constant. It was designed to model the elevation dependence of the total tropospheric delay for observations above 10°.

- **Davis et al. (*CfA*)**

The Davis et al. [1985] mapping function for the hydrostatic component of the atmospheric delay (also known as CfA-2.2) uses a third order continued fraction, with the tangent as introduced by Chao. As pointed out in their study, the substitution of ($\sin\varepsilon$) by ($\tan\varepsilon$) decreases the performance at high elevation angles (20° - 60°), as the tangent does not approach the sine with the same speed, giving 1-2 mm error. The coefficients of CfA-2.2 mapping function for the hydrostatic delay were derived from a ray tracing analysis through idealized model atmospheres, down to 5° elevation; the coefficient c is

set as a constant and a and b are expressed as linear functions (of departures with respect to standard values) of surface temperature, surface total pressure, partial water vapor pressure, temperature lapse rate, and height of the tropopause. This mapping function can also be used to map the zenith non-hydrostatic delay, although this introduces a "small" error of uncertain magnitude [Davis et al., 1985]. For the sake of completeness, the non-hydrostatic mapping function is also included in this analysis. The mathematical formulation is presented in Appendix II.

Ifadis [1986], Herring [1992] and Niell [1996] expanded the continued fraction to three terms, keeping the sin ε in all terms. To ensure that the mapping function is unity at the zenith, the unity numerator of the Chao-type fraction is substituted by the value of the mapping function denominator at the zenith, i.e.:

$$m(\varepsilon) = \frac{1 + a/(1 + b/(1 + c))}{\sin\varepsilon + a/(\sin\varepsilon + b/(\sin\varepsilon + c))}. \qquad (3.102)$$

- **Ifadis (*IF*)**

The Ifadis [1986] mapping functions were fit down to a 2° elevation angle to ray traces of radiosonde atmospheric profiles from an extensive selection of globally distributed sites. Global and climate optimized mapping functions were derived. The coefficients a and b are linear functions of surface temperature, pressure and partial water vapor pressure and c is a fitted numerical constant. The mathematical formulation for these mapping functions is presented in Appendix II.

- **Herring (*MTT*)**

The mapping functions developed by Herring [1992], also known as *Mapping Temperature Test* (MTT), were determined from ray tracing through rawinsonde profiles covering several locations in the United States, for elevation angles starting at 3°. The coefficients in the mapping functions depend on the latitude, height of the site and surface temperature, and were determined by a least squares fitting performed separately for the hydrostatic and wet components, for latitudes covering 27° to 65° and station heights ranging from 0 to 1600 m. The mathematical formulation for these mapping functions is presented in Appendix II.

- **Niell (*NMF*)**

The Niell [1996] mapping functions (NMF - *Niell (New) Mapping Functions*) present no direct dependence on specific meteorological parameters, and are based on temporal fluctuations of the bulk of the atmosphere. The coefficients in the mapping functions were derived from profiles of the U.S. Standard Atmosphere Supplements, 1966, down to 3° elevation angle. In the case of the hydrostatic mapping function, the coefficients a and b are functions of the day-of-year (or Modified Julian Date), station latitude, and station height. For the wet mapping function, only the latitude of the site is used as external information. The southern hemisphere is assumed to be anti-symmetric in time. The mathematical formulation for these mapping functions and additional discussion is presented in Appendix II.

- **Yan and Ping (*UNSW*)**

Yan and Ping [1995] developed a mapping function based on the continued expression of the complementary error function. This mapping function uses the same input parameters of CfA-2.2 and was adjusted for elevation angles above 2.5°. Yan and Ping proposed two mapping functions. The first is based on the atmospheric profile provided by CfA-2.2 and standard atmospheric parameter values and was called UNSW931 (UNSW, in this dissertation). The second mapping function is based on the atmospheric profile given by the Hopfield model, and was called UNSW932 (not analyzed in this dissertation). Even though it is not explicitly specified by the authors, the UNSW931 mapping function is to be applied for the hydrostatic component only [Yan, 1998]. Extending the use of UNSW931 to map the non-hydrostatic component introduces a small error, as in the case of CfA. The mathematical formulation for UNSW931 is presented in Appendix II.

- **Lanyi (*LA*)**

The Lanyi [1984] mapping function, which maps the total zenith delay, was developed using an analytical approach, with the fitting performed to elevation angles above 6°. It uses 3-linear section temperature profiles and the tropospheric delay is expanded up to the third order in refractivity, where the second and third order terms describe the bending effect. Latitude and site-dependent variations with respect to an average profile can be modeled by tuning the temperature lapse rate and tropopause height for the specific site. The mathematical formulation for the mapping function developed by Lanyi is presented in Appendix II.

- **Hartmann-Leitinger (*HL*)**

Hartmann and Leitinger [1984] presented a mapping function for the total delay that depends only on the height of the center of gravity of the vertical column of air, H_g, which can in turn be fixed to a constant value (e.g. at a height of 8000 m):

$$\boxed{m(\varepsilon) = \frac{1}{\sin(\varepsilon)}\left[1 - \frac{0.85H_g}{R_e}\cot^2\varepsilon + 1.5\left(\frac{0.85H_g}{R_e}\right)^2\cot^4\varepsilon\right]}, \tag{3.103}$$

where R_e is the earth radius.

Ray bending can be additionally computed from surface refractivity and atmosphere scale height, allowing their model to be applied for elevation angles above 5°:

$$d_g(\varepsilon) = -(10^{-6}N_s)^2 \frac{\cot^2\varepsilon}{4\sin\varepsilon}. \tag{3.104}$$

Unlike the mapping functions described so far, which use the non-refracted elevation angle, the remaining mapping functions in this analysis use the refracted (apparent) elevation angle. The difference between the angles is significant at low elevation angles. In the analysis of space geodetic data, the elevation angle is generally derived from the geometry of the source and the receiver, i.e., the refracted angle is not available. Whereas Saastamoinen [1973] provides a simple formula to derive the non-refracted (or geometric) from the refracted zenith angle, such is not provided by the Baby et al. [1988] and Rahnemoon [1988] formulations. This detail should not be neglected in any implementation of these models in the analysis of geodetic data that require the use of the

non-refracted elevation angle, since it may significantly affect the results if low elevation angles are used.

- **Saastamoinen (*SA*)**

Saastamoinen [1973] derived his mapping function based on Snell's law of refraction for a spherically symmetric layered atmosphere. Under this assumption, and neglecting the ray bending, the tropospheric delay can be written as:

$$d_{trop} = 10^{-6} \int_{r_s}^{r_a} \frac{N}{\sin\theta} dr \ . \tag{3.105}$$

Saastamoinen expands the $1/\sin\theta$ in a truncated binomial series, and integrates each term. In its full version, mapping functions are derived for both components, and are parameterized in terms of tropopause height, temperature lapse rate and water vapor lapse rate parameter, in addition to the standard meteorological parameters. A simplified version that maps the total delay was obtained from those solutions, and is often used in analysis of space geodetic data, due to its simplicity and accuracy. It requires the interpolation of correction quantities from two tables, which take into account the effect of ray bending, but its use is limited to elevation angles above 10°. Janes et al. [1991] have compared the performance of both versions. In this dissertation, only the simplified version is analyzed.

- **Baby et al. (*BB*)**

Baby et al. [1988] used Snell's law of refraction to expand the 1/sinθ and derived the following mapping function:

$$m_t(\theta) = \frac{1}{\sin\theta\sqrt{\left(1+\varepsilon_H \cot^2\theta\right)}}, \tag{3.106}$$

where ε_H is a term depending on the refractive index and geocentric distance of the station. For low observation angles (less than about 45°), a corrective term is introduced. The ray bending is nevertheless neglected. The model was developed to map the total delay for elevation angles above 10°.

- **Rahnemoon (*RA*)**

Rahnemoon [1988] derived a model that has to be seen in a different context, as it is a numerical-integration-based model, similar to a ray tracing procedure program. This represents a problem in the analysis of geodetic data, as the model is, computationally, one to two orders of magnitude slower than the remaining mapping functions. It uses meteorological surface data (temperature, pressure and relative humidity) to generate the refractivity components at the surface and integrates along the ray path to generate the profiles from which the delays are derived, using Snell's law.

As can be concluded from the brief descriptions given, there is a significant variability in the mathematical basis and parameterization of the available mapping functions. This is summarized in Table 3.6 for convenience.

Table 3.6 – Summary table of the main features of mapping functions.

M.F.	P_s	T_s	e_s	α	T_h	H	φ	other	$\angle$	ε_{min}	type	d_g
BB	✓	✓	✓			✓			θ	10°	t	
BE									ε	7°	t	
BL		✓							ε	5°	d,w	
CfA	✓	✓	✓	✓	✓				ε	5°	h,nh[††]	✓
CH									ε	1°	d,w	
GG	✓	✓	✓			✓			ε	n/a	d,w	
HL	✓[§]	✓[§]	✓[§]				✓	H_g	ε	5°	t	✓
HM									ε	2°	d,w	
HO		✓[†]				✓			ε	n/a	d,w	
IF	✓	✓	✓						ε	2°	h,nh	✓
LA	✓	✓		✓	✓			H_i	ε	6°	t	✓
MM	✓	✓	✓			✓	✓		ε	10°	d,w	
MTT		✓				✓	✓		ε	3°	h,nh	✓
NMF						✓[†]	✓	doy[†]	ε	3°	h,nh	✓
RA	✓	✓	✓			✓	✓		θ	n/a	d,w	✓
SA	✓	✓	✓			✓			$\varepsilon^{‡}$	10°	t	✓
ST	✓	✓	✓			✓			ε	n/a	d,w	✓
UNSW	✓	✓	✓	✓	✓				ε	2.5°	h,nh[††]	✓
YI		✓[†]							ε	n/a	d,w	

[†]hydrostatic component only; [††]extended use of the function developed for the hydrostatic component; [‡]true elevation angle is converted to apparent elevation angle before computation of mapping factor; [§]geometric delay (ray bending) only.

Legend: P_s = surface total pressure; T_s = surface temperature; e_s = surface water vapor pressure; α = temperature lapse rate; T_h = tropopause height; H = station orthometric height; φ = station latitude; H_g = height of center of gravity; H_i = inversion height; doy = day of year; $\angle$ = type of elevation angle (θ = apparent angle; ε = true elevation angle); ε_{min} = minimum elevation angle for which the mapping function was designed (n/a = not specified or valid for any elevation angle); type = underlying formalism (d = dry; w = wet; h = hydrostatic; nh = non-hydrostatic; t = total); d_g = geometric delay.

3.3.4. Hybrid models for airborne positioning

The development of atmospheric propagation delay models for navigation applications, and specifically for airborne positioning, was partially carried out parallel to the development of their counterparts for geodetic applications. Some of the reasons for this separation can be explained by the characteristics intrinsic to those applications, such as the absence of reliable real-time measurements of meteorological parameters, which are the main input of most of the "geodetic models", the frequent changes in the height of the receiving antenna in moving platforms, and the need for fast algorithms for real-time computations, typically in small, computationally limited, navigation equipment. There are clearly two classes of "navigation models": a class of models incorporated by different manufactures in the GPS receivers (generally of very simple structure), and a class of more sophisticated models, which are generally analytical approximations to refractivity profile models. Examples of the first type of models can be found in Wachowski [1980], Greenspan and Donna [1986], Brown [1989], Braasch [1990], and Lewandowski et al. [1992]. Examples of the second type of models can be found in Altshuler [1971], Kalaghan and Altshuler [1973], Altshuler and Kalaghan [1974], Mano and Altshuler [1981], and NATO [1993].

For the sake of completeness of our study, we selected five navigation models to be included in our analysis, some of which are of importance in the development and implementation of the new concepts in airborne precise positioning.

- **STI**

This model is very popular and is commonly used in GPS receivers [Braasch, 1990]. According to Wachowski [1980] and Greenspan and Donna [1986], this model has been adopted by Collins Radio Division of Rockwell International. Lewandowski et al. [1992] stated that it is "*implemented in receivers manufactured by Stanford Telecommunication Inc.*". We will label it as STI.

The only input required by the STI model is the user's orthometric height, H:

$$\boxed{d_{trop} = \frac{2.4224}{0.026 + \sin(\varepsilon)} \exp(-0.00013345H)} . \qquad (3.107)$$

- **Brown**

Brown [1989] refers to a model that is a function of the mean surface refractive index, n_s, user's altitude, H, and tropospheric scale height ($\mathcal{H} \approx 6900$ m):

$$\boxed{d_{trop} = \frac{n_s \mathcal{H}\, e^{-\frac{H}{\mathcal{H}}}}{\sin(\varepsilon)}} . \qquad (3.108)$$

- **Altshuler and Kalaghan**

Significant contributions to the atmospheric propagation modeling for airborne navigation came from the Air Force Cambridge Research Laboratory (AFCRL), in the 1970s (e.g. Altshuler [1971]; Kalaghan and Altshuler [1973]; Altshuler and Kalaghan [1974]), and some of the models currently used in airborne navigation are based on these contributions. The model developed by Altshuler and Kalaghan [1974], in particular,

reached high popularity. The model is a function of the user's height, latitude and surface refractivity, and was designed to be applied to elevation angles greater than 5°. A standard value of refractivity can be used or, as an alternative, it can be estimated using a proposed model, which is a function of the user's latitude, height above sea level, and season. The elevation angle to be used as input in this model is the refracted elevation angle. The reader should be aware that several typographical errors in the original report have been corrected through an errata sheet. The full formulation of the model is presented in Appendix II.

- **NATO**

The NATO standard troposphere model [NATO, 1993] combines a total zenith delay model, based on the CRPL Reference Atmosphere - 1958, with the Chao [1972] dry mapping function. This approach in modeling the elevation dependence of the troposphere propagation delay will obviously introduce an additional error, as the fitted parameters of this mapping function are not adequate to map the total delay. The zenith delay model is a function of the antenna height and the mean sea-level refractivity, with a global value of 324.8 N-units recommended [NATO, 1993]. The model is fully described in Appendix II.

- **WAAS**

Another model of interest to navigation users is that initially proposed for the Federal Aviation Administration's (FAA) Wide Area Augmentation System (WAAS), which is derived from the Altshuler and Kalaghan model [DeCleene, 1995]. This model is defined

for elevation angles greater than 5°, and is a function of the user's height above sea level, latitude, and day of year. Details on the mathematical formulation are given in Appendix II.

In this chapter, we have introduced important concepts in atmospheric propagation delay modeling. We gave an historical overview of refractivity model evolution and we established the radio wave propagation terminology. Zenith delay models and mapping functions to be assessed were described and major differences were highlighted. In the next chapter, we describe the data used in our accuracy assessment and we establish databases of atmospheric parameters derived from radiosonde data we used in optimization of model performance.

4. DATA DESCRIPTION AND ANALYSIS

In order to apply the ray-tracing technique, temperature, pressure, and water vapor profiles within the neutral atmosphere are required. Standard profiles of these parameters are readily available through the standard atmospheres. However, even though these standard profiles are a useful source of information and represent a variety of average climatological conditions, they are far from representing accurately the state of the atmosphere at every instant.

A better source of information of the state of the atmosphere is the set of routine observations provided by radiosondes. Other observation systems are available, but the radiosonde data have some advantages: relatively inexpensive data, with reasonable vertical resolution within the troposphere, and global coverage.

This chapter gives an overview of the data to be used in the ray-tracing process, describes the databases of additional meteorological parameters needed in neutral atmosphere model analysis, and presents strategies in the development of new models to determine the tropopause height and lapse rate.

4.1. Upper air observations

The most important source of information on the profile of the atmosphere is provided by the synoptic upper air observations, carried out worldwide twice daily (at 0^h and 12^h UTC) with weather measurement instruments called **radiosondes** [WMO, 1996a].

Radiosondes provide the meteorological community with height profiles of pressure, temperature, and relative humidity, among other parameters of interest. Thereafter this information is archived and generally reduced to the mandatory pressure levels – surface, 1000 hPa, 850 hPa, 700 hPa, 500 hPa, 400 hPa, 300 hPa – and significant pressure levels, corresponding to the levels where significant changes in temperature or moisture occur.

Despite the global nature of radiosonde observations, the spatial and temporal resolution is far from being ideal, due to the costs of operation. Moreover, the quality of the observations – specifically measurements of the moisture content – degrades significantly at high altitudes, as a result of contamination of the sensors during the flight and an increase of their time constant of response [WMO, 1996a].

4.1.1. Radiosonde instrumentation

A complete radiosonde system consists of an instrument package carried aloft by a large balloon, a ground radio receiver, and a microcomputer for data processing. If the radiosonde system has also the capability to measure the wind velocity, either directly using a radiotheodolite or radar, or aided with navigation systems (such as Omega, Loran-C or GPS), it is denominated **rawinsonde**. In this dissertation, no distinction

between the two kinds of system will be made. A variant of a radiosonde is the **dropsonde**, which is literally dropped from aircrafts or rockets [Cogan et al., 1996; WMO, 1996a]. It is specially designed to study the lowermost atmosphere and is not generally suitable for radio propagation studies.

The radiosonde instrument package consists of temperature, pressure, and humidity sensors, which sample the atmosphere at time intervals of a few seconds; radio signals are then frequency modulated with the data and transmitted to the ground system. The received signals are subsequently demodulated and converted to values of pressure, temperature and relative humidity. In order to certify that the data will contain no gross systematic errors, the radiosonde sensors can be checked against reference sensors prior to launch and these corrections can be introduced into the radiosonde data recording equipment; this procedure assures that the measured values will be automatically corrected during the ascent of the balloon.

The types of sensor used by the different radiosonde manufacturers are quite varied, but their general principles of operation do not differ significantly. Detailed information on radiosonde instrumentation is provided by the different manufacturers' literature and by the technical reports of the World Meteorological Organization (WMO) – see, for example, WMO [1986a; 1987b; 1996a; 1996b].

Two main types of **pressure sensors** are used widely: the baroswitch aneroid capsule and the capacitive aneroid capsule. For the first older sensor type, the increase of volume of the aneroid capsule with a decrease in air pressure is sensed through a mechanical

switching of a lever arm across a commutator bar. For the capacitive sensor, the volume change of the aneroid capsule is sensed as a change of the electrical capacitance, which is detected continuously.

The most used temperature sensors are of two types: thermistor and capacitive ceramic chip. The electrical resistance of the thermistor sensor changes with a change of temperature; they are generally coated with white paint, or vacuum-evaporated aluminum, to balance the infrared radiation absorbed by the sensor from the atmospheric environment, as white paints have a high emissivity in the infrared. The capacitive ceramic chip senses the change of temperature as a change of the electrical capacitance.

The **humidity sensors** vary significantly from country to country and from manufacturer to manufacturer. Five major sensor types are used: capacitive film element, carbon hygristors, resistive lithium chloride elements, goldbeater's skin hygrometer and hair hygrometer. The humidity sensor is the most problematic of the meteorological sensors and significant differences in humidity values given by the different sensors under similar environmental conditions are common [WMO, 1987b; WMO, 1996a; WMO, 1996b]. These differences are mainly due to the different response times of the sensors: slower response times result in higher values of humidity, as this variable has a tendency to decrease with height. Examples of sensors with slow response time are the goldbeater's skin and the lithium chloride elements [WMO, 1987b; Kitchen, 1989; WMO, 1996a]. All the humidity sensors are generally unreliable at high altitudes (stratosphere), due to the low number of water molecules in the air, and should be regarded as qualitative indicators

only [WMO, 1996a]. The most reliable humidity sensors, with good response times, are the carbon hygristor and the capacitive film element. For the first type, changes of air humidity are sensed as changes of the electrical resistance of the carbon element; the capacitive sensor detects the changes of air humidity as changes in the electrical capacitance of the element.

4.1.2. Measurement errors of radiosonde meteorological sensors

The performance of radiosonde meteorological sensors is generally assessed in terms of their bias with respect to a reference (accuracy or systematic error) and flight-to-flight sensor variation (reproducibility, precision, or sensor error). The performance of radiosonde instrumentation has been a matter of concern and has been documented in the literature (see, e.g., Lenhard [1973]; Schmidlin et al. [1982]; Kitchen [1989]; Elliott and Gaffen [1991]; Schwartz and Doswell [1991]; Gaffen et al. [1991]; Gaffen [1992]; Parker and Cox [1995]). As a result of significant improvement in sensors performance, the measurement errors claimed for modern radiosondes are usually small (see Table 4.1).

Table 4.1 – Characteristics of the Vaisala RS80 radiosonde. The quoted accuracy (or repeatability) corresponds to the standard deviation of differences between two successive calibrations [Vaisala, 1996].

Sensor	Type	Range	Resolution	Accuracy
Pressure	capacitive aneroid	1060 hPa to 3 hPa	0.1 hPa	0.5 hPa
Temperature	capacitive bead	60 °C to -90 °C	0.1 °C	0.2 °C
Humidity	thin film capacitor	0 % to 100 %	1%	2%

Because of the large variety of radiosondes used worldwide [WMO, 1986a; WMO, 1993], the performance of radiosonde instruments is regularly analyzed through intercomparison tests, carried out under the auspices of the WMO. This organization also sets the accuracy requirements and performance limits for upper-air measurements to be followed by its members [WMO, 1996a]: ± 1 hPa for pressure (from surface to 5 hPa), ± 0.5 °C for temperature (± 1 °C for the pressure range 100 hPa to 5 hPa), and ± 5% for relative humidity (within the troposphere).

International intercomparison of radiosonde instruments were performed recently [WMO, 1987b; WMO, 1996b]. It was concluded that most of the temperature sensors used in the 1984-1985 intercomparison test, which include the widely used Finnish Vaisala (from *Vaisala Oy*) and U.S. VIZ (from *VIZ Manufacturing Company*) radiosondes, presented a reproducibility of 0.2 °C (all quotations will be given at the 1σ level). As for relative humidity measurements, they could be obtained with a reproducibility of about 3.5%, but biases of more than 10% can be found in some sensors in certain circumstances; it is also reported that the goldbeater's skin hygrometer sensors tested showed a clear negative bias for very high values of relative humidity, and a positive bias for low relative humidity conditions; the Vaisala radiosonde sensors give higher values of humidity than other sensors when wet, for the relative humidity range 20% to 70%.

Similar conclusions were obtained during the phase IV of this intercomparison, which involved also Japanese radiosondes. Comparison between the different instruments revealed that the temperatures measured by the different sensors agreed within 0.3 °C, up

to the 70 hPa level. These biases increase with altitude and reach about 3 °C at the 10 hPa level. No significant biases were found between the different pressure sensors, which were within 1.5 hPa up to the 200 hPa level. For the humidity sensors, the biases vary according to the humidity range. Large humidity differences were observed for the low humidity range (below 20%) and for the high humidity range (above 80%), depending on the type of sensor. For example, for the high humidity range the VIZ radiosonde tended to give higher humidity values than the other radiosondes and reported frequently 100% humidity within moist layers [WMO, 1996b]. The performance of two popular radiosondes, the Finnish Vaisala RS80 (RS80) and U.S. VIZ MkII (VIZ), is summarized in Table 4.2.

Despite the good performance of modern radiosonde observations, there are other issues related with radiosonde data archives (such as changes in instrumentation, reporting practices, and data-archiving procedures) that may cause time-varying systematic biases, and need therefore to be taken into consideration when working with a large database [Elliott and Gaffen, 1991; Schwartz and Doswell, 1991; Gaffen, 1992; Parker and Cox, 1995]. Although these problems have a major impact in climatological studies, the quality control of the archived data is of particular importance in the creation of a database to be used as "ground truth".

The introduction of automated procedures in the dissemination of radiosonde data lead to poorer quality control of the data, a fact which is also common to data coded manually [Schwartz and Doswell, 1991]. Even though quality control is performed before the

radiosonde data is archived, an additional check should be performed by the user, as it is not rare to find observations that are totally useless, as shown in Figure 4.1.

Table 4.2 – Systematic errors and reproducibility of sensors (flight-to-flight variation at the 2σ level) for selected radiosondes. The quoted (range) values are compiled from the WMO international radiosonde intercomparison [WMO, 1996a].

Pressure Sensor

	Systematic error (hPa)			Reproducibility (hPa)		
	@ 850 hPa	@ 100 hPa	@ 10 hPa	@ 850 hPa	@ 100 hPa	@ 10 hPa
RS80	1 to 0.5	-1 to -0.5	-0.5 to 0	1	0.6	0.4
VIZ	0 to 1	0.7 to 1.1	0.3 to 0.7	1	0.6	0.4

Temperature Sensor

	Systematic error (K)			Reproducibility (K)		
	@ 300 hPa	@ 30 hPa	@ 10 hPa	@ 100 hPa	@ 30 hPa	@ 10 hPa
RS80	0.9	2.2	2.8	–	0.6	1
VIZ	0.4	1.6	2.5	–	0.8	1.2

Humidity Sensor

	Systematic error (%)			Reproducibility (%)		
	80-90 % U	40-60 % U	10-20 % U	80-90 % U	40-60 % U	10-20 % U
RS80	-1	0	0	6	6	4
VIZ	6	0	5	8	8	12

Among the obvious errors to be checked are missing surface data, unreasonable vertical profiles, and an unsatisfactory number of observed levels, for example. Despite the limited spatial and temporal coverage of the existing radiosonde network, the

heterogeneity of instrumentation, and other problems associated with radiosonde observations, these are probably still the best and cheapest source of global atmospheric profiles available.

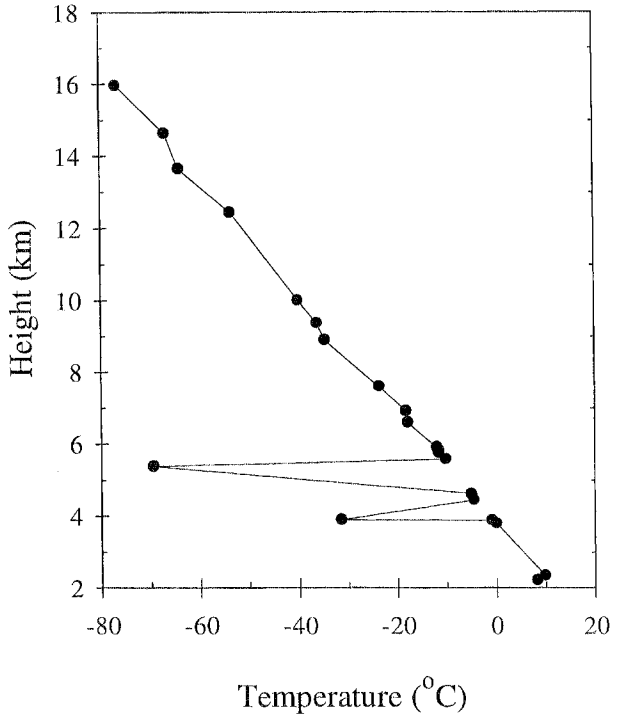

Figure 4.1 – Blunders in the temperature profile of a radiosonde sounding (sounding for Mexico City, January 30, 1992, 12^h UTC, as given in the Radiosonde Data of North America (1946-1995) CD-ROM) .

4.1.3. Radiosonde data selection

The data set chosen for this study is comprised of data from 100 stations, distributed worldwide (unfortunately not as spatially regular as desired, due to data availability constraints), and compiled from the Radiosonde Data of North America (1946-1995) CD-ROM (produced by the U.S. Forecast Systems Laboratory (FSL) and the National

Climate Data Center (NCDC)), the National Center for Atmospheric Research (NCAR), the Atmospheric Environment Service of Canada, and the Swedish Meteorological and Hydrological Institute. The identity and locations of the radiosonde stations are given in Appendix III. As a great number of the stations were provided with data for the year 1992 only, all of the analyses presented in this dissertation are based on data for this year, to ensure a homogeneous data set. The main goal of establishing a fairly large primary database is related to the need of creating accurate information concerning the three meteorological parameters needed to drive some zenith delay models and mapping functions: tropopause heights, inversion heights, and lapse rates. These three meteorological parameters are analyzed in more detail in the following sections.

The number of stations actually used in ray tracing was reduced to 50. The reasoning for this is two-fold: on one hand, the ray tracing technique is a very time-consuming task; on the other hand, the traces obtained for stations experiencing similar climate types are very similar. The 50 stations were selected in order to meet essentially three requirements: large range of climate variability, large range of station height, and proximity to VLBI and IGS (International GPS Service for Geodynamics) stations.

4.2. Meteorological parameter databases

The complete assessment of some neutral-atmosphere propagation models is only possible if in addition to the standard meteorological information, such as surface values of pressure, temperature and relative humidity, ancillary parameters related to the temperature profile (tropopause height, inversion height, and temperature lapse rate

within the troposphere) are provided. In general, values of these parameters are not available for arbitrary locations and we are not aware of any accurate model that could be applied on a global basis in the determination of those parameters, as far as radio-meteorology studies are concerned. The solution for this problem is generally sought in interpolation schemes through derived tables of mean values for certain locations and seasons (e.g. Collins et al. [1996]; Sovers and Jacobs [1996]). The establishment of large databases of these parameters is therefore of great importance and will allow the development of realistic global models for tropopause and lapse rate determinations.

4.2.1. Tropopause height

The traditional approach defines the tropopause as the boundary between the troposphere and the stratosphere, characterized by a discontinuity in the temperature gradient (see Chapter 2). This definition is rather ambiguous and a more refined definition is the one adopted by the WMO [MO, 1991]:

" *(i) The 'first tropopause' is the lowest level at which the lapse rate decreases to 2 °C km^{-1} or less, provided also that the average lapse rate between this level and all higher levels within 2 km does not exceed 2 °C km^{-1}.*

(ii) When, above the first tropopause, the average lapse rate between any level and all higher levels within 1 km exceeds 3 °C km^{-1}, then a 'second tropopause' can occur and is defined by the criteria of (i) above. This tropopause can either be above or within the 1 km layer.

(iii) Further tropopauses may be defined similarly."

Even though this definition removes some of the ambiguity in tropopause definition, its

application in regions of multiple stable areas or tropopause folding, such as in the vicinity of jet streams and upper-level fronts, is troublesome [Defant and Taba, 1957; Bean et al., 1966; Barry and Chorley, 1987; Hoerling et al., 1991]. Defant and Taba [1957] distinguish three different regions with different characteristic tropopause heights: the tropical tropopause (south of the subtropical jet stream), the middle tropopause, and the polar tropopause (north of the subpolar jet stream). In the transition between the tropical tropopause and the middle tropopause, two different tropopause levels are frequently observed, whereas no clear tropopause can be observed in the region of transition between the middle tropopause and the polar tropopause.

This lapse-rate-defined tropopause, also known as the **thermal tropopause**, is the basis of available maps of tropopause heights (e.g. Bean et al. [1966]). The criteria defined by the WMO are still used to operationally report the tropopause heights by radiosonde systems.

In order to overcome some of the drawbacks of the thermal definition, alternative definitions have been proposed, the most important of which is the dynamical tropopause.

The **dynamical tropopause** is based on the concept of potential vorticity [Hoskins et al., 1985]. There is observational evidence that the tropopause delineates a discontinuity in potential vorticity, which separates the low values characteristic of the troposphere from the much higher values characteristic of the stratosphere [Shapiro, 1980; Hoerling et al., 1991]. The dynamical tropopause has been defined as the surface with 1.6 potential vorticity units (PVU), where this unit is defined as 10^{-6} K m^2 kg^{-1} s^{-1} [WMO, 1986b], but

there is no agreement on the best threshold to be used. Hoerling et al. [1991] discusses this issue and shows comparative maps of dynamical and thermal tropopause determinations for different scenarios.

Bethan et al. [1996] also studied the feasibility of defining the tropopause in terms of ozone concentration, as the tropopause also identifies an abrupt change in the concentration of some chemical species [WMO, 1986b]. Bethan et al. [1996] found that this **ozone tropopause** was robust in situations of unambiguous thermal tropopause, but not reliable in situations of interleaved layers of high and low ozone concentration; they concluded that, on average, the ozone tropopause is about 800 m below the thermal troposphere.

As stated by Bethan et al. [1996], "no definition of the tropopause is perfect" and the different concepts complement each other, in a certain way. Yet, the thermal tropopause is still the most appropriate to be used by radiosonde data-processing algorithms and radio propagation studies, as it is dependent on the temperature profile only.

Except for a few stations in our data set, the tropopause height is generally flagged. A brief analysis of some radiosonde observations processed using different algorithms illustrated that these algorithms can lead to different tropopause height reports, as portrayed in Figure 4.2. This fact has been also noticed in the last WMO-sponsored international radiosonde intercomparison tests. In WMO [1996b], it is concluded that "the number of tropopause and the tropopause heights reported from the different participating systems differed greatly among them."

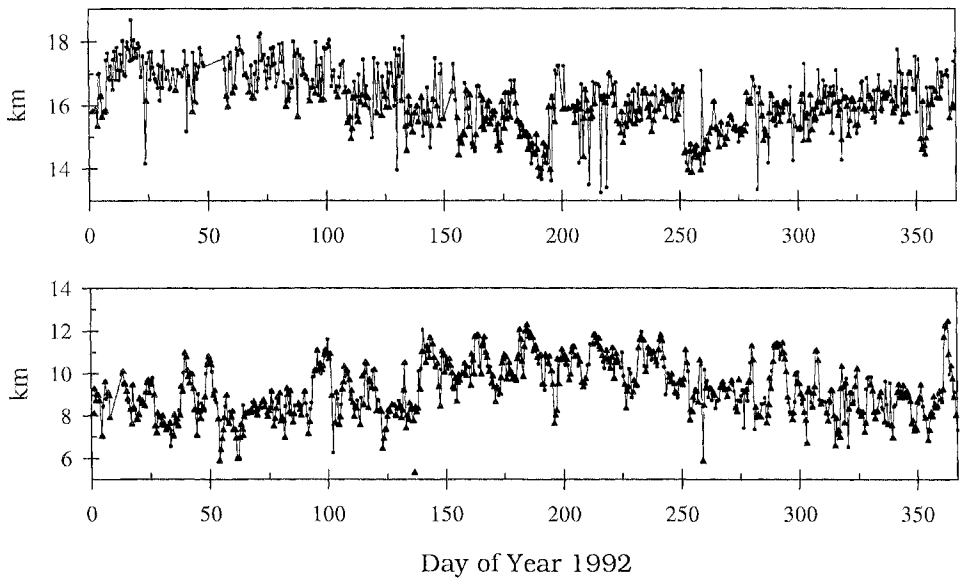

Figure 4.2 – Tropopause heights for San Juan (top plot) and Kotzebue (bottom plot), as reported in the NCAR archives (line with dots) and the FSL archives (triangles), for soundings taken at same date and time. Note the different number of tropopause reports and different tropopause heights, which are likely due to different processing strategies.

In the case of our data set, tropopause heights had to be determined only for a small number of stations (8). As the archived data has lost much of the information needed to strictly follow the WMO criteria, we found that more reliable determinations of the tropopause could be obtained by looking for temperature inversions, constrained to temperature limits, in order to avoid determining false tropopause heights (sensitivity studies of tropopause determinations to modifications of the WMO criteria have been carried out by Hoerling et al. [1991]). In order to test the reliability of our method, we used a few stations for which the tropopause heights were known (as reported in the data set), to allow a direct comparison. The method proves to be very efficient and shows no significant bias with respect to radiosonde reported tropopauses, as shown in Figure 4.3.

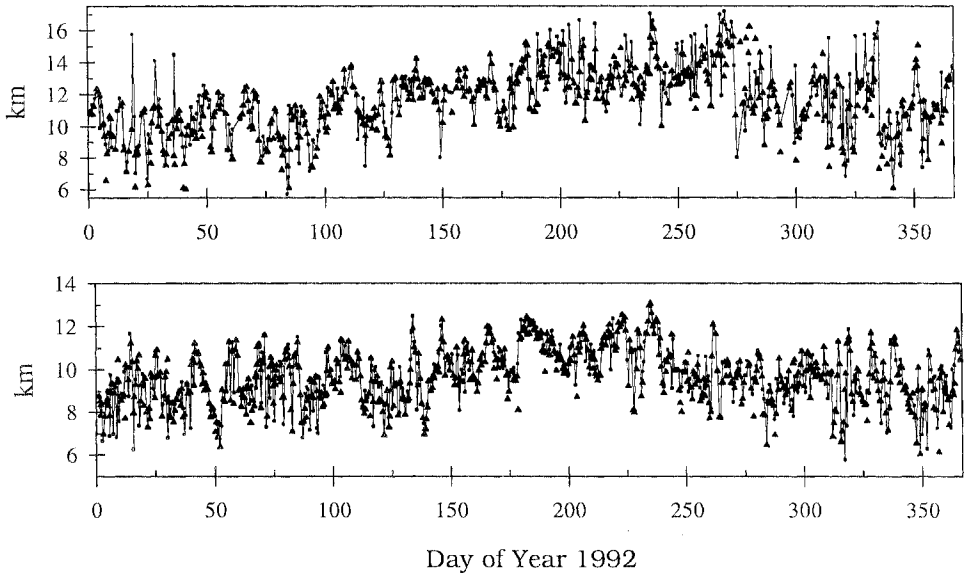

Figure 4.3 – Tropopause heights for Albany (top plot) and Whitehorse (bottom plot), as reported in the FSL soundings (triangles) and as determined using an *ad-hoc* procedure (lines with dots).

If we consider only the common determinations, our method is affected by a mean bias of 0.2 ± 1.3 km for Albany (for a total of 504 determinations) and 0.03 ± 0.62 km, for Whitehorse (661 common determinations). The distribution of the differences is shown in Figure 4.4.

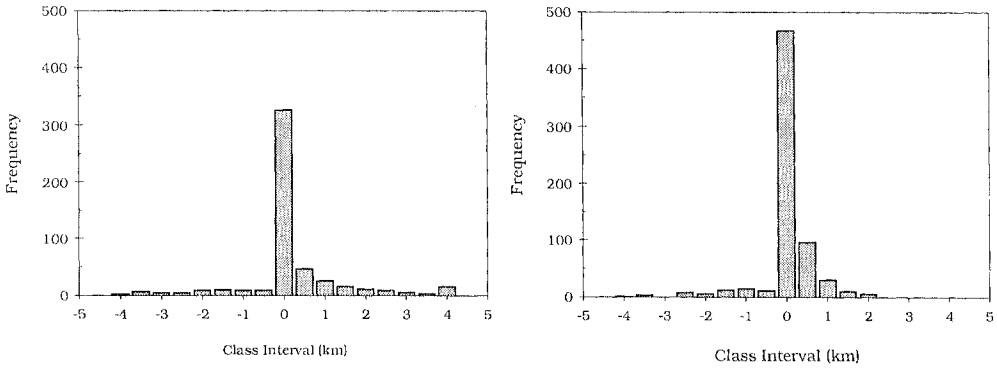

Figure 4.4 – Histograms for the differences in tropopause height determination, for Albany (left plot) and Whitehorse (right plot).

Example time series of tropopause heights are shown in Figure 4.5. We have also analyzed the differences between the 0^h and 12^h UTC tropopause heights, which are found to be not significant.

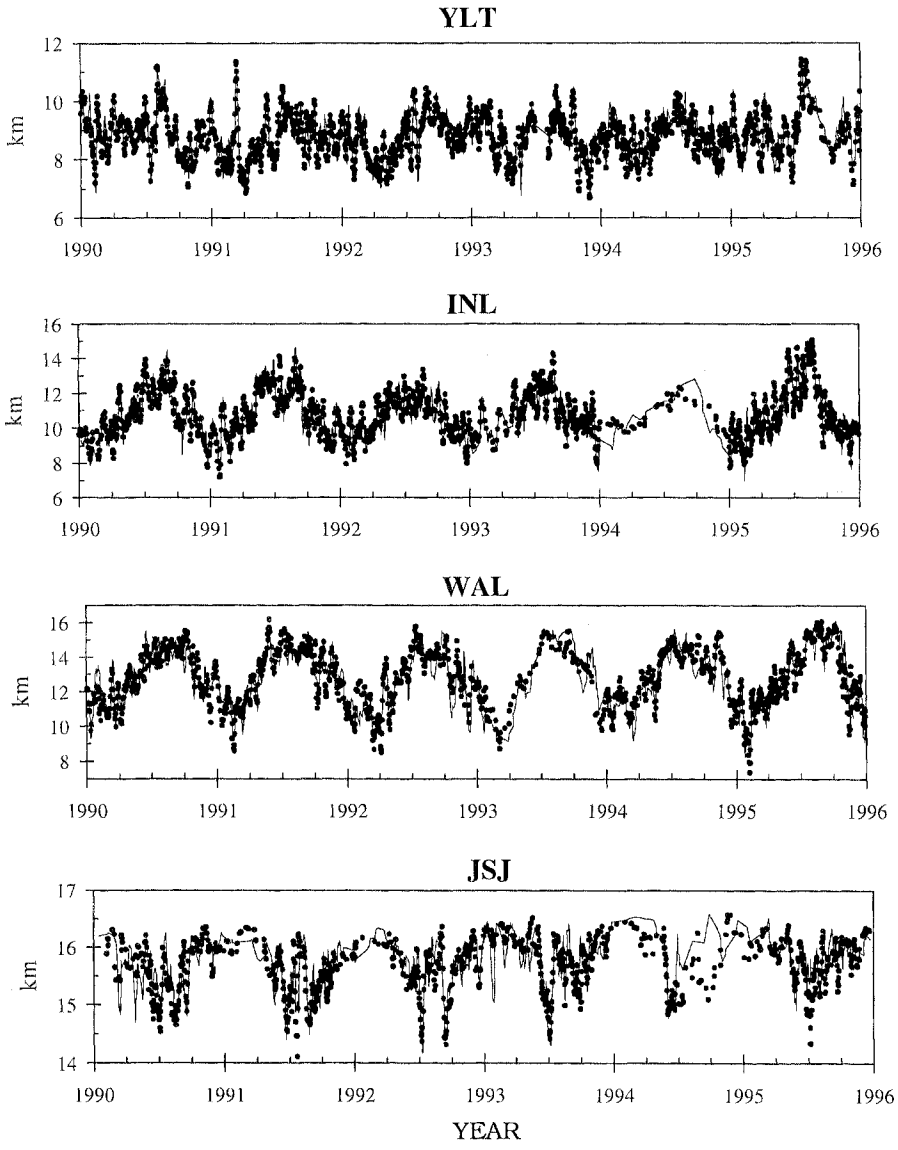

Figure 4.5 – Six-year time series of 0^h UTC (dots) and 12^h UTC (lines) tropopause heights for different stations (YLT = Alert; INL = International Falls; WAL = Wallops Island; JSJ = San Juan). The raw reported tropopause heights were filtered using a moving average of length five days.

The primary objectives delineated for our study of tropopause heights were the determination of a global mean value, the creation of a database of monthly-average tropopause heights for each station, and the development of a model allowing the determination of the tropopause height at an arbitrary latitude and time of year, as a function of readily available parameters. Before attempting any of these goals, all tropopause determinations for each station were screened for outliers, here defined as any tropopause height lying outside the interval $[\overline{x}-3\sigma, \overline{x}+3\sigma]$ where $\overline{x}$ is the station mean annual tropopause height and σ the associated standard deviation. Figure 4.6 represents the histogram of the cleaned data set, a total of 51,429 determinations.

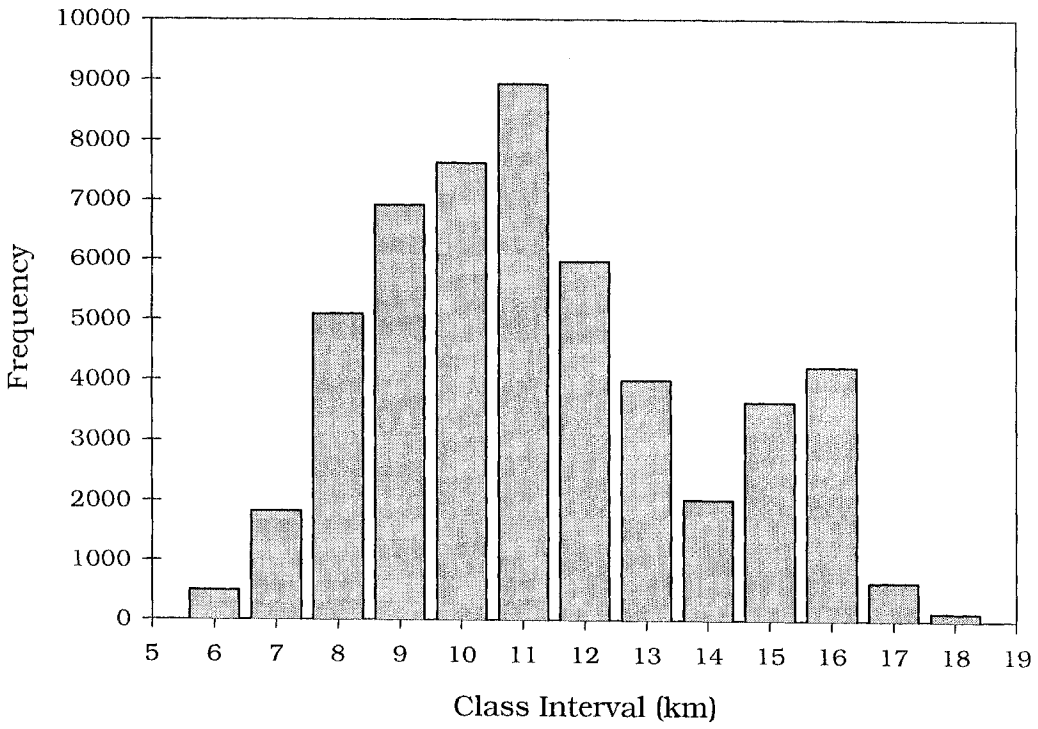

Figure 4.6 – Histogram of the distribution of the tropopause heights. The mode near 16 km is a consequence of the stability of the tropopause at low-latitudes.

The mean value of our data set appears as a natural candidate for the global mean value of the tropopause height. The analysis of this data set lead to the basic statistics shown in Table 4.3.

Table 4.3 – Basic statistics for the tropopause height.

$\overline{T}_h$	σ_{T_h}	$T_{h_{minimum}}$	$T_{h_{maximum}}$	$T_{h_{median}}$
11.3 km	2.6 km	4.8 km	19.4 km	10.9 km

The mean value obtained is remarkably close to the one suggested by Davis et al. [1985], that is, 11.231 km. However, as the distribution in latitude of the stations comprising our database is not uniform, this simple approach may lead to a biased value. Therefore we have also established another approach: we computed the means for different absolute latitude ranges (see Table 4.4), and then we took the average of these "zonal" tropopause heights.

Table 4.4 – Mean annual tropopause heights ($\overline{T}_h$) for different latitude zones. The values in parenthesis represent the standard deviation.

Latitude range (°)	$\overline{T}_h$ (km)	Latitude range (°)	$\overline{T}_h$ (km)	Latitude range (°)	$\overline{T}_h$ (km)	Latitude range (°)	$\overline{T}_h$ (km)
0 – 10	16.19 (0.79)	25 – 30	14.4 (1.7)	45 – 50	11.0 (1.5)	65 – 70	9.2 (1.3)
10 – 15	16.23 (0.77)	30 – 35	13.3 (2.1)	50 – 55	10.12 (1.6)	70 – 75	8.9 (1.2)
15 – 20	15.66 (0.60)	35 – 40	12.7 (2.2)	55 - 60	9.6 (1.5)	75 – 80	8.7 (1.1)
20 – 25	15.31 (0.96)	40 – 45	11.4 (1.8)	60 – 65	9.3 (1.5)	80 – 90	8.68 (0.99)

This approach lead to a value of 11.908 km, which is slightly lower than the one recommended by Lanyi [1984], which is 12.2 km. The mean of the zonal tropopause heights may represent more adequately a global value, as it counterbalances the larger number of high-latitude stations present in our database.

Annual and monthly means for every station – along with the associated standard deviations – were also computed and are available as electronic supplement to this dissertation (http://mat.fc.ul.pt/eg/lattex/PhD_e_sup.html). Examples of the format of these tables are presented in Appendix IV. The annual means and associated standard deviations are shown in Appendix V.

From the analysis of our database of tropopause height determinations, we can draw these major conclusions (see also the longer time series shown previously in Figure 4.5):

- the variations of tropopause height with latitude is very clear, whereas the longitudinal variations are minor;
- the seasonal variations are also prominent for mid-latitude stations but less clear for arctic and equatorial stations;
- in the tropics the summer tropopause is lower than the winter tropopause;
- the variation of the tropopause height with the station height is not very strong.

The development of any model for tropopause height determination requires an exhaustive analysis of its relation with other parameters, such as latitude, height, season, and surface temperature. The degree of correlation of the tropopause height with the

station latitude, station height, and surface temperature is well described by the correlation matrix shown in Figure 4.7. In the construction of this plot we have only considered the data for which simultaneous determinations of surface temperature, tropopause height, and lapse rate were available; a total of 48,260 observations met this requirement; furthermore, only the annual means for the 100 stations considered are shown in the plots, for the sake of clarity. It does not show the correlation of tropopause height with the day of year, which seems to exist if an analysis of longer records is performed (see Figure 4.5). As we are limited to one-year's worth of data, the analysis of the dependence on this parameter may be incomplete and we did not attempt to assess any correlations involving this parameter. However, as the variation of the tropopause height with the day of year (season) is generally in phase with the surface temperature (not shown in these plots), this seasonal dependence will be certainly absorbed by the temperature dependence. The correlation of the tropopause height with the stations height is also very weak.

In conclusion the tropopause height is best described as a function of the surface temperature and station latitude; moreover the correlation plot for annual means suggests an exponential dependence of the tropopause height with temperature, whereas a sinusoid type of equation seems to adequately describe the tropopause height dependence with latitude. However a model based on the station latitude only is not advisable, as it can not describe any seasonal variations. In our model development, and for sake of computational time reduction, we decimated our data to about one third of the total data

points (16,088), using a sampling filter (average of 3 data points), to keep the data features.

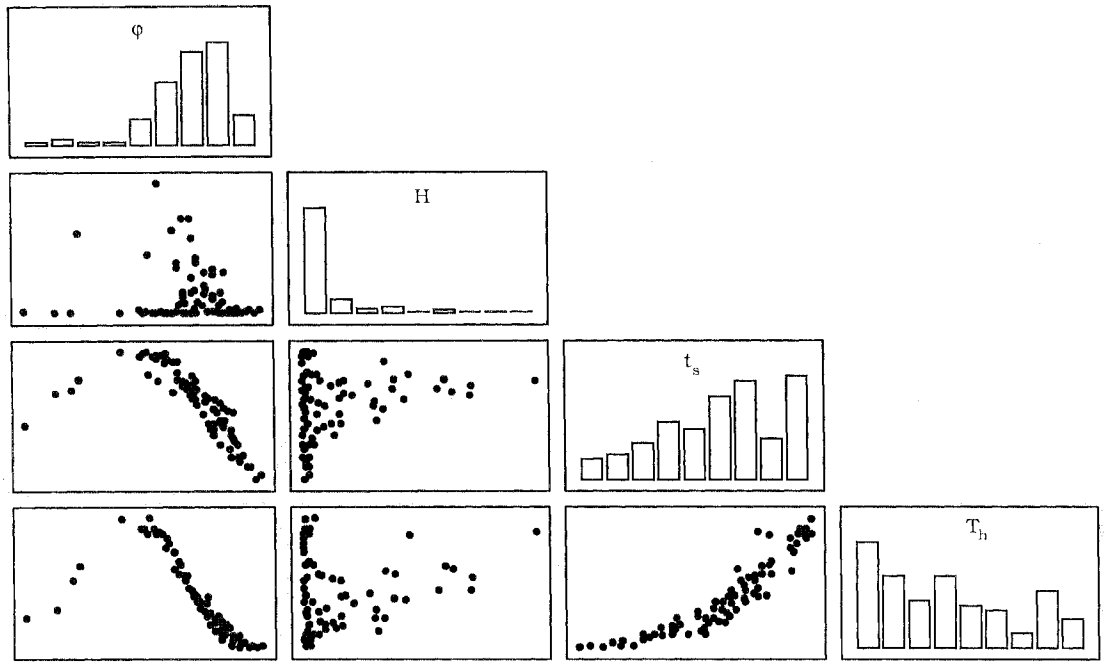

Figure 4.7 – Lower triangular matrix of correlations between latitude, station height, surface temperature, and tropopause height, for annual means of 100 radiosonde stations. In this pictorial representation, the diagonal terms are the histograms corresponding to the different variables, whereas the off-diagonal terms are the scatter plots for each pair of variables, which express their correlation.

A great number of models were found to adequately describe the tropopause dependence on the surface temperature, all yielding similar rms (root mean square) fits. Due to their simplicity, two models are proposed here.

The first model (labeled *UNB98TH1*) has the form

$$\boxed{T_h = a + b\exp\left(\frac{t_s}{c}\right)}, \tag{4.1}$$

and the least-squares fitting lead to coefficients and associated uncertainties shown in Table 4.5.

Table 4.5 – Least-squares adjustment results for UNB98TH1.

a (km)	b (km)	c ($°C^{-1}$)	rms of the fit (km)
7.508 ± 0.055	2.421 ± 0.056	22.90 ± 0.35	1.3 km

The curve-fit graph showing the observed data points, the fitted function, and the prediction 95% confidence bands is shown in Figure 4.8. The residual distribution for the model is presented in Figure 4.9.

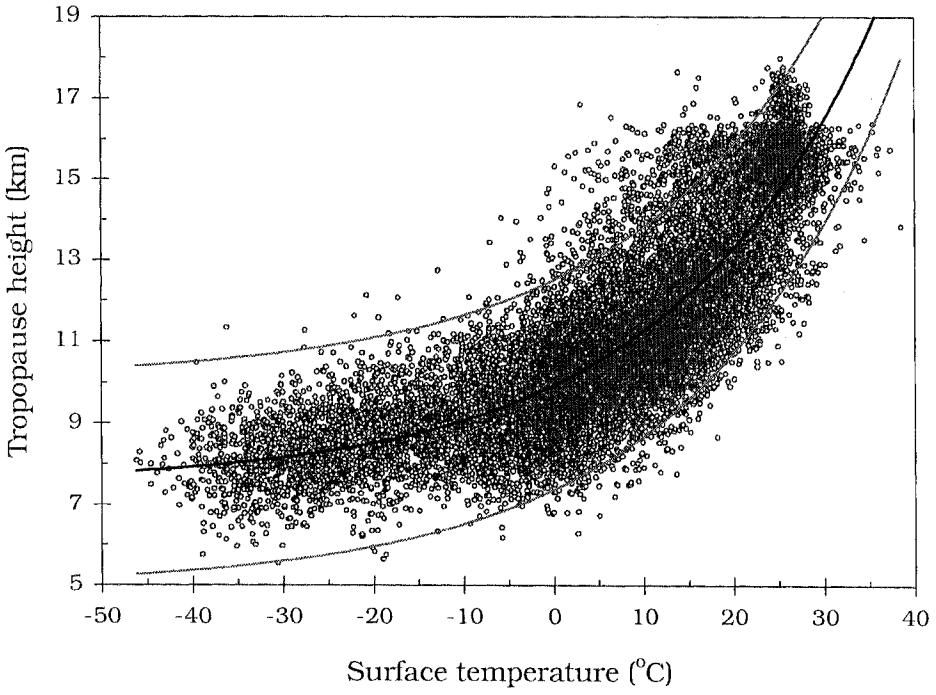

Figure 4.8 – Tropopause height versus surface temperature, for 16,088 data points. The graph shows the fitted function and the associated 95% prediction band.

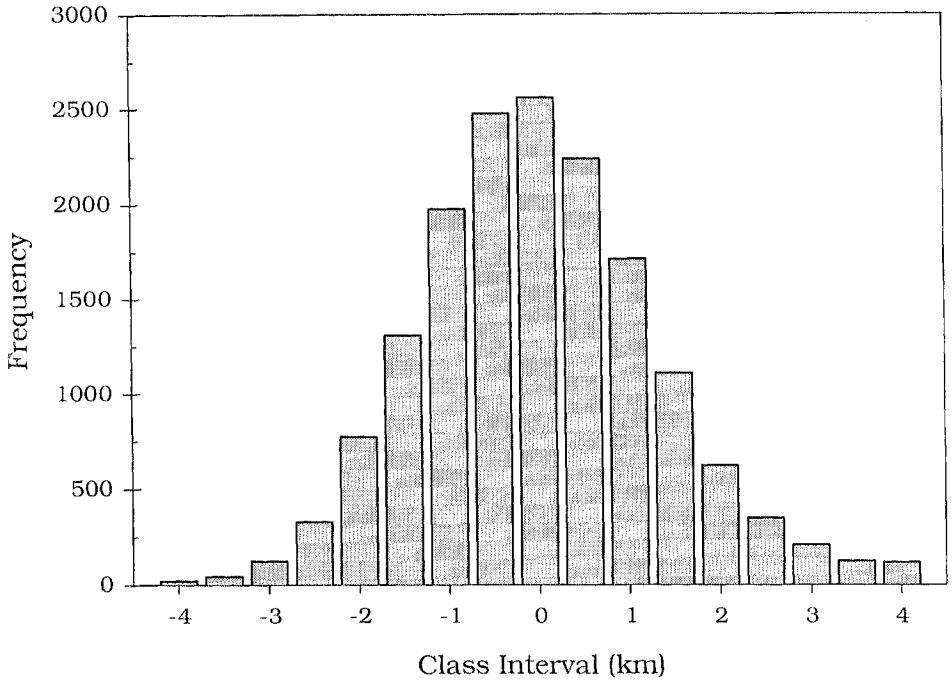

Figure 4.9 – Residual distribution for *UNB98TH1*.

The second model (named *UNB98TH2*) has the form

$$\boxed{T_h = \frac{1}{a + bt_s}}. \tag{4.2}$$

The coefficients for this model, resulting from the least squares fit, are summarized in Table 4.6.

Table 4.6 – Least-squares adjustment results for UNB98TH2.

a (km^{-1})	b ($°C\ km^{-1}$)	rms of the fit (km)
0.09443 ± 0.00012	-0.001100 ± 0.0000065	1.4 km

The rms of the fit for *UNB98TH2* is slightly larger than the rms obtained for *UNB98TH1*, but its formulation is easier to apply.

The correlation between the tropopause height and surface temperature was also seen in a recent study by Thuburn and Craig [1997]. In this study, the sensitivity of the height of tropopause to various variables was investigated. They have found that T_h was highly sensitive to the surface temperature, and less sensitive to the ozone distribution.

The form of the equations expressing the relation between tropopause height and surface temperature is very dependent on the wide range of latitudes used in the least-squares fitting and therefore from the temperature range. If we ignore the stations above 60° N and below 60° S, for example, the coefficients of the proposed equations will be less well determined. At low latitudes, the tropopause height is better expressed by a straight-line equation. This equation also applies to all data, but with a much larger rms for the fit.

The correlation between tropopause height and surface pressure suggested by Barry and Chorley [1987] was also investigated. We found a weak linear correlation between the two variables, but not strong enough to allow the determination of its coefficient with our data.

Finally we have looked for a model based on the station latitude only. The correlation plot presented in Figure 4.7 suggested that the dependence of tropopause height on station latitude could be expressed by a sinusoidal. We tried different cosine functions, the best of which turned to be a function of $\cos^4 \varphi$, as it yields lower rms of the fit. As a

compromise between accuracy and complexity, we have however selected a formulation which depends on $\cos^2 \varphi$, since the difference in the rms fit is very small (1.5 km versus 1.4 km). The final expression for this model (*UNB98TH3*) is:

$$T_h = a + b\cos^2 \varphi, \tag{4.3}$$

where a and b were listed in Table 4.7 (based on 16,088 data points).

Table 4.7 – Least-squares adjustment results for UNB98TH3.

a (km)	b (km)	rms of the fit (km)
7.588 ± 0.025	8.186 ± 0.049	1.5 km

Figure 4.10 shows the fitted function and associated 95% confidence prediction bands. The rms of the fit for this model is almost identical to *UNB98TH2*, but as discussed before, its use is not recommended for general application. This model is also biased for low latitudes, and have a much larger spread of the residuals (see Figure 4.11), confirming its poorer accuracy.

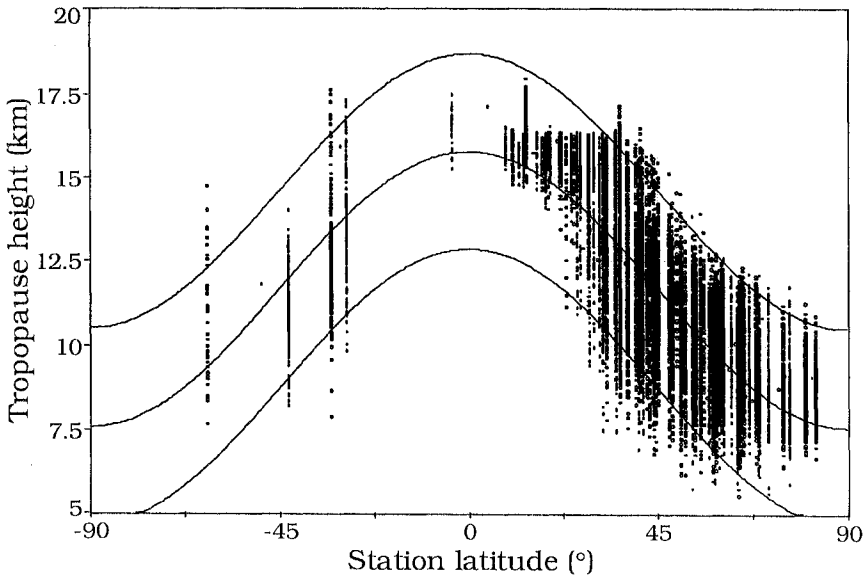

Figure 4.10 – Tropopause height versus station latitude, for 16,088 data points. The lines shown in the graph are the fitted function (*UNB98TH3*) and the associated 95% prediction intervals.

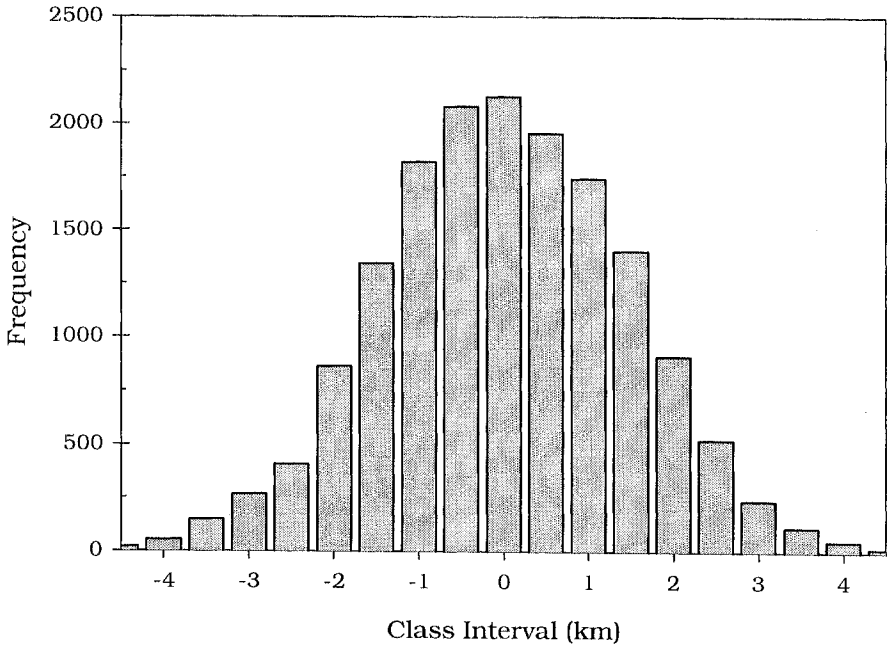

Figure 4.11 – Residual distribution for UNB98TH3.

4.2.2. Inversion height

The planetary boundary layer is a region of turbulence where important phenomena of temperature inversions can occur. The thickness of this layer is influenced by a series of factors such as topographic effects, winds, and vertical motions and shows a daily variation, as a response to the diurnal heating and cooling cycles [Peixoto, 1987; Peixoto and Oort, 1992]. The following types of temperature inversions are identified [Crutcher, 1969; Lutgens and Tarbuck, 1979; Ahrens, 1994]: radiation inversion, subsidence inversion, and frontal inversion.

Radiation inversion (or surface inversion) is the most common type of inversion and results from the daily solar heating cycle. During the day, the earth's surface is warmer than the lower atmosphere and a vertical transfer of heating into the atmosphere occurs. An inverse situation is observed during night-time and early morning periods: because the radiation is much stronger for the ground, the layers in contact with the earth's surface cool much faster than the upper layers, and a temperature inversion is observed. This temperature inversion is favored by long nights (e.g. arctic regions), no wind, dry air (e.g. semiarid regions), and clear skies [Lutgens and Tarbuck, 1979; Ahrens, 1994].

Subsidence inversion results from an adiabatic heating of a layer of sinking air, as a result of strong anticyclones or stable air masses. As the air is forced to sink to lower altitudes, it will warm by adiabatic compression, the top layer being warmer than the bottom layer. This kind of inversion rarely occurs near the earth's surface, but may persist for several days. As an example, Los Angeles is subject to a strong subsidence

inversion which persists from June to October; the cooling of the surface water of the Pacific, as a result of upwelling, creates a cold air mass below warm air mass, originating a subsidence inversion [Ahrens, 1994].

Frontal inversion is formed when a warm air mass overrides a cold air mass.

The analysis of the temperature inversions and the determination of the top of the inversion layer is in our case limited by the nature of our data. In most of the cases, the radiosonde profiles are restricted to the 0^h and 12^h UTC observations, which do not necessarily correspond to the hour of day at which stronger inversion heights may occur. For the sake of convenience, we will refer to these observations as "night" and "day", with the understanding that they do not necessarily represent local night and day.

The methodology used in determining the inversion heights is very simple and limited to the radiation inversions: any increase of temperature observed from the surface level upwards is flagged as a temperature inversion, and the top of the inversion layer corresponds to the first level showing a decrease of the temperature with height.

Figure 4.12 shows a few case studies, involving stations with different characteristics. The length of night is the main limiting factor on the depth of the temperature inversion [Kyle, 1991]; therefore the top of the inversion layer is generally of only a few hundred metres for low and mid-latitude stations, whereas the arctic stations show inversion depths of more than two kilometres. Arctic stations (e.g. Alert) clearly show a seasonal variation, with deep inversion layers in both night and day profiles during winter. The number of observed inversions for tropical stations (e.g. San Juan) is very small, and of

very limited extent, throughout the year. Stations with a semi-arid climate show a notorious difference between night and day profiles, which is associated with the high daily amplitude in temperature.

Due to the specific nature of occurrence of the inversions and to the limitations imposed by the temporal distribution of our data, any global statistics concerning this meteorological parameter are of limited use. Nevertheless they are also available in electronic supplement to this dissertation (see also Appendix IV) at http://mat.fc.ul.pt/eg/lattex/PhD_e_sup.html. The number of occurrence of these temperature inversions shown in tables of the electronic supplement, as compared with the total number of soundings (given approximately by the number of lapse rate determinations, for example) will help to judge its importance.

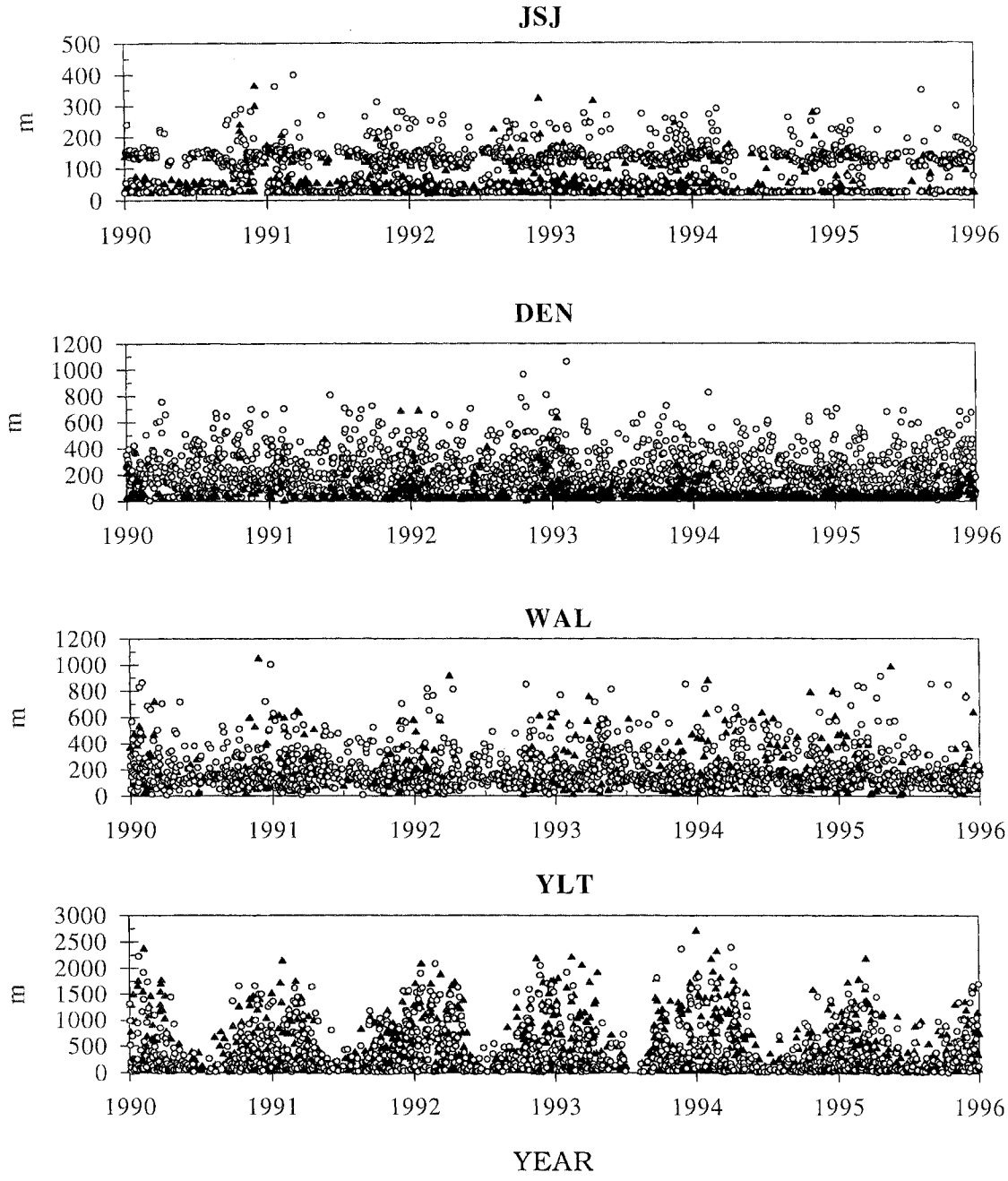

Figure 4.12 – Top of the inversion boundary layer for stations with different climatic characteristics, corresponding to the 0^h UTC (triangles) and 12^h UTC (open circles) radiosonde launches (JSJ = San Juan; DEN = Denver; WAL = Wallops Island; YLT = Alert).

4.2.3. Lapse rate

The rate of change of temperature with height is the temperature lapse rate, α, defined as [Dutton, 1966; Iribarne and Godson, 1973]:

$$\alpha = -\frac{dT}{dz} \tag{4.4}$$

that is, the negative of the vertical temperature gradient. The sign is conventionally chosen so that the lapse rate is positive when the temperatures decrease with height (as it normally does in the troposphere).

It is known that the lapse rate is highly variable in space in time, and with height [Kyle, 1991; Wallace and Hobbs, 1977; Barry and Chorley, 1987]. However there has been no global quantitative study of these variations. Some of the models and mapping functions used in modeling neutral-atmosphere propagation delay require the average value of lapse rate in the troposphere. This computation requires the knowledge of both the tropopause height and the top of any inversion layer, the meteorological parameters described in the previous sections. The exact knowledge of these parameters is very important in order to give unbiased solutions, as will be shown.

The lapse rate is nothing else but the (negative) slope of the line that best fits the temperature profile. Both a classic least-squares straight-line fit and a robust fit, which minimizes the absolute deviation of the observations to the fitted line [Press et al., 1989], were used. The robust estimation is less sensitive to outliers than the method of least squares, as illustrated in Figure 4.13. There are however advantages in using the method

of least squares: (1) it is an unbiased minimum-variance estimator; (2) the time domain plots reveal less noisy estimates than the robust approach; (3) as a data cleaning was performed *a priori* and outlier removal on estimates was performed *a posteriori*, it is not expected that any remaining outliers would bias our estimates. The good agreement between the two types of solutions is nevertheless a fact, as attested to in Figure 4.14.

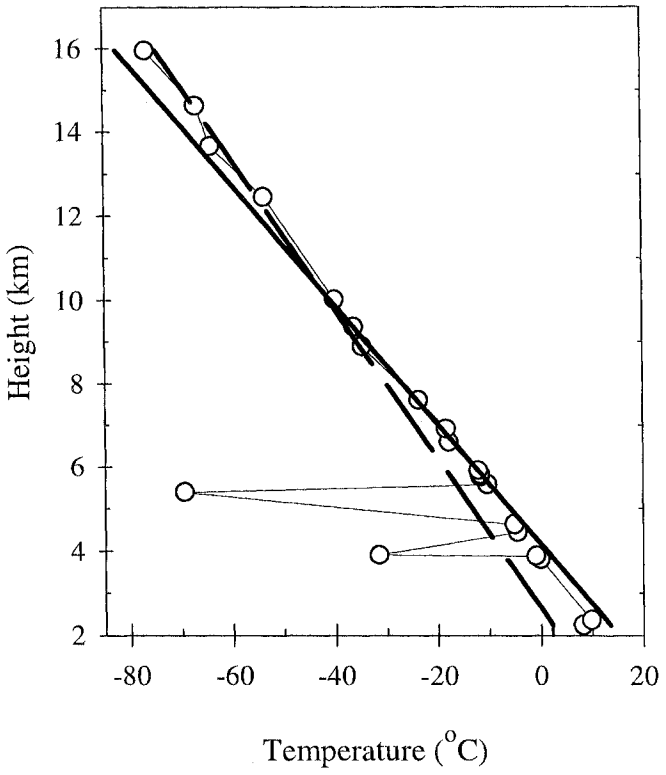

Figure 4.13 – Effect of outliers in the determination of the lapse rate. The dashed line represents the slope of the least squares line fitting to the temperature profile, whereas the solid line represents the slope obtained using a robust estimator.

The determination of the average lapse rate in the troposphere is sensitive to the approximate location of the top of the surface inversion layer, when significant, and of the

tropopause. If these boundaries are not correctly defined, a biased lapse rate will be determined, as the observations beyond the tropopause and below the inversion height will act as outliers, modifying the slope of the fitted line, as in Figure 4.13. This fact is well evident for the arctic stations, such Alert, and illustrated in Figure 4.15. When the inversion height is not considered, the winter lapse rates will be much lower than the actual lapse rates. Because of the seasonal variation of the inversion height in these regions, a false seasonal variation will be induced in the lapse rate time series.

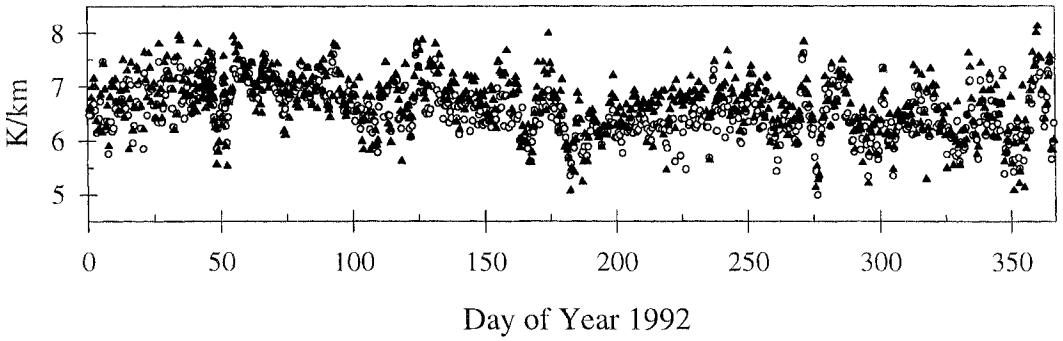

Figure 4.14 – Temperature lapse rate estimates using a least squares method (open circles) and a robust estimator (triangles), for Oakland.

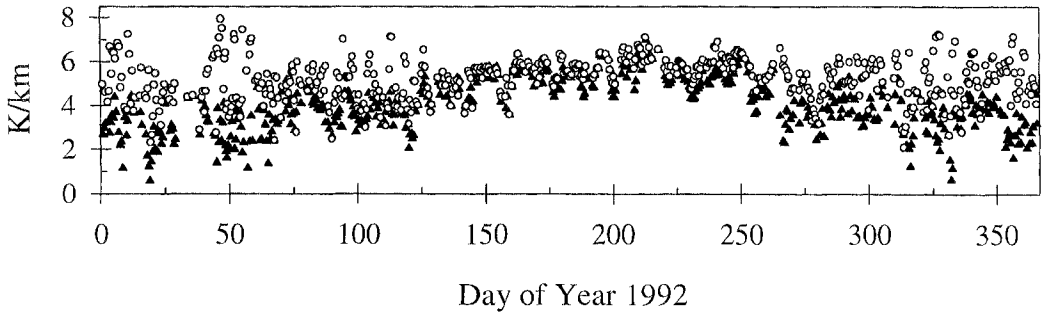

Figure 4.15 – Temperature lapse rate in the troposphere, assuming no inversion (triangles) and considering the observed inversion height (open dots), for Alert.

The approach used in the lapse rate determination and analysis can be summarized as follows: first we built the database of tropopause heights and inversion heights for each station; second we performed the least-squares straight line fit to each individual temperature profile; finally we carried out a screening of the determined lapse rates for outlier removal.

As mentioned, the straight-line fit to the temperature profile is performed within the troposphere. For each profile, an epoch synchronization with the observed tropopause and inversion heights is tried. In the case of the inversion height, if that synchronization fails, it is assumed that no inversion height is observed; in the case of the tropopause height, a new synchronization is tried with the nearest tropopause height available (within 24 hours). If this second attempt fails, the annual mean for the station in analysis is considered. This strategy allows the building of the largest database possible with essentially no biased solutions.

The data screening removes not only the lapse rates not included in the $[\bar{x}-3\sigma, \bar{x}+3\sigma]$ interval, but also the lapse rates for which the quality of the fit was revealed to be poor (based on an identical criterion).

The total number of lapse rates remaining after data cleaning totals 62,505, distributed as shown in Figure 4.16.

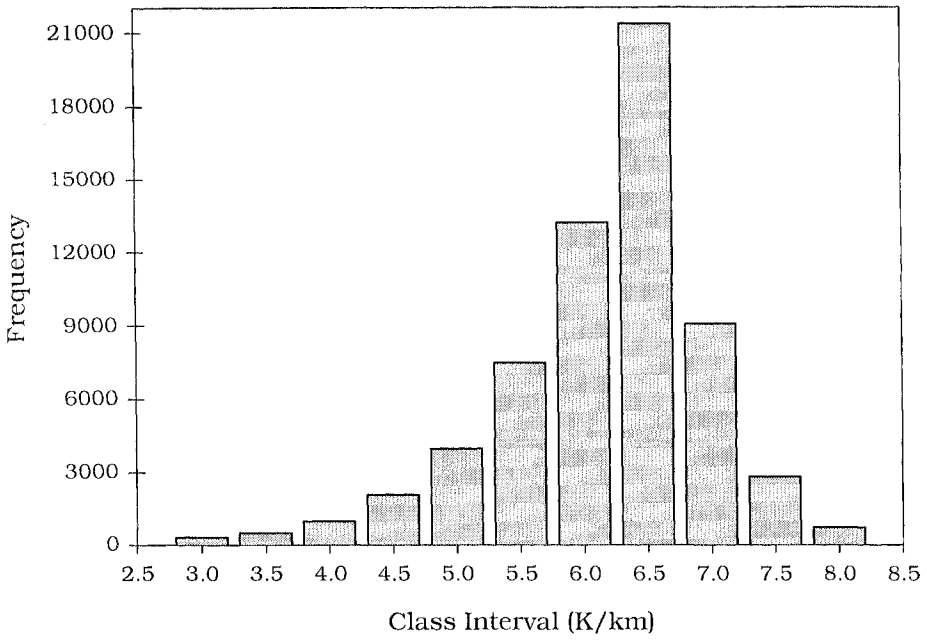

Figure 4.16 – Histogram of the lapse rates database.

The basic statistics for this data set summarized in Table 4.8.

Table 4.8 – Basic statistics for the lapse rate.

$\overline{\alpha}$	σ_α	$\alpha_{minimum}$	$\alpha_{maximum}$	α_{median}
6.17 K km^{-1}	0.82 K km^{-1}	2.07 K km^{-1}	8.94 K km^{-1}	6.32 K km^{-1}

The mean value obtained is lower than the value usually recommended, that is 6.5 K/km (e.g. Davis et al. [1985]), which seems appropriate for lower to middle latitudes, as shown in Table 4.9. Rennick [1977] have also concluded that such temperature lapse rate yields a temperature profile cooler than the observed throughout the troposphere.

Table 4.9 – Mean annual lapse rates ($\overline{\alpha}$) for different latitude zones. The numbers in parenthesis are the associated standard deviations.

Latitude range (°)	$\overline{\alpha}$ (K km^{-1})	Latitude range (°)	$\overline{\alpha}$ (K km^{-1})	Latitude range (°)	$\overline{\alpha}$ (K km^{-1})	Latitude range (°)	$\overline{\alpha}$ (K km^{-1})
0 – 10	6.61 (0.27)	25 – 30	6.49 (0.41)	45 – 50	6.20 (0.78)	65 – 70	5.78 (0.96)
10 – 15	6.47 (0.17)	30 – 35	6.43 (0.52)	50 – 55	6.00 (0.97)	70 – 75	5.29 (0.86)
15 – 20	6.54 (0.26)	35 – 40	6.42 (0.66)	55 – 60	6.01 (0.89)	75 – 80	5.37 (0.78)
20 – 25	6.34 (0.28)	40 – 45	6.38 (0.73)	60 – 65	5.89 (0.94)	80 – 90	5.17 (0.96)

If we take the average of the mean "zonal" lapse rates, we obtain 6.10±0.49 K km^{-1}, which is not significantly different from the simple average but, as in the case of the tropopause height database, this value is not biased by the non-uniform distribution of stations with latitude. The main statistics for each station (both on an annual and monthly basis) were also computed and are available electronically (http://mat.fc.ul.pt/eg/ /lattex/PhD_e_sup.html); a sample of the tables of these statistics is shown in Appendix IV. The variation of the annual mean lapse rate with latitude is shown in Appendix VI.

The analysis of our set of lapse rates allow us to draw these major conclusions: (a) the lapse rate varies significantly with location and season; (b) as illustrated in Figure 4.17, these seasonal variations are more distinct for continental stations with cold winters (e.g. FAI), and of small magnitude for other climate types (e.g. PBI); (c) the highest lapse rates occur in tropical and mid-latitude arid regions (e.g. DEN), reaching frequently 7 - 8 °C km^{-1}; (d) the lapse rate for mediterranean climates (e.g. OAK) is greater in winter than

in summer, a fact corroborated by Kyle [1991].

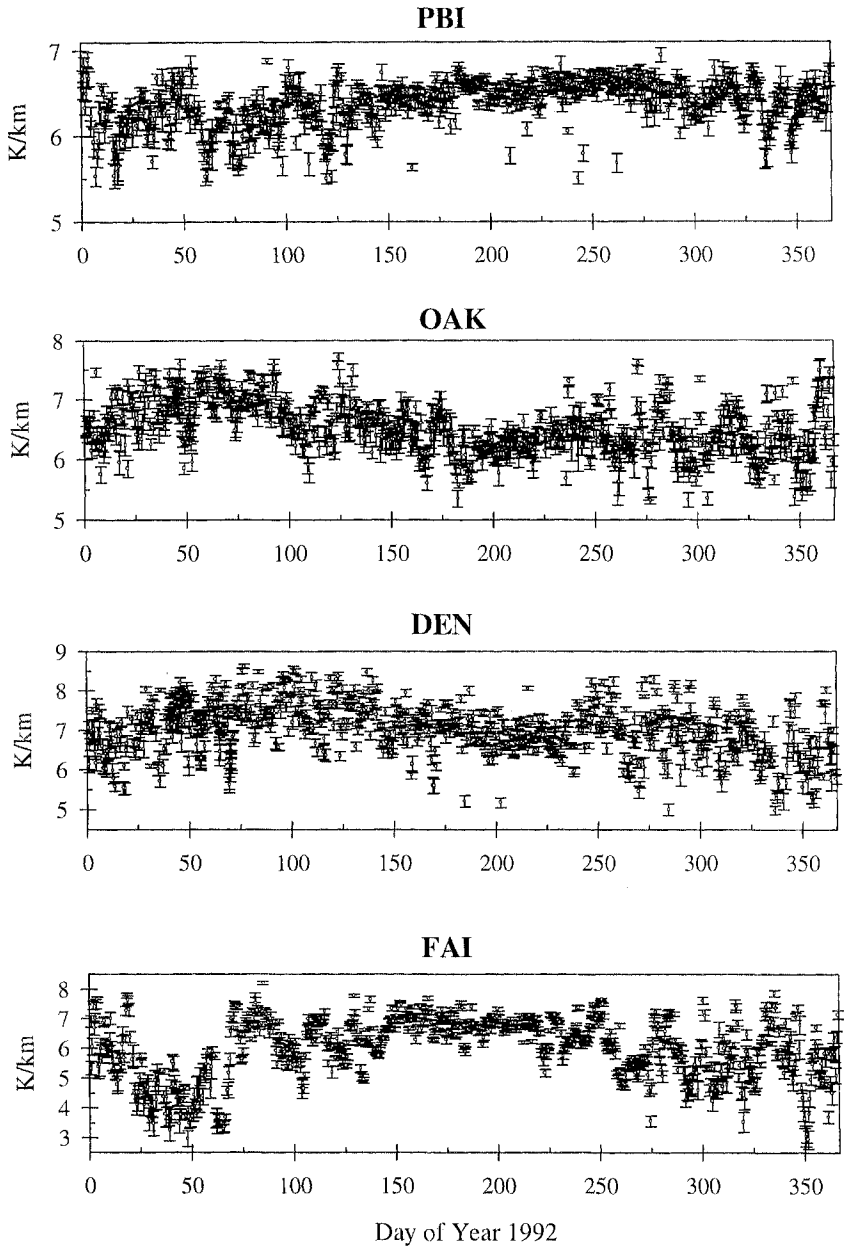

Figure 4.17 – Lapse rates and respective error bars for stations with different climatic characteristics (PBI = West Palm Beach; OAK = Oakland; DEN = Denver; FAI = Fairbanks). In order to emphasize the seasonal variations, different amplitude of the vertical scale was used.

The correlation plots shown in Figure 4.18 help us to better understand the dependence of the lapse rate on the same parameters used before. Once more, the annual means pertaining to the 100 stations with simultaneous determinations of those parameters were used in the creation of these correlation plots. It is interesting to note the weaker dependence of the lapse rate on the latitude and surface temperature, in contrast with a stronger correlation of the lapse rate with the height of the station.

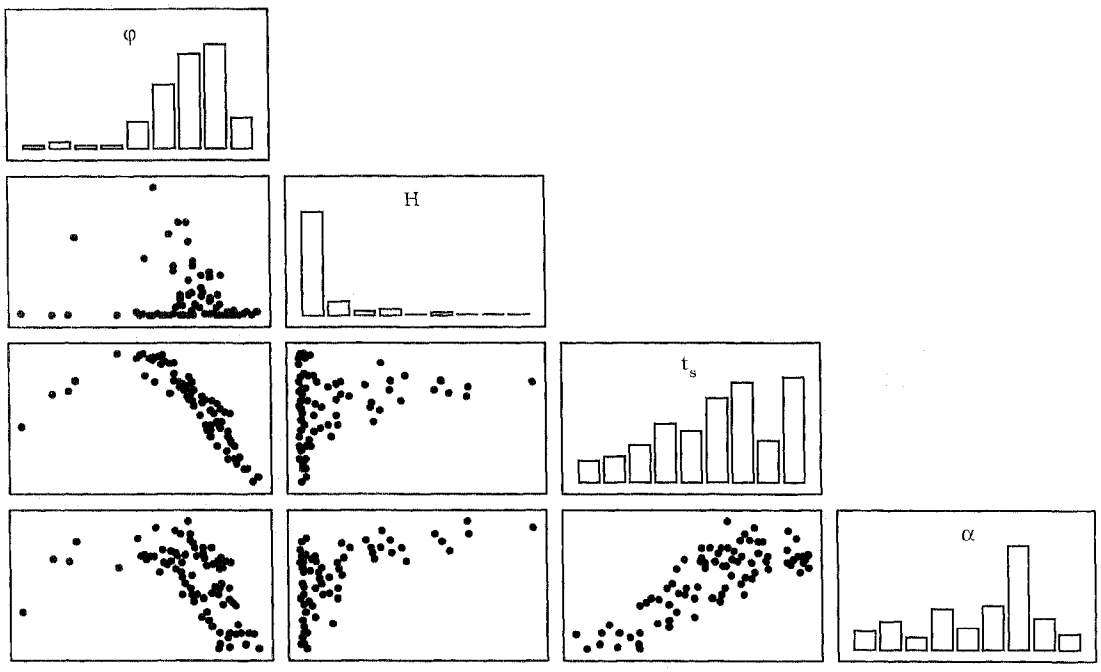

Figure 4.18 – Lower triangular matrix of correlations between station latitude, height, surface temperature, and lapse rate, for annual means of 100 radiosonde stations. Otherwise as in Figure 4.7.

As suggested by the correlation plot, the lapse rate seems to be linearly dependent on the surface temperature, and approximately described by a simple straight line equation (named as *UNB98LR1*):

$$\alpha = a + bt_s \tag{4.5}$$

From the least-squares straight line fit to the 16,088 data points (see Figure 4.19) we obtained the parameters presented in Table 4.10. The residual distribution is shown in Figure 4.20.

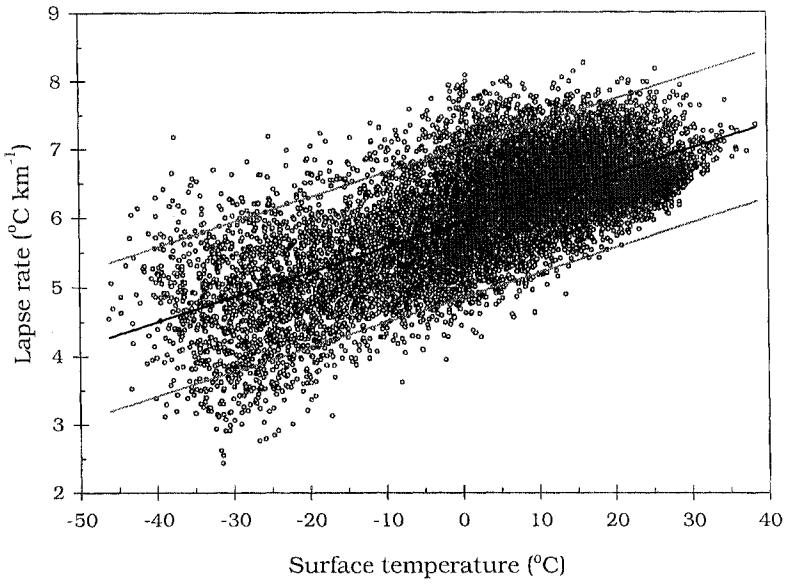

Figure 4.19 – Lapse rate straight-line least-squares fit based on 16,088 data points and 95% prediction bands.

Table 4.10 – Least-squares adjustment results for UNB98LR1.

a ($°C\ km^{-1}$)	b (km^{-1})	rms of the fit ($°C\ km^{-1}$)
5.930 ± 0.0047	0.0359 ± 0.00028	0.55

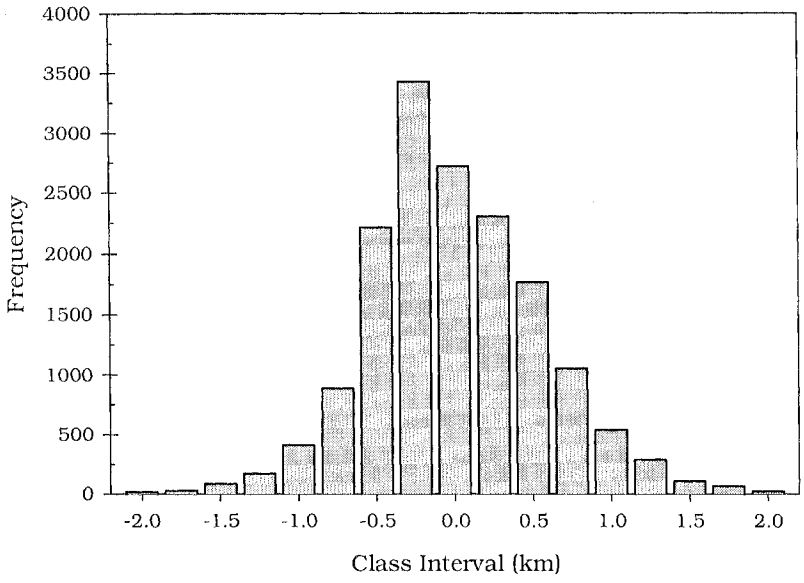

Figure 4.20 – Residual distribution for *UNB98LR1*.

Rennick [1977] also found an empirical relation between lapse rate and surface temperature. She concluded that the observed lapse rate could be compared with the moist adiabatic lapse rate at the surface and that the ratio between these two quantities could in turn be expressed as a third-order polynomial in T_s. The model developed by Rennick can not however be directly compared with the models proposed in this dissertation, as her model gives values of α in K hPa^{-1} units. Furthermore, the use of Rennick's model would be of little interest in the context of radio-meteorology applications, as it would require the additional computation of the moist adiabatic lapse rate, which is a function of several parameters (see, e.g., Hess [1959]). The range of temperatures for Rennick's model is also limited to 250 K < T_s < 300 K.

Stone and Carlson [1979] claim that the correlation of between lapse rate and surface temperature "*is likely to be purely statistical in nature*", but even though this dependence

seems to model fairly well the latitudinal and seasonal variations of observed lapse rate in a global basis.

Even though our correlation plots showed a weak dependence of the temperature lapse rate on the height of the station, we were not able to derive an expression that could take into account this dependence. As Rennick's model has an implicit dependence on the surface pressure (in the computation of the moist adiabatic lapse rate), we were motivated to develop a new model that could express this dependence. We found that the lapse rate could also be expressed as a linear function of surface pressure, and we established an alternative model for temperature lapse rate prediction that is a function of the surface temperature and pressure (labeled *UNB98LR2*):

$$\alpha = a + bt_s + cP_s \tag{4.6}$$

For the least-squares fit we used ~11,000 observations, and we obtained the parameters listed in Table 4.11.

Table 4.11 – Least-squares adjustment results for UNB98LR2.

a ($°C\ km^{-1}$)	b (km^{-1})	c ($hPa^{-1}\ °C\ km^{-1}$)	rms of the fit ($°C\ km^{-1}$)
10.3 ± 0.10	0.03182 ± 0.00040	-0.00436 ± 0.00011	0.55

The rms of the fit is identical to that obtained for UNB98LR1 for a much larger number of observations. The small improvement in scatter reduction contrasts with the significant reduction in bias, namely for high-altitude stations, and is well evident in

Figure 4.21, which shows a comparative histogram of residual distribution for both models, for a set of ~22,000 observations.

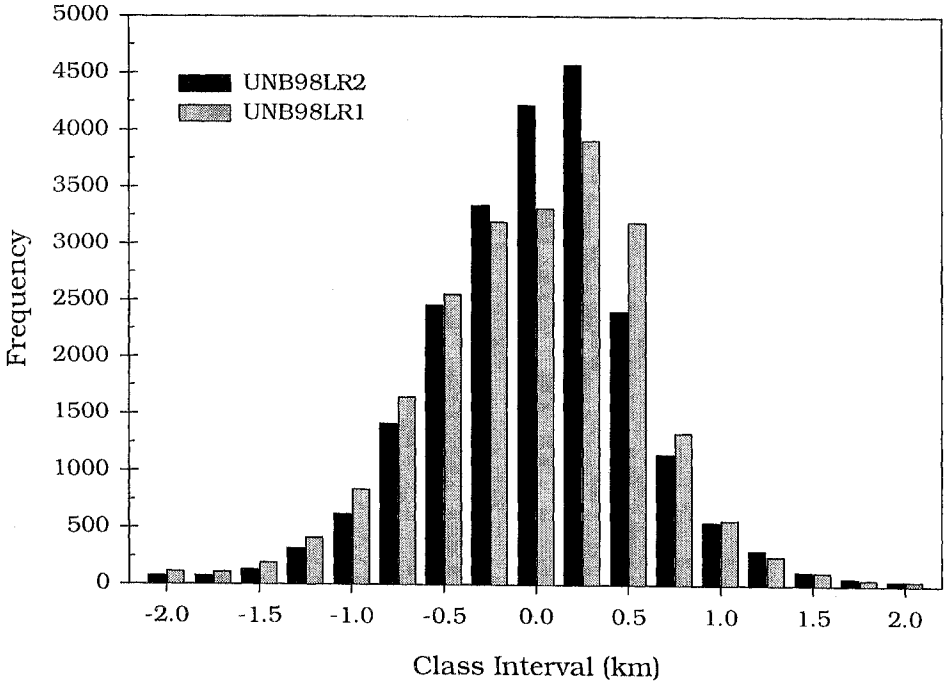

Figure 4.21 – Comparative histogram of residual distribution for UNB98LR1 and UNB98LR2, for a set of ~22,000 observations.

In this chapter we have described radiosonde instrumentation and addressed some issues regarding data quality. Based on archived data from different sources we have established large databases of meteorological parameters, which enabled us to develop models for tropopause height and temperature lapse rate prediction.

The next chapter will discuss ray-tracing accuracy and will establish the database of benchmark traces to be used in model assessment.

5. RAY TRACING

In general, the integration of the ray-trace equations established in Chapter 3 is not possible, as it requires the exact knowledge of the refractivity profile along the whole ray path as well as the elevation angle of the ray at the reception site. The problem can be solved numerically, for any arbitrary elevation angle, by **ray tracing**, which is defined as the process of determining the path of an electromagnetic signal, based on geometric optics theory applied over a series of thin spherical shells, concentric with the earth, and within which a constant refractivity (or some simple functional form of variation) is assumed [Kerr, 1953; Bean and Dutton, 1966; Bradley, 1989]. The validity of this technique relies on two basic assumptions: (1) the refractive index does not change significantly within the signal's wavelength; (2) the fractional refractivity changes between neighboring rays are small within a wavelength [Kerr, 1953; Bean and Dutton, 1966].

The ray-tracing technique implementation can vary substantially, reaching different degrees of complexity and accuracy. Examples of ray tracing algorithms are given by Bean and Dutton [1966], Thayer [1967], Davis [1986], and Schroeder and Westwater [1991]. The ray-tracing software used in this dissertation (hereafter referred to as

TRACE) is a modified version of the software developed by J.L. Davis, T.A. Herring, and A.E. Niell [Niell, 1994].

This chapter describes the different features of the ray-tracing software, discusses ray-tracing model accuracy and limitations, and assesses the ray-tracing products.

5.1. Software algorithms and models

The determination of the atmospheric delay by ray tracing considers the earth's atmosphere to be divided into a series of thin concentric spherical shells, within which a constant refractivity is generally assumed. The ray-tracing computation of the neutral-atmosphere delay is accomplished by adding the contribution of each spherical layer, until the top of the atmosphere is reached. The thickness of each layer can be kept constant, or it can vary in such a way that the changes of the refractivity within each layer are kept below a certain level. If the refractivity is assumed constant within each layer i (and represented by the average of the refractivity at the lower boundary and at the upper boundary, for example), its contribution to the delay will be given by:

$$\left(\delta d_{na}\right)_i = 10^{-6} \frac{N_i^l + N_i^u}{2} \Delta s , \tag{5.1}$$

where N_i^l and N_i^u are the refractivities at the lower and upper boundaries of layer i, respectively, and Δs the thickness of that layer (step size).

From Equation (5.1), it becomes clear that the computation of the refractivity at every layer requires profiles of pressure, temperature, and water vapor pressure (computed

from relative humidity, dew point or another moisture variable), based either on theoretical or radiosonde profiles. Two main problems have to be solved for radiosonde profiles: (1) most of the radiosonde profiles are vertically limited to the first 15-20 km of the atmosphere; (2) the radiosonde databases constitute a reduced discrete sample of the actual refractivity profile of the atmosphere. The approximation of the radiosonde profiles to a continuous atmosphere has therefore to be performed using interpolation and extrapolation schemes. By selecting the ray-tracing technique as the standard of comparison, it is also important to evaluate how sensitive are these benchmark values to changes in models and methods of computation. These issues are discussed in the following sections.

5.1.1. Profile extrapolation and interpolation

In order to approximate the pressure, temperature and relative humidity profiles to a continuous atmosphere covering the height limits of the integration process, each of the profiles has to be interpolated between the reported levels and extrapolated beyond the last (highest) reported level.

The temperature and relative humidity for each layer to be assessed is linearly interpolated between the reported levels, that is, the observation ℓ, at an interpolated level H, is obtained from the observations at reported levels H_i and H_{i+1} using the following scheme:

$$\ell_H = \ell_i + \frac{\ell_{i+1} - \ell_i}{H_{i+1} - H_i}\left(H - H_i\right). \tag{5.2}$$

A temperature profile that approximates the U.S. Standard Atmosphere, 1962 [NOAA, 1962] is used for extrapolation beyond the last reported level (for ray-tracing purposes, this standard atmosphere is identical to the U.S. Standard Atmosphere, 1976 [NOAA/NASA/USAF, 1976]). This profile assumes a linear change of temperature within the different layers considered. For heights between 25 km (a level at which a standard value of 220 K is assigned) and 100 km, for example, the following lapse rates are used:

$$\alpha = \begin{cases} -1.92\ \mathrm{K\ km^{-1}} & ,\text{if } H \in [25\ \mathrm{km}, 50\ \mathrm{km}] \\ +2.27\ \mathrm{K\ km^{-1}} & ,\text{if } H \in [50\ \mathrm{km}, 80\ \mathrm{km}] \\ -0.50\ \mathrm{K\ km^{-1}} & ,\text{if } H \in [80\ \mathrm{km}, 100\ \mathrm{km}] \end{cases}$$

The relative humidity radiosonde observations beyond the 10 km level are not considered by TRACE as they are generally unreliable. For extrapolation purposes above that height, the relative humidity is assumed to linearly decrease from 40% to 4% between 10 km and 16 km, and above 16 km the value of 4% is assumed constant. Above 32 km, the relative humidity is not taken into account; this extrapolation profile was adopted from Valley [1965].

The pressure at a given height is computed using the standard formulae for constant-lapse-rate or isothermal atmospheres (see Chapter 2), according to the temperature variation within the considered layer. The acceleration due to gravity is corrected for latitude, using the international gravity formula, and for altitude, using the Bruns's formula (see, e.g., Heiskanen and Moritz [1967]).

5.1.2. Saturation vapor pressure computation

Generally the moisture content in the atmosphere is expressed in the radiosonde databases in terms of either relative humidity or dew point. The ray-tracing algorithms, however, require the moisture to be expressed as water vapor pressure, which is in turn related to the saturation vapor pressure, as mentioned in Chapter 2.

In order to compute the saturation vapor pressure (over a planar surface of water), a large selection of formulae is available (e.g. Berry et al. [1945]; Goff and Gratch [1946]; Langlois [1967]; Tabata [1973]; Wexler [1976]; Lowe [1977]; Rasmussen [1978]; Buck [1981]; Baby et al. [1988]; WMO [1993]). Most of these and other existing formulae are approximations or simplifications of the Goff and Gratch formula, and to the more recently developed one by Wexler [1976], and are typically the result of a search for computationally more efficient models. The mathematical structure of the saturation vapor pressure formulae fall in three main categories: exponential, polynomials, and rational functions. At least partially, the accuracies of these formulae have been already analyzed and discussed (e.g. Murray [1967]; Tabata [1973]; Riegel [1974]; Hull [1974]; Wigley [1974]; Lowe [1977]; Elliott and Gaffen [1991]). In order to study the effect of the use of different formulae on ray tracing accuracy, which is clearly less well known (to the best of our knowledge such studies do not appear to exist at all), we selected four of the most widely used formulae, as described below.

One of oldest formulae used to compute the saturation vapor pressure is known in the literature as the Magnus or Tetens formula, and is implicitly recommended by the International Earth Rotation Service (IERS) [McCarthy, 1996]:

$$\boxed{e_{sw} = 6.11 \times 10^{\frac{7.5t}{237.3+t}}}, \tag{5.3}$$

where t is the temperature, in °C, and e_{sw} is the saturation vapor pressure, in hPa (the same symbol definitions and units also apply to the following formulae).

The default formula in TRACE is given by Berry et al. [1945], and will be referred to hereafter as Berry:

$$\boxed{e_{sw} = 6.105 \exp\left\{25.22\left(\frac{T-273}{T}\right) - 5.3 \ln\left(\frac{T}{273}\right)\right\}}, \tag{5.4}$$

where T is the absolute temperature, in K.

The Goff and Gratch [1946] formula was accepted internationally and was largely used as a standard for comparison; it is the basis of the well-known Smithsonian Meteorological Tables [List, 1966]. Murray [1967] transformed the original formula into a more convenient formulation:

$$\boxed{\begin{aligned} e_{sw} = 7.95357242 \times 10^{10} \exp\Bigg\{ & -18.1972839 \frac{T_{st}}{T} + 5.02808 \ln\left(\frac{T_{st}}{T}\right) \\ & - 70242.1852 \exp\left[-\frac{26.1205253 T}{T_{st}}\right] + 58.0691913 \exp\left[-8.03945282 \frac{T_{st}}{T}\right] \Bigg\} \end{aligned}}, \tag{5.5}$$

where T_{st} = 373.16 K (steam point). This formula produces no significant differences relative to the original version.

The Wexler [1976] saturation vapor formula is given as:

$$\begin{aligned} e_{sw} = 0.01\exp\{&-2991.2729T^{-2} - 6017.0128T^{-1} + 18.87643854 - 0.028354721T \\ &+ 0.17838301\times10^{-4}T^{2} - 0.84150417\times10^{-9}T^{3} + 0.44412543\times10^{-12}T^{4} \\ &+ 2.858487\ln T\} \end{aligned} \quad (5.6)$$

The Wexler formula represents an improvement over the Goff and Gratch formula, as it is based on more accurate experimental measurements, such as the experimental value of the vapor pressure of water at its triple point [Guildner et al., 1976], and a new value of the gas constant. The uncertainty associated with the formula is a few tens of parts per million, at most. It represents nowadays the standard formula against which other formulae are compared. The reader should be aware that there is a 0.01 K difference in the definition of the absolute temperature for Berry and Goff and Gratch ($T = t + 273.16$) and Wexler ($T = t + 273.15$) formulations, corresponding to the pre-1954 and post-1954 definitions, respectively.

The formulae above are to be used in the temperature range [0 °C, 100 °C], but it is current practice to use them in radiosonde data analysis in extrapolation, to compute saturation vapor pressure below 0 °C (supercooled water) – a repercussion of the WMO recommendation to have the relative humidity at temperatures below 0 °C evaluated with respect to water [WMO, 1996a]. Among other advantages of this procedure, the following are relevant: (1) the majority of clouds at temperatures below 0 °C consists of

water or mainly water; (2) nearly all the existing records of relative humidity below 0 °C are expressed on the basis of saturation with respect to water. Figure 5.1 shows the saturation vapor pressure for the temperature range [-85 °C, 50 °C], normally encountered in the region of interest for ray-tracing studies, as well as the difference between the saturation vapor pressures over water and over ice, both computed using the Wexler formulae [Wexler, 1976; Wexler, 1977].

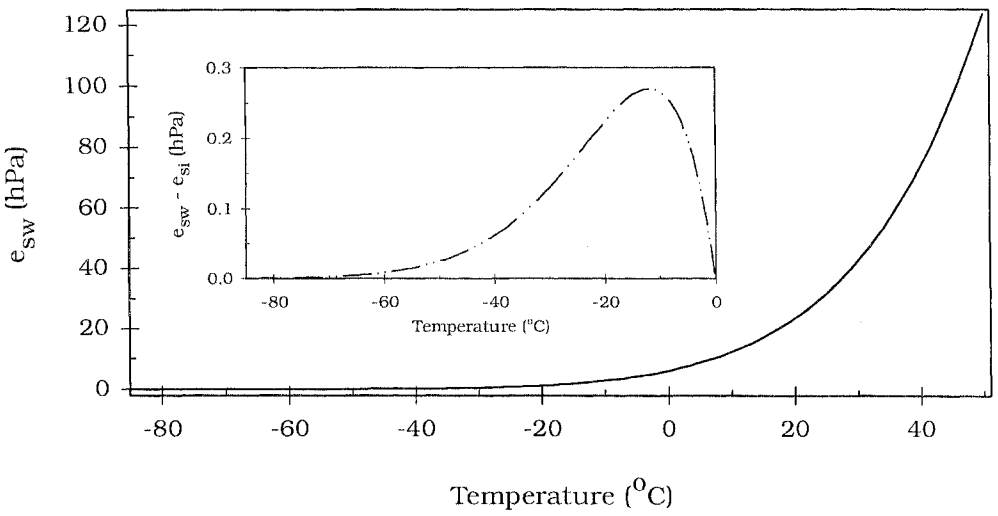

Figure 5.1 – Saturation vapor pressure over water (e_{sw}) with extrapolation for temperatures below 0 °C, and the difference between the saturation vapor pressures over water (extrapolated) and over ice (e_{si}). The computation of e_{sw} and e_{si} were performed using the Wexler [1976] and Wexler [1977] formulae, respectively.

Figure 5.2 shows the percent deviation of the Goff and Gratch, Tetens, and Berry formulae with respect to the Wexler over water formula, for the same temperature range, where the percent deviation is defined as:

$$\text{Percent Deviation (\%)} = \frac{\text{Formula} - \text{Wexler}}{\text{Wexler}} \times 100. \tag{5.7}$$

Even though the percent deviation is smaller for high temperatures, it will affect more significantly the determination of the atmosphere propagation delay, as will be shown. The Goff and Gratch formula produce estimates of the saturation vapor pressure that are systematically lower than Wexler's, particularly for low temperatures. The Berry formula overestimates e_{sw} for temperatures above about -30 °C, and underestimates it below than limit. The Tetens formula also performs poorly at low temperatures, but the differences for temperatures greater than 0 °C are small.

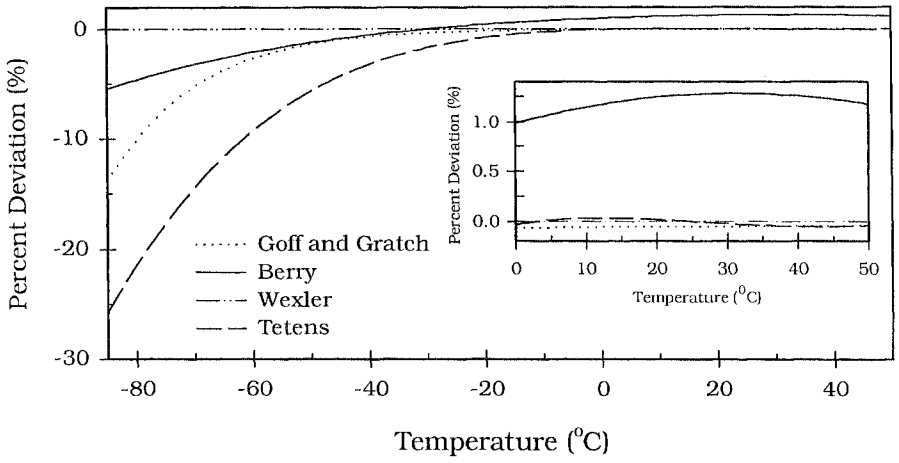

Figure 5.2 – Percent deviation for the Tetens, Berry and Goff and Gratch formulae as compared against the Wexler formula. All the formulae were extrapolated for temperatures below 0 °C. The error curves for temperatures above 0 °C are highlighted in the embedded plot.

The effect of the choice of the different formulae in ray tracing is analyzed in Table 5.1, for the USSA66. From this table, it is concluded that, at the zenith, the Goff and Gratch

and the Tetens formula produce very small (less than ~0.3 mm) differences in the traces, as compared against Wexler. On the other hand, the Berry formula leads to errors that can reach a few millimetres, at the zenith, notably for low latitude stations, as stressed in Figure 5.3. It is therefore recommended that the Wexler formula be used whenever the computation of the saturation vapor pressure is needed.

Table 5.1 – Zenith non-hydrostatic delay for USSA66, using different formulae in the computation of the saturation vapor pressure. (Note: Be = Berry; Gg = Goff and Gratch; Te = Tetens; We = Wexler).

USSA66	We	Te	Gg	Be	Te-We	Gg-We	Be-We
(°N/Month)	d^z_{nh} (m)	d^z_{nh} (m)	d^z_{nh} (m)	d^z_{nh} (m)	(m)	(m)	(m)
15 Annual	0.2443	0.2446	0.2442	0.2473	0.0003	-0.0001	0.0030
30 January	0.1323	0.1324	0.1322	0.1338	0.0001	-0.0001	0.0015
30 July	0.2577	0.2579	0.2576	0.2608	0.0002	-0.0001	0.0031
45 January	0.0573	0.0570	0.0572	0.0577	-0.0003	-0.0001	0.0004
45 July	0.1821	0.1823	0.1819	0.1842	0.0002	-0.0002	0.0021
60 January	0.0315	0.0312	0.0314	0.0317	-0.0003	-0.0001	0.0002
60 July	0.1347	0.1348	0.1346	0.1362	0.0001	-0.0001	0.0015
75 January	0.0151	0.0149	0.0150	0.0151	-0.0002	-0.0001	0.0000
75 July	0.0982	0.0981	0.0981	0.0991	-0.0001	-0.0001	0.0009

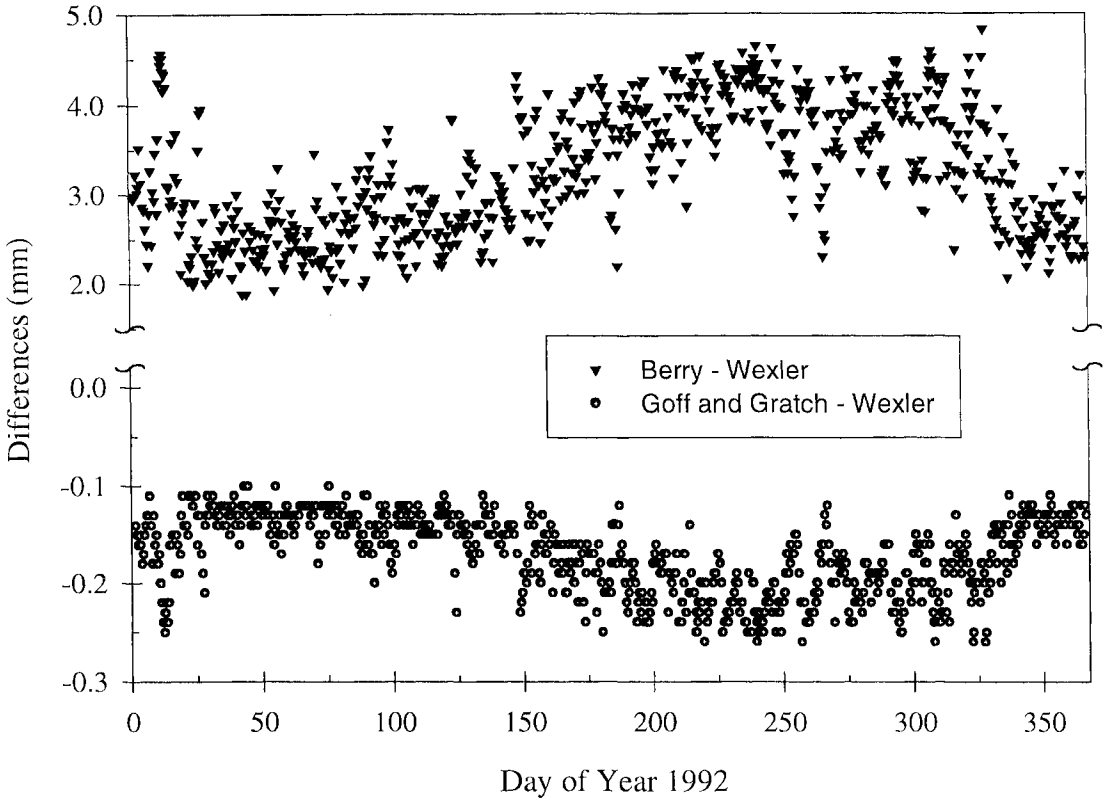

Figure 5.3 – Differences in the zenith non-hydrostatic delay due to the use of different formulae to compute the saturation vapor pressure (the Wexler formula was used as the reference). The Berry formula overestimates the zenith non-hydrostatic delay by a few millimetres, whereas the Goff and Gratch formula underestimates it at the sub-millimetre level. For this case study, radiosonde data from a station with consistently high temperature and humidity was used (Guam).

5.1.3. Refractivity constants

Some sets of refractivity constants listed in Table 3.1 and the Essen and Froome constants (as given in IAG [1963] and subsequently converted to the units used in Table 3.1) were tested. At the zenith the trace values differ for the hydrostatic component only at the sub-millimetre level. The Boudouris set of constants give the lowest values, and

Essen and Froome the highest (see Table 5.2). As the precision of the coefficients determined by Thayer [1974] is better than the others, they will be used in our ray-tracing computations.

Table 5.2 – Ray-traced zenith hydrostatic delay for USSA66, using different sets of refractivity constants. (Note: TH = Thayer; EF = Essen and Froome; SW = Smith and Weintraub; BD = Boudouris).

USSA66	Zenith hydrostatic delay (m)				Differences (m)		
(°N/Month)	TH	EF	SW	BD	EF-TH	SW-TH	BD-TH
15 Annual	2.3126	2.3132	2.3129	2.3123	0.0006	0.0003	-0.0003
30 January	2.3278	2.3284	2.3281	2.3275	0.0006	0.0003	-0.0003
30 July	2.3110	2.3115	2.3113	2.3107	0.0005	0.0003	-0.0003
45 January	2.3177	2.3183	2.3180	2.3174	0.0006	0.0003	-0.0003
45 July	2.3078	2.3084	2.3081	2.3075	0.0006	0.0003	-0.0003
60 January	2.3043	2.3049	2.3046	2.3040	0.0006	0.0003	-0.0003
60 July	2.2967	2.2973	2.2970	2.2964	0.0006	0.0003	-0.0003
75 January	2.3019	2.3025	2.3022	2.3016	0.0006	0.0003	-0.0003
75 July	2.3001	2.3007	2.3004	2.2998	0.0006	0.0003	-0.0003

5.1.4. Compressibility factors

At the zenith, the error induced by not taking into account the non-ideal gas behavior of dry air and water vapor is about 0.1-0.2 mm. This effect is visible only for the non-hydrostatic delay, and is modeled in our ray-tracing computations.

5.1.5. Enhancement factor

The saturation vapor pressure computation was performed by considering the water vapor as pure, a situation for which the formulae analyzed apply. Rigorously, as we deal

with moist air rather than pure water vapor, computations have to be corrected using the enhancement factor (cf. Chapter 2). As shown in Table 5.3, not taking into account the enhancement factor in the computation of the saturation vapor pressure, induces an error in the computation of the zenith non-hydrostatic delay that amounts to more than 1 mm, for locations with high-humidity. The enhancement factor used in our ray-tracing computations is given in Buck [1981].

Table 5.3 – Effect of the enhancement factor on the zenith non-hydrostatic delay, for USSA66. (Note: pw = pure water; ma = moist air).

USSA66	Non-hydrostatic delay (m)		
(°N/Month)	pw	ma	ma-pw
15 Annual	0.2443	0.2455	0.0012
30 January	0.1323	0.1330	0.0007
30 July	0.2577	0.2590	0.0013
45 January	0.0573	0.0574	0.0001
45 July	0.1821	0.1830	0.0009
60 January	0.0315	0.0316	0.0001
60 July	0.1347	0.1355	0.0008
75 January	0.0151	0.0152	0.0001
75 July	0.0982	0.0987	0.0005

5.1.6. Initial integration step

Under normal conditions, the refractivity decreases by about 40 N-units per kilometre in the lower atmosphere. In order to meet the ray-tracing assumptions, the refractivity can not change significantly within a signal carrier wavelength, a condition that is satisfied if

$$\frac{\Delta n_l}{N} < 0.002 f_c \,, \tag{5.8}$$

where Δn_l is the gradient of the refractive index per kilometre, and f_c is the carrier frequency, in kHz [Bean and Dutton, 1966]. Therefore, for radio frequencies this postulate is accomplished easily, but the choice of the initial step size should be nevertheless adequately small to prevent abnormal variations of the refractivity, to approximate the series of layers to a smooth continuous atmosphere, and to assure that the fractional changes between neighboring rays are kept small compared to a wavelength, a basic requirement for the application of Fermat's principle.

The differences found by changing the initial integration step from 5 m up to 100 m were at the sub-millimetre level, with the largest effect for the high latitude atmospheres. Small step sizes provide smoother atmosphere profiles, but increase considerably the computation time. Large step sizes allow faster computations, but may lead to violations to the ray-tracing assumptions. In our ray-tracing computations, an initial step size of 5 m was used.

5.1.7. Integration limits

As already mentioned, radiosonde profiles do not provide observations for all of the neutral atmosphere and have therefore to be completed using an extrapolation scheme. The effect of changes to the upper limit in the ray-tracing computations is presented in Table 5.4. From this table, it is concluded that the stratosphere contribution to the hydrostatic delay is significant (and the reason why the term "tropospheric" delay is

misleading). This test shows how important is the extrapolation of the meteorological parameter profiles in the generation of the traces to be used as benchmarks, as the radiosonde profiles can terminate at low levels (below 20 km). The simplest approach for extrapolating to upper levels is through the use of profiles of a standard atmosphere; a more sophisticated and laborious approach is to use monthly mean values specific to each radiosonde location, based on historical data, for example (the error introduced by replacing the temperature profile of the USSA atmospheres by the U.S. Standard Atmosphere - 1962 for heights above the 25-km limit is negligible (0.1-0.3 mm), therefore no significant error is expected from this procedure). The contribution of the atmosphere above 75 km can be ignored, even though we kept the 100 km boundary as the upper limit in our ray-trace computations.

Table 5.4 – Effect of changing the upper boundary in the ray-tracing computations of the zenith hydrostatic delay, for USSA66.

USSA66	Zenith hydrostatic delay (m)						
(°N/Month)	100 km	75 km	50 km	25 km	20 km	15 km	10 km
15 Annual	2.3126	2.3125	2.3108	2.2537	2.1847	2.0117	1.6597
30 January	2.3278	2.3278	2.3261	2.2712	2.2031	2.0417	1.6984
30 July	2.3110	2.3109	2.3090	2.2514	2.1776	2.0079	1.6553
45 January	2.3177	2.3177	2.3163	2.2631	2.1959	2.0504	1.7323
45 July	2.3078	2.3077	2.3057	2.2445	2.1725	2.0115	1.6677
60 January	2.3043	2.3043	2.3030	2.2528	2.1889	2.0475	1.7421
60 July	2.2967	2.2966	2.2945	2.2339	2.1633	2.0108	1.6876
75 January	2.3019	2.3019	2.3006	2.2552	2.1973	2.0645	1.7716
75 July	2.3001	2.3000	2.2981	2.2354	2.1644	2.0165	1.7027

Table 5.5 – Effect of changing the upper boundary in the ray-tracing computations of the zenith non-hydrostatic delay, for USSA66.

USSA66	Zenith non-hydrostatic delay (m)						
(°N/Month)	15 km	10 km	8 km	6 km	4 km	2 km	1 km
15 Annual	0.2443	0.2434	0.2415	0.2347	0.2160	0.1633	0.0953
30 January	0.1323	0.1318	0.1307	0.1275	0.1178	0.0857	0.0512
30 July	0.2577	0.2567	0.2537	0.2442	0.2185	0.1542	0.0967
45 January	0.0571	0.0568	0.0563	0.0546	0.0489	0.0332	0.0193
45 July	0.1819	0.1811	0.1793	0.1741	0.1587	0.1138	0.0684
60 January	0.0313	0.0310	0.0309	0.0291	0.0250	0.0156	0.0083
60 July	0.1343	0.1336	0.1326	0.1285	0.1144	0.0782	0.0462
75 January	0.0150	0.0148	0.0147	0.0143	0.0128	0.0089	0.0044
75 July	0.0975	0.0964	0.0958	0.0932	0.0838	0.0555	0.0320

As the water vapor content of the atmosphere is mainly concentrated in the first few kilometres above sea level, it is not surprising to see that the contribution of the layers above 8 km is already less than 2% of the non-hydrostatic delay, being negligible beyond a level of about 15 km (see Table 5.5).

5.1.8. Radiosonde data precision and accuracy

In order to evaluate the precision limitation of the radiosonde instrumentation in the ray-tracing accuracy, a second set of profiles based on the USSA66 atmospheres was generated by adding white noise (uncorrelated between levels). In the generation of this simulated data, we used the standard deviations correspondent to the accuracy limits established by the WMO for radiosonde instrumentation: 1 hPa for pressure, 0.5 °C for

temperature, and 5% for relative humidity [WMO, 1996a], even though such levels of noise are likely not to appear in modern radiosonde instrumentation. It is concluded that the influence of radiosonde random errors in the generation of the zenith traces can be of a few millimetres, at most (see Table 5.6). Due to the higher noise attributed to the relative humidity sensors, the accuracy of the ray tracing due to radiosonde errors is much poorer for the non-hydrostatic component.

Table 5.6 – Simulation of the effect of the limitations in precision of the radiosonde instrumentation, for USSA66. (Note: O = Original data; S = Simulated data).

USSA66	Hydrostatic delay (m)			Non-hydrostatic delay (m)		
(°N/Month)	O	S	S-O	O	S	S-O
15 Annual	2.3126	2.3100	-0.0026	0.2443	0.2480	0.0037
30 January	2.3278	2.3284	-0.0006	0.1323	0.1255	-0.0068
30 July	2.3110	2.3100	0.0010	0.2577	0.2415	-0.0162
45 January	2.3177	2.3195	0.0018	0.0573	0.0587	0.0014
45 July	2.3078	2.3088	0.0010	0.1821	0.1831	0.0010
60 January	2.3043	2.3031	-0.0012	0.0315	0.0302	-0.0013
60 July	2.2967	2.2969	0.0002	0.1347	0.1345	-0.0002
75 January	2.3019	2.3037	0.0018	0.0151	0.0144	-0.0007
75 July	2.3001	2.2989	-0.0012	0.0982	0.0975	-0.0007

The same simulation was performed with 9 randomly-chosen radiosonde soundings from Guam, as shown in Table 5.7. The differences obtained were higher than in the case of the USSA66 traces, which can be explained by the larger number of levels at which the

meteorological data is reported compared to the number of levels tabulated for the USSA66, especially in the lower atmosphere.

Table 5.7 – Simulation of the effect of the limitations in precision of the radiosonde instrumentation, for some radiosonde observations collected over Guam. (Note: O - original data; S - Simulated data)

RAOB	Hydrostatic delay (m)			Non-hydrostatic delay (m)		
	O	S	S-O	O	S	S-O
920101	2.2853	2.2827	-0.0026	0.2421	0.2388	-0.0033
920111	2.2758	2.2734	-0.0024	0.3577	0.3593	0.0016
920208	2.2881	2.2914	0.0033	0.2178	0.2186	0.0008
920412	2.2860	2.2905	0.0045	0.2250	0.2303	0.0053
920602	2.2826	2.2842	0.0016	0.2737	0.2692	-0.0045
920727	2.2815	2.2814	-0.0001	0.3669	0.3690	0.0021
920918	2.2861	2.2901	0.0040	0.3141	0.3117	-0.0024
921024	2.2804	2.2814	0.0010	0.3378	0.3386	0.0008
921225	2.2892	2.2889	-0.0003	0.2195	0.2174	-0.0021

If we assume a constant bias (equal to the upper boundary of the WMO accuracy limits) throughout the radiosonde ascent path for those sensors (as a measure of accuracy), and for the USSA66 profiles, the zenith hydrostatic delay will be biased by about 2.3 mm (as it is essentially dependent on the surface pressure). The biases for the zenith non-hydrostatic component are larger, ranging from ~2 mm to almost 3 cm, as documented in Table 5.8. Nevertheless, one should note that the accuracy of many of the current radiosonde instruments is also better than the imposed WMO limits. Special care should be given to the calibration of sensors prior to launch.

Table 5.8 – Simulation of the effect of the limitations in accuracy of the radiosonde instrumentation, for USSA66. (Note: O = Original data; S = Simulated data).

USSA66	Hydrostatic delay (m)			Non-hydrostatic delay (m)		
(°N/Month)	O	S	S-O	O	S	S-O
15 Annual	2.3126	2.3149	0.0023	0.2443	0.2731	0.0288
30 January	2.3278	2.3301	0.0023	0.1323	0.1490	0.0167
30 July	2.3110	2.3133	0.0023	0.2577	0.2874	0.0297
45 January	2.3177	2.3200	0.0023	0.0573	0.0641	0.0068
45 July	2.3078	2.3101	0.0023	0.1821	0.2050	0.0229
60 January	2.3043	2.3066	0.0023	0.0315	0.0352	0.0037
60 July	2.2967	2.2990	0.0023	0.1347	0.1495	0.0148
75 January	2.3019	2.3042	0.0023	0.0151	0.0170	0.0019
75 July	2.3001	2.3024	0.0023	0.0982	0.1092	0.0110

5.2. Ray tracing limitations

The dry gases and the water vapor in the atmosphere are responsible for the bulk of the total atmospheric propagation delay, but minor contributions to this delay follow from the presence of other forms of water substance (hydrometeors, such as rain, suspended water droplets, clouds, snow, and ice) and aerosols (such as smog and fine soil particles) in the atmosphere. The propagation delay due to aerosols can be considered negligible and will not be considered in this dissertation (for details, see Solheim [1993]).

The information given by radiosondes do not allow the effects of these minor constituents to be rigorously incorporated in ray tracing, but the quantification of their contributions to the delay can be simulated for different scenarios.

5.2.1. Propagation delay due to non-gaseous atmosphere constituents

As in the case of dry gases and water vapor in the atmosphere, the zenith delay due to any i^{th} atmospheric constituent can be evaluated if the real part of its refractive index (or refractivity) is known:

$$d^{z}_{na_i} = 10^{-6} \int_{r_s}^{r_a} N \, dz \,. \tag{5.9}$$

The refractivity model for all kinds of water substances and ice crystals in the atmosphere are derived from the following basic model [Liebe et al., 1989]:

$$N_i = 10^6 \, W_i \frac{3}{2\rho_i} \left[\frac{\epsilon_i - 1}{\epsilon_i + 2} \right] \tag{5.10}$$

where, for each constituent i, W is the mass content per unit volume (kg m^{-3}), ρ is the density (kg m^{-3}), and ϵ is the relative permittivity.

- Propagation delay due to rain

Flock et al. [1982] present graphically values of refractivity for rain, N_{rain}, which are function of the rain rate, signal frequency, and temperature. For extraordinary situations of heavy rain (150 mm/h), and for a frequency of 1.5 GHz, the delay obtained is about 8 mm per each kilometre, which may be significant for rainstorm conditions. According to Ishimaru [1985], the typical values of precipitation rate vary between 0.25 mm/h, for drizzle, and 100 mm/h, for extremely heavy rain; in general, the vertical thickness of rain is of about 3-4 km.

If we follow Liebe et al. [1989], the refractivity for rain can be computed from Equation (5.10); as $\rho_{H_2O} \approx 10^3$ kg m^{-3} [Lide, 1997], we obtain:

$$N_{rain} = 10^3 \, W_{rain} \frac{3}{2}\left[\frac{\epsilon_o - 1}{\epsilon_o + 2}\right], \tag{5.11}$$

where W is the rain mass content per unit volume (kg m^{-3}) and ϵ_o is the relative permitivitty of water, which can be computed using the following expression [Liebe et al., 1989]:

$$\epsilon_o = 77.66 + 103.3\left(\frac{300}{T} - 1\right). \tag{5.12}$$

- Propagation delay due to suspended water droplets

Suspended water droplets (SWDs) consist of water droplets whose size have radii small enough to be kept suspended by turbulence ($\leq 50\mu m$), and are present in the atmosphere in the form of clouds, fog, and haze. Taking into consideration that $\rho_{SWD} \approx 10^3$ kg m^{-3}, Equation (5.10) can be approximated by

$$\boxed{N_i \approx 10^3 \, 1.5 W_{SWD}}, \tag{5.13}$$

which is in agreement with Flock et al. [1982].

According to this simplification, a cloud with a thickness of 1 km and $W_{SWD} = 10^{-3}$ kg m^{-3} (nonprecipitating clouds show generally a mass content of $10^{-4} - 10^{-3}$ kg m^{-3} [Liebe et al., 1989], but peak values of 5×10^{-3} kg m^{-3} or greater are possible for

cumulus clouds when associated with thunderstorms [Ishimaru, 1985]) contributes about 1.5 mm of zenith delay. The effect can therefore be significant as the thickness of cumulus clouds is typically 2-8 km [Ishimaru, 1985]. For fog conditions, the mass content can vary between 10^{-6} kg m^{-3} and 10^{-3} kg m^{-3}. Assuming the highest value for mass content and a fog layer 500 m thick, which corresponds to a thick fog [Ahrens, 1994], the contribution to the propagation delay is less than 1 mm.

- Propagation delay due to ice crystals

Taking for the density of suspended ice crystals (SICs) – snow, ice fog, and glaciated clouds – the value $\rho_{SIC} = 0.916 \times 10^3$ kg m^{-3} [Liebe et al., 1989], we can approximate Equation (5.10) with

$$\boxed{N_i \approx 10^3\, 1.6 W_{SIC}}. \tag{5.14}$$

The propagation effects induced by suspended ice crystals are insignificant, as they have a very small associated mass content (less than ~10^{-6} kg m^{-3}) and occur at high altitudes [Liebe et al., 1989].

Even though the formulae presented here are easy to apply, the determination of the mass content of the components along the signal path is naturally troublesome. As the presence of significant values of SWDs is generally associated with saturated air masses, it is nevertheless possible to simulate its effect by analyzing the radiosonde relative humidity profiles (see, e.g., Schroeder and Westwater [1991]).

5.2.2. Horizontal gradients

The assumption we have made so far on the spherical symmetry of the atmosphere is only approximately valid and the deliberate disregard of horizontal gradients is most likely the largest error source in ray tracing, especially for low elevation angles. Saastamoinen [1973] estimated a maximum error due to horizontal gradients of 2.0 cm at a 10° elevation angle, which is equivalent to a zenith delay error of less than 4 mm. This theoretical estimate of the gradient error was later confirmed by Gardner [1977], considered the pioneer in the development of gradient correction models, who concluded that the horizontal gradients introduce an rms error of almost 3 cm at 10° elevation angle. It is interesting to note that the size of this error is comparable to others resulting from the incorrect use of models and processing strategies in ray tracing computations, as analyzed in previous sections.

Most of the gradient correction models are still mostly based on local experiments and small datasets, and a feasible model to be applied on a global scale has not been developed yet. Judging by the recent literature in this domain, it seems that the conclusions obtained by Gardner two decades ago are still valid and apropos of current horizontal gradient studies.

Gardner [1977] derived his correction formula to compensate for the horizontal gradient effects based on radiosonde data obtained from eight different locations near Washington, D.C. The formula is for application to optical wavelengths, ignoring therefore the water vapor gradient contribution. He concluded that the errors due to the horizontal gradients

are sinusoidal functions of the azimuth of the satellite α, comprising a $\sin\alpha$ dependence, which is due to the east-west gradients induced by diurnal, seasonal and local variations of the surface temperature profile, and a $\cos\alpha$ dependence, which is due to the north-south gradients induced by the decrease of the temperature from the equator to the poles. Gardner found that the pressure gradients are dominated by the temperature gradients. Variations on the model developed by Gardner [1977] are presented by Herring [1992], Davis et al. [1992, 1993], and MacMillan [1995].

Herring [1992] presents an expression to model azimuthal asymmetry based on a "tilted" atmosphere assumption:

$$d_{na}^{az} = m_{az}(\varepsilon)[\Xi_{NS}\cos\alpha + \Xi_{EW}\sin\alpha] \tag{5.15}$$

where d_{na}^{az} represents the additional delay due to the horizontal gradients, Ξ_{NS} and Ξ_{EW} are parameters representing the delays due to the azimuthal asymmetry (north and east components of the gradient vector), and $m_{az}(\varepsilon)$ is a mapping function for a tilted atmosphere, given by the following expression:

$$m_{az}(\varepsilon) = \frac{1}{\sin\varepsilon\tan\varepsilon + 0.0032}. \tag{5.16}$$

Based on the analysis of VLBI data spanning a almost 3-year period (for stations Westford, Richmond, Mojave, Wettzell, and Onsala), Herring concluded that the atmospheric azimuthal asymmetry contribution is generally less than 10 cm, at 5° elevation angle, but can occasionally be highly significant.

MacMillan [1995] used a similar expression to model azimuthal asymmetry which allows any choice of mapping function:

$$d_{na}^{az} = m(\varepsilon)\ \cot(\varepsilon)\left[\Xi_{NS}\cos\alpha + \Xi_{EW}\ \sin\alpha\right]. \qquad (5.17)$$

MacMillan concluded that the daily average gradient effects can amount to up to 5 cm of delay at 7° elevation angle (in his study only gradients varying on a time scale of one day were considered).

A more complete model was adopted by Davis et al. [1992, 1993] to specifically model horizontal gradients in the non-hydrostatic component of the delay for the Onsala VLBI site determined by WVR. These horizontal gradients can be caused by weather front passages, for example [Elgered, 1992]. The model allows for the temporal variation of the non-hydrostatic component of the delay by including the gradient rates and a time derivative of the zenith delay. From their analyses, it was concluded that the estimated gradient and gradient-rate vectors had preferred directions, likely an indication of a predominant structure in the three-dimensional temperature and humidity fields.

Chen and Herring [1997] applied different methods to evaluate azimuthal asymmetry effects. They have used a 12-day series of experiments and concluded that there was a good agreement between the atmospheric delay gradients estimated from VLBI data and those calculated from three-dimensional weather analysis fields from the National Center for Environmental Prediction. They have found that the north-south gradients have average values of up to 20 mm of delay, for mid-latitude sites, and for an elevation angle of 10°. The east-west gradients were found to be not as significant.

Additional information concerning horizontal gradients can be found in Chao [1971b], von Roos [1971], Davis [1986], Ifadis [1986], Bender [1992], Rogers et al. [1993], and Coster et al. [1997].

5.2.3. Hydrostatic equilibrium violation

Another assumption in our ray tracing computations is hydrostatic equilibrium of the atmosphere. Saastamoinen [1973] estimated a maximum error from the violation of the assumption of hydrostatic equilibrium of 1.5 cm, at 10° elevation angle. Hauser [1989] concluded that the expected error due to deviations from hydrostatic equilibrium is less than 1 cm most of the time, for elevation angles greater than 20° (about 3 mm at the zenith) . This estimate is based on limited data for mountain sites and there is shortage of information on the size and frequency of these deviations for other situations. The values presented by Bender [1992] for three different datasets agree with this estimate, but more studies are needed in order to fully evaluate this effect.

From this discussion, we can identify three main areas that can contribute to errors in our ray-trace values: errors in radiosonde data, effect of hydrometeors, and atmospheric horizontal asymmetry. The exact quantification of these errors is however troublesome or even impossible, due to the variability of the contribution of each of these errors for each radiosonde profile. The good agreement between ray-traced radiosonde data and independent techniques (see Chapter 1 for literature review about this subject) is nevertheless a good indication that those values may be accurate to the 1-cm level or less (rms).

5.3. Product analysis

The basic quantities determined by the ray-tracing program are the components of the atmospheric propagation delay (hydrostatic and non-hydrostatic), at selected elevation angles, which will constitute the benchmark values for model assessment. The hydrostatic component includes the geometric delay (bending). As by-products, the computation of the precipitable water vapor, and the mean temperature (as defined by Equation 5.18) is also performed.

As already mentioned, a total of 50 radiosonde stations were selected for ray tracing purposes. The ray tracing was performed using the settings summarized in Table 5.9, at seven elevation angles: 90°, 30°, 20°, 15°, 10°, 6°, and 3°. For each elevation angle, 32,467 traces were generated (nominally two per day per station for the whole of 1992).

The ray-traced radiosonde data provided a full range of neutral atmosphere delays, which express the meteorological conditions usually encountered all over the world. The histograms of the zenith hydrostatic and non-hydrostatic delays corresponding to the traces are presented in Figure 5.4. As the hydrostatic component is essentially a function of the surface pressure (which in turn is a function of the station height), the histogram clearly shows the uneven distribution with respect to the heights of the radiosonde stations.

Other ray-tracing products (mean temperature, precipitable water, geometric delay) are also of interest and will be analyzed in detail in the following sections.

Table 5.9 – Settings for ray tracing computation.

Refractivity constants	Thayer [1974]
Compressibility factors	Owens [1967]
Saturation vapor pressure	Wexler [1976]
Enhancement factor	Buck [1981]
Gravity	corrected for φ and H
Integration limits	[station height, 100 km]
Initial step size	5 m
Constants	
M_d	28.96415 Kg $Kmol^{-1}$
M_w	18.01528 Kg $Kmol^{-1}$
R	8.314510 J K^{-1} $Kmol^{-1}$

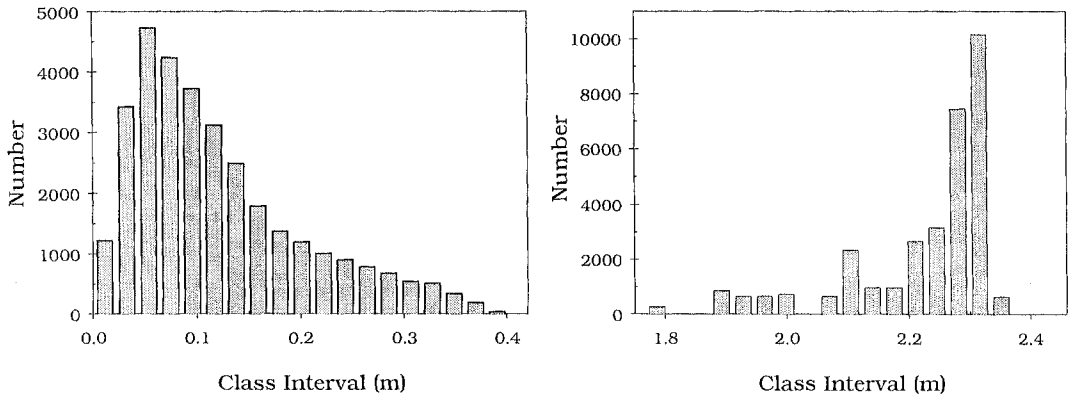

Figure 5.4 – Histograms of the traces of the zenith non-hydrostatic (left) and hydrostatic (right) delays.

5.3.1. Precipitable water

One of the most interesting and innovative applications of space geodetic techniques (namely GPS and VLBI) developed in recent years is the estimation of the precipitable water vapor of the atmosphere. As a by-product of the estimation process of geodetic parameters, the zenith non-hydrostatic delay is included as a nuisance parameter and can subsequently be related to the precipitable water, according to the process described hereafter.

In Chapter 3, we established that the neutral atmosphere delay is given by:

$$d_{na} = d_h^z m_h(\varepsilon) + d_{nh}^z m_{nh}(\varepsilon).$$

The zenith hydrostatic delay can be predicted with good accuracy provided good surface pressure measurements are available. For example, considering the Saastamoinen [1973] prediction model:

$$d_h^z = \frac{0.002277\, P_s}{1 - 0.0026\cos(2\varphi) - 0.000\,000\,28H},$$

the partial derivative with respect to the surface pressure gives:

$$\frac{\partial d_h^z}{\partial P_s}(\text{m hPa}^{-1}) = \frac{0.002277}{1 - 0.0026\cos(2\varphi) - 0.000\,000\,28H}.$$

As an example, for $\varphi = 45°$, $H = 100$ m, and $P_s = 1013.25$ hPa, we obtain:

$$\partial d_h^z(\text{m}) \approx 0.0023\, \partial P_s.$$

If the measurements of surface pressure are kept below 0.5 hPa, we can expect an accuracy in zenith hydrostatic delay of about 1 mm, assuming: (1) no error in the model; (2) no errors in latitude determination; (3) no errors in height determination.

If we also assume no errors in the mapping functions (see the next chapter), the only variable remaining is the zenith non-hydrostatic delay, which is very difficult to predict. For high-precision applications of space techniques this quantity is therefore typically estimated as a nuisance parameter in the adjustment process. Finally we need to establish a relation between this estimated parameter and the precipitable water.

In Chapter 3 we concluded that

$$d_{nh}^{z} = 10^{-6} \int_{r_s}^{r_a} \left[K_2' \left(\frac{e}{T} \right) + K_3 \left(\frac{e}{T^2} \right) \right] Z_w^{-1} \, dz \, .$$

This expression can be further modified by introducing the weighted mean temperature of the (wet part of the) atmosphere, defined as

$$T_m = \frac{\int_{r_s}^{r_a} \frac{e}{T} Z_w^{-1} \, dz}{\int_{r_s}^{r_a} \frac{e}{T^2} Z_w^{-1} \, dz} , \tag{5.18}$$

in which case we get

$$d_{nh}^{z} = 10^{-6} \left[K_2' + \frac{K_3}{T_m} \right] \int_{r_s}^{r_a} \left(\frac{e}{T} \right) Z_w^{-1} \, dz \, . \tag{5.19}$$

Using the equation of state – see Equation (2.12) – we have

$$\left(\frac{e}{T}\right)Z_w^{-1} = R_w \rho_w$$

and Equation (5.19) can therefore be written as

$$d_{nh}^z = 10^{-6} R_w \left[K_2' + \frac{K_3}{T_m} \right] \int_{r_s}^{r_a} \rho_w \, dz \,. \tag{5.20}$$

The integral in Equation (5.20) is the integrated water vapor (IWV) – the total mass of water vapor in a column of air with cross section of 1 m^2 extending from the surface to the top of the atmosphere – and is usually given in units of kg m^{-2}:

$$IWV = \int_{r_s}^{r_a} \rho_w \, dz \,. \tag{5.21}$$

This quantity can be easily converted to length units by dividing by the density of water ($\rho_{H_2O} \approx 10^3 \, kg \, m^{-3}$), in which case it can be interpreted as the height of an equivalent column of liquid water that would result if the water vapor were condensed, denominated as integrated precipitable water vapor (PW) or simply precipitable water (see Dutton [1986]; Peixoto and Oort [1987]):

$$PW = \frac{1}{\rho_{H_2O}} \int_{r_s}^{r_a} \rho_w \, dz \,. \tag{5.22}$$

From these results it is clear that 1 kg m^{-2} IWV is equivalent to 1 mm PW.

Substituting Equation (5.21) into Equation (5.20), we obtain:

$$d_{nh}^z = \xi \, IWV \,, \tag{5.23}$$

where ξ is a "constant" of proportionality given by:

$$\xi = 10^{-6} R_w \left[K_2' + \frac{K_3}{T_m} \right]. \tag{5.24}$$

The mean temperature is the only unknown in this equation. Being a function of the water vapor pressure and temperature profiles, this parameter is therefore variable with location and time. In order to provide accurate measurements of precipitable water from estimates of zenith non-hydrostatic delay, the determination of T_m is therefore essential. This quantity was calculated for each profile from our radiosonde stations, for a total of 32,467 profiles, with the basic statistics presented in Table 5.10.

Table 5.10 – Basic statistics for the mean temperature.

$\overline{T}_m$	σ_{T_m}	$T_{m_{minimum}}$	$T_{m_{maximum}}$
270 K	11 K	232 K	306 K

As already discussed in Bevis et al. [1992], the mean temperature shows a strong correlation with the surface temperature, as witnessed by our correlation plot in Figure 5.5, which shows the correlations of the annual means for the 50 stations we have ray-traced. The correlation with latitude is also very clear, but the dependence on this parameter is well modeled by the surface temperature, which shows a similar correlation. The dependence on station height is very weak.

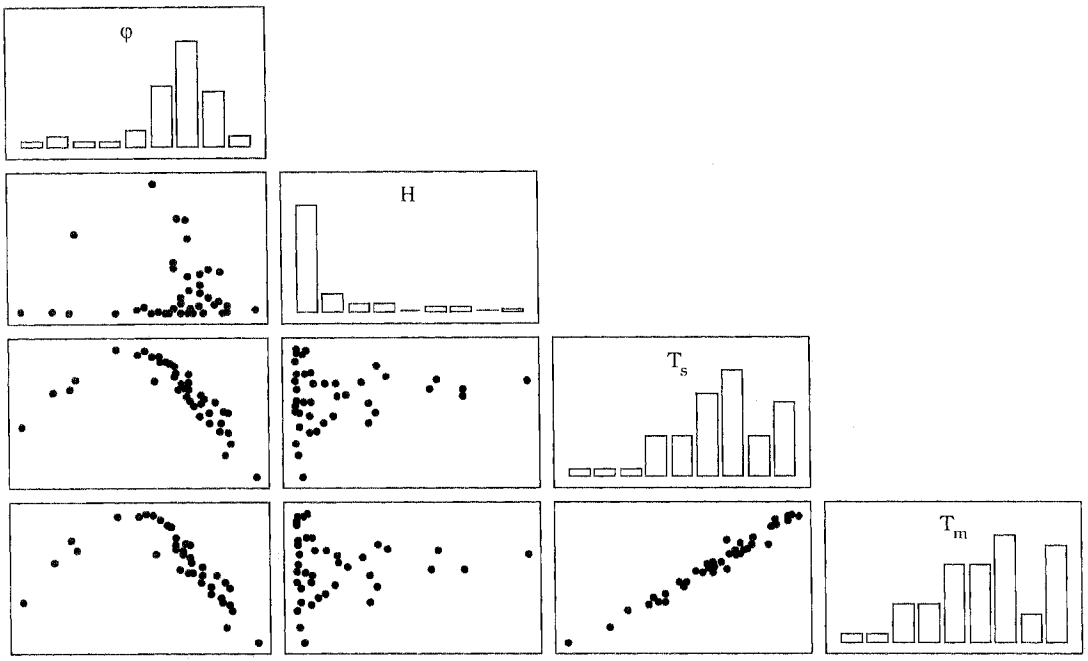

Figure 5.5 – Correlation plot for the mean temperature, for annual means of ray-traced radiosonde stations. Otherwise as in Figure 4.7.

As suggested by the correlation plot, we fitted a straight line through our data (referred to as *UNB98Tm1*), which lead to the results presented in Table 5.11 and plotted, together with the ray-traced values, in Figure 5.6.

Table 5.11 – Least-squares fit adjustment results for the UNB98Tm1 model.

Functional Model	a	b	rms of the fit
$T_m = a + bT_s$	50.4 ± 0.66 K	0.789 ± 0.0023	3.07 K

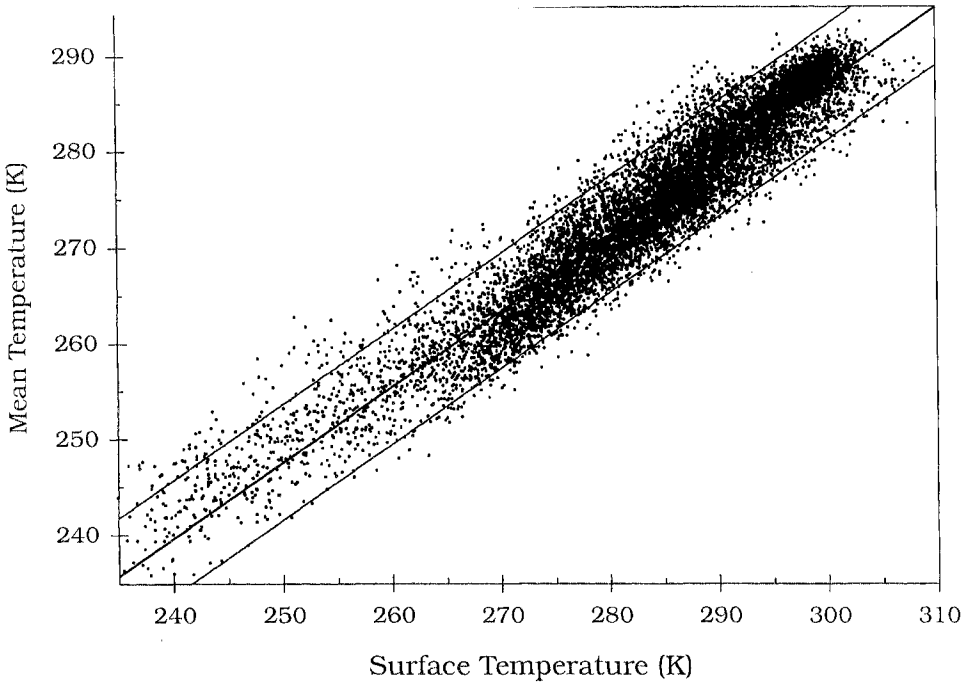

Figure 5.6 – Plot of ray-traced mean temperature versus surface temperature, along with the fitted straight line and associated 95% prediction band.

The parameters of this straight line model are slightly different from the ones obtained by Bevis et al. [1992], and there is a significant improvement concerning the quality of the fit (rms of 3.07 K versus 4.7 K obtained by Bevis et al. [1992]). The residuals for this fit are presented in Figure 5.7. Despite its simplicity, this model describes very accurately the functional relationship between the two meteorological parameters.

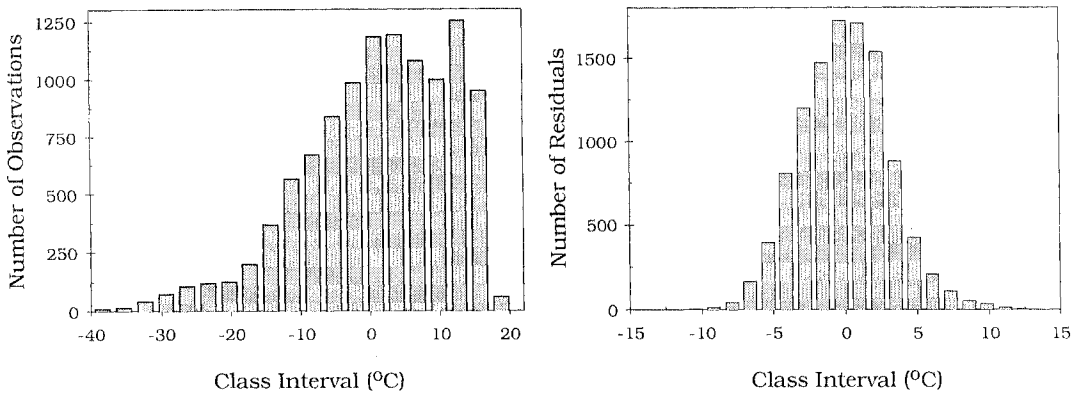

Figure 5.7 – Distribution of the mean temperature observations (left) and of the residuals of the least-squares straight line fit (right).

Another model that fits to the data better than the straight line model, particularly for high latitudes (as depicted in Figure 5.8), was also derived (and named as *UNB98Tm2*). The coefficients and associated uncertainties for the *UNB98Tm2* model are presented in Table 5.12.

Table 5.12 – Least-squares adjustment results for *UNB98Tm2*.

Functional Model	a	b	rms of the fit
$T_m = a + bT_s^3$	196.05 ± 0.23 K	$(3.402 \pm 0.0098) \times 10^{-6}$ K^{-2}	3.01 K

This particular empirical model reflects the high variability of radiosonde stations used in our study, which leads to a large temperature range. If we ignore some of the high-latitude stations, different models and constants can be derived.

Once an expression for the mean temperature is established, a model to express the relationship between the zenith non-hydrostatic delay and the precipitable water can be determined using an appropriate set of refractivity constants.

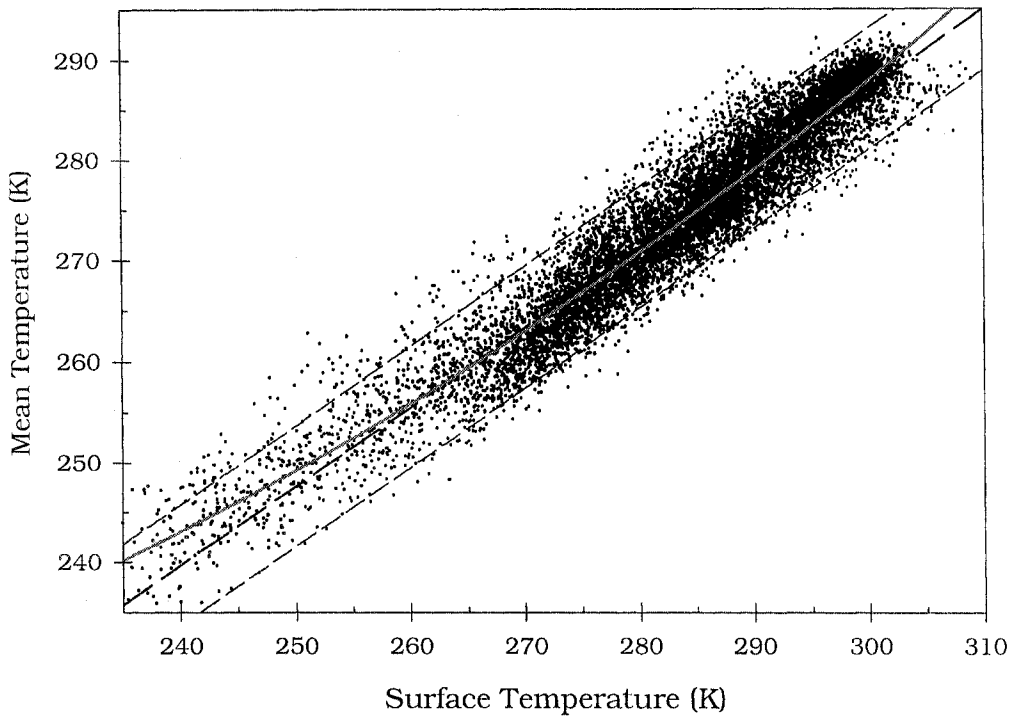

Figure 5.8 – Plot of surface temperature versus ray-traced mean temperature. The dashed lines represent the least-squares fitted line and corresponding 95% prediction band, whereas the solid line is the proposed *UNB98Tm2* model.

5.3.2. Geometric delay

As a consequence of Fermat's principle, the variability of the refractive index in the atmosphere induces an angular bending of the electromagnetic ray (ray bending), which translates into an additional delay (geometric delay), as discussed in Chapter 3. The

geometric delay is essentially a function of the elevation angle, and it is significant at elevation angles below 15°, reaching more than 50 cm at 3°.

Crane [1976] concluded that most of the ray bending occurs near the earth's surface; for each individual elevation angle studied, he also concluded that the ray bending is well correlated with the surface refractive index. Saastamoinen [1973] also presents a formula that allows the ray bending correction based on the surface pressure, temperature, and water vapor pressure.

Kouba [1979] presents a simple formula to compute the geometric delay which is a function of the elevation angle only:

$$d_g = \frac{1.92}{(\varepsilon^\circ)^2 + 0.6} \tag{5.25}$$

where d_g is the geometric delay in metres, and ε° is the elevation angle, in degrees.

Hartmann and Leitinger [1984] use a more complex complete formula, also based on the surface refractivity and the scale height of the atmosphere.

Based on the results of our ray tracing – and for a total of 4692 traces for each elevation angle – we have derived a new expression for the geometric delay (*dg.v1*) as a function of the elevation angle (see Table 5.13).

Table 5.13 – Least-squares adjustment results.

Functional Model	a	b	rms of the fit
$d_g = a \exp\left(-\frac{\varepsilon^\circ}{b}\right)$	2.256 ± 0.0092 m	2.072 ± 0.0054 °	0.033 m

As depicted in Figure 5.9, the model by Kouba clearly underestimates the geometric delay at low elevation angles, and overestimates it for high elevation, a fact already discussed by van der Wal [1995].

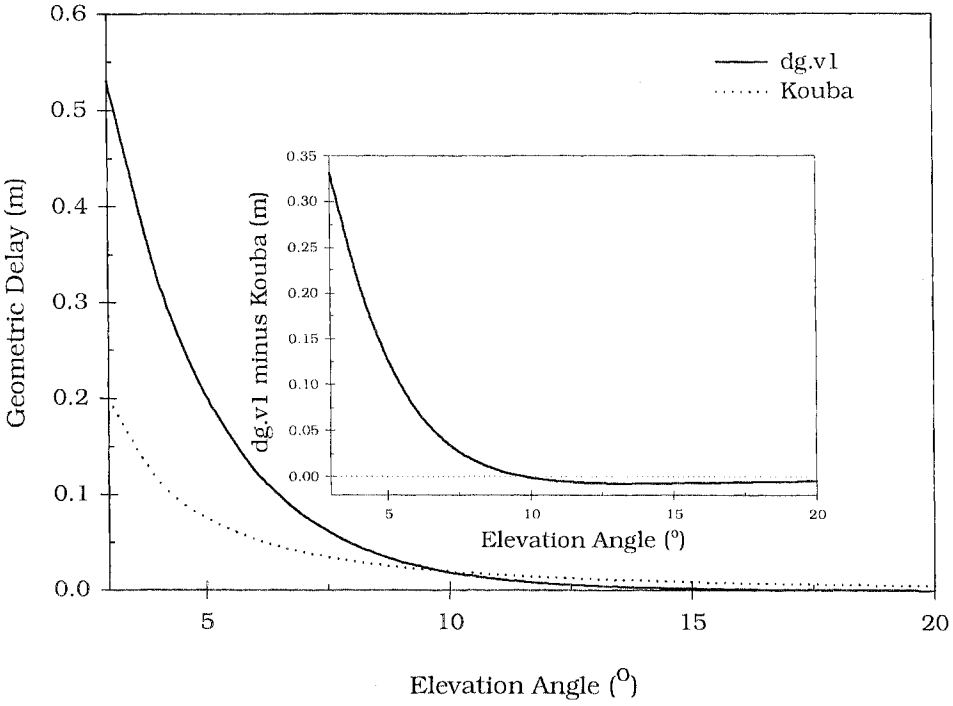

Figure 5.9 – Geometric delay prediction using dg.v1 and Kouba [1979].

A better model can be derived by including the height of the station, which largely absorbs the dependence of the geometric delay on the surface refractivity, avoiding the computation of this quantity. The empirical functional model (*dg.v2*) that we found to better describe this relationship is given by:

$$d_g = \frac{1}{a + bH + c(\varepsilon^\circ)^3}, \tag{5.26}$$

and the coefficients resulting from the least-squares adjustment are presented in Table 5.14.

Table 5.14 – Coefficients for the dg.v2 geometric delay model.

a (m^{-1})	b (m^{-2})	c $m^{-1}(°)^{-3}$	rms of the fit (m)
0.776 ± 0.0044	$(67.12 \pm 0.70) \times 10^{-5}$	0.0301 ± 0.00015	0.025

These developed models may be useful to correct mapping functions that ignore this effect (see discussion in Chapter 3).

In this chapter we have discussed in detail ray-tracing accuracy, as a measure of the quality of our ground truth. This accuracy study involved the assessment of ray-tracing models and methods of computation, and the main limitations were pointed out. Radiosonde data from 50 stations was ray-traced, resulting in 32,467 traces. Based on the ray-tracing product databases we derived models for mean temperature and geometric delay computation.

In the next chapter, the database of traces will be used as ground truth for atmospheric propagation delay model assessment.

6. MODEL ASSESSMENT

This chapter presents the results of our assessment of atmospheric propagation delay models against ray tracing. Fifty radiosonde stations covering a wide range of latitudes and climate types were ray traced and a total of 32,467 benchmark traces was generated. The assessment is performed for the zenith prediction models and mapping functions, and separately for the hydrostatic, non-hydrostatic and total delays. A series of hybrid models is also intercompared.

6.1. Methodology and nomenclature

The assessment methodology consists in evaluating the performance of the different selected models and mapping functions against the ray-traced values obtained at the 50 radiosonde stations, which total 32,467 benchmark traces. As a rule, the models were tested using the standard formulations specified by the authors. The general features of each of the tested models were described in Chapter 3, which also presents the mathematical formulation of selected zenith delay models. Additional mathematical formulations for selected mapping functions are presented in Appendix II. For the sake of simplicity, the models will be named in text after the author (or first author) of the main reference, unless an acronym is provided by the author(s). In most cases, an additional short code will be used to identify the models in graphs and figures.

When required, all models are driven by the standard meteorological parameters provided by the radiosonde observations (P, T, e), and our databases of tropopause height, inversion height, and lapse rate. As concerns the assessment of mapping functions, we based our analysis on the differences of the projected delay and not of the "ratio" they represent, as this is a more abstract entity for discussion. Therefore we used the ray-traced zenith delay values as the quantity to be mapped, and we assume those values errorless (obviously an erroneous assumption with no consequences in this analysis).

The accuracy of a model will be evaluated in terms of its bias, rms scatter, and total error. The **bias** (δ) corresponds to the difference between the predicted value given by the model and the ray-traced value (model minus trace). The **rms scatter** (σ) corresponds to the standard deviation of the differences or rms scatter about the mean value. We will use this term to be in agreement with other authors. For ranking purposes, we will define the **total error** (ζ) of a model as

$$\zeta = \sqrt{\delta^2 + \sigma^2} \quad . \tag{6.1}$$

A series of tables presenting the bias and rms scatter for each model is electronically available as an appendix to this dissertation (http://mat.fc.ul.pt/eg/lattex/PhD_e_sup.html), but in order to facilitate the discussion of the analysis, a series of graphs will be presented. A station-by-station intercomparison analysis for most of the models will be represented in series of error bar plots (as a function of the radiosonde station latitude), whereas box-and-whisker plots will be used to assess the global accuracy. The statistical quantities represented in box-and-whisker plots are: median and mean (thinner and

thicker lines inside the boxes, respectively), 25th and 75th percentiles (vertical box limits), 10th and 90th percentiles (whiskers), and 5th and 95th percentiles (open circles).

6.2. Zenith hydrostatic delay prediction models

Four different zenith hydrostatic delay models were selected for accuracy assessment (see Table 6.1).

Table 6.1 – Names and codes for the tested zenith hydrostatic delay prediction models.

Model name	Reference	Code
Baby	Baby et al. [1988]	BB_ZH
Hopfield[†]	Hopfield [1969]	HO_ZH
Rahnemoon	Rahnemoon [1988]	RA_ZH
Saastamoinen	Saastamoinen [1973]	SA_ZH

[†]The equivalent height was computed as in Hopfield [1972].

As mentioned in Chapter 3, the zenith hydrostatic delay is essentially a function of the surface (station) pressure, with theoretical expressions similar in the case of the "dry" and "hydrostatic" formalisms (except for the molar mass used):

$$d_h^z = 10^{-6} K_1 \frac{R}{M_d g_m} P_s . \tag{6.2}$$

The differences between models of this type include the gravity modeling strategy and choice of the K_1 refractivity constant. This is the case of the Saastamoinen and Baby models. The two other models were chosen because they represent clear alternative approaches.

Figure 6.1 shows a box-and-whisker plot for the differences (model minus trace) with respect to ray tracing.

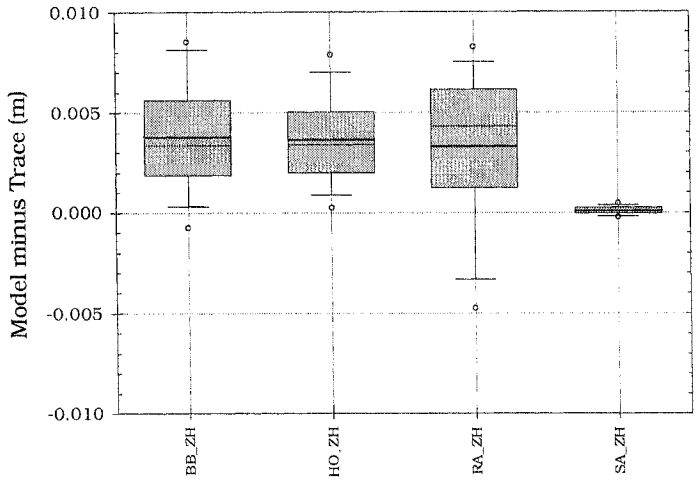

Figure 6.1 – Box-and-whisker plot for the differences between the zenith hydrostatic delay prediction models and ray tracing (model minus trace).

This global analysis shows clearly an outstanding performance of the Saastamoinen model, which has submillimetre bias and submillimetre rms. The other models show biases of 3-4 mm and rms scatter of 2-4 mm (see Table 6.2).

Table 6.2 – Accuracy assessment for the zenith hydrostatic delay prediction models, based on the total number of traces.

	Saastamoinen	Hopfield	Baby	Rahnemoon
Bias	0.1 mm	3.6 mm	3.8 mm	3.3 mm
Rms scatter	0.2 mm	2.3 mm	2.8 mm	3.9 mm
Total error	**0.2 mm**	**4.3 mm**	**4.7 mm**	**5.1 mm**

The evaluation of each model is better understood by analyzing its performance at each of the radiosonde stations (Appendix VI). A residual latitudinal effect is clear for all

models, even though it may be considered insignificant for the Saastamoinen model (note that the latitude is used as an input parameter in this model).

The visible latitude signature seen for the Hopfield model might be explained by partial contributions of an inadequate value of the equivalent dry height, unmodeled gravity variations, and variations of the molar mass of moist air (note that the Hopfield model is based on a "dry/wet" formalism). The rms scatter is nevertheless not much different from the expected, as Hopfield [1972] quotes values of 1-2 mm. Although less visible, the Hopfield model shows also an additional mismodeling of station height, a fact that is also shared by the Rahnemoon model.

The Baby model performs much like the Hopfield model in terms of mean bias, but shows a rms comparable to Saastamoinen. The results are in agreement with the ones obtained in the comparison carried out by Baby et al. [1988]. In their study, biases as high as 6.1 mm were obtained, but the data set was much smaller than the one used in this study.

Even though the Rahnemoon model is the most complex, as it requires numerical integration, its performance is exceeded by all of the other models in analysis. The mean bias is similar to Baby and Hopfield for medium and high latitudes, but shows always the largest rms scatter, which is likely an indication of unmodeled seasonal variations of the delay. This high rms scatter was also seen in the comparison study against ray tracing performed by Rahnemoon [1988].

Overall the models analyzed tend to over-predict the zenith delay, except for low latitudes. The rms scatter is generally smaller at low latitudes (where the surface pressure

variation is also very small) and increases towards the high latitudes. The Saastamoinen performance is extremely good for all the analyzed radiosonde stations and it is therefore expected that this model will provide very accurate predictions of the zenith hydrostatic atmospheric delay. The precision of the predictions is essentially a function of the precision of the surface pressure measurements, as the model is not very sensitive to errors in latitude and height, as confirmed in the sensitivity analysis shown in Table 6.3.

Table 6.3 – Expected error in the zenith hydrostatic delay (applied to the Saastamoinen model) due to random errors of the input parameters, for different scenarios.

P	φ	H	σ_P	σ_φ	σ_H	$\sigma_{d_h^z}$
1020 hPa	45°	10 m	1 hPa	1°	1 m	2.3 mm
1020 hPa	45°	10 m	1 hPa	1°	100 m	2.3 mm
1020 hPa	45°	10 m	0.5 hPa	1°	1 m	1.2 mm
1020 hPa	45°	10 m	0.5 hPa	1°	100 m	1.2 mm

6.3. Zenith non-hydrostatic delay prediction models

For this analysis we selected a total of 12 models (see Table 6.4), a selection that embodies an interesting range of approaches in zenith non-hydrostatic (and wet) delay prediction, both regarding theoretical background and parameterization.

Despite the heterogeneity of models, the global analysis of the total number of differences illustrated by the box-and-whisker plot shown in Figure 6.2 reveals an interesting feature: with exception of the Berman 74, Berman TMOD, Callahan, and Chao models, all the models show comparable rms scatter about the mean (~3 cm), with Saastamoinen,

Hopfield, Rahnemoon and Ifadis performing slightly better. As regards the bias, the best global performance is attained by the Chao, Baby 1, and Ifadis.

Table 6.4 – Names and codes for zenith non-hydrostatic delay prediction models.

Model Name	Reference	Code
Askne	Askne and Nordius [1987]	AN_ZW
Baby 1[†]	Baby et al. [1988]	BB1_ZW
Baby 2[†]	Baby et al. [1988]	BB2_ZW
Berman 70	Berman [1976]	B70_ZW
Berman 74	Berman [1976]	B74_ZW
Berman TMOD	Berman [1976]	BTM_ZW
Callahan	Callahan [1973]	CA_ZW
Chao	Chao [1973]	CH_ZW
Hopfield	Hopfield [1972]	HO_ZW
Ifadis	Ifadis [1986]	IF_ZW
Rahnemoon	Rahnemoon [1988]	RA_ZW
Saastamoinen	Saastamoinen [1973]	SA_ZW

[†]Baby 1 = "theoretical" version; Baby 2 = "semi-empirical" version.

The ranking of the functions based on their absolute mean bias and total error is represented in Figure 6.3. This figure shows clearly that the differences between the models are primarily in the mean bias; the differences concerning the total error are minimum. The differences obtained for the models are in fact highly correlated; if we use the Saastamoinen model as reference, for example, we will find correlation coefficients ranging from 0.86 (for Berman TMOD) to 0.99 (for Rahnemoon).

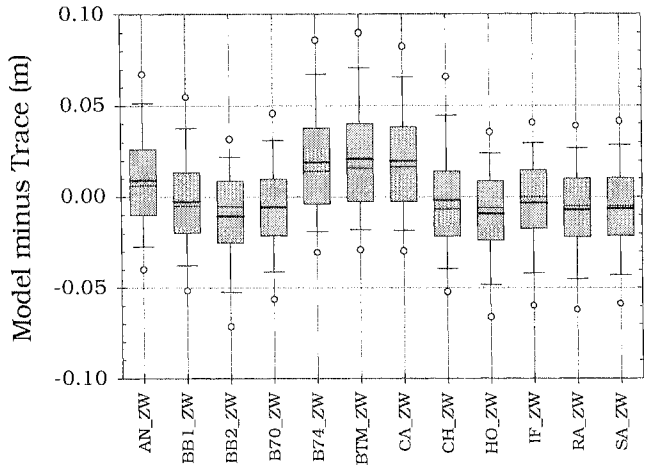

Figure 6.2 – Box-and-whisker plot for the differences between the zenith non-hydrostatic delay prediction models and ray tracing (model minus trace).

A station-by-station analysis (see Appendix VII) reflects very much this coincidence, which can be explained by the fact that all models depend strongly on the water vapor pressure, a highly variable quantity. Even the more complex models, such as Rahnemoon and Askne, achieved no better performance than simple models, such as Saastamoinen. The relatively poor performance of all models is a clear warning of the weakness of the zenith non-hydrostatic delay prediction based on surface meteorological measurements.

The equatorial and tropical regions are clearly the most problematic, likely due to high and variable water vapor content in the atmosphere. The Berman 74, Berman TMOD, Callahan and Chao perform particularly unsatisfactorily in these regions, with a clear over-prediction of the delay. The best predictions are obtained by Hopfield, Ifadis, Rahnemoon, and Saastamoinen, except for the radiosonde stations FOR (Fortaleza, Brazil) and BLB (Balboa, Panama), which are quite troublesome for most of the models.

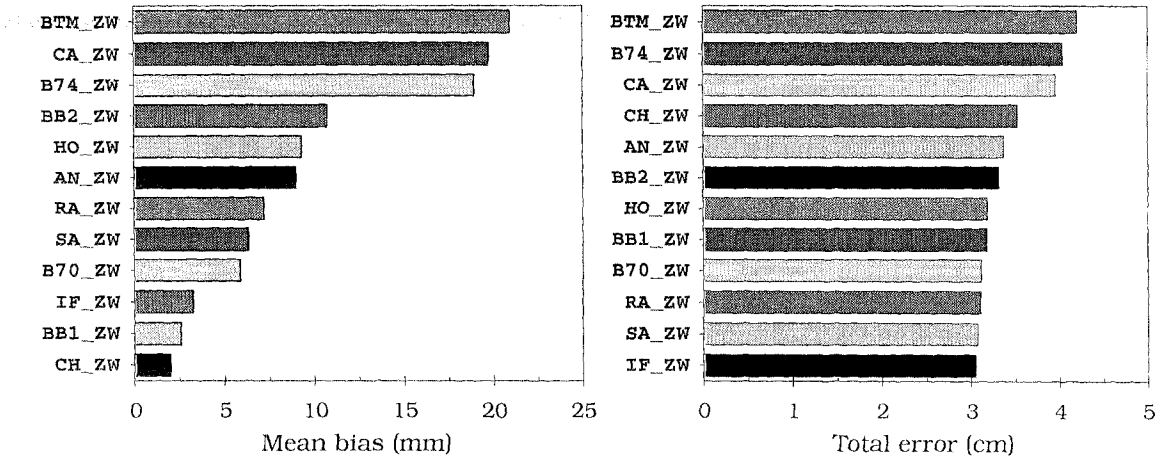

Figure 6.3 – Ranking of the zenith non-hydrostatic models by absolute mean bias (left) and total error (right).

Although the mid- and high-latitude regions show a marked seasonal variation of the zenith non-hydrostatic delay, they are characterized by a small water vapor content and practically all the models show comparable performances.

With such a wide choice of candidates exhibiting similar levels of accuracy, the most adequate choice seems to be the one that combines minimum bias and simplicity, and that depends on the minimum number of parameters, to avoid error propagation due to measurement errors. Model complexity is the main handicap for choosing Rahnemoon, whereas the lack of suitable information on temperature lapse rates may make Askne, Baby 1, Berman 70, and Chao also inconvenient. It is important to note that we have only tested global versions of the models; Askne, Baby 2, and Ifadis models can be tuned to a particular location or season. However, even admitting that the tuned versions may lead to a reduction of the mean bias, a reduction of the rms scatter is very unlikely (see also Ifadis [1986], Baby et al. [1988], and Mironov et al. [1993]).

In addition to the fact that Ifadis and Saastamoinen showed the best global accuracy, they are also characterized by simplicity. Notwithstanding the Ifadis requirement of surface pressure as an input parameter, this is no real issue as the model is not very sensitive to changes in pressure, as shown by the error propagation analysis presented in Table 6.5. In cases where the user relies totally on the use of models to predict the zenith delay, the combination of the Saastamoinen hydrostatic with its non-hydrostatic counterpart may be advantageous, yielding a more consistent zenith delay prediction.

Table 6.5 – Propagated error in the zenith non-hydrostatic delay prediction due to random errors of the input parameters, applied to Saastamoinen (SA) and Ifadis (IF).

P	T	e	σ_P	σ_T	σ_e	$\sigma_{d^z_{nh}}$ (SA)	$\sigma_{d^z_{nh}}$ (IF)
1015 hPa	288.15 K	20 hPa	1 hPa	0.5 K	1 hPa	10.0 mm	9.9 mm
1015 hPa	288.15 K	30 hPa	1 hPa	0.5 K	1 hPa	10.0 mm	9.9 mm

6.4. Zenith total delay models

In some zenith delay models, a separation between the two components of the delay is not performed and a prediction of the zenith total delay is carried out instead. Such a procedure is quite frequent in development of models designed for airborne applications ("navigation" models). We have selected some models of this type to be intercompared with four "geodetic" models (Baby, Hopfield, Rahnemoon, and Saastamoinen); in this case, the predicted zenith total delay is obtained by adding the contribution of the

hydrostatic and non-hydrostatic components. The set of models analyzed is listed in Table 6.6.

Two versions for the Altshuler model were tested: in the first version (Altshuler 1) the refractivity is computed using the surface meteorological parameters measured by the radiosonde; the second version (Altshuler 2) computes the refractivity using the formulation presented by the authors, which is based on the user's latitude and month of year.

Table 6.6 – Codes for zenith hydrostatic delay models.

Model Name	Reference	Code
Baby 2[†]	Baby et al. [1988]	BB2_ZT
Altshuler 1	Altshuler and Kalaghan [1974]	AL1_ZT
Altshuler 2	Altshuler and Kalaghan [1974]	AL2_ZT
Hopfield	Hopfield [1972]	HO_ZT
NATO	NATO [1993]	NATO_ZT
STI	Wachowski [1980]	STI_ZT
WAAS	DeCleene [1995]	WAAS_ZT
Brown	Brown [1989]	BR_ZT
Rahnemoon	Rahnemoon [1988]	RA_ZT
Saastamoinen	Saastamoinen [1973]	SA_ZT

[†]The non-hydrostatic model chosen for Baby is the semi-empirical.

The assessment of the models' accuracy for the total number of traces (see Figure 6.4) is essentially characterized by a clear separation between the two groups of models, with the navigation group performing poorly both in a relative and absolute sense.

Within this navigation group, the NATO and WAAS models perform the best, the latter showing a larger bias but a lower rms scatter. The Brown model performs the worst, which is somewhat expected as no provision to adjust the surface refractivity to the user's location was made. It is noteworthy that the distribution of the differences with respect to ray-tracing is remarkably skewed for all the navigation group of models.

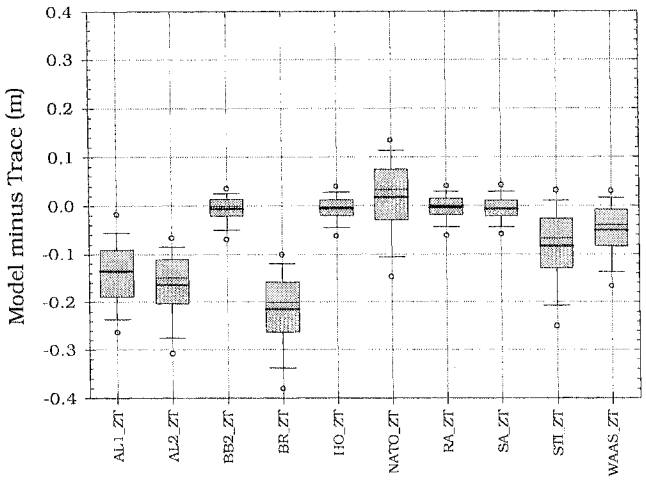

Figure 6.4 – Box-and-whisker plot for the differences between the total zenith delay prediction models and ray tracing (model minus trace).

The ranking of the models based on absolute mean bias and total error is presented in Figure 6.5. As a remark, it is interesting to note that when the individual contributions of the delay are added, the performance of Baby 2, Hopfield, and Rahnemoon is closer to Saastamoinen. This can be explained by the use of different strategies in the separation of the dry gases from the water vapor contributions in the ray-tracing computations. The mean positive offset observed for the hydrostatic component combined with the negative offset observed for the non-hydrostatic component results in an overall improvement of the three models.

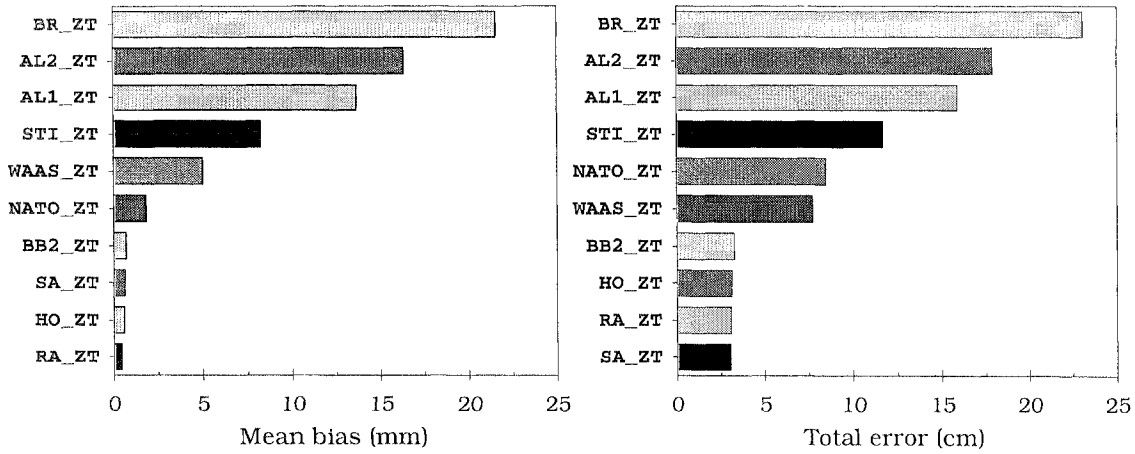

Figure 6.5 – Ranking of the zenith total delay models based on the absolute mean bias (left) and total error (right), for the total number of differences.

If we observe the distribution of the mean differences at every radiosonde station (see Appendix VIII), we conclude that the NATO model performs reasonably well at mid-latitudes but degrades towards high and low latitudes. The WAAS model does not show this latitudinal effect as much, but the model clearly under-predicts the zenith delay at almost all the stations analyzed. In addition to the clear under-prediction of the delay, the Altshuler 2 model (Altshuler 1 and Brown are not shown in these detailed graphs) shows an additional mismodeling of the station height, clearly observed as "jumps" in the graph of mean differences. The STI model is visibly biased in the equatorial and tropical regions, but shows an acceptable performance level at high latitudes, with small mean offsets.

We therefore conclude that all the navigation models have clear limitations in predicting the zenith delay, with serious implications in precise positioning. However the prediction

of the zenith delay for airborne applications is a rather complex problem, as meteorological data to be used with the geodetic models is rarely available. This difficulty can be somehow mollified by assuming average profiles, an approach that has been investigated recently (see, e.g., Collins and Langley [1996]; Collins et al. [1996]).

6.5. Hydrostatic mapping functions

As in the case of the atmospheric zenith delay models, some mapping functions do not map separately the two components of the atmospheric delay. Usually we are interested in modeling the elevation dependence of the total atmospheric delay, but certain applications may require independent modeling of each component. As an example, if a WVR is used to estimate the non-hydrostatic component of the delay, we only need to map the hydrostatic component. Keeping in mind these possible applications, we will briefly discuss the hydrostatic and non-hydrostatic mapping functions performance. A more detailed analysis is carried out in Section 6.7, in the context of the total atmospheric delay elevation dependence modeling.

The hydrostatic mapping functions to be analyzed are evaluated in a single version only (for the cases where multiple functions have been published or multiple parameterizations are possible), corresponding to the one expected to perform the best. Other options will be discussed later. A total of twelve mapping functions have been analyzed (the respective names and codes are listed in Table 6.7). The model by Rahnemoon [1988] will not be included in this discussion, as breaking the model into the zenith delay components and corresponding mapping functions would constitute in our opinion a

disparagement of the model itself. We will discuss concisely the performance of this model later in the chapter. The CfA and UNSW mapping functions are evaluated using monthly values of lapse rates and tropopause heights from our databases.

Table 6.7 – Names and codes for hydrostatic (h) and non-hydrostatic (n-h) mapping functions.

Model Name	Reference	Code (h)	Code (n-h)
Black	Black [1978]	BL_HMF	BL_WMF
CfA	Davis et al. [1985]	CfA_HMF	CfA_WMF
Chao 1	Chao [1972]	CH1_HMF	CH1_WMF
Chao 2[†]	Estefan and Sovers [1994]	CH2_HMF	CH2_WMF
Goad	Goad and Goodman [1974]	GG_HMF	GG_WMF
Ifadis	Ifadis [1986]	IF_HMF	IF_WMF
Moffett	Moffett [1973]	HM_HMF	HM_WMF
MTT	Herring [1992]	MTT_HMF	MTT_WMF
NMF	Niell [1996]	NMF_HMF	NMF_WMF
Santerre	Santerre [1987]	ST_HMF	ST_WMF
UNSW	Yan and Ping [1995]	UNSW_HMF	UNSW_WMF
Yionoulis	Yionoulis [1970]	YI_HMF	YI_WMF

[†] The Chao 2 model corresponds to the so-called *Chao's Standard Mapping Tables*, as presented in Estefan and Sovers [1994].

The global performance of the hydrostatic mapping functions analyzed have been summarized in the box-and-whisker plots shown in Figure 6.6. These plots show the differences with respect to ray tracing (model minus trace) for the total number of traces, at three different elevation angles.

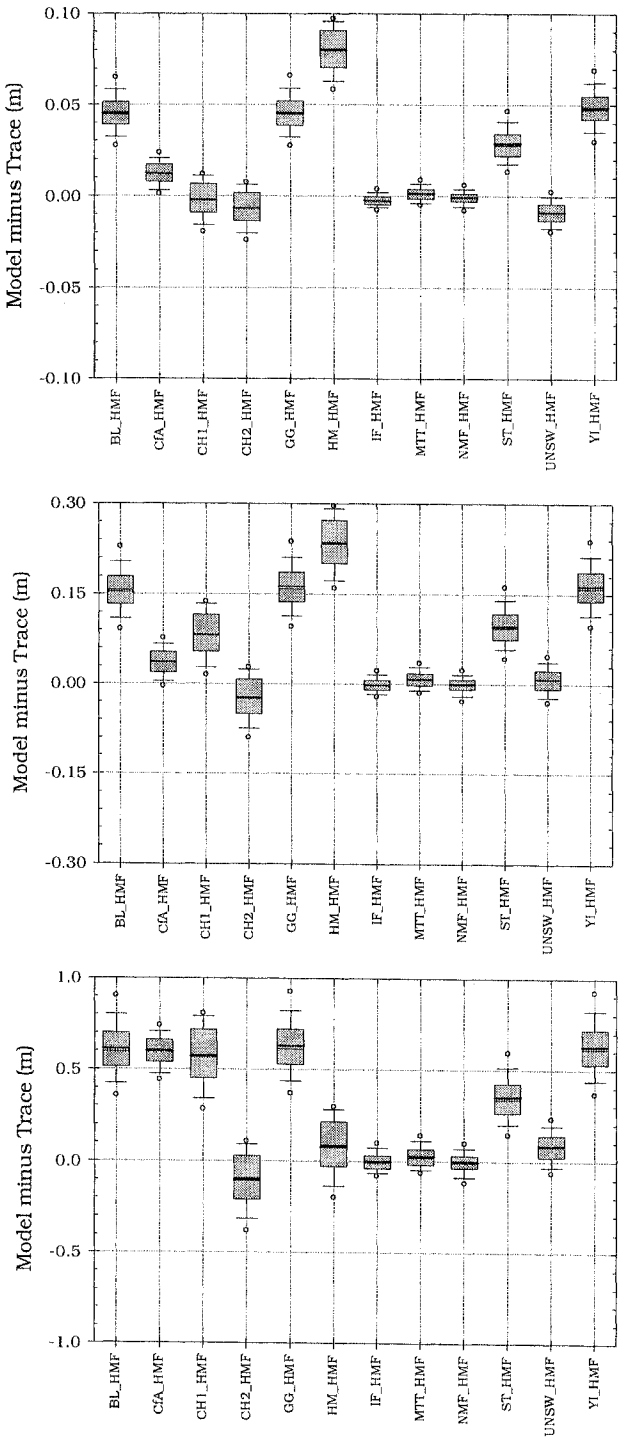

Figure 6.6 – Box-and-whisker plot for the differences between the hydrostatic mapping functions and ray tracing (model minus trace), for 10° (top), 6° (middle) and 3° (bottom) elevation angles.

From these plots it is possible to conclude that Ifadis, MTT and NMF represent the best group of functions, both in terms of mean bias and rms scatter, and for all the elevation angles used. The differences among these functions is very small; MTT performs slightly better than Ifadis and NMF for elevation angles above 15°, whereas NMF shows some advantage below this angle. At very low elevation angles (3°), Ifadis shows the best overall accuracy.

CfA, UNSW and both of Chao's functions compose a group with relatively good performance. UNSW performs better than CfA for low elevation angles, with regard to both mean bias and rms scatter. The degradation of CfA below 5° is very clear and expected, as the function was fitted to elevation angles above 5°. As regards the mean bias, Chao 2 is clearly superior to Chao 1. As both functions are independent of any external information, the rms scatter is similar for both versions.

The Hopfield-based functions constitute the group with worst performance. Within this group, the improvement of Santerre in reducing the mean bias is noted. The models by Black, Goad, and Yionoulis achieve identical levels of accuracy, whereas the weakness of the simplified Moffett function is reflected in the large bias and rms scatter shown. The ranking of the functions by mean bias and total error is presented in Figures 6.7 and 6.8.

The performance of the mapping functions at each radiosonde station for different elevation angles is illustrated in the group of plots in Appendix IX. These plots are a good image of what was revealed by our global analysis. Furthermore, they reveal that in

general the worst performance of most of the functions happens at high and low latitude stations, as well at high altitude stations.

The importance of these plots is also evident in analyzing certain trends that were not revealed previously, as in the case of the Chao functions. Despite the reasonable performance in terms of total error, the Chao functions show a very clear trend for the mean bias (the best performance of Chao 1 and Chao 2 are at mid-latitudes, and degrade rapidly towards lower and higher latitudes). By way of illustration, at 10° elevation angle the peak-to-peak variation of the mean bias for these functions is greater than 3 cm, much larger than that achieved by UNSW, for instance (~1 cm), which ranks lower than Chao 1 regarding the total error.

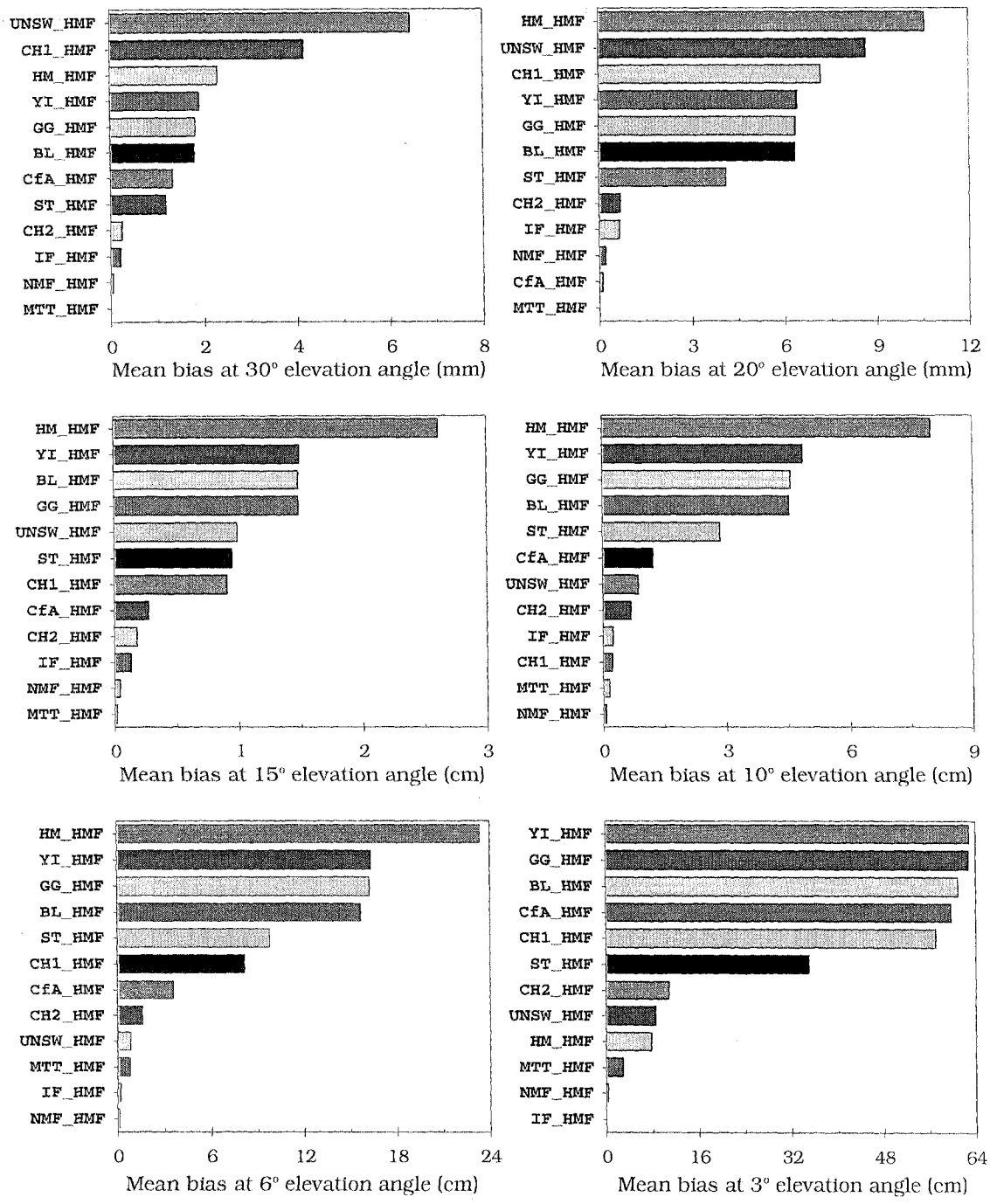

Figure 6.7 – Ranking of the hydrostatic mapping functions by absolute mean bias.

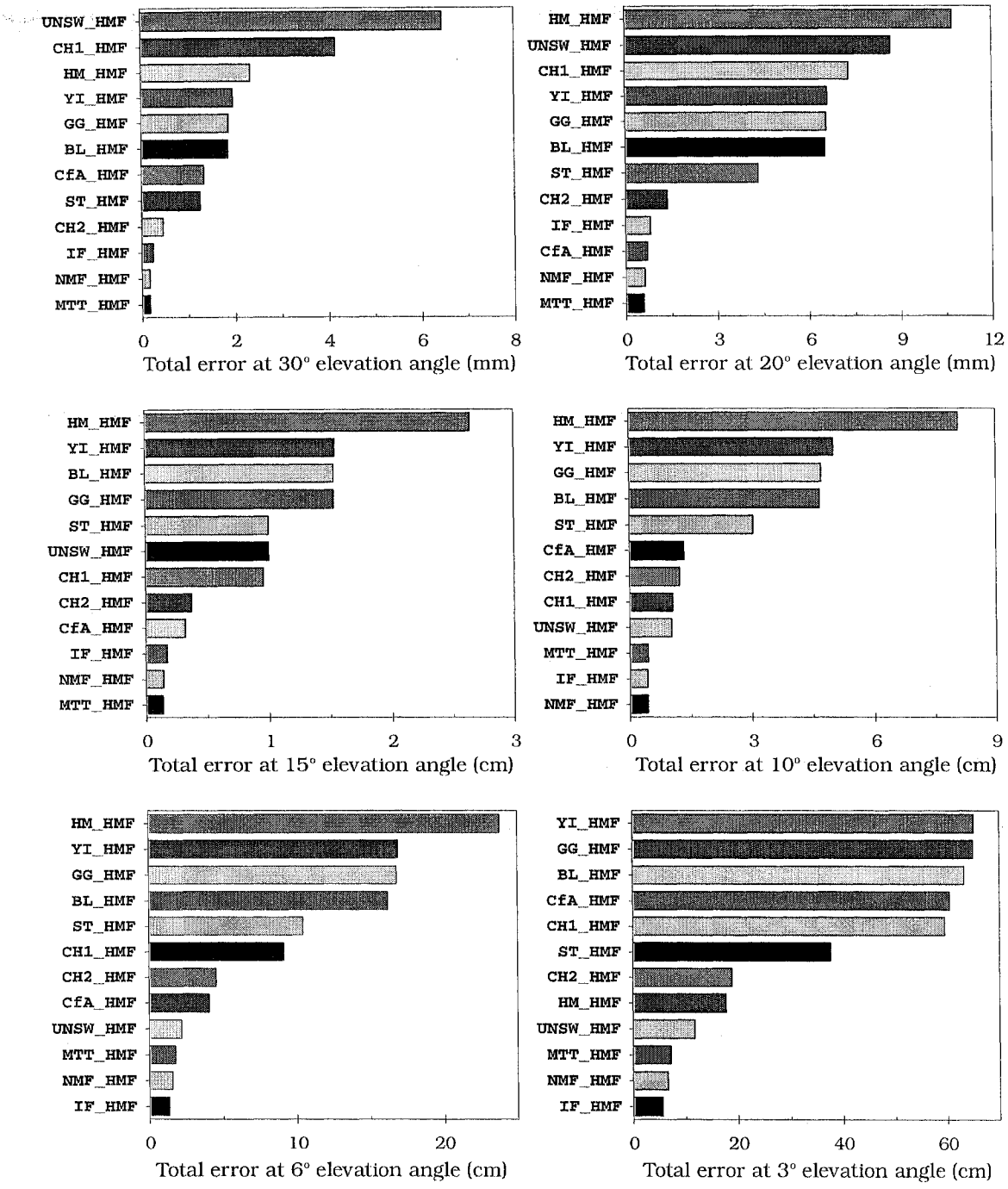

Figure 6.8 – Ranking of the hydrostatic mapping functions by total error.

6.6. Non-hydrostatic mapping functions

The distribution of the differences with respect to ray tracing for the non-hydrostatic mapping functions is illustrated in the box-and-whisker plots of Figures 6.9. We have restricted these plots to elevation angles below 10°, as the differences for elevation angles above 10° are very small (mean bias and rms scatter less than ~2 mm, for an elevation angle of 15°, as an example).

From the analysis of these plots, we conclude that the non-hydrostatic mapping functions can be grouped according to their performance into three major classes. As in the case of the non-hydrostatic functions, the Ifadis, MTT, and NMF functions are superior to any of the others, both regarding mean bias and rms scatter.

The worst group is constituted by CfA and UNSW. This is explained by the fact that these mapping functions were not designed to map the non-hydrostatic component of the atmospheric delay (although this is not totally clear in Yan and Ping [1995], such has been confirmed [Yan, 1998]). Both Chao versions and all the Hopfield-based functions show identical mean bias, except at 3° elevation angle, for which a greater dissimilarity between functions is observed. As a remark, it is interesting to notice the good performance of Moffett, in contrast to the poor quality of its hydrostatic counterpart.

The box-and-whisker plot also warns about the skewness of the residuals' distribution. This fact is easily understood if we analyze the behavior of the functions at each radiosonde station separately, shown in the series of plots of Appendix X.

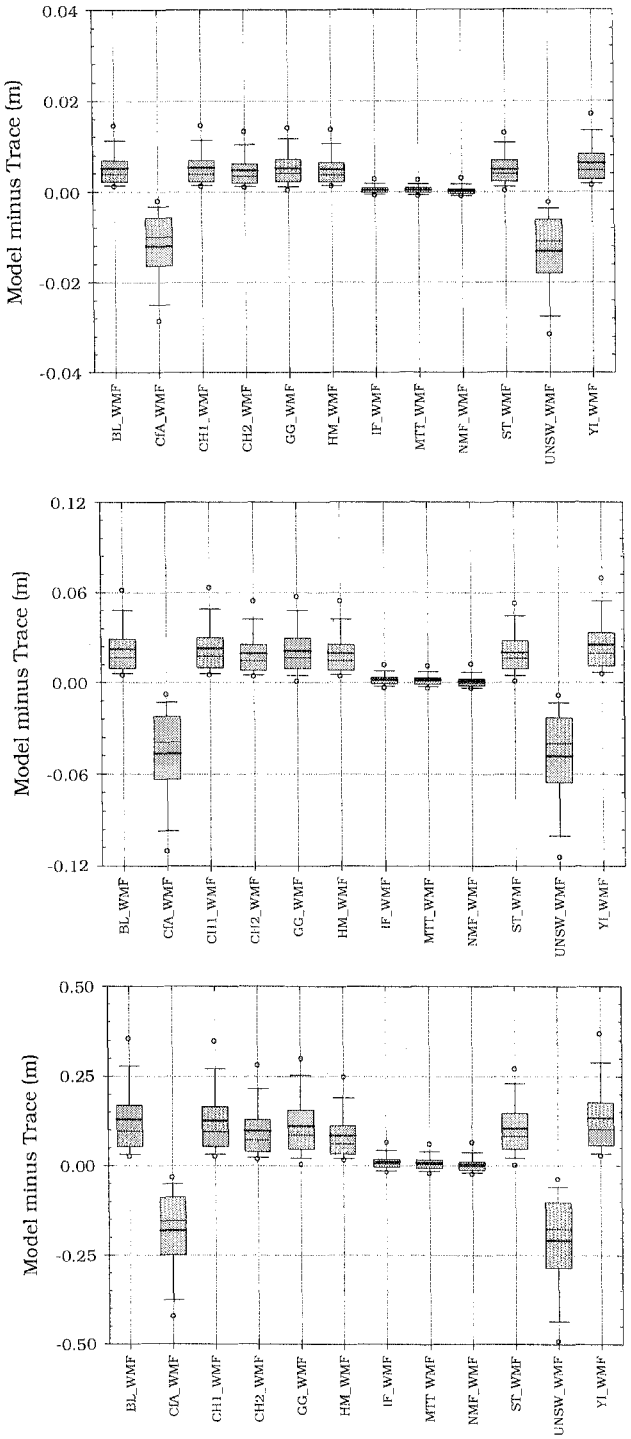

Figure 6.9 – Box-and-whisker plot for the differences between non-hydrostatic mapping functions and ray tracing (model minus trace), for 10° (top), 6° (middle) and 3° (bottom) elevation angles.

These plots show that all functions show larger bias and rms scatter at low latitudes, which is a result of the higher water vapor content and variability associated to these regions.

The ranking of the non-hydrostatic mapping functions by absolute mean bias and total error are also presented in Figure 6.10 and Figure 6.11, respectively. The plots shown in these figures clearly illustrate the good performance of the group Ifadis, MTT and NMF functions and the poor performance of the two functions due to the error introduced in using these hydrostatic functions in mapping the non-hydrostatic component also. The remaining functions have very similar performances.

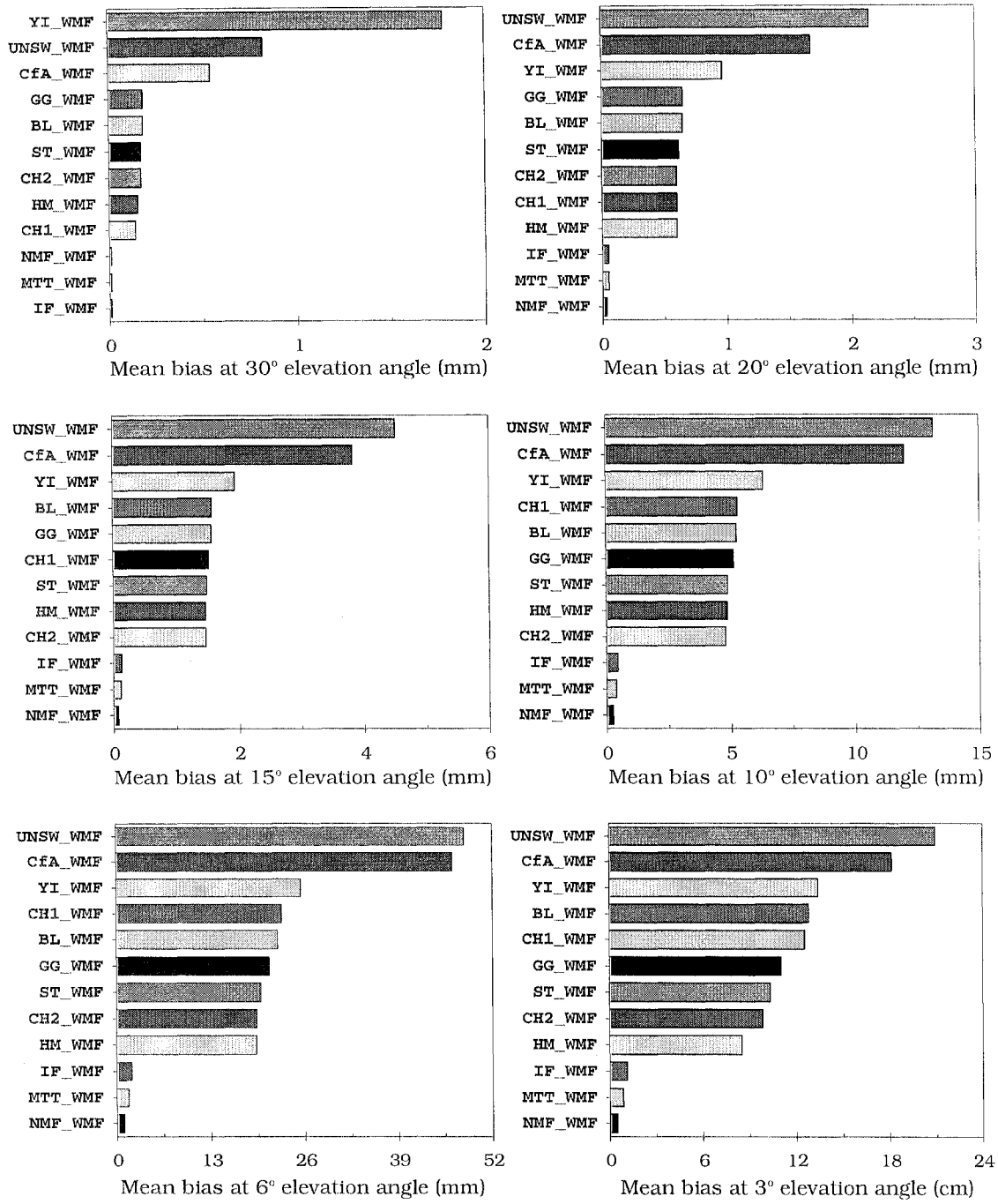

Figure 6.10 – Ranking of the non-hydrostatic mapping functions by absolute mean bias.

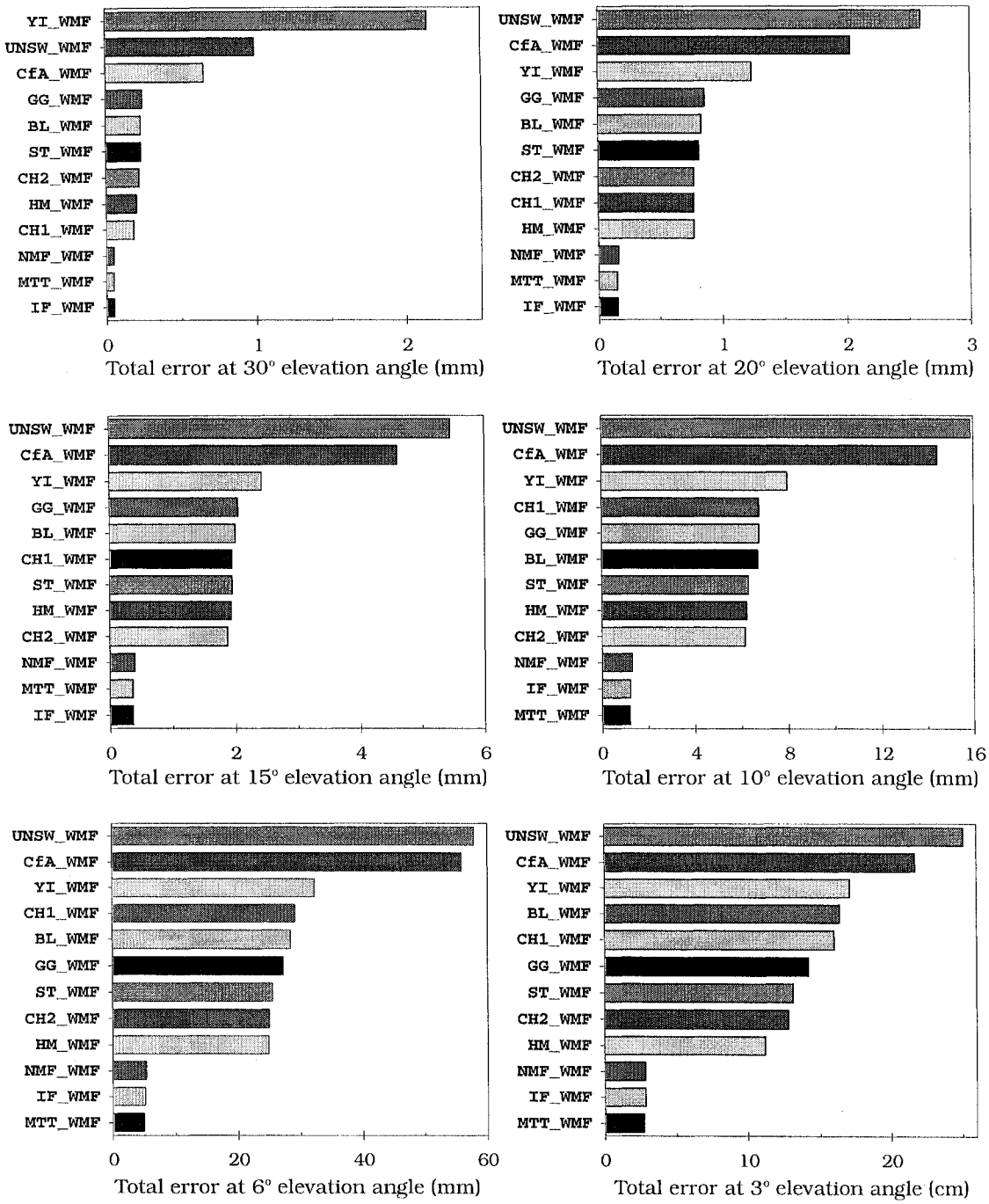

Figure 6.11 – Ranking of the non-hydrostatic mapping functions based on the total error.

6.7. Total mapping functions

The group of mapping functions that model the elevation dependence of the atmospheric delay is significantly larger than the group that allows a separate modeling of its components. Moreover there are mapping functions that can be driven using different input settings, which permits an adjustment to local conditions. Examples of mapping functions of this type are the ones developed by Lanyi [1984], Davis et al. [1985], and Yan and Ping [1995]. In order to systematize our analysis we chose therefore to initially evaluate the accuracy of these functions under different input strategies and select the best versions for intercomparison assessment with other mapping functions.

The CfA and UNSW mapping functions were tested under three different inputs for tropopause height and lapse rate: a) monthly mean of our databases at each radiosonde station; b) global default values suggested by the authors for these parameters, 11.231 km and 6.5 K km^{-1}, respectively c) predictions given by our models (UNB98TH1 and UNB98LR1), using the surface temperature of radiosonde soundings. The code names for these "versions" are presented in Table 6.8. The global performance of the different versions (for 10° and 6° elevation angles) is illustrated in Figure 6.12.

CfA's performance is clearly superior for the last strategy, as the rms scatter is significantly reduced. In order to better understand this improvement, it is useful to analyze the sensitivity of CfA to changes in tropopause height and lapse rate, presented in Table 6.9.

Table 6.8– Different processing strategies for CfA and UNSW mapping functions.

Version Code	α (K/km)	T_h (km)
CfA1_TMF	Mean†	Mean†
CfA2_TMF	6.5	11.231
CfA3_TMF	UNB98LR1	UNB98TH1
UNSW1_TMF	Mean†	Mean†
UNSW2_TMF	6.5	11.231
UNSW3_TMF	UNB98LR1	UNB98TH1

† site-dependent monthly mean values based on radiosonde observations.

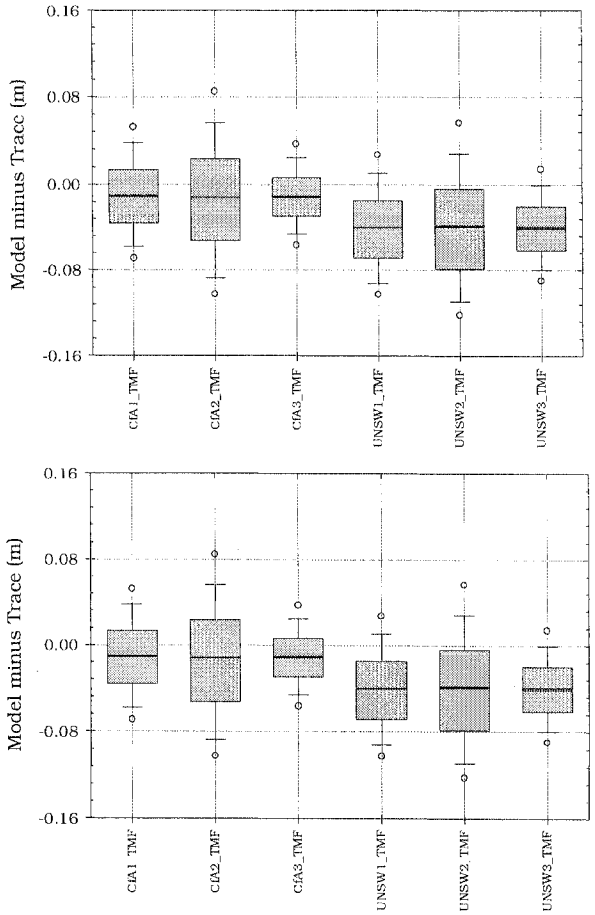

Figure 6.12 – Box-and-whisker plot for the differences between the different versions of CfA and UNSW mapping functions and ray tracing (models minus trace), for 10° (top) and 6° (bottom) elevation angles.

Table 6.9 – Sensitivity of CfA to changes in lapse rate and tropopause height, for an atmospheric zenith delay of 2.4 m (From Davis et al. [1985]).

ε	α (mm per K km^{-1})	H_t (mm per km)
10°	-8.8	2.5
5°	-44	11

From this table, we conclude that changes in the lapse rate value will more likely affect the high-latitude stations, as the differences with respect to the nominal value of 6.5 K km^{-1} will be in most cases very significant. Despite the apparent lower sensitivity of CfA to changes in tropopause height, the large variations of this meteorological parameter will likely be responsible for the bulk of the variations between the different strategies. This fact is corroborated by the plots presented in Figure 6.13.

From this figure, we can conclude that the improvement in performance for CfA (when using site-specific values of tropopause height and lapse rate and, particularly, when parameterized with the predictions for these parameters given by our models) is especially considerable for low- and high-latitude stations. At low latitudes this improvement is certainly due to the better modeling of the tropopause height, as the lapse rates do not deviate significantly from the nominal value of 6.5 K km^{-1}. At high latitudes both the changes in lapse rate and tropopause height are expected to contribute to this improvement, as the nominal values are particularly high in both cases. At mid-latitudes this improvement is marginal as far as the mean bias, but the reduction of the rms scatter is still significant, and again better when our models are used.

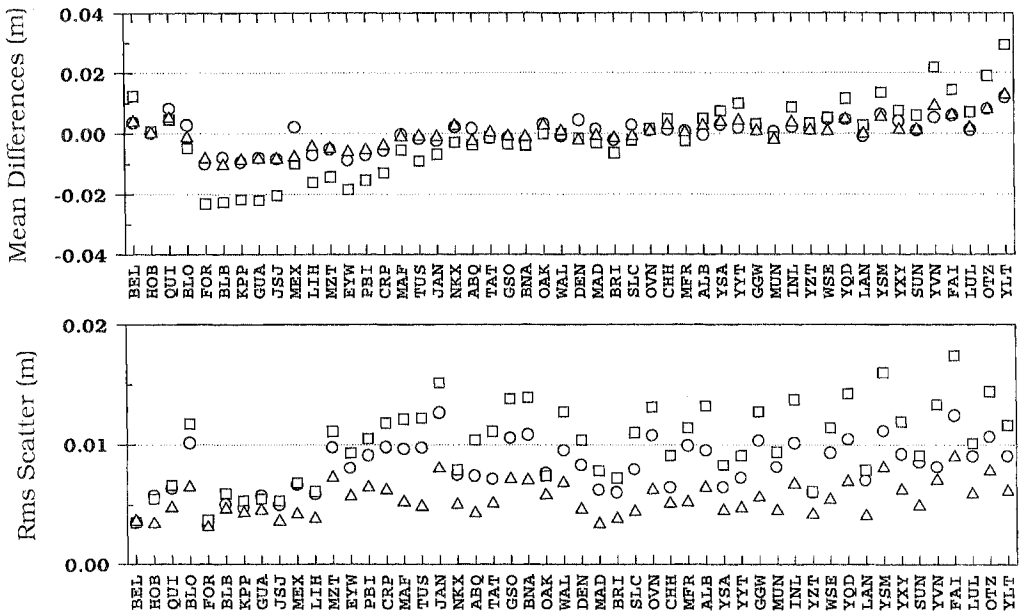

Figure 6.13 – Mean bias (top plot) and associated rms scatter (bottom plot) for CfA1_TMF (circle), CfA2_TMF (square), and CfA3_TMF (triangle), at 10° elevation angle, for 50 radiosonde stations.

The mapping function has a good global performance at 10° elevation angle, but a small bias can be observed at 6°, worsening significantly for lower elevation angles.

The improvement in the reduction of the mean bias in the UNSW mapping functions under strategies a) and c) is not as significant as in the case of CfA, as illustrated in Figure 6.14. As far as the rms scatter is concerning, the improvement under both strategies a) and c) is notable for virtually all stations. Our models yield once again the best solution of all.

UNSW is characterized by a marked bias with respect to our traces, at all elevation angles, and for most of the stations analyzed. The rms scatter for the different strategies is essentially identical to that observed for CfA.

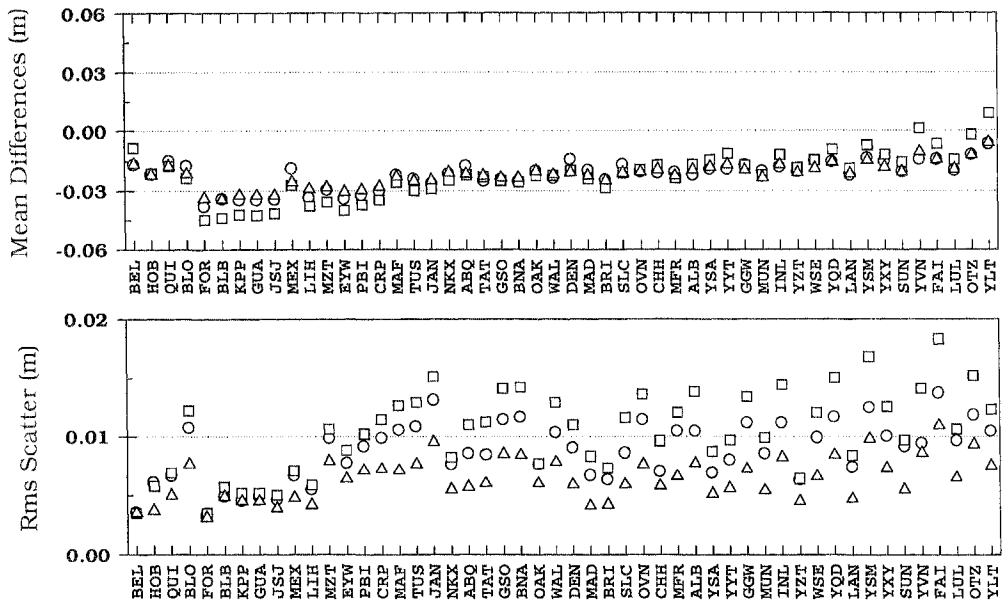

Figure 6.14 – Mean bias (top plot) and associated rms scatter (bottom plot) for UNSW1_TMF (circle), UNSW2_TMF (square), and UNSW3_TMF (triangle), at 10° elevation angle, for 50 radiosonde stations.

In summary, we can conclude that both CfA and UNSW perform significantly better if parameterized by UNB98TH1 and UNB98LR1. In addition to their efficiency, these models also share the ease of use in obtaining those meteorological parameters, avoiding therefore the use of nominal values, which generally lead to a serious degradation in the performance of these mapping functions. Therefore, and for mapping function intercomparison purposes, we will use these "optimized versions"; the statistics for the other versions will be presented in the tables available as a supplement to this dissertation (http://mat.fc.ul.pt/eg/lattex/PhD_e_sup.html).

The Lanyi mapping function was tested using six different parameter settings, as follows:

a) In this strategy, all the default nominal values suggested by Lanyi [1984] were used.

The surface temperature is based on the average temperature of the Deep Space Network (DSN) stations. According to Estefan and Sovers [1994] and Sovers and Jacobs [1996], this parameter represents not the actual surface temperature but the average temperature of the surface layer.

b) The temperature profile parameters (surface temperature, lapse rate, and tropopause height) used for this version are based on an interpolation scheme through the U.S. Standard Atmosphere Supplements, recommended by Sovers and Jacobs [1996], and based on the scheme used by Niell [1996] in the development of his mapping functions. The estimated temperature profile parameters corresponding to each of the atmospheres are presented in Table 6.10. Those parameters are subsequently linearly interpolated to match the latitude and height of the station of interest, and finally interpolated to the appropriate day of year, using a sinusoid with extrema in January and July. As in Niell [1996], the southern hemisphere is considered to be half a year out of phase with respect to the northern hemisphere. The inversion height in this version is set to zero.

c) In this strategy, we use the mean monthly values for the inversion height, tropopause height and lapse rate of each station in our databases, coupled with the radiosonde surface temperature and pressure for each launch.

d) As strategy c), but with mean monthly values of surface temperature at every radiosonde station. The motivation for this strategy is to avoid the use of the actual true surface temperature. The monthly values are used as the best representation of the average temperature of the surface layer.

Table 6.10 – U.S. Standard Atmosphere Supplements Profile Parameters (from Sovers and Jacobs [1996]).

Date	φ (°)	T (K)	α (K/km)	H_i (km)	H_t (km)
January 28	15	300.940	6.33961	0	13.7889
	30	291.642	6.19987	0	12.1382
	45	275.593	5.43813	0	9.83468
	60	266.007	5.37249	0	8.51284
	75	256.212	4.21860	0	11.5115
July 28	15	300.940	6.33961	0	13.7889
	30	301.074	6.14791	0	13.6649
	45	296.381	6.01369	0	12.6266
	60	288.455	5.93926	0	9.67076
	75	283.577	5.84173	0	9.50090

e) The mean monthly values of temperature of our database, coupled with global values of lapse rate and tropopause height suggested by Davis et al. [1985] were used as input. As in strategy b), the observed pressure was used and the inversion height was set to zero.

f) In this strategy we use the predictions of lapse rate and tropopause height given by our models (UNB98LR1 and UNB98TH1).

A comparative summary of different Lanyi versions is presented in Table 6.11.

The global performance of the different versions (for 10° and 6° elevation angles) is illustrated in Figure 6.15.

Table 6.11 – Different processing strategies for the Lanyi mapping function (S - associated symbol in graphs; RAOB - radiosonde observed values; SJ96 - interpolation scheme suggested by Sovers and Jacobs [1996] (see text for details); Mean - monthly mean values based on radiosonde observations).

Version	S	P (hPa)	T (K)	α (K/km)	H_i (km)	H_t (km)
LA1_TMF	○	1013.25	292	6.8165	1.25	12.2
LA2_TMF	□	RAOB	SJ96	SJ96	0	SJ96
LA3_TMF	Δ	RAOB	RAOB	Mean	Mean	Mean
LA4_TMF	◇	RAOB	Mean	Mean	Mean	Mean
LA5_TMF	∇	RAOB	Mean	6.5	0	11.231
LA6_TMF	⬡	RAOB	Mean	UNB98LR1	0	UNB98TH1

This global analysis allows us to conclude that the two versions driven with nominal values for the tropopause height and lapse rate, that is, strategies a) and e) present high rms scatter as compared with the other versions. Furthermore, the distribution of the differences with respect to ray tracing is unequivocally skewed towards the lower end, in the case a), and the upper end, in the case of e). The strategies that yield the best performances are clearly b) and d), despite the small bias (note the opposite sign of the bias in the two approaches). This last strategy improved significantly the rms scatter with respect to strategy c), but the reduction of the mean bias is marginal. The solution using UNB98TH1 and UNB98LR1 lead to an improvement comparatively to LA1_TMF, LA5_TMF, and LA3_TMF (in this case just slightly), but did not exceed the performance of LA2_TMF and LA4_TMF.

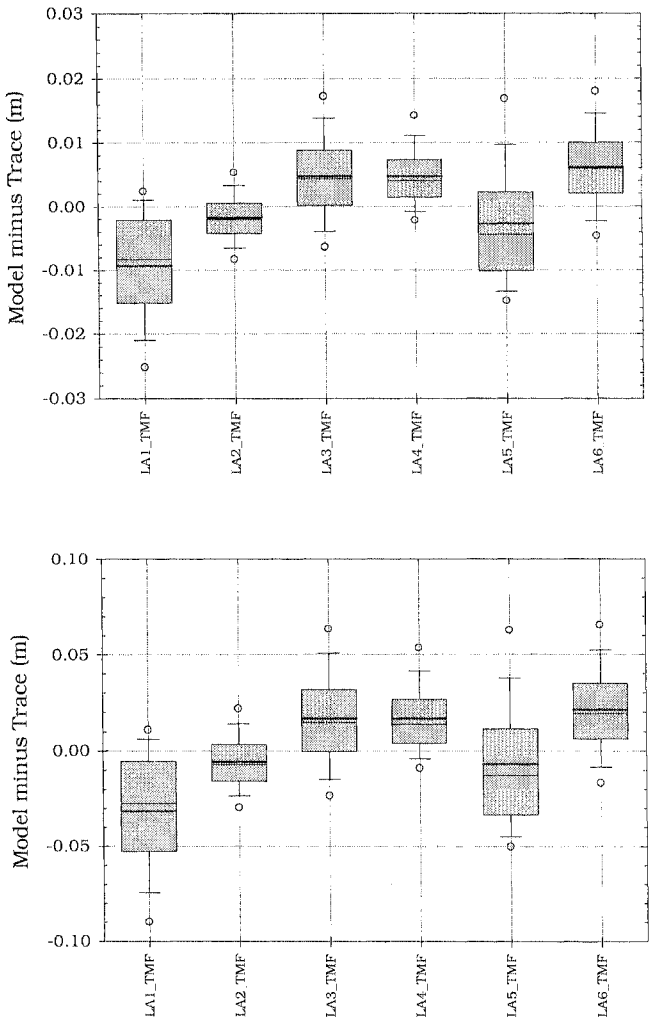

Figure 6.15 – Box-and-whisker plot for the differences between the different versions of the Lanyi mapping function and ray tracing (models minus trace), for 10° and 6° elevation angle.

The Lanyi mapping function is less sensitive than CfA to changes in the lapse rate and tropopause height, but it is very sensitive to changes in the inversion height, as illustrated in Table 6.12. This will pose some problems at high latitude stations, where a large variability of this parameter is expected.

Table 6.12 – Sensitivity of the Lanyi mapping function to changes in lapse rate, inversion height and tropopause height, at 6° elevation angle. (From Sovers and Jacobs [1996]).

ε	α (mm per K km^{-1})	H_i (mm per km)	H_t (mm per km)
6°	20	-20	5

Figure 6.16 shows the mean differences and corresponding rms scatter for the 50 radiosonde stations, for an elevation angle of 10°.

The version parameterized with the default values suggested by Lanyi [1984] performs very well at low latitudes (low bias and low rms scatter), but degrades rapidly with the increase in latitude. The same applies to strategy e), which shows a significant bias for high latitudes.

The use of a mean instead of the instantaneous surface temperature leads to an identical mean bias but it improved remarkably the rms scatter at all radiosonde stations. This fact also explains the relative bad performance of the parameterization with our models. These were also driven by the instantaneous surface temperature. Due to the high correlation of the derived temperature-profile parameters with the surface temperature, and to the high sensitivity of the Lanyi mapping function to changes in temperature, our models induce a large scatter. When we drive our models with site-specific monthly means of temperature, we obtain levels of performance close to strategy b), as confirmed in Figure 6.17, which shows the residual differences at station Denver. We have adopted to set the inversion height to zero.

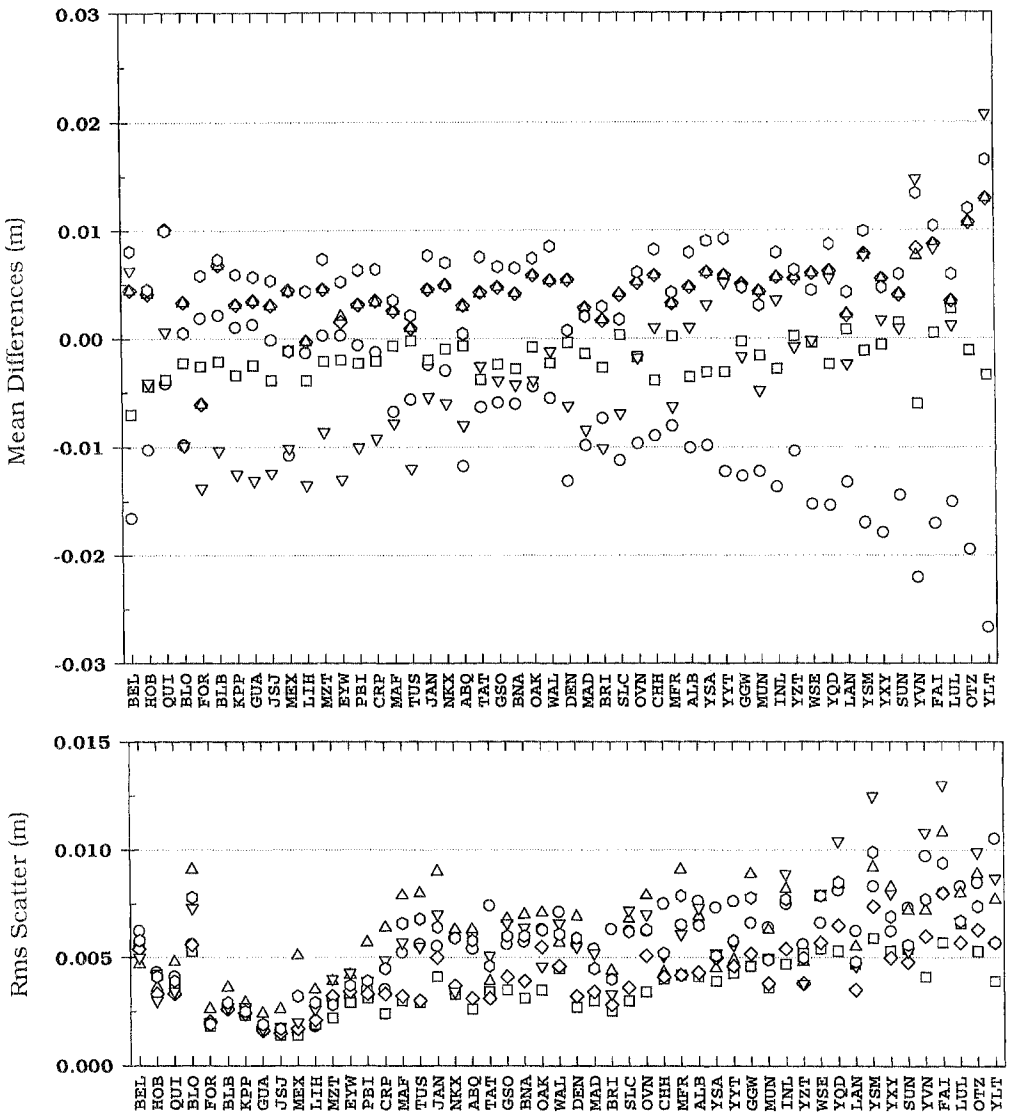

Figure 6.16 – Mean bias (top plot) and associated rms scatter (bottom plot) for different parameterizations of the Lanyi mapping function, at 10° elevation angle, for 50 radiosonde stations (see Table 6.11 for explanation of the symbols).

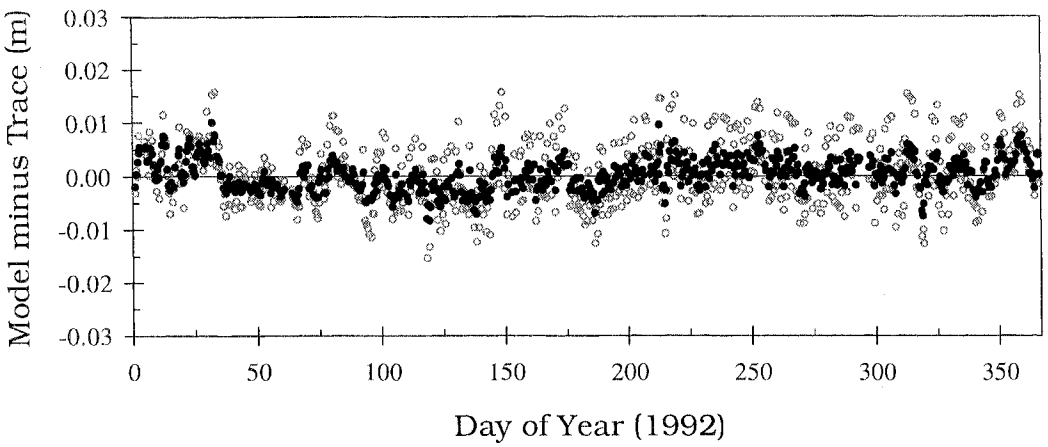

Figure 6.17 – Residual differences (model minus trace) for the LA6_TMF with UNB98TH1 and UNB98LR1 driven by the instantaneous surface temperature (gray open circles) and driven by the mean monthly values of temperature (black circles), for the station Denver, for 10° elevation angle.

As conclusion, the solutions LA4_TMF and LA2_TMF constitute the best optimizations for the Lanyi mapping function we have generated (the parameterization with our models driven by mean temperature was performed only for a limited set of stations); as they represent two different approaches in parameter settings for Lanyi, both versions will be used in our intercomparison assessment. The statistics for the other versions are included in our supplemental statistical tables (http://mat.fc.ul.pt/eg/lattex/PhD_e_sup.html).

The mapping functions that model the elevation dependence of the zenith total delay to be intercompared will include the optimized versions of CfA, UNSW, and Lanyi just selected, the mapping functions developed by Saastamoinen [1973], Black and Eisner [1984], Marini and Murray [1973], Baby et al. [1988], and the mapping functions already analyzed in terms of delay components. For these functions, the total delay is obviously

defined as the sum of the hydrostatic and non-hydrostatic delays. As an exception, we will not include the Chao 2 functions in this analysis. The complete list is presented in Table 6.13.

The global performance of the total mapping functions is illustrated in Figure 6.18, for 15°, 10° and 6° elevation angles. From the analysis of this group of plots, the following conclusions can be drawn:

- The Moffett simplification to the Hopfield mapping function performs poorly at all elevation angles, both concerning its mean bias and rms scatter. The performance of this function degrades significantly both in equatorial/tropical regions and for stations with high altitude, as illustrated in the supplementary series of error bar plots presented in Appendix XI.

- A large group of functions, which includes all the remaining functions based on the Hopfield quartic model and the Marini-Murray mapping function, tends to over-estimate the delay at all three elevation angles. Furthermore the following features are observed:

  - Black, Goad, and Yionoulis perform similarly at all elevation angles both regarding mean bias and rms scatter. All these functions perform worst for the arctic high latitude stations (see Appendix XI). The Marini-Murray function presents a mean bias that is close to the values achieved by that small group, but the rms scatter is significantly higher. The performance of Marini-Murray degrades towards the equatorial/tropical regions.

Table 6.13 – Names and codes for the total mapping functions.

Model Name	Reference	Code
Baby	Baby et al. [1988]	BB_TMF
Black	Black [1978]	BL_TMF
Black-Eisner	Black and Eisner [1984]	BE_TMF
CfA	Davis et al. [1985]	CfA_TMF
Chao	Chao [1972]	CH_TMF
Goad	Goad and Goodman [1974]	GG_TMF
Hartmann	Hartmann and Leitinger [1984]	HL_TMF
Ifadis	Ifadis [1986]	IF_TMF
Lanyi 2	Lanyi [1984]	LA2_TMF
Lanyi 4	Lanyi [1984]	LA4_TMF
Marini-Murray	Marini and Murray [1973]	MM_TMF
Moffett	Moffett [1973]	HM_TMF
MTT	Herring [1992]	MTT_TMF
NMF	Niell [1996]	NMF_TMF
Saastamoinen	Saastamoinen [1973]	SA_TMF
Santerre	Santerre [1987]	ST_TMF
UNSW	Yan and Ping [1995]	UNSW_TMF
Yionoulis	Yionoulis [1970]	YI_TMF

- Black-Eisner is less accurate than Black, Goad, and Yionoulis for high elevation angles, but more accurate for low elevation angles. The performance of this function is less dependent of the latitude of the stations, but shows a slight handicap concerning stations with high altitudes (see Appendix XI).

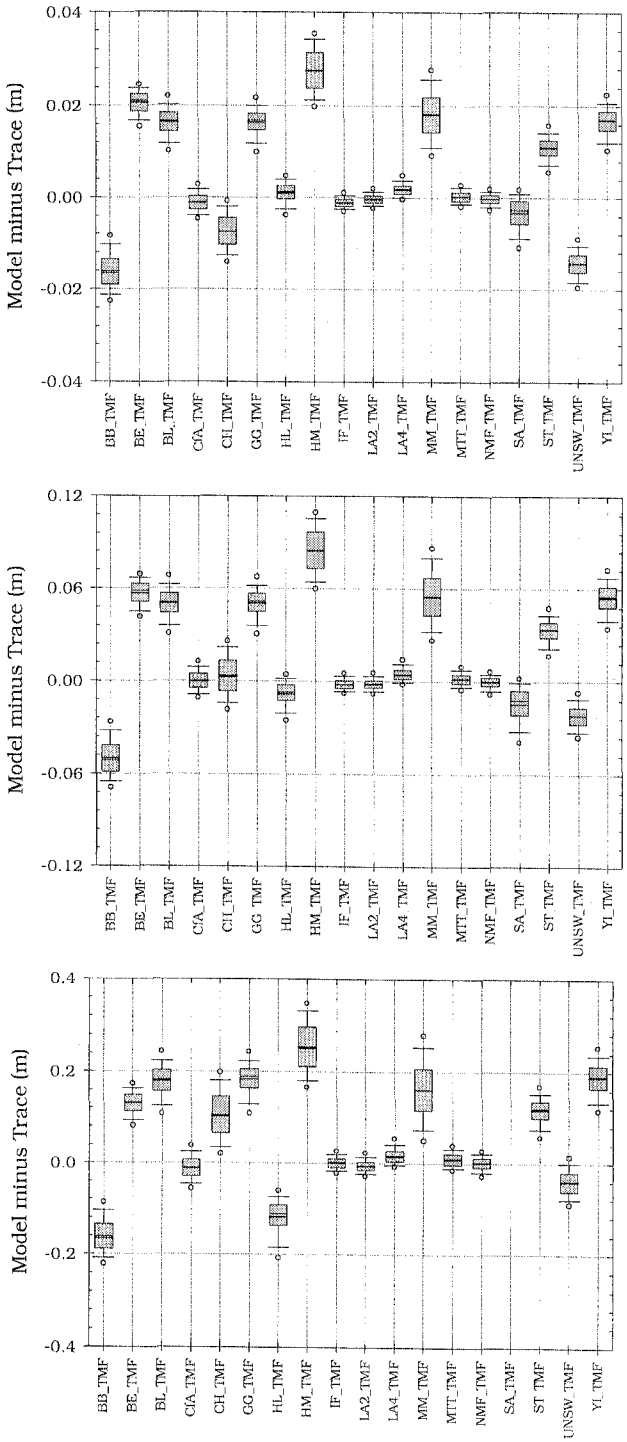

Figure 6.18 – Box-and-whisker plot for the differences between the total mapping functions and ray tracing (model minus trace), for 15° (top), 10° (middle), and 6° (bottom) elevation angles (Saastamoinen not shown for 10°).

- Santerre is clearly superior to any of the functions of this group, as the mean bias is reduced by the inclusion of the effect of the ray bending. Nevertheless the degradation in performance for the arctic stations is still manifest.

♦ Baby's precision is at the same level as Goad and Black. The absolute value of the mean bias is also identical to those functions, but Baby under-estimates the delay. The degradation of Baby towards the lower elevation angles is expected, as it also neglects the ray bending. Despite the similarity of this global performance, Baby is less dependent on the latitude and height of the stations than Goad and Black (see Appendix XI).

♦ Saastamoinen and Hartmann achieve a fair performance for elevation angles above 10°, but both break down rapidly at lower elevation angles. This fact is not surprising for Saastamoinen, as it was developed for observations above 10° and no correction tables are provided below this cutoff angle. These functions also share a high degree of skewness of the differences with respect to our traces. As regards Hartmann, this is explained by the poor performance at low latitudes; as regards Saastamoinen, by the poor performance at high latitudes (see Appendix XI). This function has also a poor accuracy for the radiosonde stations at high altitudes.

♦ The Chao function reveals a fair global performance for elevation angles above 10° (curiously the function shows the best agreement with our traces at this angle), but degrades significantly for lower elevation angles. This global accuracy is nevertheless misleading, as the mean bias is very much latitude-dependent. The function over-

estimates the delay for low latitudes and under-estimates it for high latitudes, with an additional erratic behavior for stations at high altitudes (see Appendix XI).

- The error introduced by the CfA and UNSW non-hydrostatic mapping functions produces different results in the accuracy of the total contribution. In the case of UNSW, the negative bias of the non-hydrostatic component adds to the already negative bias of the hydrostatic component, resulting in an increased bias concerning the total contribution. Yet CfA improves the already good performance of the hydrostatic mapping function, as the mean bias achieved by the non-hydrostatic component is of the opposite sign. Both functions perform less well for lower latitudes.

- The accuracy of CfA is at the same level as the best group of functions analyzed, which encompasses Ifadis, Lanyi (both versions), MTT and NMF. However the rms scatter is much higher than that achieved by this group of functions.

- The differences between the best group of functions is relatively small and almost insignificant for certain elevation angles. MTT is more accurate for higher elevation angles (above 15°), whereas NMF's accuracy is best at lower elevation angles. As regards the rms scatter, Ifadis has the best performance, for all elevation angles, followed closely by Lanyi 2. Both Lanyi versions show poor overall accuracy for the arctic regions. Some stations at these latitudes are also problematic for the remaining functions of this group.

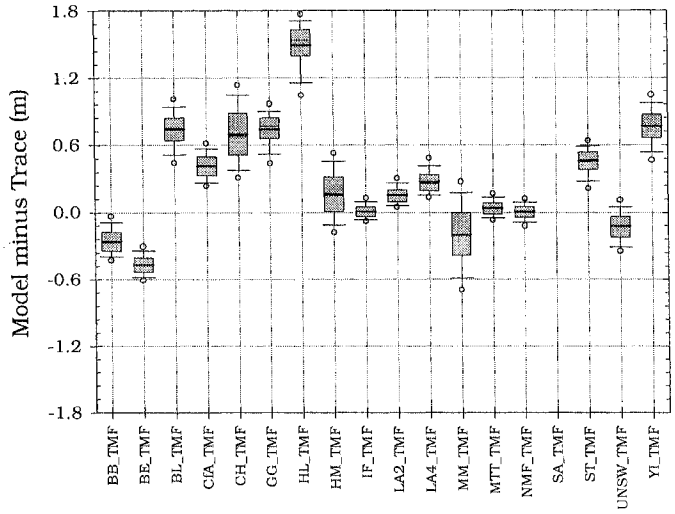

Figure 6.19 – Box-and-whisker plot for the differences between the total mapping functions and ray tracing (models minus trace), at an elevation angle of 3°. The plot for the Saastamoinen model is not shown, as it exceeds the limits of the graph.

Lanyi was developed to handle observations above 6°, a fact well evidenced in the graph of differences observed at the 3° elevation angle of Figure 6.19.

At this elevation angle only Ifadis, MTT and NMF perform with a reasonable level of accuracy. NMF is the least biased, whereas Ifadis maintains the best overall precision. The ranking of the mapping functions by mean bias, rms scatter and total error is presented in Figures 6.20, 6.21, and 6.22, respectively.

The selection of "the best" mapping function based on "accuracy" criteria only is a arduous task, as the best functions do not show large differences among them and they rank differently according to the criteria and elevation angle we use. In spite of the closeness of the mean bias and rms scatter values shown by the different functions in some cases, the differences are nevertheless statistically different, as a result of the large

sample of data used. A suitable choice will definitely embrace the Ifadis, Lanyi, MTT, and NMF mapping functions, for a cutoff angle of 6°, whereas only Ifadis, MTT, and NMF will be adequate for lower observation angles. A more refined choice will have to consider other aspects, such as ease of use, computational speed, and versatility.

As regards ease of use, NMF is the best choice, as it requires no meteorological data. In our analysis, we have always assumed that the surface meteorological data obtained from the radiosonde was errorless. Therefore the overall accuracy of the functions based on meteorological data may degrade if accurate information is not provided. This is particularly important if the meteorological parameter values are obtained from standard atmospheres.

Ifadis, MTT, and NMF are all based upon the same mathematical structure and will therefore provide identical levels of computational speed; NMF is the slowest of these functions, due to the interpolation schemes required. Lanyi is clearly the most complex of all the functions. Mendes and Langley [1993] concluded that Lanyi is 4-5 times slower than the Marini-based algorithms, which may be significant in processing large amounts of data or for real-time applications.

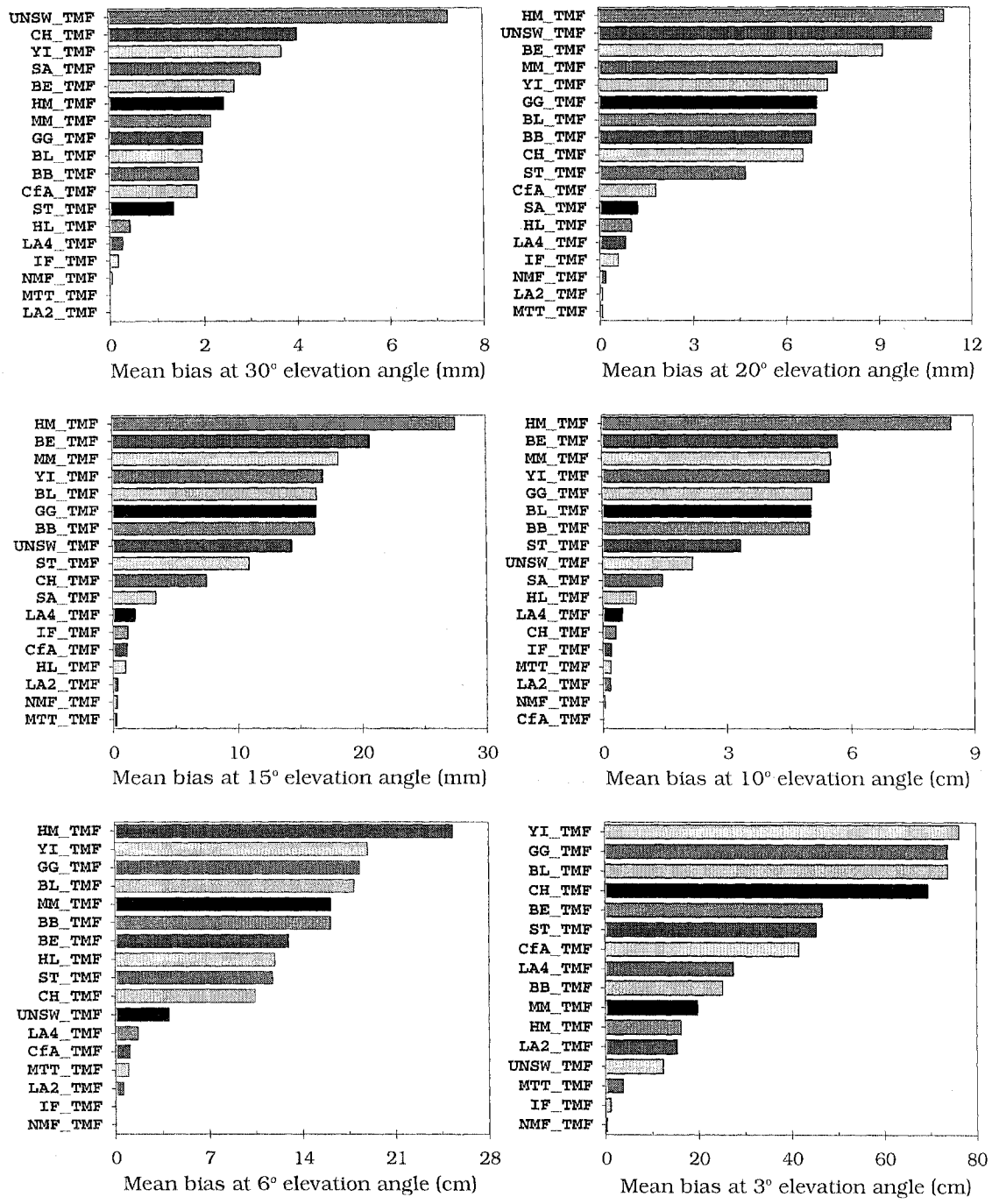

Figure 6.20 – Ranking of the total mapping functions based on the absolute mean bias.

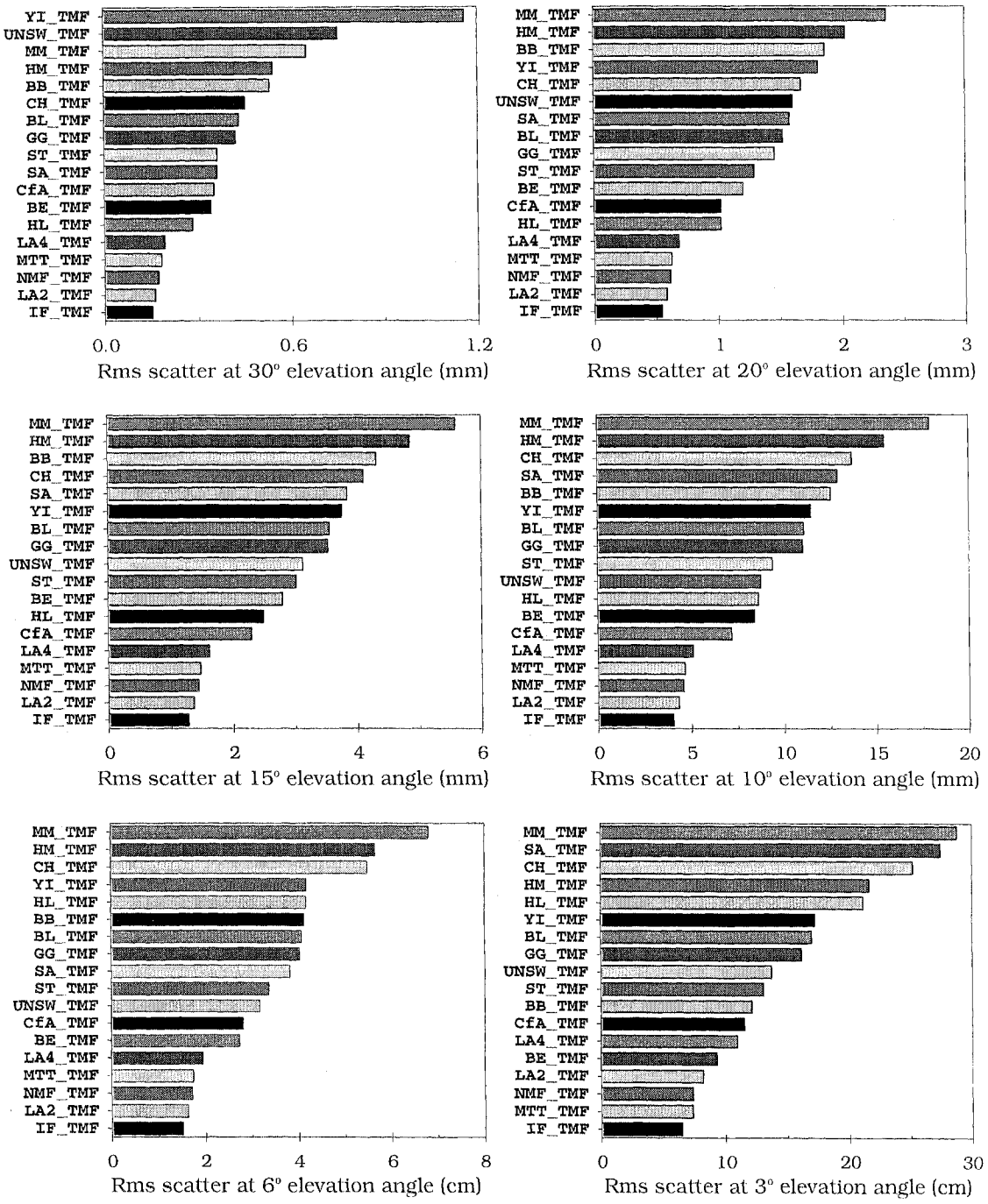

Figure 6.21 – Ranking of the total mapping functions based on the rms scatter.

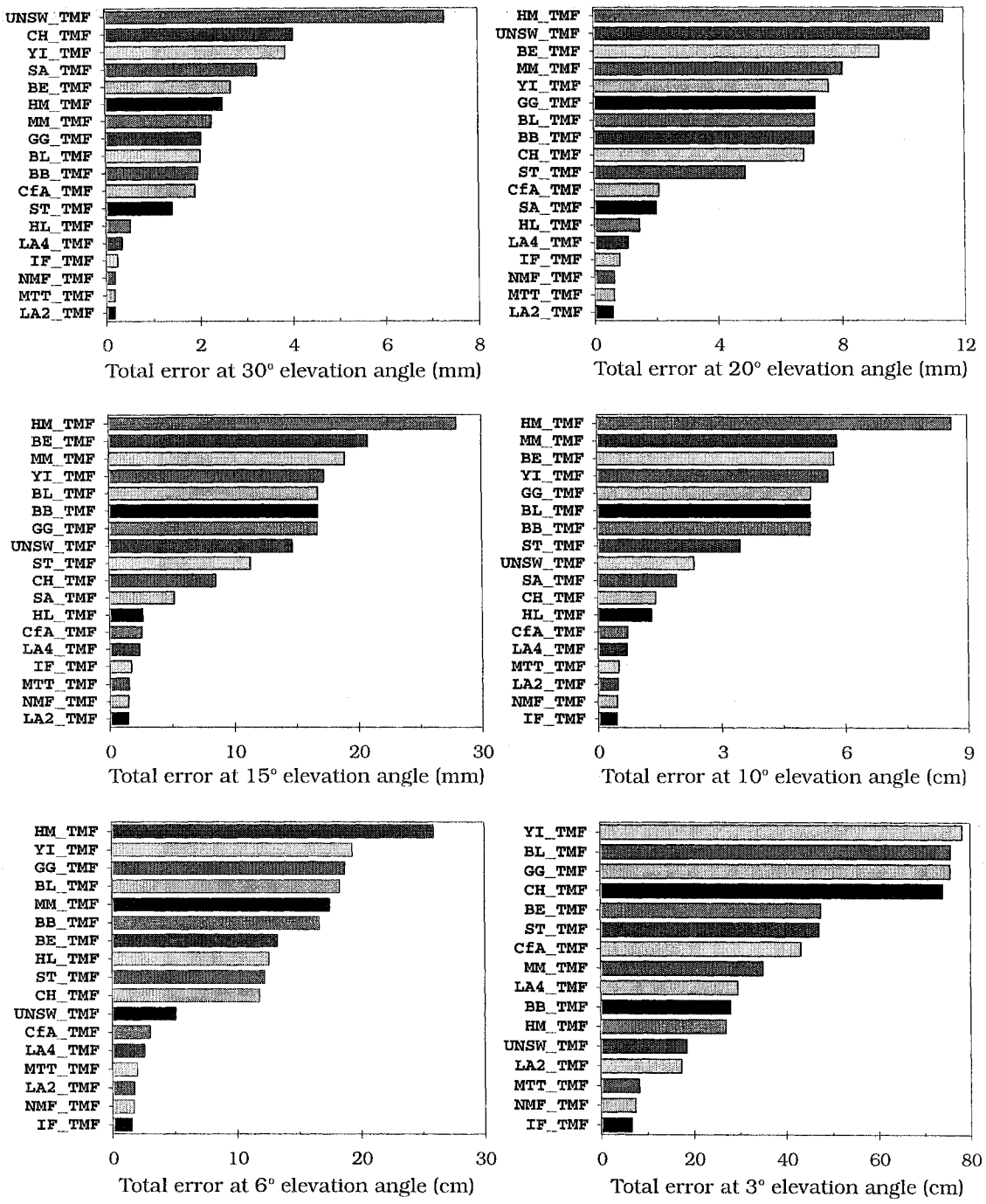

Figure 6.22 – Ranking of the total mapping functions based on the total error.

Lanyi is no doubt the most versatile of the functions analyzed, and can therefore be tuned for a particular location, if all the meteorological parameters are available. CfA also presents some tuning capability, as regards the tropopause height and lapse rate parameterization. However, in both cases this versatility may become the major problem in using these functions, as nominal values lead to a considerable worsening in the functions' accuracy. In the absence of meteorological data describing the temperature profile at a given location, the Lanyi parameterization scheme proposed by Sovers and Jacobs [1996] or the use of UNB98TH1 and UNB98LR1 driven by average values of surface temperature is recommended.

In summary, we recommend NMF in all space geodetic data analysis where no reliable meteorological data is available. If this information (including the temperature vertical profile) is available to the user, then Ifadis, Lanyi and MTT are expected to provide essentially identical levels of accuracy. For very low elevation angles (below ~6°), Ifadis, NMF, and MTT are preferred.

6.8. Hybrid models

For the sake of completeness we conclude our assessment study with an analysis of a selection of models for navigation applications which are listed in Table 6.14.

Table 6.14 – Codes for hybrid models.

Model Name	Reference	Code
Altshuler†	Altshuler and Kalaghan [1974]	AL_HM
NATO	NATO [1993]	NATO_HM
STI	Wachowski [1980]	STI_HM
WAAS	DeCleene [1995]	WAAS_HM
Rahnemoon	Rahnemoon [1988]	RA_HM
NMFS‡	–	NMFS_HM

†Surface refractivity predicted by the model; ‡See text for details.

This analysis was carried out using a different strategy, as we evaluated the models in their full formulation, that is, the differences with respect to ray tracing include both the error in zenith delay prediction and the error in mapping that delay to a certain elevation angle. The main reason that lead us to adopt a different strategy is the existence of models for which the separation of the "zenith delay prediction" and "mapping" components is not totally clear; furthermore, in some cases the mapping-function component of the model is based either on a "flat earth" (or a modification of it) or an other already analyzed mapping function, which is listed in our supplementary tables. In order to compare the performance of these models with their geodetic counterparts, we also include two other hybrid models. The first of these models is the one developed by Rahnemoon, which we deliberately decided to keep as a full model; the second is a

combination of the Saastamoinen [1973] hydrostatic and the Ifadis [1986] non-zenith hydrostatic prediction models (due to their good performance), coupled with the NMF (total) mapping function, and designated as NMFS (see Table 6.14). As the performance in zenith delay prediction is expected to be similar in both cases, the qualitative assessment of the mapping component of Rahnemoon can also be done by comparison with NMF.

The accuracy of the different models can be inferred from the analysis of the distribution of the differences with respect to ray tracing presented in the plots of Figure 6.23.

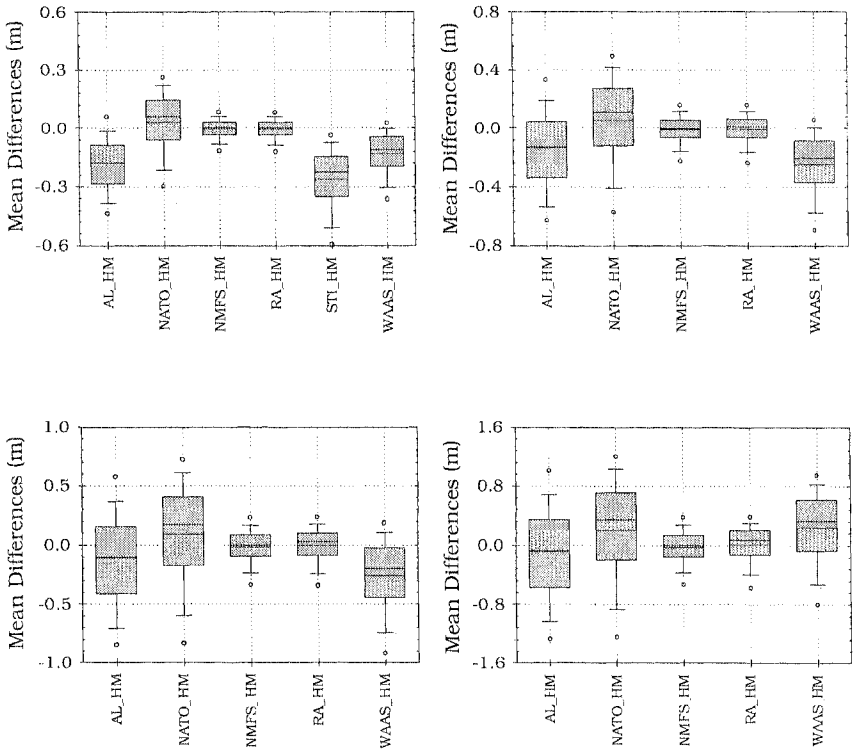

Figure 6.23 – Box-and-whisker plot for the differences between total delay hybrid models and ray tracing (model minus trace), for 30° (top left), 15° (top right), 10° (bottom left) and 6° (bottom right) elevation angles.

The plot for 30° elevation angle shows already clearly that all the navigation models have large rms scatters as compared to the two selected geodetic models. The STI model, in particular, has a large bias and the largest rms scatter of the navigation models. The further degradation of this model with decrease of the elevation angle is very abrupt, as expected from a flat earth mapping function (we have removed it from the plots for other elevation angles to highlight the differences among the remaining models). As regards the other navigation models, the WAAS model shows consistently the smallest rms scatter. The NATO has the smallest bias for elevation angles above 10°, and the Altshuler for elevation angles below 10°. These two models present identical levels of rms scatter. All the models are characterized by a skewness of the differences distribution.

The analysis of these plots reveal a good performance of the Rahnemoon model, with mean bias and rms scatter close to NMFS, for elevation angles above 10°. At lower elevation angles, the differences between these models increases significantly and is very large for an elevation angle of 3°, as illustrated in Figure 6.24.

From Figure 6.24 it is possible to conclude that the differences are more significant than the box plots may suggest, and that they are especially high for low- and high-latitude regions. This analysis suggests that the mapping component of Rahnemoon will not perform better than the mapping functions recommended in Section 6.7.

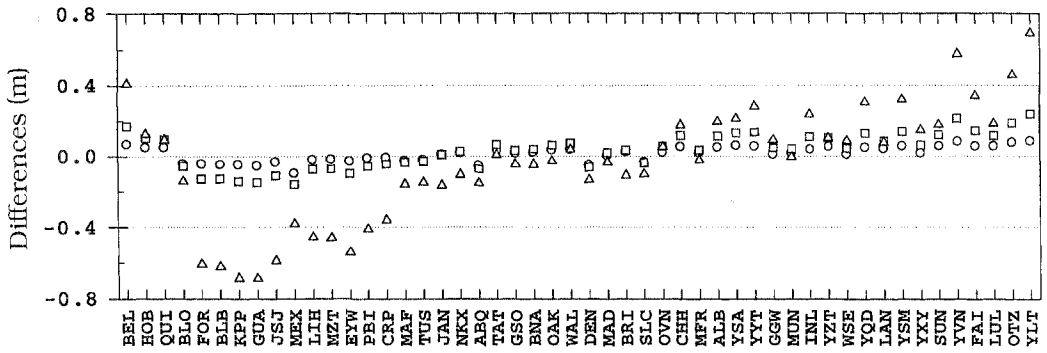

Figure 6.24 – Differences between the Rahnemoon and NMFS atmospheric models (Rahnemoon minus NMFS), at 10° (circles), 6° (squares) and 3° (triangles) elevation angles, for 50 radiosonde stations.

In this chapter, we have performed the assessment of virtually all neutral-atmosphere propagation delay models used in space data analysis. The results of this assessment against near 32,467 benchmark values, obtained by ray tracing through radiosonde data, allowed us to set recommendations on the best choices for zenith delay prediction and elevation angle dependence modeling of this delay.

The next chapter gives a syllabus of this dissertation and reinforces the recommendations that result from our research study.

7. CONCLUSIONS AND RECOMMENDATIONS

In this dissertation we have assessed a large number of models used in neutral-atmosphere propagation delay modeling. These models are separated into two major groups: prediction models, which predict the propagation delay at the zenith; and mapping functions, which model the elevation angle dependence of the propagation delay. The assessment was performed using 32,467 benchmark values obtained from ray tracing through one-year radiosonde data relative to fifty stations, covering a broad variety of climatological conditions. In order to fully accomplish our goal, other related issues were also pointed at in our research: the analysis of the accuracy and precision of our ground-truth, the establishment of databases for meteorological parameters, and development of models for their determination. The main conclusions to be withdrawn for the different research areas are summarized in the following paragraphs.

We have studied the sensitivity of ray tracing to data extrapolation and interpolation schemes, saturation vapor pressure computation formulae, refractivity constants, compressibility and enhancement factors use, and initial integration step and integration limits changes. The effect of radiosonde instrumentation precision in ray-tracing precision was also simulated.

As concerns the choice of physical models, the factors contributing with less weight in ray-tracing accuracy are related to the choice of refractivity constants, and to disregarding the compressibility and enhancement factors. The use of different refractivity constants produced differences in traces at the sub-millimetre level, for the zenith hydrostatic delay only. From the tested set of refractivity constants, the ones determined by Boudouris produce the lowest traces, whereas the ones by Essen and Froome yield to the highest values. Neglecting the compressibility factor induces a ray-tracing error of less than 0.2 mm, for the zenith non-hydrostatic delay. The omission of the effect of the enhancement factor in ray-tracing computations contributes with about 1 mm in zenith non-hydrostatic delay traces.

The computation of the saturation vapor pressure revealed an important issue in ray tracing, with implications in other routine computations of water vapor pressure. We have tested four of the most widely used formulae, and we found differences as large as ~3 mm, for the zenith non-hydrostatic delay. The differences between the Wexler, Goff and Gratch, and Tetens formulae are not significant (less than 0.3 mm, at the zenith), but *we recommend the Wexler formula to be used in saturation vapor pressure computations*, as it based in more accurate experimental measurements.

One significant shortcoming in radiosonde data is the limited height extent of the profiles. This limitation is not very crucial in computing the non-hydrostatic delay, as the atmosphere above 8 km contributes with less than ~2% of the total non-hydrostatic delay. In contrast, we have found that the layers above 20 km, for example, still contributes with

~5% of the zenith hydrostatic delay. *We therefore recommend that ray-tracing computations should be performed up to at least 75 km*, using appropriated extrapolation schemes to complement the radiosonde data. Changing the initial integration step from 5 m to 100 m produces trace differences at the sub-millimetre level, but a low value (5 - 20 m, depending on computational limitations) is nevertheless recommended.

We concluded that the limitations in radiosonde instrumentation precision and accuracy produce variations in ray-tracing computations that can amount to a few centimetres. The use of large amounts of data, as in the case of our study, will likely average out this effect.

In addition to the surface temperature, pressure, and water vapor pressure, some models require information concerning the temperature profile. In order to optimize the performance of these models, we have created large databases of inversion heights, tropopause heights, and lapse rates. Based upon these databases we have developed models for tropopause height and lapse rate determination. Furthermore, as a by-product of our ray-tracing computations, models for the computation of the mean temperature and geometric delay were also developed.

Our models for tropopause height and lapse rate determination are based on radiosonde profiles relative to 100 stations.

Our recommended model for tropopause height (UNB98TH1) is an exponential function of the surface temperature and is based on a set of 16,088 data points. For lapse rate determination, we recommend the UNB98LR2 model, which is a linear function of

surface temperature and pressure, and based on ~11,000 data points. The use of our model lead to a significant improvement in mapping function performance that use this information, both in bias and rms scatter reduction.

In our research, we have developed new models for mean temperature determination, which are of interest in the context of GPS-meteorology applications. The models are a function of the surface temperature only and yield identical precision.

Our assessment of prediction models indicated that the zenith hydrostatic delay can be predicted from surface pressure measurements with a total error below 5 mm. The Saastamoinen model performed the best, and the predictions obtained with this model agreed with our ray-tracing results at the sub-millimetre level. Consequently, *we recommend the Saastamoinen model to be used in predicting the zenith hydrostatic delay*. Contrariwise all the 12 prediction models for the zenith non-hydrostatic delay we have analyzed revealed that it is very unlikely that this component can be predicted from surface meteorology with an accuracy better than a few centimetres. Due to its simplicity and consistency with the prediction of the hydrostatic component, *we recommend the Saastamoinen model to be used in predicting the zenith non-hydrostatic delay*. We have also studied the performance of a few models used in navigation applications. We concluded that these models perform poorly and *we recommend these models not to be used in airborne precise positioning*.

We performed the assessment of 12 hydrostatic and non-hydrostatic mapping functions and 17 total mapping functions. In the cases of mapping functions allowing input settings, different versions were also analyzed. For the hydrostatic mapping functions, we concluded that Ifadis, MTT, and NMF perform the best, with very small differences in mean bias and rms scatter. We have also reached similar conclusions in the analysis of the non-hydrostatic mapping functions. For the total delay, the mapping function developed by Lanyi provides a good level of accuracy, for elevation angles above 6°, as long as accurate temperature profile information is provided. Below this elevation angle, the degradation in performance is significant. The choice of "the best" mapping function has to be based in other criteria than the overall accuracy, as no mapping function has a clear improved performance at all elevation angles. The Lanyi mapping function is the only one providing tuning capability. In general, NMF – which is independent of meteorological measurements – provides an overall accuracy at least at the same level of the one provided by Ifadis and MTT, which are driven by surface meteorological measurements. *In the cases where no reliable meteorological measurements are available, we recommend NMF to be used in modeling the elevation dependence of the zenith delay. If that information is available, and for elevation angles above 6°, Ifadis, Lanyi, and MTT will likely lead to identical results. For elevation angles below 6°, the Lanyi mapping function is no longer recommended.*

REFERENCES

Abshire, J.B. and C.S. Gardner (1985). "Atmospheric refractivity corrections in satellite laser ranging." *IEEE Transactions on Geoscience and Remote Sensing*, Vol. GE-23, No. 4, pp. 414-425.

Ahrens, C.D. (1994). *Meteorology Today – An Introduction to Weather, Climate, and the Environment*. 5th ed., West Publishing Company, New York.

Albani, M., V. Beruti, and S. D'Elia (1994). "Two years of ERS-1 data exploitation." *ESA Bulletin*, No. 77, pp. 87-97.

Alber, C., R. Ware, C. Rocken, and F. Solheim (1997). "GPS surveying with 1 mm precision using corrections for atmospheric slant path delay." *Geophysical Research Letters*, Vol. 24, No. 15, pp. 1859-1862.

Altshuler, E.E. (1971). "Corrections for tropospheric range error." AFCRL-71-0419, Air Force Cambridge Research Laboratories, Bedford, Mass.

Altshuler, E.E. and P.M. Kalaghan (1974). "Tropospheric range error corrections for the NAVSTAR system." AFCRL-TR-74-0198, Air Force Cambridge Research Laboratories, Bedford, Mass.

American National Standards Institute, and American Institute of Aeronautics and Astronautics (ANSI/AIAA) (1990). *Guide to Reference and Standard Atmosphere Models*. ANSI/AIAA G-003-1990, American Institute of Aeronautics and Astronautics, Washington, D.C.

Argus, D.F. (1996). "Postglacial rebound from VLBI geodesy: On establishing vertical reference." *Geophysical Research Letters*, Vol. 23, No. 9, pp. 973-976.

Argus, D.F. and R.G. Gordon (1990). "Pacific-North American plate motion from very long baseline interferometry compared with motion inferred from magnetic anomalies, transform faults, and earthquake slip vectors." *Journal of Geophysical Research*, Vol. 95, No. B11, pp. 17,315-17,324.

Askne, J. and H. Nordius (1987). "Estimation of tropospheric delay for microwaves from surface weather data." *Radio Science,* Vol. 22, No. 3, pp. 379-386.

Baby, H.B., P. Golé, and J. Lavergnat (1988). "A model for the tropospheric excess path length of radio waves from surface meteorological measurements." *Radio Science,* Vol. 23, No. 6, pp. 1023-1038.

Bannon, P.R., C.H. Bishop, and J.B. Kerr (1997). "Does the surface pressure equal the weight per unit area of a hydrostatic atmosphere?" *Bulletin of the American Meteorological Society*, Vol. 78, No. 11, pp. 2637-2642.

Barry, R.G. and R.J. Chorley (1987). *Atmosphere, Weather, and Climate*. 5th ed., Methuen, New York.

Bar-Sever, Y.E. and P.M. Kroger (1996). "Strategies for GPS-based estimates of troposphere delay." *Proceedings of ION GPS-96, the 9th International Technical Meeting of the Satellite Division of The Institute of Navigation*, Kansas City, Mo., 17-20 September, pp. 615-623.

Bassiri, S. and G.A. Hajj (1993). "Higher-order ionospheric effects on the global positioning system observables and means of modeling them." *Manuscripta geodaetica*, Vol. 18, pp. 280-289.

Bean, B.R. (1961). "Concerning the bi-exponential nature of the tropospheric radio refractive index." *Beiträge zur Physik der Atmosphäre*, Vol. 34, pp. 81-91.

Bean, B.R. and E.J. Dutton (1966). *Radio Meteorology*. National Bureau of Standards Monograph 92, U.S. Government Printing Office, Washington, D.C.

Bean, B.R. and G.D. Thayer (1959). "Models of the atmospheric radio refractive index." *Proceedings of the Institute of Radio Engineers*, pp. 740-755.

Bean, B.R., B.A. Cahoon, C.A. Samson, and G.D. Thayer (1966). *A World Atlas of Atmospheric Radio Refractivity*. Environmental Sciences Service Administration, Monograph 1, U.S. Department of Commerce, Washington, D.C.

Bender, P.L. (1992). "Atmospheric refraction and satellite laser ranging." *Proceedings of Symposium on Refraction of Transatmospheric Signals in Geodesy*, J.C. de Munck and T.A.Th. Spoelstra (Eds.), The Hague, The Netherlands, 19-22 May, Netherlands Geodetic Commission, Publications on Geodesy, Delft, The Netherlands, No. 36, New Series, pp. 117-125.

Berman, A.L. (1976). "The prediction of zenith range refraction from surface measurements of meteorological parameters." JPL Technical Report 32-1602, Jet Propulsion Laboratory, California Institute of Technology, Pasadena, Calif.

Berry, F.A., E. Bollay, and N.R. Beers (1945). *Handbook of Meteorology*. McGraw-Hill Book Co., New York.

Bethan, S., G. Vaughan, and S.J. Reid (1996). "A comparison of ozone and thermal tropopause heights and the impact of tropopause definition on quantifying the ozone content of the troposphere." *Quarterly Journal of the Royal Meteorological Society*, Vol. 122, No. 532, pp. 929-944.

Beutler, G., I. Bauersima, W. Gurtner, M. Rothacher, T. Schildknecht, and A. Geiger (1988). "Atmospheric refraction and other important biases in GPS carrier phase observations." In *Atmospheric Effects on Geodetic Space Measurements,* Ed. F.K. Brunner. Monograph 12, School of Surveying, The University of New South Wales, Kensington, New South Wales, Australia, pp. 15-43.

Bevis, M., S. Businger, S. Chiswell, T.A. Herring, R.A. Anthes, C. Rocken, and R.H. Ware (1994). "GPS meteorology: Mapping zenith wet delays onto precipitable water." *Journal of Applied Meteorology*, Vol. 33, No. 3, pp. 379-386.

Bevis, M., S. Businger, T.A. Herring, C. Rocken, R.A. Anthes, and R.H. Ware (1992). "GPS meteorology: Remote sensing of atmospheric water vapor using the Global Positioning System." *Journal of Geophysical Research*, Vol. 97, No. D14, pp. 15,787-15,801.

Black, H.D. (1978). "An easily implemented algorithm for the tropospheric range correction." *Journal of Geophysical Research*, Vol. 83, No. B4, pp. 1825-1828.

Black, H.D. and A. Eisner (1984). "Correcting satellite Doppler data for tropospheric effects." *Journal of Geophysical Research*, Vol. 89, No. D2, pp. 2616-2626.

Born, M. and E. Wolf (1975). *Principles of Optics.* 5th ed., Pergamon Press, New York.

Boudouris, G. (1963). "On the index of refraction of air, the absorption and dispersion of centimeter waves by gases." *Journal of Research of the National Bureau of Standards – D. Radio Propagation*, Vol. 67D, No. 6, pp. 631-684.

Braasch, M.S. (1990). "A signal model for GPS." *Navigation*, Journal of The Institute of Navigation (U.S.), Vol. 37, No. 4, pp. 363-377.

Bradley, P.A. (1989). "Propagation of radiowaves in the ionosphere." In *Radiowave Propagation,* M.P.M. Hall and L.W. Barclay (Eds.), IEE Electromagnetic Waves Series, Peter Peregrinus Ltd. on behalf of the Institution of Electrical Engineers, London.

Brown, A. (1989). "Extended differential GPS." *Navigation*, Journal of The Institute of Navigation (U.S.), Vol. 36, No. 3, pp. 265-285.

Brunner, F.K. and M. Gu (1991). "An improved model for the dual frequency ionospheric correction of GPS observations." *Manuscripta geodaetica*, Vol. 16, pp. 205-214.

Brunner, F.K. and S. McCluskey (1991). "Tropospheric zenith delay parameters: How many should be estimated in GPS processing." *Australian Journal of Geodesy, Photogrammetry, and Surveying,* No. 55, pp. 67-75.

Buck, A.L. (1981). "New equations for computing vapor pressure and enhancement factor." *Journal of Applied Meteorology*, Vol. 20, pp. 1527-1532.

Bürki, B., M. Cocard, A. Geiger, R. Gyger, and H.-G. Kahle (1992). "Development of a portable dual frequency microwave water vapor radiometer for geodetic applications." *Proceedings of Symposium on Refraction of Transatmospheric Signals in Geodesy,* Eds. J.C. de Munck and T.A.Th. Spoelstra, The Hague, The Netherlands, 19-22 May, Netherlands Geodetic Commission, Publications on Geodesy, Delft, The Netherlands, No. 36, New Series, pp. 129-133.

Callahan, P.S. (1973). "Prediction of tropospheric wet-component range error from surface measurements." Jet Propulsion Laboratory, California Institute of Technology, Pasadena, Calif., JPL Technical Report 32-1526, Vol. XVIII, pp. 41-46.

Carter, W.E., D.S. Robertson, and J.R. MacKay (1985). "Geodetic radio interferometric surveying: Applications and results." *Journal of Geophysical Research*, Vol. 90, No. B6, pp. 4577-4587.

Carter, W.E., D.S. Robertson, J.E. Pettey, B.D. Tapley, B.E. Schutz, R.J. Eanes, and M. Lufeng (1984). "Variations in the rotation of the earth." *Science*, Vol. 224, pp. 957-961.

Cazenave, A., P. Gegout, L. Soudarin, K. Dominh, F. Barlier, P. Exertier, and Y. Boudon (1993). "Geodetic results from Lageos 1 and Doris satellite data." In *Contributions of Space Geodesy to Geodynamics: Crustal Dynamics*, Eds. D.E. Smith, and D.L. Turcotte. Geodynamics Series, Vol. 23, American Geophysical Union, Washington, D.C., pp. 81-98.

Chao, C.C. (1971a). "New tropospheric range corrections with seasonal adjustment." Jet Propulsion Laboratory, California Institute of Technology, Pasadena, Calif., JPL Technical Report 32-1526, Vol. VI, pp. 67-82.

Chao, C.C. (1971b). "Tropospheric range effect due to simulated inhomogeneities by ray tracing." Jet Propulsion Laboratory, California Institute of Technology, Pasadena, Calif., JPL Technical Report 32-1526, Vol. VI, pp. 57-66.

Chao, C.C. (1972). "A model for tropospheric calibration from daily surface and radiosonde balloon measurement." Technical Memorandum 391-350, Jet Propulsion Laboratory, Pasadena, Calif.

Chao, C.C. (1973). "A new method to predict wet zenith range correction from surface measurements." In: The Deep Space Network Progress Report, Jet Propulsion Lab, Pasadena, Calif., JPL Technical Report 32-1526, Vol. XIV, pp. 33-41.

Chao, C.C. (1974). "The tropospheric calibration model for Mariner Mars 1971." Jet Propulsion Laboratory, California Institute of Technology, Pasadena, Calif., JPL Technical Report 32-1587, pp. 61-76.

Chen, G. and T.A. Herring (1997). "Effects of atmospheric azimuthal asymmetry on the analysis of space geodetic data." *Journal of Geophysical Research*, Vol. 102, No. B9, pp. 20,489-20,502.

Chen, X., R.B. Langley, and H. Dragert (1996). "Investigation of annual variations in the WCDA GPS solutions." *Proceedings of ION GPS-96, the 9th International Technical Meeting of the Satellite Division of The Institute of Navigation*, Kansas City, Mo., 17-20 September, pp. 1809-1818.

Clark, T.A., B.E. Corey, J.L. Davis, G. Elgered, T.A. Herring, H.F. Hinteregger, C.A. Knight, J.I. Levine, G. Lundqvist, C. Ma, E.F. Nesman, R.B. Phillips, A.E.E. Rogers, B.O. Ronnang, J.W. Ryan, B.R. Schupler, D.B. Shaffer, I.I. Shapiro, N.R. Vandenberg, J.C. Webber, and A.R. Whitney (1985). "Precision geodesy using the Mark-III very-long-baseline interferometer system." *IEEE Transactions on Geoscience and Remote Sensing*, Vol. GE-23, No. 4, pp. 438-449.

Coco, D.S., T.L. Guassiran II, and C. Coker (1995). "Passive detection of sporadic E using GPS phase measurements." *Radio Science*, Vol. 30, No. 6, pp. 1869-1874.

Cogan, J., T. Greenling, S.A. Luces, and J. Thomas (1996). "Dropsondes with GPS windfinding". *Meteorological Applications*, Vol. 3, No. 3, pp. 223-228.

Cole, A. E. and A.J. Kantor (1978). "Air Force Reference Atmospheres." AFGL-TR-78-0051; AFSG-382, Air Force Geophysics Laboratory, Meteorology Division, Hanscom AFB, Mass.

Cole, A.E., A. Court, and A.J. Kantor (1965). "Model atmospheres." In *Handbook of Geophysics and Space Environments*, Ed. S.L. Valley. McGraw-Hill Book Company, New York.

Collins, J.P. and R.B. Langley (1996). "Mitigating tropospheric propagation delay errors in precise airborne GPS navigation." *Proceedings of IEEE Position, Location and Navigation Symposium*, Atlanta, Georgia, April 22-26, pp. 582-589.

Collins, J.P., R.B. Langley, and J. LaMance (1996). "Limiting factors in tropospheric propagation delay error modelling for GPS airborne navigation." *Proceedings of The Institute of Navigation 52nd Annual Meeting*, Cambridge, Mass., 19-21 June, pp. 519-528.

Coster, A.J., A.E. Niell, F.S. Solheim, V.B. Mendes, P.C. Toor, and R.B. Langley (1997). "The effect of gradients in the GPS estimation of tropospheric water vapor." *Proceedings of The Institute of Navigation 53rd Annual Meeting*, Albuquerque, New M., 30 June-2 July, pp. 107-114.

Coster, A.J., A.E. Niell, F.S. Solheim, V.B. Mendes, P.C. Toor, K.P. Buchmann, and C.A. Upham (1996a). "Measurements of precipitable water vapor by GPS, radiosondes, and a microwave water vapor radiometer." *Proceedings of ION GPS-96, the 9th International Technical Meeting of the Satellite Division of The Institute of Navigation*, Kansas City, Mo., 17-20 September, pp. 625-634.

Coster, A.J., A.E. Niell, F.S. Solheim, V.B. Mendes, P.C. Toor, R.B. Langley, and C.A. Ruggles (1996b). "The Westford water vapor experiment: Use of GPS to determine total precipitable water vapor." *Proceedings of the Institute of Navigation 52nd Annual Meeting*, Cambridge, Mass., 19-21 June, pp. 529-538.

Crane, R.K. (1976). "Refraction effects in the neutral atmosphere." In *Methods of Experimental Physics*, Vol. 12B, Ed. M.L. Meeks. Academic Press, New York, pp. 186-200.

Crutcher, H.L. (1969). "Temperature and humidity in the troposphere." *In Climate of the Free Atmosphere*, Ed. D.F. Rex, World Survey of Climatology, Vol. 4, Elsevier Publishing Company, New York, pp. 45-83.

Davis, J.L. (1986). "Atmospheric propagation effects on radio interferometry." AFGL Technical Report 86-0243, U.S. Air Force Geophysics Laboratory, Hanscom AFB, Mass..

Davis J.L., G. Elgered, A.E. Niell, and I.I. Shapiro (1992). "Horizontal gradients in the 'wet' atmospheric propagation delay." *Proceedings of Symposium on Refraction of Transatmospheric Signals in Geodesy*, J.C. de Munck and T.A.Th. Spoelstra (Eds.), The Hague, The Netherlands, 19-22 May, Netherlands Geodetic Commission, Publications on Geodesy, Delft, The Netherlands, No. 36, New Series, pp. 25-28.

Davis, J.L., G. Elgered, A.E. Niell, and C.E. Kuehn (1993). "Ground-based measurement of gradients in the 'wet' radio refractivity of air." *Radio Science*, Vol. 28, No. 6, pp. 1003-1018.

Davis, J.L., T.A. Herring, I.I. Shapiro, A.E.E. Rogers, and G. Elgered (1985). "Geodesy by radio interferometry: Effects of atmospheric modeling errors on estimates of baseline length." *Radio Science,* Vol. 20, No. 6, pp. 1593-1607.

DeCleene, B. (1995). Personal communication, Federal Aviation Administration, May.

Defant, F. and H. Taba (1957). "The threefold structure of the atmosphere and the characteristics of the tropopause." *Tellus*, Vol. 9, pp. 259-274.

Degnan, J.J. (1993). "Millimeter accuracy satellite laser ranging: A review." In *Contributions of Space Geodesy to Geodynamics: Technology*, Eds. D.E. Smith, and D.L. Turcotte. American Geophysical Union, Washington, D.C., Geodynamics Series, Vol. 25, pp. 133-162.

Derks, H., H.K. Baltink, A. van Lammeren, B. Ambrosius, H. van der Marel, and A. Kösters (1997). "GPS water vapour meteorology - status report." Scientific report: WR 97-04, Koninklijk Nederlands Meteorologisch Instituut, De Bilt, The Netherlands.

Dixon, T.H., G. Gonzalez, S.M. Lichten, D.M. Tralli, G.E. Ness, and J.P. Dauphin (1991). "Preliminary determination of Pacific-North America relative motion in the southern Gulf of California using the Global Positioning System." *Geophysical Research Letters*, Vol. 18, No. 5, pp. 861-864.

Dodson, A. and P. Shardlow (1995). "The Global Positioning System as a passive integrated atmospheric water vapour sensing device." *Atmospheric Sensing and Modeling II*, Proceedings Series, SPIE, Vol. 2582, pp. 166-177.

Dodson, A.H., P.J. Shardlow, L.C.M. Hubbard, G. Elgered, and P.O.J. Jarlemark (1996). "Wet tropospheric effects on precise relative GPS height determination." *Journal of Geodesy*, Vol. 70, No. 4, pp. 188-202.

Dow, J.M., M. Rosengren, X. Marc, R. Zandbergen, R. Piriz, and M.R. Merino (1996). "Achieving, assessing and exploiting the ERS-1/2 tandem orbit configuration." *ESA Bulletin*, No. 85, pp. 13-21.

Dow, J.M., T.J.M. Mur, and M.M.R. Merino (1994). "ESA's precise orbit determination facility." *ESA Bulletin*, No. 78, pp. 40-49.

Dunn, P.J., J.W. Robbins, J.M. Bosworth, and R. Kolenkiewicz (1996). "Crustal deformation around the Gulf of California." *Geophysical Research Letters*, Vol. 23, No. 2, pp. 193-196.

Dutton, J.A. (1986). *The Ceaseless Wind: An Introduction to the Theory of Atmospheric Motion*. Dover Publications, New York.

Elgered, G. (1992). "Refraction in the troposphere." *Proceedings of Symposium on Refraction of Transatmospheric Signals in Geodesy*, J.C. de Munck and T.A.Th. Spoelstra (Eds.), The Hague, The Netherlands, 19-22 May, Netherlands Geodetic Commission, Publications on Geodesy, Delft, The Netherlands, No. 36, New Series, pp. 13-19.

Elgered, G. (1993). "Tropospheric radio-path delay from ground-based microwave radiometry." In *Atmospheric Remote Sensing by Microwave Radiometry*, Ed. M.A. Janssen, John Wiley & Sons, pp. 215-258.

Elgered, G. and G. Lundqvist (1984). "A three-year study of radio wave propagation delays due to tropospheric water vapor." *IEEE Transactions on Antennas and Propagation*, Vol. AP-32, No. 4, pp. 390-395.

Elgered, G., B.O. Rönnäng, and J.I.H. Askne (1982). "Measurements of atmospheric water vapor with microwave radiometry." *Radio Science,* Vol. 17, No. 5, pp. 1258-1264.

Elgered, G., J.L. Davis, T.A. Herring, and I.I. Shapiro (1991). "Geodesy by radio interferometry: Water vapor radiometry for estimation of the wet delay." *Journal of Geophysical Research,* Vol. 96, No. B4, pp. 6541-6555.

Elgered, G., J.M. Johansson, B. Rönnäng, and J.L. Davis (1997). "Measuring regional atmospheric water vapor using the Swedish permanent GPS network." *Geophysical Research Letters*, Vol. 24, No. 21, pp. 2663-2666.

Elgered, G.K. (1982). "Tropospheric wet path-delay measurements." *IEEE Transactions on Antennas and Propagation*, Vol. AP-30, No. 3, pp. 502-505.

Elliott, W.P. and D.J. Gaffen (1991). "On the utility of radiosonde humidity archives for climate studies." *Bulletin of the American Meteorological Society*, Vol. 72, No. 10, pp. 1507-1520.

England, M.N., F.J. Schmidlin, and J. M. Johansson (1993). "Atmospheric moisture measurements: A microwave radiometer-radiosonde comparison." *IEEE Transactions on Geoscience and Remote Sensing*, Vol. 31, No. 2, pp. 389-398.

England, M.N., R.A. Ferrare, S.H. Melfi, D.N. Whiteman, and T.A. Clark (1992). "Atmospheric water vapor measurements: Comparison of microwave radiometry and lidar." *Journal of Geophysical Research*, Vol. 97, No. D1, pp. 899-916.

Environmental Science Services Administration, National Aeronautics and Space Administration, and United States Air Force (ESSA/NASA/USAF) (1966). *U.S. Standard Atmosphere Supplements, 1966*. U.S. Government Printing Office, Washington, D.C.

Estefan, J.A. and O.J. Sovers (1994). "A comparative survey of current and proposed tropospheric refraction-delay models for DSN radio metric data calibration." JPL Publication 94-24, Jet Propulsion Laboratory, California Institute of Technology, Pasadena, Calif.

Feigl, K.L., D.C. Agnew, Y. Bock, D. Dong, A. Donnellan, B.H. Hager, T.A. Herring, D.D. Jackson, T.H. Jordan, R.W. King, S. Larsen, K.M. Larson, M.H. Murray, Z. Shen, and F.H. Webb (1993). "Space geodetic measurement of crustal deformation in central and southern California, 1984-1992." *Journal of Geophysical Research*, Vol. 98, No. B12, pp. 21,677-21,712.

Felli, M. and R.E. Spencer (Eds.) (1989). *Very Long Baseline Interferometry. Techniques and Applications.* Proceedings of the NATO Advanced Study Institute, Bologna, Italy, 12-23 September, Kluwer Academic Publishers, Dordrecht, The Netherlands.

Fleagle, R.G. and J.A. Businger (1980). *An Introduction to Atmospheric Physics*, 2nd ed., Academic Press, New York.

Flock, W.L., S.D. Slobin, and E.K. Smith (1982). "Propagation effects on radio range and noise in earth-space telecommunications." *Radio Science*, Vol. 17, No. 6, pp. 1411-1424.

Forgues, I. (1996). *Étude de Fonctions de Projection Troposphérique et de Leurs Impacts Dans le Positionnement GPS.* M.Sc. thesis, Départment des Sciences Géomatiques, Faculté de Foresterie et de Géomatique, Université Laval, Québec.

Francis, C.R., G. Graf, P.G. Edwards, M. McCaig, C. McCarthy, A. Lefebvre, B. Pieper, P.-Y. Pouvreau, R. Wall, F. Weschler, J. Louet, W. Schumann, and R. Zobl (1995). "The ERS-2 spacecraft and its payload." *ESA Bulletin*, No. 83, pp. 13-31.

Freedman, A.P. (1991). "Measuring Earth orientation with the global positioning system." *Bulletin Géodésique*, Vol. 65, No. 1, pp. 53-65.

Gaffen, D.J. (1992). "Observed annual and interannual variations in tropospheric water vapor." NOAA Technical Memorandum ERL ARL-198, Air Resources Laboratory, Silver Spring, Md.

Gaffen, D.J., T.P. Barnett, and W.P. Elliott (1991). "Space and time scales of global tropospheric moisture." *Journal of Climate*, Vol. 4, No. 10, pp. 989-1008.

Gardner, C.S. (1976). "Effects of horizontal refractivity gradients on the accuracy of laser ranging to satellites." *Radio Science*, Vol. 11, No. 12, pp. 1037-1044.

Gardner, C.S. (1977). "Correction of laser tracking data for the effects of horizontal refractivity gradients." *Applied Optics*, Vol. 16, No. 9, pp. 2427-2432.

Goad, C.C. and L. Goodman (1974). "A modified Hopfield tropospheric refraction correction model." Paper presented at the AGU Fall Annual Meeting, 12-17 December, San Francisco, Calif. (abstract: *EOS*, Vol. 55, p. 1106, 1974)

Goff, J.A. and S. Gratch (1946). "Low-pressure properties of water from -160 to 212 F." *Transactions of the American Society of Heating and Ventilating Engineers*, pp. 95-122.

Goldstein, R. (1995). "Atmospheric limitations to repeat-track radar interferometry." *Geophysical Research Letters*, Vol. 22, No. 18, pp. 2517-2520.

Gontier, A.-M., M. Feissel, and C. Ma (1997). "The contribution of VLBI to the realization of a celestial reference system." In *Definition and Realization of the International Celestial Reference System by VLBI Astrometry of Extragalactic Objects*. IERS Technical Note 23, Eds. C. Ma, and M. Feissel, Observatoire de Paris, Paris, pp. I3-I20.

Greenspan, R.L. and J.I. Donna (1986). "Measurement errors in GPS observables." *Navigation*, Journal of The Institute of Navigation (U.S.), Vol. 33, No. 4, pp. 319-334.

Guildner, L.A., D.P. Johnson, and F.E. Jones (1976). "Vapor pressure of water at its triple point." *Journal of Research of the National Bureau of Standards - A. Physics and Chemistry*, Vol. 80A, No. 3, pp. 505-521.

Guiraud, F.O., J. Howard, and D.C. Hogg (1979). "A dual-channel microwave radiometer for measurement of precipitable water vapor and liquid." *IEEE Transactions on Geoscience Electronics,* Vol. GE-17, No. 4, pp. 129-136.

Hartmann, G.K. (1993). "The determination of tropospheric conditions (especially H_2O) affecting the accuracy of position measurements." In *Environmental Effects on Spacecraft Positioning and Trajectories*. Ed. A. Vallance Jones, International Union of Geodesy and Geophysics and the American Geophysical Union, Washington, D.C., Geophysical Monograph 73, IUGG Volume 13, pp. 73-82.

Hartmann, G.K. and R. Leitinger (1984). "Range errors due to ionospheric and tropospheric effects for signal frequencies above 100 MHz." *Bulletin Géodésique*, Vol. 58, pp. 109-136.

Hauser, J.P. (1989). "Effects of deviations from hydrostatic equilibrium on atmospheric corrections to satellite and lunar laser range measurements." *Journal of Geophysical Research*, Vol. 94, No. B8, pp. 10,182-10,186.

Hefty, J. and A.M. Gontier (1997). "Sensitivity of UT1 determined by single-baseline VLBI to atmospheric delay model, terrestrial and celestial reference frames." *Journal of Geodesy*, Vol. 71, No. 5, pp. 253-261.

Heiskanen, W.A. and H. Moritz (1967). *Physical Geodesy*. W. H. Freeman and Company, San Francisco.

Herring, T.A. (1988). "VLBI studies of the nutations of the earth." In *The Impact of VLBI on Astrophysics and Geophysics*, Eds. M.J. Reid, and J.M. Moran. Kluwer Academic Publishers, Dordrecht.

Herring, T.A. (1992). "Modeling atmospheric delays in the analysis of space geodetic data." *Proceedings of Symposium on Refraction of Transatmospheric Signals in Geodesy*, J.C. de Munck and T.A.Th. Spoelstra (Eds.), The Netherlands, 19-22 May, Netherlands Geodetic Commission, Publications on Geodesy, Delft, The Netherlands, No. 36, New Series, pp. 157-164.

Herring, T.A. and M.R. Pearlman (1993). "Future developments and synergism of space geodetic measurement techniques." In *Contributions of Space Geodesy to Geodynamics: Technology*, Eds. D.E. Smith, and D.L. Turcotte. American Geophysical Union, Washington, D.C., Geodynamics Series, Vol. 25, pp. 21-25.

Herring, T.A., D. Dong, and R.W. King (1991). "Sub-milliarcsecond determination of pole position using Global Positioning System data." *Geophysical Research Letters*, Vol. 18, No. 10, pp. 1893-1896.

Herring, T.A., I.I. Shapiro, T.A. Clark, C. Ma, J.W. Ryan, B.R. Schupler, C.A. Knight, G. Lundqvist, D.B. Shaffer, N.R. Vandenberg, B.E. Corey, H.F. Hinteregger, A.E.E. Rogers, J.C. Weber, A.R. Whitney, G. Elgered, B.O. Ronnang, and J.L. Davis (1986). "Geodesy by radio interferometry: Evidence for contemporary plate motion." *Journal of Gephysical Research*, Vol. 91, No. B8, pp. 8341-8347.

Herring, T.A., J.L. Davis, and I.I. Shapiro (1990). "Geodesy by radio interferometry: The application of Kalman filtering to the analysis of very long baseline interferometry data." *Journal of Geophysical Research*, Vol. 95, No. B8, pp. 12,561-12,581.

Hess, S.L. (1959). *Introduction to Theoretical Meteorology*. Krieger Publishing Company, Malabar, Flor. (Reprint 1979)

Hill, R.J. (1988). "Dispersion by atmospheric water vapor at frequencies less than 1 THz." *IEEE Transactions on Antennas and Propagation*, Vol. 36, No. 3, pp. 423-430.

Hill, R.J., R.S. Lawrence, and J.T. Priestley (1982). "Theoretical and calculational aspects of the radio refractive index of water vapor." *Radio Science,* Vol. 17, No. 5, pp. 1251-1257.

Hoerling, M.P., T.K. Schaack, and A.J. Lenzen (1991). "Global objective tropopause analysis." *Monthly Weather Review*, Vol. 119, No. 8, pp. 1816-1831.

Hofmann-Wellenhof, B., H. Lichtenegger, and J. Collins (1997). *GPS Theory and Practice*. 4th rev. ed., Springer-Verlag, Wien.

Hogg, D.C. and J.B. Snider (1988). "Microwave radiometry in measurement of radio pathlength through the troposphere." In *Atmospheric Effects on Geodetic Space Measurements*. Ed. F. K. Brunner. Monograph 12, School of Surveying, The University of New South Wales, Kensington, New South Wales, Australia, pp. 63-70.

Hogg, D.C., F.O. Guiraud, and M.T. Decker (1981). "Measurement of excess radio transmission length on earth-space paths." *Astronomy and Astrophysics*, Vol. 95, pp. 304-307.

Hopfield, H.S. (1969). "Two-quartic tropospheric refractivity profile for correcting satellite data." *Journal of Geophysical Research,* Vol. 74, No. 18, pp. 4487-4499.

Hopfield, H.S. (1971). "Tropospheric effect on electromagnetically measured range: Prediction from surface weather data." *Radio Science,* Vol. 6, No. 3, pp. 357-367.

Hopfield, H.S. (1972). "Tropospheric refraction effects on satellite range measurements." *APL Technical Digest,* Vol. 11, No. 4, pp. 11-21.

Hopfield, H.S. (1978). "Tropospheric correction of electro-magnetic ranging signals to a satellite: Study of parameters." In: *Proceedings of the International Symposium on Electromagnetic Distance Measurement and the Influence of Atmospheric Refraction*, Ed. P. Richardus, Wageningen, The Netherlands, 23-28 May 1977, Netherlands Geodetic Commission, Delft, The Netherlands, pp. 205-215.

Hopfield, H.S. (1979). "Improvements in the tropospheric refraction correction for range measurement." *Philosophical Transactions of the Royal Society of London*, Vol. 294, pp. 341-352.

Hoskins, B.J., M.E. McIntyre, and A.W. Robertson (1985). "On the use and significance of isentropic potential vorticity maps." *Quarterly Journal of the Royal Meteorological Society*, Vol. 111, No. 470, pp. 877-946.

Hull, A.N. (1974). "Comments on «A simple but accurate formula for the saturation vapor pressure over liquid water» – 2." *Journal of Applied Meteorology*, Vol. 13, p. 607.

Hyland (1975). "A correlation for the second interaction virial coefficients and enhancement factors for moist air." *Journal of Research of the National Bureau of Standards*, Vol. A79, pp. 551-560.

Ifadis, I. (1986). "The atmospheric delay of radio waves: Modeling the elevation dependence on a global scale." Technical Report No. 38L, School of Electrical and Computer Engineering, Chalmers University of Technology, Göteborg.

Ifadis, I. (1993). "Space to earth techniques: some considerations on the zenith wet path delay parameters." *Survey Review*, Vol. 32, No. 249, pp. 130-144.

Institute of Electrical and Electronics Engineers, The (1990). *IEEE Standard Definitions of Terms for Radio Wave Propagation.* IEEE Std 211-1990 (Revision of IEEE Std 211-1977), The Institute of Electrical and Electronics Engineers, New York.

International Association of Geodesy (IAG) (1963). "Resolutions." *Bulletin Géodésique*, Vol. 70, pp. 389-415.

International Earth Rotation Service (IERS) (1994). *Results from the SEARCH'92 Campaign.* IERS Technical Note 16, Eds. J.O. Dickey and M. Feissel, Observatoire de Paris, Paris.

International Earth Rotation Service (IERS) (1995). *Earth orientation, reference frames and atmospheric excitation functions submitted for the 1994 IERS annual report.* IERS Technical Note 19, Ed. P. Charlot, Observatoire de Paris, Paris.

International Earth Rotation Service (IERS) (1997a). *Definition and realization of the international celestial reference system by VLBI astrometry of extragalactic objects.* IERS Technical Note 23, Eds. C. Ma and M. Feissel, Observatoire de Paris, Paris.

International Earth Rotation Service (IERS) (1997b). *IERS missions, present and future. Report on the 1996 IERS workshop.* IERS Technical Note No. 22, Eds. C. Reigber, and M. Feissel, Observatoire de Paris, Paris.

International Organization for Standardization (ISO) (1982). *Reference Atmospheres for Aerospace Use.* ISO International Standard 5878-1982, Technical Committee ISO/TC 20, International Organization for Standardization, Geneva.

International Organization for Standardization (ISO) (1983). *Reference Atmospheres for Aerospace Use, Addendum 2: Air Humidity in the Northern Hemisphere.* ISO International Standard 5878-1982/Addendum 2-1983, Technical Committee ISO/TC 20, International Organization for Standardization, Geneva.

Iribarne, J.V. and H.-R. Cho (1980). *Atmospheric Physics*, D. Reidel Publishing Company, Dordrecht, Holland.

Iribarne, J.V. and W.L. Godson (1973). *Atmospheric Thermodynamics.* Geophysics and Astrophysics Monographs, Vol. 6, D. Reidel Publishing Company, Dordrecht, Holland.

Ishimaru, A. (1985). "Wave propagation." In *Handbook of Applied Meteorology.* Ed. D.D. Houghton, John Wiley & Sons, New York. pp. 1031-1064.

Jackson, D.M. and A.J. Gasiewski (1995). "Millimeter-wave radiometric observations of the troposphere: A comparison of measurements and calculations based on radiosonde and Raman lidar." *IEEE Transactions on Geoscience and Remote Sensing*, Vol. 33, No. 1, pp. 3-14.

Jackson, M.E. and R. Bilham (1994). "1991-1992 GPS measurements across the Nepal Himalaya." *Geophysical Research Letters*, Vol. 21, No. 12, pp. 1169-1172.

James, T.S. and A. Lambert (1993). "A comparison of VLBI data with the ICE-3G glacial rebound model." *Geophysical Research Letters*, Vol. 20, No. 9, pp. 871-874.

Janes, H.W., R.B. Langley, and S.P. Newby (1991). "Analysis of tropospheric delay prediction models: Comparisons with ray-tracing and implications for GPS relative positioning." *Bulletin Géodésique*, Vol. 65, No. 3, pp. 151-161.

Janssen, M.A. (1985). "A new instrument for the determination of radio path delay variations due to atmospheric water vapor." *IEEE Transactions on Geoscience and Remote Sensing*, Vol. GE-23, No. 4, pp. 485-490.

Johansson, J.M., G. Elgered, and J.L. Davis (1993). "Wet path delay algorithms for use with microwave radiometer data." In *Contributions of Space Geodesy to Geodynamics: Technology*, Eds. D.E. Smith, and D.L. Turcotte, Geodynamics Series, Vol. 25, American Geophysical Union, Washington, D.C., pp. 81-98.

Kalaghan, P.M. and E.E. Altshuler (1973). "Tropospheric refraction corrections for airborne systems." AFCRL-TR-73-0376, Air Force Cambridge Research Laboratories, Bedford, Mass.

Keihm, S.J. (1995). "Water vapor radiometer measurements of the tropospheric delay fluctuations at Goldstone over a full year." *The Telecommunications and Data Acquisition Progress Report 42-122*, Jet Propulsion Laboratory, Pasadena, Calif., pp. 1-11.

Keihm, S.J. and C.S. Ruf (1995). "Role of water vapor radiometers for in-flight calibration of the TOPEX microwave radiometer." *Marine Geodesy*, Vol. 18, pp. 139-156.

Keihm, S.J. and K.A. Marsh (1996). "Advanced algorithm and system development for Cassini radio science tropospheric calibration." *The Telecommunications and Data Acquisition Progress Report 42-127*, Jet Propulsion Laboratory, Pasadena, Calif., pp. 1-20.

Keihm, S.J., M.A. Janssen, and C.S. Ruf (1995). "TOPEX/Poseidon microwave radiometer (TMR): III. Wet troposphere range correction algorithm and pre-launch error budget." *IEEE Transactions on Geoscience and Remote Sensing*, Vol. GE-33, No. 1, pp. 147-161.

Kerr, D.E. (Ed.) (1953). *Propagation of Short Radiowaves*. McGraw-Hill, New York.

Kitchen, M. (1989). "Representativeness errors for radiosonde observations." *Quarterly Journal of the Royal Meteorological Society*, Vol. 115, pp. 673-700.

Kleusberg, A. and P.J.G. Teunissen (1996). *GPS for Geodesy*. Springer-Verlag, New York.

Kouba (1979) . "Improvements in Canadian geodetic Doppler programs." *Proceedings of the Second International Geodetic Symposium on Satellite Doppler Positioning*, Applied Research Laboratories, University of Texas at Austin, Austin, Texas, pp. 63-82.

Kroger, P.M., G.A. Lyzenga, K.S. Wallace, and J.M. Davidson (1987). "Tectonic motion in the western United States inferred from very long baseline interferometry measurements, 1980-1986." *Journal of Geophysical Research*, Vol. 92, No. B13, pp. 14,151-14,163.

Kuehn, C.E., G. Elgered, J.M. Johansson, T.A. Clark, and B.O. Rönnäng (1993). "A microwave radiometer comparison and its implication for the accuracy of wet delays." In *Contributions of Space Geodesy to Geodynamics: Technology*, Eds. D.E. Smith, and D.L. Turcotte, Geodynamics Series, Vol. 25, American Geophysical Union, Washington, D.C., pp. 99-114.

Kuo, Y.-H., Y.-R. Guo, and E.R. Westwater (1993). "Assimilation of precipitable water measurements into a mesoscale numerical model." *Monthly Weather Review*, Vol. 121, No. 4, pp. 1215-1238.

Kyle, T.G. (1991). *Atmospheric Transmission, Emission, and Scattering*. Pergamon Press, New York.

Langley, R.B., W. Wells, and V.B. Mendes (1995). "Tropospheric propagation delay: A bibliography." 2nd ed., unpublished report, Department of Geodesy and Geomatics Engineering University of New Brunswick, Fredericton, New Brunswick, Canada. Report available at http://gauss.gge.unb.ca/papers.pdf/TropoBiblio.pdf.

Langlois, W.E. (1967). "A rational approximation for saturation vapor pressure over the temperature range of sea water." *Journal of Applied Meteorology*, Vol. 6, p. 451.

Lanyi, G. (1984). "Tropospheric delay effects in radio interferometry." *The Telecommunications and Data Acquisition Progress Report 42-78*, Jet Propulsion Laboratory, Pasadena, Calif., pp. 152-159.

Larson, K.M., J.T. Freymueller, and S. Philipsen (1997). "Global plate velocities from the Global Positioning System." *Journal of Geophysical Research,* Vol. 102, No. B5, pp. 9961-9981.

Leick, A. (1994). *GPS Satellite Surveying*. 2nd ed., John Wiley & Sons, New York.

Lenhard, R.W. (1973). "A revised assessment of radiosonde accuracy." *Bulletin of the American Meteorological Society*, Vol. 54, pp. 691-693.

Lewandowski, W. and C. Thomas (1991). "GPS time transfer". *Proceedings of the IEEE*, Vol. 79, No. 7, pp. 991-1000.

Lewandowski, W., G. Petit, and C. Thomas (1992). "GPS standardization for the needs of time transfer." *Proceedings of the 6th European Frequency and Time Forum*, Noordwijk, The Netherlands, 17-19 March, ESA SP-340, pp. 243-248.

Li, P. (1994). *Determination of Earth Rotation Parameters and Adjustment of a Global Geodetic Network Using the Global Positioning System*. M.Sc.E. thesis, Department of Geodesy and Geomatics Engineering Technical Report No. 171, University of New Brunswick, Fredericton, New Brunswick.

Lide, D.R. (Ed.) (1997). *CRC Handbook of Chemistry and Physics.* 78th ed., CRC Press, Boca Raton, Flor.

Liebe, H.J. (1985). "An updated model for millimeter wave propagation in moist air." *Radio Science,* Vol. 20, No. 5, pp. 1069-1089.

Liebe, H.J., T. Manabe, and G.A. Hufford (1989). "Millimeter-wave attenuation and delay rates due to fog/cloud conditions." *IEEE Transactions on Antennas and Propagation*, Vol. 37, No. 12, pp. 1617-1623.

Lindqwister, U.J., A.P. Freedman, and G. Blewitt (1992). "Daily estimates of the earth's pole position with the Global Positioning System." *Geophysical Research Letters*, Vol. 19, No. 9, pp. 845-848.

Lindqwister, U.J., J.F. Zumberg, F.H. Webb, and G. Blewitt (1991). "Few millimeter precision for baselines in the California permanent GPS geodetic array." *Geophysical Research Letters*, Vol. 18, No. 6, pp. 1135-1138.

Linfield, R., Y. Bar-Sever, P. Kroger, and S. Keihm (1997). "Comparison of Global Positioning System and water vapor radiometer wet tropospheric delay estimates." *The Telecommunications and Data Acquisition Progress Report 42-130*, Jet Propulsion Laboratory, Pasadena, Calif., pp. 1-9.

Linfield, R.P, L.P. Teitelbaum, L.J. Skjerve, S.J. Keihm, S.J. Walter, M.J. Mahoney and R.N. Treuhaft (1995). "A test of water vapor radiometer-based troposphere calibration using VLBI observations on a 21-kilometer baseline." *The Telecommunications and Data Acquisition Progress Report 42-122*, Jet Propulsion Laboratory, Pasadena, Calif., pp. 12-31.

List, R.J. (1966). *Smithsonian Meteorological Tables.* 6th rev. ed., Smithsonian Miscellaneous Collections, Vol. 114, Smithsonian Institution Press, Washington, D.C.

Lowe, P.R. (1977). "An approximating polynomial for the computation of saturation vapor pressure." *Journal of Applied Meteorology*, Vol. 16, pp. 100-103.

Lutgens, F.K. and E.J. Tarbuck (1979). T*he Atmosphere - An Introduction to Meteorology*. Prentice-Hall, Englewood Cliffs, New Jersey.

Ma, C., J.M. Sauber, L.J. Bell, T.A. Clark, D. Gordon, W.E. Himwich, and J.W. Ryan (1990). "Measurement of horizontal motion in Alaska using very long baseline interferometry." *Journal of Geophysical Research*, Vol. 95, No. B13, pp. 21 991-22 011.

MacMillan, D.S. (1995). "Atmospheric gradients from very long baseline interferometry observations." *Geophysical Research Letters*, Vol. 22, No. 9, pp. 1041-1044.

MacMillan, D.S. and C. Ma (1994). "Evaluation of very long baseline interferometry atmospheric modeling improvements." *Journal of Geophysical Research*, Vol. 99, No. B1, pp. 637-651.

MacMillan, D.S. and C. Ma (1997). "Atmospheric gradients and the VLBI terrestrial and celestial reference frames." *Geophysical Research Letters*, Vol. 24, No. 4, pp. 453-456.

Mano, K. and E.E. Altshuler (1981). "Tropospheric refractive angle and range error corrections utilizing exoatmospheric sources." *Radio Science*, Vol. 16, No. 2, pp. 191-195.

Marini, J.W. (1972). "Correction of satellite tracking data for an arbitrary tropospheric profile." *Radio Science*, Vol. 7, No. 2, pp. 223-231.

Marini, J.W. and C.W. Murray (1973). "Correction of laser range tracking data for atmospheric refraction at elevations above 10 degrees." NASA-TM-X-70555, Goddard Space Flight Center, Greenbelt, Md.

Matsuzaka, S., M. Tobita, and Y. Nakahori (1991). "Detection of Philippine Sea plate motion by very long baseline interferometry." *Geophysical Research Letters*, Vol. 18, No. 8, pp. 1417-1419.

McCarthy, D.D. (Ed.) (1996). *IERS Conventions*. IERS Technical Note 21, Central Bureau of IERS, Observatoire de Paris, Paris.

Mendes, V.B. and R.B. Langley (1993). "Application of the Global Positioning System to the assessment of crustal deformation in the Charlevoix seismic zone." *Proceedings of ION GPS-93, the Sixth International Technical Meeting of the Satellite Division of The Institute of Navigation*, Salt Lake City, Utah, 22-24 September, The Institute of Navigation, Alexandria, Va., Vol. II, pp. 1205-1219.

Mendes, V.B., P. Collins, and R.B. Langley (1995). "The effect of tropospheric propagation delay errors in airborne GPS precision positioning." *Proceedings of ION GPS-95, the 8th International Technical Meeting of the Satellite Division of The Institute of Navigation*, Palm Springs, Calif., 12-15 September, pp. 1681-1689.

Meteorological Office (MO) (1991). *Meteorological Glossary*. 6th ed., HMSO, London.

Miller, A. and J.C. Thompson (1979). *Elements of Meteorology*. 3rd ed., Charles E. Merril Publishing Company, Toronto.

Mironov, N.T. (1993). "Correction of satellite laser ranging for atmospheric refraction." *Artificial Satellites, Planetary Geodesy No. 20*, Vol. 28, No. 3, pp. 171-177.

Mironov, N.T., K. Linkwitz, and J. Bahndorf (1993). "Wet component of tropospheric delay for microwaves from surface meteorological data." *Artificial Satellites, Planetary Geodesy No. 20*, Vol. 28, No. 3, pp. 151-170.

Mitrovica, J.X., J.L. Davis, and I.I. Shapiro (1993). "Constraining proposed combinations of ice history and earth rheology using VLBI determined baseline length rates in North America." *Geophysical Research Letters*, Vol. 20, No. 21, pp. 2387-2390.

Moffett, J.B. (1973). "Program requirements for two-minute integrated Doppler satellite navigation solution." Technical Memorandum TG 819-1 (rev. 2), The Johns Hopkins University, Applied Physics Laboratory, Silver Spring, Md.

Murray, F.W. (1967). "On the computation of saturation vapor pressure." *Journal of Applied Meteorology*, Vol. 6, pp. 203-204.

Nam, Y.S., D. Kuang, and B.E. Schutz (1996). "Comparison of GPS estimates of wet tropospheric delays with WVR measurements." *Proceedings of ION GPS-96, the 9th International Technical Meeting of the Satellite Division of The Institute of Navigation*, Kansas City, Mo., 17-20 September, pp. 641-646.

National Oceanic and Atmospheric Administration (NOAA) (1962). *U.S. Standard Atmosphere Supplements, 1962*. U.S. Government Printing Office, Washington, D.C.

National Oceanic and Atmospheric Administration, National Aeronautics and Space Administration, and United States Air Force (NOAA/NASA/USAF) (1976). *U.S. Standard Atmosphere, 1976*. U.S. Government Printing Office, Washington, D.C., NOAA-S/T 76-1562.

North Atlantic Treaty Organization (NATO) (1993). Standardization Agreement (STANAG) Doc. 4294 EL (Edition 1), Appendix 6 to Annex A, pp. A-6-34 – A-6-37. North Atlantic Treaty Organization, Brussels.

Niell, A.E. (1994). Personal communication. MIT Haystack Observatory, Westford, MA, April.

Niell, A.E. (1996). "Global mapping functions for the atmosphere delay at radio wavelengths." *Journal of Geophysical Research*, Vol. 101, No. B2, pp. 3227-3246.

Owens, J.C. (1967). "Optical refractive index of air: Dependence on pressure, temperature and composition." *Applied Optics,* Vol. 6, No. 1, pp. 51-59.

Pan, M. and L.E. Sjöberg (1993). "Baltic sea level project with GPS." *Bulletin Géodésique*, Vol. 67, No. 1, pp. 51-59.

Parker, D.E. and D.I. Cox (1995). "Towards a consistent global climatological rawinsonde data-base." *International Journal of Climatology*, Vol. 15, pp. 473-496.

Peixoto, J.P. (1987). *O Sistema Climático e as Bases Físicas do Clima*. Gabinete de Estudos e Planeamento da Administração do Território, Secretaria de Estado do Ambiente e dos Recursos Naturais, Ministério do Plano e da Administração do Território, Lisboa.

Peixoto, J.P. and A.H. Oort (1992). *Physics of Climate*. American Institute of Physics, New York.

Peiyuan, X. (1992). "Water vapor radiometer for Chinese VLBI and GPS geodesy." *Proceedings of Symposium on Refraction of Transatmospheric Signals in Geodesy,* Eds. J.C. de Munck, T.A. Th. Spoelstra, The Hague, The Netherlands, 19-22 May, Netherlands Geodetic Commission, Publications on Geodesy, Delft, The Netherlands, No. 36, New Series, pp. 147-150.

Peltier, W.R. (1995). "VLBI baseline variations from the ICE-4G model of postglacial rebound." *Geophysical Research Letters*, Vol. 22, No. 4, pp. 465-468.

Peltier, W.R. (1996). "Global sea level rise and glacial isostatic adjustment: An analysis of data from the east coast of North America." *Geophysical Research Letters*, Vol. 23, No. 7, pp. 717-720.

Press, W.H., B.P. Flannery, S.A. Teukolsky, and W.T. Vetterling (1989). *Numerical Recipes - The Art of Scientific Computing*. Cambridge University Press, New York.

Rahnemoon, M. (1988). *Ein neues Korrekturmodell für Mikrowellen – Entfernungsmessungen zu Satelliten*. Dr.-Ing. Dissertation, Bayerischen Akademie der Wissenschaften, Deutsche Geodätische Kommission, Reihe C, Heft Nr. 335, München.

Rasmussen, L.A. (1978). "On the approximation of saturation vapor pressure." *Journal of Applied Meteorology*, Vol. 17, pp. 1564-1565.

Ray, J.R. (1996). "Measurements of length of day using the Global Positioning System." *Journal of Geophysical Research*, Vol. 101, No. B9, pp. 20,141-20,149.

Reid, M.J. and J.M. Moran (Eds.) (1988). *The Impact of VLBI on Astrophysics and Geophysics*. Proceedings of the 129th Symposium of the IAU, Cambridge, Mass., May 10-15, 1987, Kluwer Academic Publishers, Dordrecht.

Reilinger, R.E., S.C. McClusky, M.B. Oral, R.W. King, M.N. Toksoz, A.A. Barka, I. Kinik, O. Lenk, and I. Sanli (1997). "Global Positioning System measurements of present-day crustal movements in the Arabia-Africa-Eurasia plate collision zone." *Journal of Geophysical Research,* Vol. 102, No. B5, pp. 9983-9999.

Rennick, M.A. (1977). "The parameterization of tropospheric lapse rates in terms of surface temperature." *Journal of the Atmospheric Sciences*, Vol. 34, No. 6, pp. 854-862.

Resch, G.M. (1984). "Water vapor radiometry in geodetic applications." Chapter E in *Geodetic Refraction Effects of Electromagnetic Wave Propagation Through the Atmosphere,* Ed. F.K. Brunner, Springer-Verlag, New York, pp. 53-84.

Riegel, C.A. (1974). "Comments on «A simple but accurate formula for the saturation vapor pressure over liquid water» – 1." *Journal of Applied Meteorology*, Vol. 13, pp. 606-607.

Rignot, E. (1996). "Dual-frequency interferometric SAR observations of a tropical rain-forest." *Geophysical Research Letters*, Vol. 23, No. 9, pp. 993-996.

Robinson, S.E. (1988). "The profile algorithm for microwave delay estimation from water vapor radiometer data." *Radio Science*, Vol. 23, No. 3, pp. 401-408.

Rocken, C., J.M. Johnson, R.E. Neilan, M. Cerezo, J.R. Jordan, M.J. Falls, L.D. Nelson, R.H. Ware, and M. Hayes (1991). "The measurement of atmospheric water vapor: Radiometer comparison and spatial variations." *IEEE Transactions on Geoscience and Remote Sensing,* Vol. GE-29, No. 1, pp. 3-8.

Rocken, C., T. van Hove, J. Johnson, F. Solheim, R. Ware, M. Bevis, S. Chiswell, and S. Businger (1995). "GPS/STORM – GPS sensing of atmospheric water vapor for meteorology." *Journal of Atmospheric and Oceanic Technology*, Vol. 12, pp. 468-478.

Rogers, A.E.E. (1990). "The accuracy of position determination by VLBI expected by the year 2000." In *Geodesy in the Year 2000.* Committee on Geodesy, Board on Earth Sciences and Resources, Commission on Physical Sciences, Mathematics, and Resources, National Research Council, National Academy Press, Washington, D.C., pp. 114-123.

Rogers, A.E.E., R.J. Cappallo, B.E. Corey, H.F. Hinteregger, A.E. Niell, R.B. Phillips, D.L. Smythe, A.R. Whitney, T.A. Herring, J.M. Bosworth, T.A. Clark, C. Ma, J.W. Ryan, J.L. Davis, I.I. Shapiro, G. Elgered, K. Jaldehag, J.M. Johansson, B.O. Rönnäng, W.E. Carter, J.R. Ray, D.S. Robertson, T.M. Eubanks, K.A. Kingham, R.C. Walker, W.E. Himwich, C.E. Kuehn, D.S. MacMillan, R.I. Potash, D.B. Shaffer, N.R. Vandenberg, J.C. Webber, R.L. Allshouse, B.R. Schupler, and D. Gordon (1993). "Improvements in the accuracy of geodetic VLBI." In Contributions of Space Geodesy to Geodynamics: Technology, Eds. D.E. Smith and D.L. Turcotte, Geodynamics Series, Vol. 25, American Geophysical Union, Washington, DC, pp. 47-63.

Rogers, R.R. and M.K. Yau (1989). *A Short Course in Cloud Physics.* 3rd ed. Pergamon Press, New York.

Ruf, C.S., S.J. Keihm, and M.A. Janssen (1995). "TOPEX/Poseidon microwave radiometer (TMR): I. Instrument description and antenna temperature calibration." *IEEE Transactions on Geoscience and Remote Sensing*, Vol. GE-33, No. 1, pp. 125-137.

Saastamoinen, J. (1973). "Contributions to the theory of atmospheric refraction." In three parts. *Bulletin Géodésique*, No. 105, pp. 279-298; No. 106, pp. 383-397; No. 107, pp. 13-34.

Santerre, R. (1987). "Modification to the Goad and Goodman tropospheric refraction model." Unpublished internal report of the Department of the Surveying Engineering, University of New Brunswick, Fredericton, New Brunswick, Canada.

Schäfer, W. and W. Schumann (1995). "PRARE-2 - Building on the lessons learnt from ERS-1." *ESA Bulletin*, No. 83, pp. 38-40.

Schelleng, J.C., C.R. Burrows, and E.B. Ferrell (1933). "Ultra-short-wave propagation." *Proceedings of the Institute of Radio Engineers,* Vol. 21, pp. 427-463.

Schlüter, W., R. Dassing, K-H Haufe, S. Riepl, W. Maier, and U. Schreiber (1993). "First results with two-colour satellite laser ranging at the Fundamentalstation Wettzell." In *Geodesy and Physics of the Earth*, Eds. H. Montag and C. Reigber, Proceedings of the International Association of Geodesy Symposium 112, Potsdam, October 5-10, 1992, Springer-Verlag, pp. 56-60.

Schmidlin, F.J., J.J. Olivero, and M.S. Nestler (1982). "Can the standard radiosonde system meet special atmospheric research needs?" *Geophysical Research Letters*, Vol. 9, No. 9, pp. 1109-1112.

Schroeder, J.A. and E.R. Westwater (1991). "Users' guide to WPL microwave radiative transfer software." NOAA Technical Memorandum ERL WPL-213, Wave Propagation Laboratory, Boulder, Colo.

Schwartz, B.E. and C. A. Doswell III (1991). "North American rawinsonde observations: Problems, concerns, and a call to action." *Bulletin of the American Meteorological Society*, Vol. 72, No. 12, pp. 1885-1896.

Seeber, G. (1993). *Satellite Geodesy: Foundations, Methods, and Applications*. Walter de Gruyter, New York.

Shapiro, M.A. (1980). "Turbulent mixing within tropopause folds as a mechanism for the exchange of chemical constituents between the stratosphere and the troposphere." *Journal of Atmospheric Sciences*, Vol. 37, No. 5, pp. 994-1004.

Shi, J. and M.E. Cannon (1995). "Critical error effects and analysis in carrier phase-based airborne GPS positioning over large areas." *Bulletin Géodésique*, Vol. 69, No. 4, pp. 261-273.

Sierk, B., B. Bürki, H. Becker-Ross, S. Florek, R. Neubert, L.P. Kruse, and H.-G. Kahle (1997). "Tropospheric water vapor derived from solar spectrometer, radiometer, and GPS measurements." *Journal of Geophysical Research*, Vol. 102, No. B10, pp. 22,411-22,424.

Smith, E.K. and S. Weintraub (1953). "The constants in the equation for atmospheric refractive index at radio frequencies." *Proceedings of the Institute of Radio Engineers,* Vol. 4, pp. 1035-1037.

Smith, W.L. (1966). "Note on the relationship between total precipitable water and surface dew point." *Journal of Applied Meteorology,* Vol. 5, pp. 726-727.

Solheim, F.S. (1993). "Use of pointed water vapor radiometer observations to improve vertical GPS surveying accuracy." Ph.D. dissertation, Department of Physics, University of Colorado, Boulder, Colo.

Soudarin, L. and A. Cazenave (1995). "Large-scale tectonic plate motions measured with the DORIS space geodesy system." *Geophysical Research Letters*, Vol. 22, No. 4, pp. 469-472.

Sovers, O.J. and C.S. Jacobs (1996). "Observation model and parameter partials for the JPL VLBI parameter estimation software "MODEST" – 1996", JPL Publication 83-39, Rev. 6, Jet Propulsion Laboratory, California Institute of Technology, Pasadena, Calif.

Stone, P.H. and J.H. Carlson (1979). "Atmospheric lapse rate regimes and their parameterization." *Journal of the Atmospheric Sciences*, Vol. 36, No. 3, pp. 415-423.

Strang, G. and K. Borre (1997). *Linear Algebra, Geodesy, and GPS*. Wellesley-Cambridge Press, Wellesley, Mass..

Tabata, S. (1973). "A simple but accurate formula for the saturation vapor pressure over liquid water." *Journal of Applied Meteorology*, Vol. 12, pp. 1410-1411.

Tabei, T., T. Ozawa, Y. Date, K. Hirahara, and T. Nakano (1996). "Crustal deformation at the Nankai subduction zone, southwest Japan, derived from GPS measurements." *Geophysical Research Letters*, Vol. 23, No. 21, pp. 3059-3062.

Tarayre, H. and D. Massonnet (1996). "Atmospheric propagation heterogeneities revealed by ERS-1 interferometry." *Geophysical Research Letters*, Vol. 23, No. 9, pp. 989-992.

Thayer, G.D. (1967). "A rapid and accurate ray tracing algorithm for a horizontally stratified atmosphere." *Radio Science*, Vol. 1, No. 2, pp. 249-252.

Thayer, G.D. (1974). "An improved equation for the radio refractive index of air." *Radio Science,* Vol. 9, No. 10, pp. 803-807.

Thompson, A.R., J.M. Moran, and G.W. Swenson (1986). *Interferometry and Synthesis in Radio Astronomy*. John Wiley & Sons, New York.

Thuburn, J. and G. Craig (1997). "GCM tests of theories for the height of the tropopause." *Journal of Atmospheric Sciences*, Vol. 54, No. 7, pp. 869-882.

Tralli, D.M. and S.M. Lichten (1990). "Stochastic estimation of tropospheric path delays in Global Positioning System geodetic measurements." *Bulletin Géodésique*, Vol. 64, No. 2, pp. 127-159.

Tralli, D.M. and T.H. Dixon (1988). "A few parts in 10^8 geodetic baseline repeatability in the Gulf of California using the Global Positioning System." *Geophysical Research Letters*, Vol. 15, No. 4, pp. 353-356.

Tralli, D.M., S.M. Lichten, and T.A. Herring (1992). "Comparison of Kalman filter estimates of zenith atmospheric path delays using the Global Positioning System and very long baseline interferometry." *Radio Science,* Vol. 27, No. 6, pp. 999-1007.

Treuhaft, R.N. (1992). "Tropospheric and charged particle propagation errors in very long baseline interferometry." *Proceedings of Symposium on Refraction of Transatmospheric Signals in Geodesy*, Eds. J.C. de Munck, T.A.Th. Spoelstra, The Hague, The Netherlands, 19-22 May, Netherlands Geodetic Commission, Publications on Geodesy, Delft, The Netherlands, No. 36, New Series, pp. 45-53.

Trupin, A.S., D.A. Easson, and D. Han (1996). "Vertical motion and ice thickness variation in western North America." *Geophysical Research Letters*, Vol. 23, No. 3, pp. 253-256.

Tushingham, A.M. (1991). "Potential effects of ongoing postglacial adjustment on very long baseline interferometry measurements." *Geophysical Research Letters*, Vol. 18, No. 7, pp. 1281-1284.

Vaisala (1996). RS80 Radiosondes. Ref. A571en 1996-01,Vaisala Oy, Finland.

Valley, S.L. (Ed.) (1965). *Handbook of Geophysics and Space Environments*. McGraw-Hill Book Company, New York.

van der Wal, A.D. (1995). *Evaluation of Strategies for Estimating Residual Neutral-Atmosphere Propagation Delay in High Precision Global Positioning System Data Analysis*. M.Sc.E. thesis, Department of Geodesy and Geomatics Engineering Technical Report No. 177, University of New Brunswick, Fredericton, New Brunswick, Canada.

Vanícek, P. and E. Krakiwsky (1986). *Geodesy: The Concepts*. 2nd ed., Elsevier Science Publishers, Amsterdam.

Varghese, T., C. Clarke, T. Oldham, and M. Selden (1993). "Streak camera based SLR receive system for high accuracy multiwavelength atmospheric differential delay measurements." In *Contributions of Space Geodesy to Geodynamics: Technology*, Eds. D.E. Smith, and D.L. Turcotte. American Geophysical Union, Washington, D.C., Geodynamics Series, Vol. 25, pp. 163-173.

von Roos, O.H. (1971). "Tropospheric and ionospheric range corrections for an arbitrary inhomogeneous atmosphere (first-order theory)." Jet Propulsion Laboratory, California Institute of Technology, Pasadena, Calif., JPL Technical Report 32-1526, Vol. VI, pp. 99-105.

Wachowski, H.M. (1973). "A model for correcting radar tracking data for the effects of tropospheric refraction." Aerospace Report No. TOR-0074(4461-02)-4, The Aerospace Corporation, El Segundo, Calif.

Wachowski, H.M. (1980). "A program for the computation of tropospheric range corrections from meteorological data." Aerospace Report No. TOR-0080(5473-04)-6, The Aerospace Corporation, El Segundo, Calif.

Wallace, J.M. and P.V. Hobbs (1977). *Atmospheric Science : An Introductory Survey*. Academic Press, New York.

Walter, S.J. and P.L. Bender (1992). "The slant path atmospheric refraction calibrator: An instrument to measure the microwave propagation delays induced by atmospheric water vapor." *IEEE Transactions on Geoscience and Remote Sensing*, Vol. GE-30, No. 3, pp. 462-471.

Ward, S.N. (1990). "Pacific-North America plate motions: New results from very long baseline interferometry." *Journal of Geophysical Research*, Vol. 95, No. B13, pp. 21,965-21,981.

Ware, R., C. Alber, C. Rocken, and F. Solheim (1997). "Sensing integrated water vapor along GPS ray paths." *Geophysical Research Letters*, Vol. 24, No. 4, pp. 417-420.

Wells, D., N. Beck, D. Delikaraoglou, A. Kleusberg, E.J. Krakiwsky, G. Lachapelle, R.B. Langley, M. Nakiboglou, K.P. Schwarz, J. Tranquilla, and P. Vanícek (1986). *Guide to GPS Positioning*. Canadian GPS Associates, Fredericton, New Brunswick.

Wells, D.E. (1974). "Doppler satellite control." Ph.D. dissertation, Department of Surveying Engineering Technical Report No. 29, University of New Brunswick, Fredericton, New Brunswick.

Westwater, E.R., M.J. Falls, and I.A.P. Fotino (1989). "Ground-based microwave radiometric observations of precipitable water vapor: A comparison with ground truth from two radiosonde observing systems." *Journal of Atmospheric and Oceanic Technology*, Vol. 6, No. 4, pp. 724-730.

Wexler, A. (1976). "Vapor pressure formulation for water in range 0 to 100 °C. A revision." *Journal of Research of the National Bureau of Standards - A. Physics and Chemistry*, Vol. 80A, Nos. 5 and 6, pp. 775-785.

Wexler, A. (1977). "Vapor pressure formulation for ice." *Journal of Research of the National Bureau of Standards - A. Physics and Chemistry*, Vol. 81A, No. 1, pp. 5-20.

Whitney, A.R., A.E.E. Rogers, H.F. Hinteregger, C.A. Knight, J.I. Levine, S. Lippincott, T.A. Clark, I.I. Shapiro, and D.S. Robertson (1976). "A very-long-baseline interferometer system for geodetic applications." *Radio Science*, Vol. 11, No. 5, pp. 421-432.

Wigley, T.M.L. (1974). "Comments on «A simple but accurate formula for the saturation vapor pressure over liquid water» – 3." *Journal of Applied Meteorology*, Vol. 13, p. 608.

Williams, C.R., T. Arnadottir, and P. Segall (1993). "Coseismic deformation and dislocation models of the 1989 Loma Prieta earthquake derived from Global Positioning System measurements." *Journal of Geophysical Research*, Vol. 98, No. B3, pp. 4567-4578.

Willis, P., C. Boucher, M. Kasser, R. Biancale, A. Cazenave, M. Dorrer, and F. Nouël (1990). "The DORIS satellite radio tracking system: Status and plans." In *Global Positioning System: An Overview,* Proceedings of International Association of Geodesy Symposium No. 102, Eds. Y. Bock, and N. Leppard, Edinburgh, Scotland, 7-8 August 1989, Springer-Verlag, New York, pp. 391-399.

World Meteorological Organization (WMO) (1986a). "WMO catalogue of radiosondes and upper-air wind systems in use by members." Instruments and Observing Methods Report No. 27, WMO/TD-No. 176, Geneva.

World Meteorological Organization (WMO) (1986b). "Atmospheric ozone 1985." WMO Report No. 16, Geneva.

World Meteorological Organization (WMO) (1987a). "WMO Assmann aspiration psychrometer intercomparison (Potsdam, GDR, 1987): Final report (D. Sonntag)" Instruments and Observing Methods Report No. 34, WMO/TD-No. 289, Geneva.

World Meteorological Organization (WMO) (1987b). "WMO international radiosonde comparison (UK, 1984, USA, 1985): Final report (J. Nash and F.J. Schmidlin)." Instruments and Observing Methods Report No. 30, WMO/TD-No. 195, Geneva.

World Meteorological Organization (WMO) (1993). "Historical changes in radiosonde instruments and practices: Final report (D.J. Gaffen)." Instruments and Observing Methods Report No. 50, WMO/TD-No. 541, Geneva.

World Meteorological Organization (WMO) (1995). *Scientific Assessment of Ozone Depletion: 1994.* WMO Global Ozone Research and Monitoring Project, Report No. 37, Geneva.

World Meteorological Organization (WMO) (1996a). *Guide to Meteorological Instruments and Methods of Observation.* 6th ed., WMO-No. 8, Secretariat of the World Meteorological Organization, Geneva.

World Meteorological Organization (WMO) (1996b). "WMO international radiosonde comparison - Phase IV: Final report (S. Yagi, A. Mita, and N. Inoue)." Instruments and Observing Methods Report No. 59, WMO/TD-No. 742, Geneva.

Wu, S.C. (1979). "Optimum frequencies of a passive microwave radiometer for tropospheric path-length correction." *IEEE Transactions on Antennas and Propagation*, Vol. AP-27, No. 2, pp. 233-239.

Yan, H. (1996). "A new expression for astronomical refraction." *The Astronomical Journal*, Vol. 112, No. 3, pp. 1312-1316.

Yan, H. (1998). Personal communication. Shanghai Astronomical Observatory, Shanghai, China, March.

Yan, H. and J. Ping (1995). "The generator function method of the tropospheric refraction corrections." *The Astronomical Journal*, Vol. 110, No. 2, pp. 934-939.

Yionoulis, S.M. (1970). "Algorithm to compute tropospheric refraction effects on range measurements." *Journal of Geophysical Research*, Vol. 75, No. 36, pp. 7636-7637.

Zieger, A.R., G.C. Cleven, E.S. Davis, F.S. Soltis, and C.L. Purdy (1995). "Satellite/Sensors for monitoring earth's oceans from space." *Marine Geodesy*, Vol. 18, pp. 1-24.

APPENDIX I

Integral solution of the neutral-atmosphere propagation delay

Any point on the ray path can be uniquely defined by a set of generalized coordinates, such as the spherical coordinates. If we assume a spherically symmetric atmosphere, for which the properties are only a function of the radial variable, two spherical coordinates are needed: the geocentric radius, *r*, and geocentric angle, $\phi = \phi(r)$. Hence, expressing the differential element *ds* in terms of the spherical coordinates leads to (see Figure I.1):

$$ds = \sqrt{dr^2 + r^2 d\phi^2} \tag{I.1}$$

or

$$ds = \sqrt{1 + r^2 \left(\frac{d\phi}{dr}\right)^2}\, dr. \tag{I.2}$$

Denoting $\phi' = \phi'(r) = \frac{d\phi}{dr}$, we write equivalently:

$$ds = \sqrt{1 + r^2 \phi'^2}\, dr. \tag{I.3}$$

Substituting Equation (I.3) into the variational equation for Fermat's principle,

$$\delta \int_{ray} n\, ds = 0,$$

we get the variational:

$$\delta \int_{ray} n\sqrt{1 + r^2 \phi'^2}\, dr = 0, \tag{I.4}$$

where the refractive index is now expressed as a function of the geocentric radius, $n = n(r)$. The problem can be solved applying the Euler-Lagrange equation:

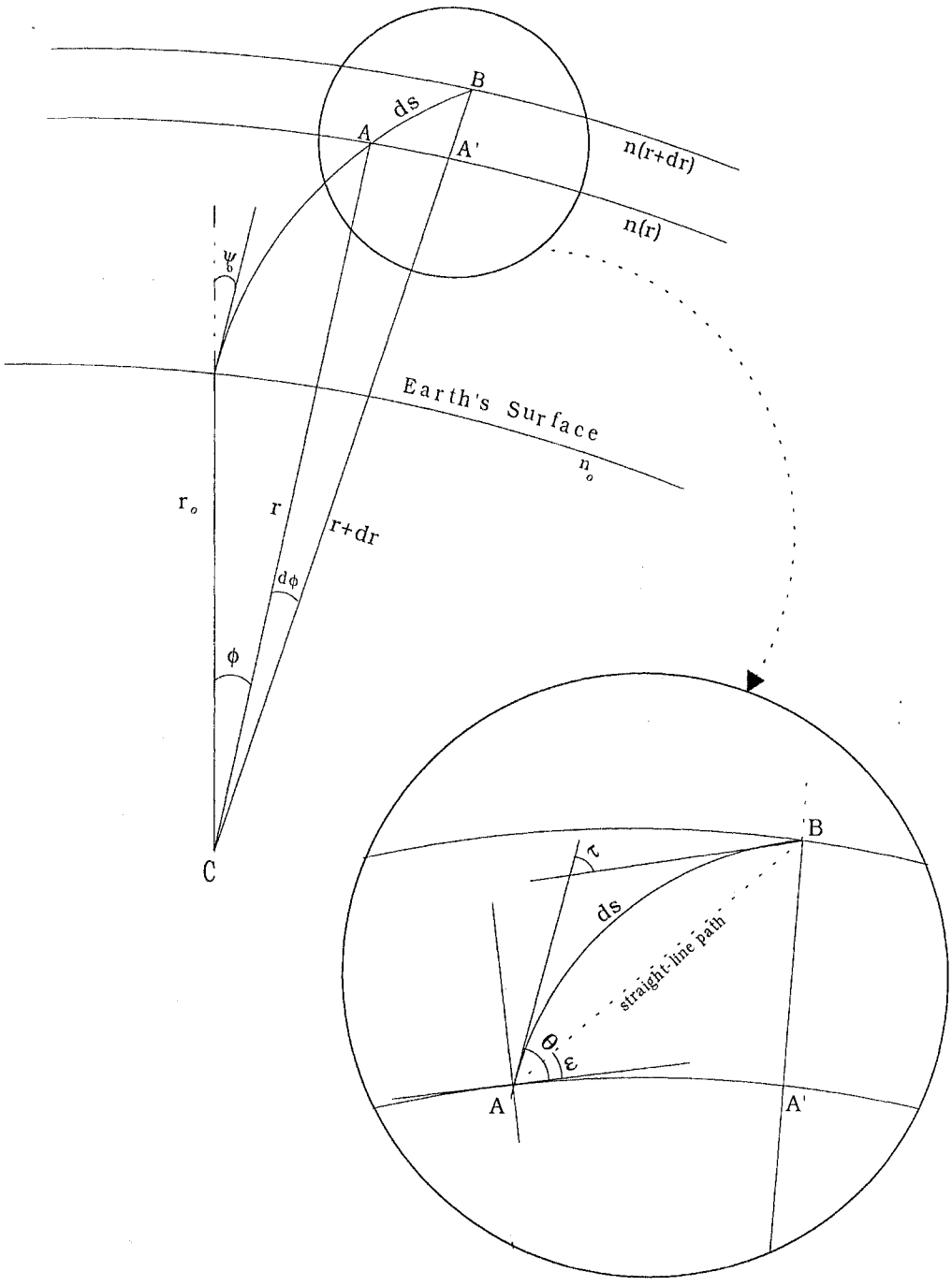

Figure I.1 – The ray trace geometry

$$\frac{d}{dr}\left(\frac{\partial \mathcal{L}}{\partial \phi'}\right)-\frac{\partial \mathcal{L}}{\partial \phi}=0, \tag{I.5}$$

where $\mathcal{L}$ is the Lagrangian:

$$\mathcal{L}(\phi,\phi',r)=n\sqrt{1+r^2\phi'^2}\ . \tag{I.6}$$

Expanding Equation (I.5), we get:

$$\frac{d}{dr}\left(\frac{nr^2\phi'}{\sqrt{1+r^2\phi'^2}}\right)-\frac{\partial \mathcal{L}}{\partial \phi}=0 \tag{I.7}$$

or, as the Lagrangian $\mathcal{L}$ is independent of ϕ:

$$\frac{d}{dr}\left(\frac{nr^2\phi'}{\sqrt{1+r^2\phi'^2}}\right)=0, \tag{I.8}$$

that is,

$$\frac{nr^2\phi'}{\sqrt{1+r^2\phi'^2}}=K, \tag{I.9}$$

where K is a constant to be determined.

Therefore, let's consider the triangle ABC, shown in Fig. I.1. Applying the sine law, we have:

$$\frac{\sin(\psi-d\phi)}{r}=\frac{\sin\psi}{r+dr} \tag{I.10}$$

where ψ is the angle between the radial vector and the tangent to the ray (zenith angle), at the position (r,ϕ), dr and dϕ are respectively the differential geocentric radius and angle, when the ray travels from B to A. Noting that

$$\frac{1}{r+dr} \cong \frac{1}{r}\left(1-\frac{dr}{r}\right) \tag{I.11}$$

and

$$\sin(\psi - d\phi) \cong \sin\psi - d\phi\cos\psi\,, \tag{I.12}$$

we write Equation (I.10) as

$$\frac{d\phi}{dr} = \frac{1}{r}\tan\psi \tag{I.13}$$

or

$$\phi' = \frac{1}{r}\tan\psi\,. \tag{I.14}$$

Using the following identity

$$\sec\psi = \sqrt{1+\tan^2\psi}\,, \tag{I.15}$$

we can express (I.14) as

$$\sin\psi = \frac{r\phi'}{\sqrt{1+\tan^2\psi}} \tag{I.16}$$

and, again from Equation (I.14)

$$\sin\psi = \frac{r\phi'}{\sqrt{1 + r^2 \phi'^2}}. \tag{I.17}$$

Substituting Equation (I.17) into Equation (I.8), we get

$$\frac{d}{dr}(n r \sin\psi) = 0 \tag{I.18}$$

that is, $nr\sin\psi$ is a constant, or

$$\boxed{nr\sin\psi = n_s r_s \sin\psi_s}, \tag{I.19}$$

where the subscript "s" denotes values at a reference position (e.g. surface level). The equation just derived can be recognized as the **Snell's law**.

From this equation, we have:

$$\sin\psi = \frac{n_s r_s \sin\psi_s}{nr}. \tag{I.20}$$

From the triangle in Figure I.1, we write:

$$ds \cong \sec\psi\, dr = \frac{dr}{\sqrt{1 - \sin^2\psi}} \tag{I.21}$$

and, from Equation (I.20),

$$ds = \frac{nr}{\sqrt{n^2 r^2 - n_s^2 r_s^2 \sin^2\psi_s}} dr. \tag{I.22}$$

To derive an expression for the geocentric angle at position (r, ϕ), we integrate both sides of Equation (I.13), the integration being performed between the reference position (e.g. a

surface level, r_s) and the top of the neutral-atmosphere (r_a), to obtain:

$$\phi = \int_{r_s}^{r_a} \frac{\tan\psi}{r} dr, \tag{I.23}$$

or

$$\phi = \int_{r_s}^{r_a} \frac{1}{r} \frac{\sin\psi}{\sqrt{1-\sin^2\psi}} dr \tag{I.24}$$

and finally, using Equation (I.20)

$$\phi = \int_{r_s}^{r_a} \frac{1}{r} \frac{n_s r_s \sin\psi_s}{\sqrt{n^2 r^2 - n_s^2 r_s^2 \sin^2\psi_s}} dr \tag{I.25}$$

or

$$\phi = n_s r_s \sin\psi_s \int_{r_s}^{r_a} \frac{1}{r} \frac{1}{\sqrt{n^2 r^2 - n_s^2 r_s^2 \sin^2\psi_s}} dr. \tag{I.26}$$

The integral expression for the excess path delay, ΔL, is obtained by substitution of Equation (I.22) into the integral $\int_{ray} (n-1)\, ds$; we get:

$$\Delta L = \int_{ray} (n-1)\, ds = \int_{r_s}^{r_a} \frac{(n-1)nr}{\sqrt{n^2 r^2 - n_s^2 r_s^2 \sin^2\psi_s}}\, dr \tag{I.27}$$

Likewise, the integral expression for geometric length of the ray path is given by:

$$S = \int_{ray} ds = \int_{r_s}^{r_a} \frac{nr}{\sqrt{n^2 r^2 - n_s^2 r_s^2 \sin^2\psi_s}} dr \tag{I.28}$$

The last integral expression to be evaluated concerns the geometric path, G. As the integration is performed in vacuum, the refractive index at every point along the ray path is equal to unity; the angle between the radial vector and the ray is now a non-refracted (geometric or true) zenith angle (or distance), Z. Therefore, the integral expression sought is given by:

$$G = \int_{vac} ds = \int_{r_s}^{r_a} \frac{r}{\sqrt{r^2 - r_s^2 \sin^2 Z}} dr \tag{I.29}$$

Finally, by substitution of (I.27), (I.28), and (I.29) into the equation defining the neutral-atmosphere propagation delay:

$$d_{na} = \int_{ray} (n-1) ds + \left[\int_{ray} ds - \int_{vac} ds \right] = \Delta L + [S - G]$$

we get the complete integral expression:

$$\boxed{d_{na} = \int_{r_s}^{r_a} \frac{(n-1)nr}{\sqrt{n^2 r^2 - n_0^2 r_0^2 \sin^2 \psi_0}} dr + \int_{r_s}^{r_a} \left(\frac{nr}{\sqrt{n^2 r^2 - n_0^2 r_0^2 \sin^2 \psi_0}} - \frac{r}{\sqrt{r^2 - r_0^2 \sin^2 Z}} \right) dr} \tag{I.30}$$

Using elevation angles rather than zenith angles, the equivalent expression is:

$$\boxed{d_{na} = \int_{r_s}^{r_a} \frac{(n-1)nr}{\sqrt{n^2 r^2 - n_0^2 r_0^2 \cos^2 \theta_0}} dr + \int_{r_s}^{r_a} \left(\frac{nr}{\sqrt{n^2 r^2 - n_0^2 r_0^2 \cos^2 \theta_0}} - \frac{r}{\sqrt{r^2 - r_0^2 \cos^2 \varepsilon}} \right) dr} \tag{I.31}$$

where θ is the refracted (apparent) elevation angle and ε is the geometric (true) elevation angle.

APPENDIX II

Mathematical structure of selected models

Mathematical structure of selected mapping functions and hybrid models.

- CfA-2.2 [Davis et al., 1985]
- Ifadis [Ifadis, 1986]
- Lanyi [Lanyi, 1984]
- MTT [Herring, 1992]
- NMF [Niell, 1996]
- UNSW931 [Yan and Ping, 1995]
- Altshuler and Kalaghan [Altshuler and Kalaghan, 1974]
- NATO [NATO, 1993]
- WAAS [DeCleene, 1995]

Mathematical model:

$$m_{h,nh}(\varepsilon) = \frac{1}{\sin\varepsilon + \dfrac{a}{\tan\varepsilon + \dfrac{b}{\sin\varepsilon + c}}},$$

where:

$$a = 0.001185\left\{1 + 0.6071\times10^{-4}(P_s - 1000) - 0.1471\times10^{-3}e_s + 0.3072\times10^{-2}(t_s - 20) + 0.01965(6.5 - \alpha) - 5.645\times10^{-6}(H_t - 11231)\right\}$$

$$b = 0.001144\left\{1 + 0.1164\times10^{-4}(P_s - 1000) + 0.2795\times10^{-3}e_s + 0.3109\times10^{-2}(t_s - 20) + 0.03038(6.5 - \alpha) - 1.217\times10^{-5}(H_t - 11231)\right\}$$

$c = -0.0090$.

Comment: *The mapping function was designed for the hydrostatic component only, but may be used for the non-hydrostatic component also.*

Symbols and Units

$m_{h,nh}$	hydrostatic (non-hydrostatic) mapping function (unitless)
ε	elevation angle (rad)
P_s	surface total pressure (hPa)
e_s	water vapor pressure (hPa)
t_s	surface temperature (°C)
α	temperature lapse rate ($K\,km^{-1}$)
H_t	tropopause height (m)

Mathematical model:

$$m_i(\varepsilon) = \frac{1 + \dfrac{a_i}{1 + \dfrac{b_i}{1 + c_i}}}{\sin\varepsilon + \dfrac{a_i}{\sin\varepsilon + \dfrac{b_i}{\sin\varepsilon + c_i}}},$$

where, for i = h (hydrostatic mapping function),

$$a_h = 0.001237 + 0.1316\times10^{-6}(P_s - 1000) + 0.1378\times10^{-5}(t_s - 15) + 0.8057\times10^{-5}\sqrt{e_s}$$

$$b_h = 0.003333 + 0.1946\times10^{-6}(P_s - 1000) + 0.1040\times10^{-6}(t_s - 15) + 0.1747\times10^{-4}\sqrt{e_s}$$

$$c_h = 0.078;$$

for i = nh (non-hydrostatic mapping function),

$$a_{nh} = 0.0005236 + 0.2471\times10^{-6}(P_s - 1000) - 0.1724\times10^{-6}(t_s - 15) + 0.1328\times10^{-4}\sqrt{e_s}$$

$$b_{nh} = 0.001705 + 0.7384\times10^{-6}(P_s - 1000) + 0.3767\times10^{-6}(t_s - 15) + 0.2147\times10^{-4}\sqrt{e_s}$$

$$c_{nh} = 0.05917.$$

Comment: *the coefficients for the b_h term are incorrect in some publications. The ones listed here agree with the original publication and have been confirmed by Ioannis Ifadis (personal communication, Aristotle University of Thessaloniki - School of Engineering, June, 1994). Optimized climate-dependent mapping functions were also developed by Ifadis [1986].*

$m_{h,nh}$	hydrostatic (non-hydrostatic) mapping function (unitless)
ε	elevation angle (rad)
P_s	surface total pressure (hPa)
e_s	water vapor pressure (hPa)
t_s	surface temperature (°C)

Mathematical model:

$$d_{trop} = \frac{F(\varepsilon)}{\sin \varepsilon},$$

where:

$$F(\varepsilon) = d_d^z \, F_d(\varepsilon) + d_w^z \, F_w(\varepsilon) + \frac{1}{\Delta}\left[\left(d_d^z\right)^2 F_{bend1}(\varepsilon) + 2 d_d^z \cdot d_w^z F_{bend2}(\varepsilon) + \left(d_w^z\right)^2 F_{bend3}(\varepsilon)\right] + \frac{1}{\Delta^2}\left(d_d^z\right)^3 F_{bend4}(\varepsilon)$$

$$\Delta = \frac{kT_o}{mg_e}$$

$$F_d(\varepsilon) = A_{10}(\varepsilon)\, G\left(\lambda M_{110}, u\right) + \frac{3}{2}\sigma u \, M_{210} G^3\left(M_{110}, u\right)$$

$$F_w(\varepsilon) = \frac{A_{01}(\varepsilon)\, G\left(\dfrac{\lambda M_{101}}{M_{001}}, u\right)}{M_{001}}$$

$$F_{bend1}(\varepsilon) = \frac{1}{2\tan^2 \varepsilon}\left[\frac{\sigma}{\sin^2 \varepsilon} G^3\left(M_{110}, u\right) - M_{020} G^3\left(\frac{M_{120}}{M_{020}}, u\right)\right]$$

$$F_{bend2}(\varepsilon) = -\frac{1}{2\tan^2 \varepsilon}\frac{M_{011}}{M_{001}} G^3\left(\frac{M_{111}}{M_{011}}, u\right)$$

$$F_{bend3}(\varepsilon) = -\frac{1}{2\tan^2 \varepsilon}\frac{M_{002}}{M_{001}^2} G^3\left(\frac{M_{102}}{M_{002}}, u\right)$$

$$F_{bend4}(\varepsilon) = \frac{1}{\tan^4 \varepsilon} M_{030} \, G^3\left(\frac{M_{130}}{M_{030}}, u\right)$$

$$G(q,u)=\frac{1}{\sqrt{1+qu}}$$

$$u=\frac{2\sigma}{\tan^2\varepsilon}$$

$$\sigma=\frac{\Delta}{R_c}$$

The quantities $A_{lm}(\varepsilon)$, which involve the dry (lm=10) and wet (lm=01) components of the refractivity, are defined as:

$$A_{lm}(\varepsilon)=M_{0lm}+\sum_{n=1}^{10}\sum_{k=0}^{n}(-1)^{n+k}\frac{(2n-1)!!M_{(n-k)lm}}{2^n k!(n-k)!}\left[u\left(1+\lambda u\frac{M_{1lm}}{M_{0lm}}\right)^{-1}\right]^n\left[\frac{\lambda M_{1lm}}{M_{0lm}}\right]^k,$$

where λ is a scale factor ($\lambda = 3$, for $\varepsilon < 10°$, and $\lambda = 1$, for $\varepsilon > 10°$).

The n-order moments of the dry and wet refractivities can be expressed as function of the surface-normalized dry and wet refractivity, $f_{d,w}(q), f^2_{d,w}(q)$ and $f^3_{d,w}(q)$:

$$M_{nij}=\int_0^\infty q^n\, f_d^i(q)\, f_w^i(q)\, dq$$

where n ranges from 0 to 10, i from 0 to 3, and j from 0 to 2 (not all combinations are needed).

For a three-section temperature profile model, in particular, we have:

$$M_{nij}=n!\left[\frac{1-e^{-aq_1}}{a^{n+1}}+e^{-aq_1}\left(1-\hat{T}_2^{b+n+1}(q_1,q_2)\right)\left(\prod_{i=0}^{n}\frac{\chi}{b+i+1}\right)+\frac{e^{-aq_1}\hat{T}_2^{b+n+1}(q_1,q_2)}{a^{n+1}}\right]$$

where

$$\hat{T}_2(q_1,q_2)=1-\frac{q_2-q_1}{\chi}$$

$$\chi=\frac{mg_e}{k\alpha}$$

$$q_1=\frac{h_1}{\Delta}$$

$$q_2=\frac{h_2}{\Delta}$$

The parameters a and b dependent on the powers of the refractivities i and j pertaining to the moment definitions are listed in Table II. 1.

Comment: *As pointed out in Lanyi [1984], the Saastamoinen and Black mapping functions can be obtained by neglecting the bending terms and setting some of the variables to constant values. The term* F_{bend4} *was correct for a misprint in Lanyi's original publication (see also Sovers and Jacobs [1996]).*

Table II. 1 - Dependence of the constants a and b on the dry and wet model parameters χ and β [Lanyi, 1984].

Moment type	i	j	a	b
M_{110} – dry	1	0	1	χ - 1
M_{101} – wet	0	1	β	$\beta\chi$ - 2
M_{020} - dry squared	2	0	2	2χ - 2
M_{111} - product of dry and wet	1	1	β + 1	$\beta(\chi + 1)$ - 3
M_{002} - wet squared	0	2	2β	$2\beta\chi$-4
M_{130} - dry cubed	3	0	3	3χ-3

Symbols, Units and Nominal Values (default)

d_{trop}	total neutral atmospheric propagation delay (m)
d_d^z	zenith dry delay (m)
d_w^z	zenith wet delay (m)
ε	elevation angle (rad)
T_o	average temperature of the surface layer (292 K)
m	mean molecular mass (4.8097×10^{-26} kg)
g_c	gravity acceleration at the center of gravity of the air column (9.7837 $m\,s^{-2}$)
k	Boltzmann's constant (1.380658×10^{-23} J K^{-1})
R_c	earth's radius of curvature (6 378 140 m)
α	temperature lapse rate (6.8165 $K\,km^{-1}$)
h_1	inversion height (1.25 km)
h_2	tropopause height (12.2 km)
χ	dry model parameter (5)
β	wet model parameter (3.5)
Δ	atmospheric scale height (8.567 km)
q_1	scale height-normalized inversion height (0.1459)
q_2	scale height-normalized tropopause height (1.424)

Mathematical model:

$$m_i(\varepsilon) = \cfrac{1 + \cfrac{a_i}{1 + \cfrac{b_i}{1 + c_i}}}{\sin\varepsilon + \cfrac{a_i}{\sin\varepsilon + \cfrac{b_i}{\sin\varepsilon + c_i}}},$$

where, for i = h (hydrostatic mapping function),

$$a_h = \{1.2320 + 0.0139\cos\varphi - 0.0000209H_s + 0.00215(t_s - 10)\}\times 10^{-3}$$

$$b_h = \{3.1612 - 0.1600\cos\varphi - 0.0000331H_s + 0.00206(t_s - 10)\}\times 10^{-3}$$

$$c_h = \{71.244 - 4.293\cos\varphi - 0.000149H_s - 0.0021(t_s - 10)\}\times 10^{-3};$$

for i = nh (non-hydrostatic mapping function),

$$a_{nh} = \{0.583 - 0.011\cos\varphi - 0.000052H_s + 0.0014(t_s - 10)\}\times 10^{-3}$$

$$b_{nh} = \{1.402 - 0.102\cos\varphi - 0.000101H_s + 0.0020(t_s - 10)\}\times 10^{-3}$$

$$c_{nh} = \{45.85 - 1.91\cos\varphi - 0.00129H_s + 0.015(t_s - 10)\}\times 10^{-3}.$$

Symbols and Units

$m_{h,nh}$	hydrostatic (non-hydrostatic) mapping function (unitless)
ε	elevation angle (rad)
φ	station latitude (rad)
H_s	station orthometric height (m)
t_s	surface temperature (°C)

Mathematical model:

$$m_i(\varepsilon) = \frac{1+\dfrac{a_i}{1+\dfrac{b_i}{1+c_i}}}{\sin\varepsilon+\dfrac{a_i}{\sin\varepsilon+\dfrac{b_i}{\sin\varepsilon+c_i}}} + H_s\times10^{-3}\left[\frac{1}{\sin\varepsilon} - \frac{1+\dfrac{a_{ht}}{1+\dfrac{b_{ht}}{1+c_{ht}}}}{\sin\varepsilon+\dfrac{a_{ht}}{\sin\varepsilon+\dfrac{b_{ht}}{\sin\varepsilon+c_{ht}}}}\right].$$

The second term of the right-hand-side of this equation represents an **analytic height correction to be applied to the hydrostatic component only**. The fitted parameters are for this correction term are:

$$a_{ht} = 2.53\times10^{-5}$$

$$b_{ht} = 5.49\times10^{-3}$$

$$c_{ht} = 1.14\times10^{-3}.$$

The coefficients for the hydrostatic component are functions of the station latitude and day of year (identical formulae for b and c coefficients):

$$a_h(\varphi_i, t) = a_{h_{avg}}(\varphi_i) + a_{h_{amp}}(\varphi_i)\cos\left(2\pi\frac{doy-28}{365.25}\right),$$

where $a_{h_{avg}}$ (average) and $a_{h_{amp}}$ (amplitude) are coefficients determined for the five latitudes correspondent to the U.S. Standard Atmosphere Supplements (see Table

below). For latitudes at and below 15°, the parameters are constant. The coefficients for non-tabulated latitudes are obtained by linear interpolation.

For the non-hydrostatic component, the coefficients are a function of the latitude only, and as in the case of the hydrostatic counterpart, linear interpolation is used to obtain the coefficients for non-tabulated latitudes.

Coefficients	Latitude				
	15°	30°	45°	60°	75°
$a_{h_{avg}} \times 10^3$	1.2769934	1.2683230	1.2465397	1.2196049	1.2045996
$b_{h_{avg}} \times 10^3$	2.9153695	2.9152299	2.9288445	2.9022565	2.9024912
$c_{h_{avg}} \times 10^3$	62.610505	62.837393	63.721774	63.824265	64.258455
$a_{h_{amp}} \times 10^5$	0	1.2709626	2.6523662	3.4000452	4.1202191
$b_{h_{amp}} \times 10^5$	0	2.1414979	3.0160779	7.2562722	11.723375
$c_{h_{amp}} \times 10^5$	0	9.0128400	4.3497037	84.795348	170.37206
$a_{nh} \times 10^4$	5.8021897	5.6794847	5.8118019	5.9727542	6.1641693
$b_{nh} \times 10^3$	1.4275268	1.5138625	1.4572752	1.5007428	1.7599082
$c_{nh} \times 10^2$	4.3472961	4.6729510	4.3908931	4.4626982	5.4736038

Symbols and Units

$m_{h,nh}$	hydrostatic (non-hydrostatic) mapping function (unitless)
ε	elevation angle (rad)
φ	station latitude (rad)
H_s	station orthometric height (m)
doy	day of year (UT days past January 0.0)

Mathematical model:

$$m_{h,nh}(\varepsilon) = \frac{1}{\sin\varepsilon + \dfrac{a}{I^2\csc\varepsilon + \dfrac{b}{\sin\varepsilon + \dfrac{c}{I^2\csc\varepsilon + d}}}},$$

where:

$$I = \sqrt{\frac{R_e}{2\pi}}\tan\varepsilon,$$

$$\begin{aligned} a = {} & 0.461\,398\,3 + 2.864\times10^{-5}(P_s - 1013.25) + 8.99\times10^{-6}e_s - 6.98\times10^{-6}e_s^2 \\ & - 1.0914\times10^{-4}(t_s - 15) + 1.30\times10^{-6}(t_s - 15)^2 + 9.4694\times10^{-3}(6.5 - \alpha) \\ & - 2.4946\times10^{-6}(H_t - 11\,231) + 1.8072\times10^{-10}(H_t - 11\,231)^2 \end{aligned}$$

$$\begin{aligned} b = {} & 0.827\,647\,6 + 2.056\times10^{-5}(P_s - 1013.25) + 2.382\times10^{-4}e_s - 4.76\times10^{-6}e_s^2 \\ & + 5.1125\times10^{-4}(t_s - 15) + 1.23\times10^{-6}(t_s - 15)^2 + 3.6479\times10^{-2}(6.5 - \alpha) \\ & - 1.5321\times10^{-5}(H_t - 11\,231) + 9.4802\times10^{-10}(H_t - 11\,231)^2 \end{aligned}$$

$$\begin{aligned} c = {} & 2.531\,492 + 1.093\times10^{-4}(P_s - 1013.25) + 2.6179\times10^{-3}e_s + 1.33\times10^{-5}e_s^2 \\ & + 3.7103\times10^{-3}(t_s - 15) + 4.95\times10^{-6}(t_s - 15)^2 + 0.160\,22(6.5 - \alpha) \\ & - 8.9980\times10^{-5}(H_t - 11\,231) + 4.9496\times10^{-9}(H_t - 11\,231)^2 \end{aligned}$$

$$\begin{aligned} d = {} & 47.078\,44 + 1.595\times10^{-3}(P_s - 1013.25) + 3.9026\times10^{-2}e_s + 2.41\times10^{-4}e_s^2 \\ & - 4.1713\times10^{-2}(t_s - 15) + 2.16\times10^{-4}(t_s - 15)^2 + 1.6313(6.5 - \alpha). \\ & - 9.9757\times10^{-4}(H_t - 11\,231) + 4.4528\times10^{-8}(H_t - 11\,231)^2 \end{aligned}$$

Comment: *Although not clearly stated, this mapping function is to be applied to the hydrostatic component only (Haojian Yan, personal communication, Shanghai Astronomical Observatory, March 1998).*

Symbols and Units

$m_{h,nh}$	hydrostatic (non-hydrostatic) mapping function (unitless)
ε	elevation angle (rad)
R_e	earth radius (km)
H	effective (scale) height of (dry) atmosphere (km)
P_s	surface total pressure (hPa)
e_s	water vapor pressure (hPa)
t_s	surface temperature (°C)
α	temperature lapse rate ($K\,km^{-1}$)
H_t	tropopause height (m)

Mathematical model:

$$d_{trop} = 0.3048\, f_1 f_2 f_3$$

where

$$f_1 = (g_0 + g_1\theta^{-1} + g_2\theta^{-2} + g_3\theta^{-3}) \cdot \left[g_4 + g_6(\theta - g_5)^2\right],$$

$$f_2 = \left[b_0 + b_1(H_s^{tf} + 8.6286)^{-1} + b_2(H_s^{tf} + 8.6286)^{-2} + b_3(H_s^{tf} + 8.6286)^{-3}\right],$$

$$f_3 = c_0\left[c_1(H_s^{tf} + c_0)^{-1} + c_2(H_s^{tf} + c_0) + c_3 N_s - c_4\right]\left[1 - c_5(N_s - c_6)^2\right],$$

$$N_s = a_0 + a_1 H_s^f + a_2\varphi_s^o + a_3 H_s^f s^2 + a_4\varphi_s^o s^2 + a_5 H_s^f c + a_6\varphi_s^o c,$$

$$s = \sin\left(\frac{\pi M}{12}\right),$$

$$c = \cos\left(\frac{\pi M}{12}\right).$$

As mentioned in the errata to the Altshuler and Kalaghan [1974] report, the height dependence in Equation (5) is to be considered only if the user at the surface. For situations in which the antenna is airborne, the formula to compute N_s reduces to:

$$N_s = a_0 + a_2\varphi_s^o + a_4\varphi_s^o s^2 + a_6\varphi_s^o c.$$

The coefficients for equations (1) to (8) are listed in Table 1.

i	g_i	b_i	c_i	a_i
0	0.1556	0.00970	3.28084	369.03000
1	138.8926	-2.08809	6.81758	-0.01553
2	-105.0574	122.73592	0.30480	-0.92442
3	31.5070	-703.82166	0.00423	0.00160
4	1.0000		1.33333	0.19361
5	30.0000		1.41723×10^{-6}	0.00063
6	0.0001		315.00000	-0.05958

Table 1 – Coefficients for equations (1) to (8).

Symbols and Units

d_{trop}	atmosphere propagation delay, in metres
$\theta°$	apparent elevation angle, in degrees
H_s^{tf}	user's orthometric height, in thousands of feet
H_s^{f}	user's orthometric height, in feet
N_s	surface refractivity
φ_s^0	user's latitude, in degrees
M	calendar month

Mathematical model:

$$d_{trop} = d_{trop}^{z} \frac{1}{\sin(\varepsilon) + \frac{0.00143}{\tan(\varepsilon) + 0.0455}},$$

where:

- For $0\ \text{km} \le H_s^k \le 1\ \text{km}$

$$d_{trop}^{z} = 1.430 + 0.732 + \left\{ N_s + 0.5\Delta N - \left(N_s H_s^k + 0.5\Delta N \left(H_s^k \right)^2 \right) \right\} \times 10^{-3}$$

- For $1\ \text{km} \le H_s^k \le 9\ \text{km}$

$$d_{trop}^{z} = 0.732 + \left\{ -\frac{8N_1}{c} \exp(-c) + \left(\frac{8N_1}{c} \right) \exp\left[0.125(1 - H_s^k)c \right] \right\} \times 10^{-3}$$

- For $H_s^k \ge 9\ \text{km}$

$$d_{trop}^{z} = \left\{ \frac{105}{0.1424} \exp\left[-0.1424\left(H_s^k - 9 \right) \right] \right\} \times 10^{-3}$$

$$\Delta N = -7.32 \exp\left\{ 0.005577 N_s \right\}$$

$$N_1 = N_s + \Delta N$$

$$c = \ln\left(\frac{N_1}{105} \right)$$

Comment: *the mapping function associated to this model is the Chao [1972] dry mapping function.*

Symbols and Units

d_{trop}	atmosphere propagation delay, in metres
d^{z}_{trop}	atmosphere zenith propagation delay, in metres
ε	elevation angle, in radians
H^{k}_{s}	orthometric height, in kilometres
N_{s}	mean sea level surface refractivity
N_{1}	refractivity at 1 km above sea level

Mathematical model:

$$d_{trop} = 2.506\left(1 + 0.00125\delta N_s\right)\left[\frac{1 - 1.264\times10^{-4} H_s}{\sin(\varepsilon^0 + 0.35°)}\right],$$

if $H_s \leq 1500$ m; for $H_s > 1500$ m, the model is written as:

$$d_{trop} = 2.484\left[1 + 0.0015363\exp\left\{-2.133\times10^{-4} H_s\right\}\delta N_s\right]\left[\frac{\exp\left\{-1.509\times10^{-4} H_s\right\}}{\sin(\varepsilon° + 0.35°)}\right],$$

where

$$\delta N_s = \delta N_h + \delta N_h$$

$$\delta N_h = \begin{cases} 3.61\times10^{-3} H_s \cos\left[\dfrac{2\pi(doy - 152)}{365}\right], & \text{if } \varphi_s^0 > 0° \\ 3.61\times10^{-3} H_s \cos\left[\dfrac{2\pi(doy - 335)}{365}\right], & \text{if } \varphi_s^0 < 0° \end{cases}$$

$$\delta N_\varphi = \begin{cases} \left(\left|\varphi_s^0\right|\right)\left(-0.8225 + 0.1\cos\left[\dfrac{2\pi(doy - 213)}{365}\right]\right), & \text{if } \varphi_s^0 > 0° \\ \left(\left|\varphi_s^0\right|\right)\left(-0.8225 + 0.1\cos\left[\dfrac{2\pi(doy - 30)}{365}\right]\right), & \text{if } \varphi_s^0 < 0° \end{cases}$$

Note: The model is not defined for $\varphi_s^0 = 0°$.

d_{trop}	atmosphere propagation delay, in metres
ε°	elevation angle, in degrees
H_s	orthometric height, in metres
δN_s	correction to the surface refractivity
φ_s^0	latitude, in degrees
doy	day of year

APPENDIX III

Locations and codes of the radiosonde stations

List of the approximate geographic coordinates of the radiosonde stations (as given in the Radiosonde Data from North America 1946 - 1995, produced by the U.S. Forecast Systems Laboratory and the U.S. National Climatic Data Center [1996]) used in computing databases of tropopause heights, inversion heights, and lapse rates, along with an identifying three-letter code. A subset of these radiosonde stations, shown in bold in the table, was used in computing traces used in model and mapping function assessment.

STATION	CODE	φ (° N)	λ (° E)	H (m)
Bellingshausen, BTA	**BEL**	**-62.20**	**-58.93**	**46**
Hobart, Tasmania, Australia	**HOB**	**-42.83**	**147.50**	**28**
Quintero, Chile	**QUI**	**-32.78**	**-71.52**	**8**
Bloemfontein, South Africa	**BLO**	**-29.10**	**26.30**	**1359**
Fortaleza, Brazil	**FOR**	**-3.72**	**-38.55**	**19**
Balboa, Panama	**BLB**	**8.98**	**-79.60**	**66**
Trinidad, Trinidad and Tobago	**KPP**	**10.58**	**-61.35**	**12**
Curacao, Netherlands	ACC	12.20	-68.97	54
Seawell APT, Bahamas	BDI	13.07	-59.50	47
Guam, Mariana Islands, USA	**GUA**	**13.55**	**144.83**	**111**
Tegucigalapa, Honduras	HTG	14.03	-87.23	1014
Point a Pitre, Guatemala	FFR	16.27	-61.52	8
Belize, Belize	ZBZ	17.53	-88.30	5
San Juan, Puerto Rico	**JSJ**	**18.43**	**-66.00**	**3**
Manzanillo, Mexico	MAN	19.07	-104.33	3
Grand Cayman, Cayman Islands	KCR	19.30	-81.37	3
Mexico City, Mexico	**MEX**	**19.43**	**-99.07**	**2234**
Lihue, HI, USA	**LIH**	**21.98**	**-159.35**	**36**
Mazatlan Sinaloa, Mexico	**MZT**	**23.18**	**-106.42**	**4**
Key West, FL, USA	**EYW**	**24.55**	**-81.75**	**3**
Nassau, Bahamas	YNN	25.05	-77.47	2
Brownsville, TX, USA	BRO	25.90	-97.43	7
West Palm Beach, FL, USA	**PBI**	**26.68**	**-80.12**	**7**
Cape Kennedy, FL, USA	XMR	28.48	-80.55	5
Chihuahua , Mexico	MCV	28.70	-106.07	1428
Corpus Christi, TX, USA	CRP	29.77	-97.50	14
Waycross, GE, USA	AYS	31.25	-82.40	44
Midland, TX, USA	MAF	31.93	-102.20	873
Tuscon, AZ, USA	**TUS**	**32.12**	**-110.93**	**788**
Jackson, MS, USA	**JAN**	**32.32**	**-90.07**	**91**
Miramar, CA, USA	**NKX**	**32.87**	**-117.15**	**147**
Charlston, SC, USA	CHS	32.90	-80.03	15
Little Rock, AR, USA	1M1	34.83	-92.27	172
Albuquerque, NM, USA	ABQ	35.05	-106.62	1619
Norman, OK, USA	OUN	35.23	-97.47	362
Tateno, Japan	**TAT**	**36.05**	**140.13**	**27**
Greensboro, NC	**GSO**	**36.08**	**-79.95**	**277**

Nashville, TN, USA	**BNA**	**36.25**	**-86.57**	**180**
Oakland, CA, USA	**OAK**	**37.75**	**-122.22**	**6**
Wallops Island, VA, USA	**WAL**	**37.93**	**-75.48**	**13**
Denver, CO, USA	**DEN**	**39.77**	**-104.88**	**1611**
Madrid, Spain	**MAD**	**40.50**	**-3.58**	**633**
Pittsburgh, PA, USA	PIT	40.53	-80.23	360
Brindisi, Italy	**BRI**	**40.65**	**17.95**	**15**
Salt Lake City, UT, USA	SLC	40.77	-111.97	1288
Omaha, NE, USA	OVN	41.37	-96.02	400
Chatham, MA, USA	**CHH**	**41.67**	**-69.97**	**16**
Medford, OR, USA	MFR	42.37	-122.87	397
Albany, NY, USA	ALB	42.75	-73.80	85
Boise, ID, USA	BOI	43.57	-116.22	871
Sable Island, NS, Canada	**YSA**	**43.93**	**-60.02**	**4**
Rapid City, SD, USA	RAP	44.05	-103.07	966
Green Bay, WI, USA	GRB	44.48	-88.13	210
Salem, OR, USA	SLE	44.92	-123.02	61
St.John's, NF, Canada	**YYT**	**47.67**	**-52.75**	**140**
Glasgow, MT, USA	GGW	48.22	-106.62	696
Munique, Germany	**MUN**	**48.25**	**11.58**	**484**
International Falls, MN, USA	**INL**	**48.57**	**-93.38**	**359**
Garmersdorf, Germany	GAR	49.43	11.90	419
Sept Iles, PQ, Canada	YZV	50.22	-66.27	52
Port Hardy, BC, Canada	**YZT**	**50.68**	**-127.37**	**17**
Moosonee, PQ, Canada	YMO	51.27	-80.65	10
Goose Bay, NFW, Canada	YYR	53.30	-60.37	36
Edmonton, AB, Canada	WSE	53.55	-114.10	766
La Grande, PQ, Canada	YAH	53.75	-73.67	307
Prince George, BC, Canada	YXS	53.88	-122.68	675
The Pas, MB, Canada	**YQD**	**53.97**	**-101.10**	**273**
Annette Island, AK, USA	ANN	55.03	-131.57	37
Cold Bay, AK, USA	CDB	55.20	-162.72	30
Copenhagen, Denmark	COP	55.77	12.52	40
St. Paul Island, AK, USA	SNP	57.15	-170.22	10
Landvetter, Sweden	**LAN**	**57.67**	**12.30**	**155**
Kuujjuaq, PQ, Canada	YVP	58.10	-68.42	60
Inukjuak, PQ, Canada	YPH	58.45	-78.12	7
King Salmon, AK, USA	AKN	58.68	-156.65	15
Churchill, MB, Canada	YYQ	58.75	-94.07	29
Fort Nelson, BC, Canada	YYE	58.83	-122.60	377
Bromma, Sweden	BRM	59.35	17.95	22

Yakutat, AK, USA	YAK	59.52	-139.67	12
Ft. Smith, NWT, Canada	YSM	60.03	-111.95	203
Gardermoen, Norway	GMO	60.20	11.10	201
Whitehorse, YK, Canada	**YXY**	**60.72**	**-135.07**	**704**
Bethel, AK, USA	BET	60.78	-161.80	36
Sundsvall, Sweden	**SUN**	**62.53**	**17.45**	**6**
Iqaluit, NWT, Canada	**YVN**	**63.75**	**-68.55**	**21**
Coral Harbour, NWT, Canada	YZS	64.20	-83.37	57
Baker Lake, AK, USA	YBK	64.30	-96.00	49
Nome, AK, USA	OME	64.50	-165.43	5
Fairbanks, AK, USA	**FAI**	**64.82**	**-147.87**	**135**
Norman Wells, NWT, Canada	YVQ	65.28	-126.75	95
Lulea, Sweden	**LUL**	**65.55**	**22.13**	**34**
Kotzebue, AK, USA	**OTZ**	**66.87**	**-162.63**	**5**
Inuvik, NWT, Canada	YEV	68.32	-133.53	103
Hall Lake NWT, Canada	YUX	68.78	-81.25	7
Cambridge Bay, NWT, Canada	YCB	69.10	-105.12	25
Point Barrow, AK, USA	BRW	71.30	-156.78	12
Resolute, NWT, Canada	YRB	74.72	-94.98	40
Mould Bay, NWT, Canada	YMD	76.23	-119.33	58
Eureka, NWT, Canada	YEU	79.98	-85.93	10
Alert, NWT, Canada	**YLT**	**82.50**	**-62.33**	**66**

APPENDIX IV

Sample of statistical tables available in electronic format

Samples of statistical tables of tropopause heights, inversion heights, and lapse rates for the stations listed in Appendix III. The full tables are electronically available in http://mat.fc.ul.pt/eg/lattex/PhD_e_sup.html.

Notation:

MEAN	Mean
STD	Standard deviation
MIN	Minimum value
MAX	Maximum value
#	Number of determinations
SIGB	Precision of the *b* coefficient in the least-squares fit of the line $y = a + bx$
STDS	Standard deviation of the SIGB.

STATION	MONTH	MEAN (km)	STD	MIN (km)	MAX	#
BEL						
	JANUARY	9.230	0.915	7.999	11.007	19
	FEBRUARY	9.329	0.914	8.007	11.012	13
	MARCH	9.073	1.161	7.499	11.977	21
	APRIL	9.745	1.407	6.491	12.496	23
	MAY	10.214	1.413	8.523	12.490	9
	OCTOBER	12.656	3.030	9.000	17.113	7
	NOVEMBER	12.776	2.420	8.489	18.247	23
	DECEMBER	11.958	1.501	9.998	15.031	12
	ANNUAL	10.466	2.187	6.491	18.247	127
HOB						
	JANUARY	11.599	1.233	8.790	14.485	59
	FEBRUARY	11.798	1.444	8.441	15.517	51
	MARCH	12.089	1.018	9.163	14.670	55
	APRIL	11.612	1.120	8.120	13.242	60
	MAY	11.298	1.017	8.078	13.106	60
	JUNE	10.370	1.150	6.973	12.056	58
	JULY	10.380	1.079	7.342	12.272	57
	AUGUST	9.714	0.974	6.987	11.463	54
	SEPTEMBER	9.802	0.992	6.995	11.233	39
	OCTOBER	10.657	1.131	8.068	13.194	52
	NOVEMBER	10.724	1.245	7.644	14.377	57
	DECEMBER	11.488	0.991	9.007	13.763	57
	ANNUAL	10.995	1.339	6.973	15.517	659
QUI						
	JANUARY	14.187	2.214	10.281	18.118	42
	FEBRUARY	14.045	2.064	11.384	17.840	38
	MARCH	14.278	2.051	10.351	17.795	56
	APRIL	12.998	1.594	10.494	18.384	54
	MAY	12.256	1.299	9.636	15.982	59
	JUNE	11.700	1.246	7.483	13.060	49
	JULY	11.445	1.406	8.692	16.713	49
	AUGUST	11.223	1.221	7.702	15.092	42
	SEPTEMBER	11.305	0.939	9.206	12.527	25
	OCTOBER	12.210	1.830	9.366	18.525	48
	NOVEMBER	12.128	1.774	9.687	16.721	50
	DECEMBER	14.096	2.439	9.685	18.266	57
	ANNUAL	12.721	2.073	7.483	18.525	569

IIA – Tropopause height statistics for BEL, HOB, and QUI.

STATION	MONTH	MEAN (m)	STD (m)	MIN (m)	MAX (m)	#
BEL						
	FEBRUARY	262.0	181.9	157.0	472.0	3
	MARCH	321.6	356.9	160.0	960.0	5
	APRIL	512.6	367.7	8.0	1165.0	7
	MAY	88.3	80.6	7.0	162.0	4
	OCTOBER	123.7	66.5	47.0	166.0	3
	NOVEMBER	224.7	114.7	155.0	357.0	3
	DECEMBER	197.4	87.7	153.0	354.0	5
	ANNUAL	277.8	262.9	7.0	1165.0	32
HOB						
	JANUARY	72.8	49.6	42.0	146.0	4
	FEBRUARY	130.9	167.2	41.0	532.0	8
	MARCH	103.4	91.9	42.0	348.0	10
	APRIL	93.2	64.5	32.0	267.0	17
	MAY	137.7	125.4	33.0	753.0	44
	JUNE	144.0	97.7	16.0	452.0	45
	JULY	109.3	65.4	8.0	303.0	44
	AUGUST	99.5	75.8	8.0	323.0	30
	SEPTEMBER	58.9	24.6	16.0	121.0	16
	OCTOBER	68.9	50.7	8.0	252.0	18
	NOVEMBER	48.1	31.1	8.0	118.0	9
	DECEMBER	67.0	34.7	49.0	119.0	4
	ANNUAL	109.1	91.4	8.0	753.0	249
QUI						
	JANUARY	394.8	400.8	74.0	1149.0	12
	FEBRUARY	297.3	245.6	32.0	778.0	20
	MARCH	269.8	265.0	66.0	1036.0	24
	APRIL	218.0	190.2	40.0	867.0	46
	MAY	203.5	188.3	40.0	984.0	50
	JUNE	250.3	247.8	39.0	913.0	44
	JULY	173.2	144.4	40.0	858.0	43
	AUGUST	488.8	337.6	88.0	1254.0	25
	SEPTEMBER	349.9	328.8	48.0	1024.0	11
	OCTOBER	280.3	208.5	40.0	718.0	32
	NOVEMBER	235.1	217.5	48.0	746.0	14
	DECEMBER	377.4	311.6	40.0	1166.0	24
	ANNUAL	270.2	252.6	32.0	1254.0	345

IIA – Inversion height statistics for BEL, HOB, and QUI.

STATION	MONTH	MEAN (K/km)	STD	SIGB STDS (K/km)		MIN (K/km)	MAX	#
BEL								
	JANUARY	5.87	0.45	0.17	0.05	5.05	6.51	19
	FEBRUARY	5.77	0.46	0.16	0.05	5.06	6.60	13
	MARCH	5.87	0.59	0.15	0.07	4.45	6.79	21
	APRIL	6.11	0.54	0.21	0.07	4.93	7.37	24
	MAY	6.12	0.37	0.19	0.07	5.26	6.45	9
	OCTOBER	5.52	0.70	0.18	0.05	4.39	6.72	8
	NOVEMBER	4.91	0.69	0.18	0.06	3.59	5.93	23
	DECEMBER	5.26	0.59	0.17	0.06	4.47	6.13	12
	ANNUAL	5.67	0.70	0.18	0.06	3.59	7.37	129
HOB								
	JANUARY	6.22	0.33	0.16	0.05	5.55	6.90	56
	FEBRUARY	6.11	0.38	0.17	0.05	5.25	7.06	54
	MARCH	6.24	0.30	0.17	0.06	5.65	6.91	58
	APRIL	6.54	0.31	0.15	0.04	5.73	7.08	60
	MAY	6.67	0.22	0.14	0.04	6.10	7.13	60
	JUNE	6.79	0.33	0.15	0.04	6.16	7.47	58
	JULY	6.68	0.38	0.15	0.05	5.74	7.71	57
	AUGUST	6.82	0.33	0.16	0.04	6.11	7.48	54
	SEPTEMBER	6.53	0.39	0.18	0.07	5.87	7.59	37
	OCTOBER	6.46	0.37	0.17	0.06	5.71	7.31	51
	NOVEMBER	6.46	0.36	0.14	0.05	5.19	7.01	51
	DECEMBER	6.38	0.31	0.16	0.04	5.66	6.89	56
	ANNUAL	6.49	0.40	0.16	0.05	5.19	7.71	652
QUI								
	JANUARY	6.16	0.36	0.18	0.06	5.40	6.89	53
	FEBRUARY	6.26	0.38	0.16	0.05	5.53	7.17	50
	MARCH	6.40	0.44	0.17	0.04	5.50	7.34	56
	APRIL	6.52	0.48	0.15	0.05	5.07	7.58	54
	MAY	6.51	0.30	0.13	0.04	5.79	7.10	58
	JUNE	6.61	0.48	0.13	0.04	5.73	7.60	48
	JULY	6.49	0.41	0.18	0.07	5.11	7.39	48
	AUGUST	6.82	0.48	0.19	0.08	5.83	7.78	42
	SEPTEMBER	6.67	0.33	0.19	0.06	6.11	7.47	24
	OCTOBER	6.42	0.45	0.20	0.08	5.05	7.63	47
	NOVEMBER	6.46	0.32	0.20	0.07	5.57	7.03	49
	DECEMBER	6.31	0.39	0.14	0.04	5.40	7.09	56
	ANNUAL	6.45	0.44	0.17	0.06	5.05	7.78	585

IIA – Lapse rate statistics for BEL, HOB, and QUI.

APPENDIX V

Tropopause height and lapse rate statistics

Annual mean tropopause heights and lapse rates for the 100 stations listed in Appendix III ordered by increasing absolute latitude. The error bars represent the associated standard deviation.

Lapse Rate (K/km)
4
5
6
7
8
FOR
BLB
KPP
ACC
BDI
GUA
HTG
FFR
ZBZ
JSJ
MAN
KCR
MEX
LIH
MZT
EYW
YNN
BRO
PBI
XMR
MCV
BLO
CRP
AYS
MAF
TUS
JAN
QUI
NKX
CHS
1M1
ABQ
OUN
TAT
GSO
BNA
OAK
WAL
DEN
MAD
PIT
BRI
SLC
OVN
CHH
MFR
ALB
HOB
BOI
YSA
RAP
GRB
SLE
YYT
GGW
MUN
INL
GAR
YZV
YZT
YMO
YYR
WSE
YAH
YXS
YQD
ANN
CDB
COP
SNP
LAN
YVP
YPH
AKN
YYQ
YYE
BRM
YAK
YSM
GMO
YXY
BET
BEL
SUN
YVN
YZS
YBK
OME
FAI
YVQ
LUL
OTZ
YEV
YUX
YCB
BRW
YRB
YMD
YEU
YLT

Tropopause Height (km)
8
10
12
14
16
18
FOR
BLB
KPP
ACC
BDI
GUA
HTG
FFR
ZBZ
JSJ
MAN
KCR
MEX
LIH
MZT
EYW
YNN
BRO
PBI
XMR
MCV
BLO
CRP
AYS
MAF
TUS
JAN
QUI
NKX
CHS
1M1
ABQ
OUN
TAT
GSO
BNA
OAK
WAL
DEN
MAD
PIT
BRI
SLC
OVN
CHH
MFR
ALB
HOB
BOI
YSA
RAP
GRB
SLE
YYT
GGW
MUN
INL
GAR
YZV
YZT
YMO
YYR
WSE
YAH
YXS
YQD
ANN
CDB
COP
SNP
LAN
YVP
YPH
AKN
YYQ
YYE
BRM
YAK
YSM
GMO
YXY
BET
BEL
SUN
YVN
YZS
YBK
OME
FAI
YVQ
LUL
OTZ
YEV
YUX
YCB
BRW
YRB
YMD
YEU
YLT

APPENDIX VI

Zenith hydrostatic delay model statistics

Annual mean bias and rms scatter (one-sigma level) of the differences with respect to ray tracing for different zenith hydrostatic delay prediction models, for 50 radiosonde stations listed in Appendix III.

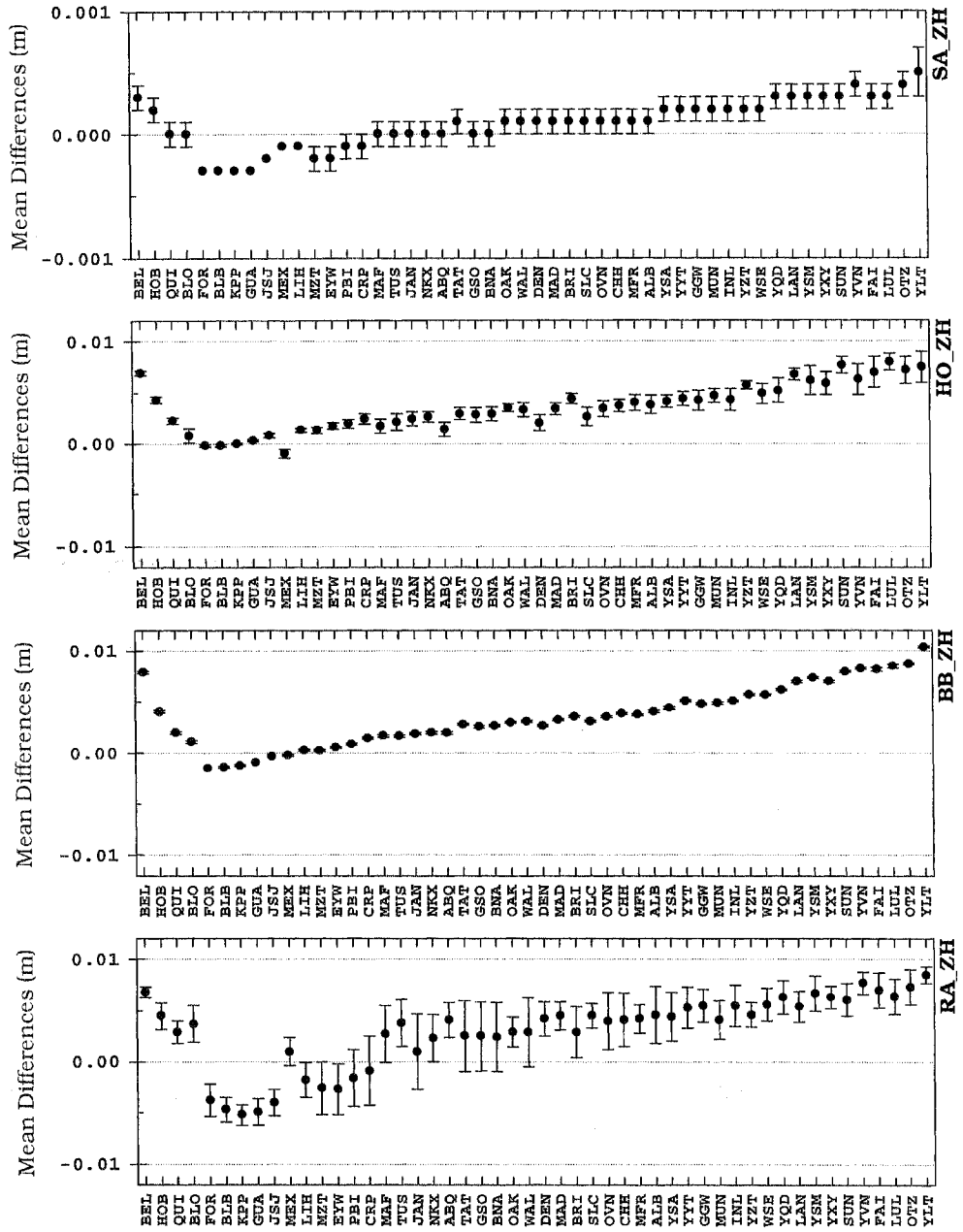
Mean Differences (m)
0.001
0.000
-0.001
SA_ZH
BEL HOB QUI BLO FOR BLB KPP GUA JSJ MEX LIH MZT EYW PBI CRP MAF TUS JAN NKX ABQ TAT GSO BNA OAK WAL DEN MAD BRI SLC OVN CHH MFR ALB YSA YYT GGW MUN INL YZT WSE YQD LAN YSM YXY SUN YVN FAI LUL OTZ YLT
Mean Differences (m)
0.01
0.00
-0.01
HO_ZH
BEL HOB QUI BLO FOR BLB KPP GUA JSJ MEX LIH MZT EYW PBI CRP MAF TUS JAN NKX ABQ TAT GSO BNA OAK WAL DEN MAD BRI SLC OVN CHH MFR ALB YSA YYT GGW MUN INL YZT WSE YQD LAN YSM YXY SUN YVN FAI LUL OTZ YLT
Mean Differences (m)
0.01
0.00
-0.01
BB_ZH
BEL HOB QUI BLO FOR BLB KPP GUA JSJ MEX LIH MZT EYW PBI CRP MAF TUS JAN NKX ABQ TAT GSO BNA OAK WAL DEN MAD BRI SLC OVN CHH MFR ALB YSA YYT GGW MUN INL YZT WSE YQD LAN YSM YXY SUN YVN FAI LUL OTZ YLT
Mean Differences (m)
0.01
0.00
-0.01
RA_ZH
BEL HOB QUI BLO FOR BLB KPP GUA JSJ MEX LIH MZT EYW PBI CRP MAF TUS JAN NKX ABQ TAT GSO BNA OAK WAL DEN MAD BRI SLC OVN CHH MFR ALB YSA YYT GGW MUN INL YZT WSE YQD LAN YSM YXY SUN YVN FAI LUL OTZ YLT

APPENDIX VII

Zenith non-hydrostatic delay model statistics

Annual mean bias and rms scatter (one-sigma level) of the differences with respect to ray tracing for different zenith non-hydrostatic delay prediction models, for 50 radiosonde stations listed in Appendix III.

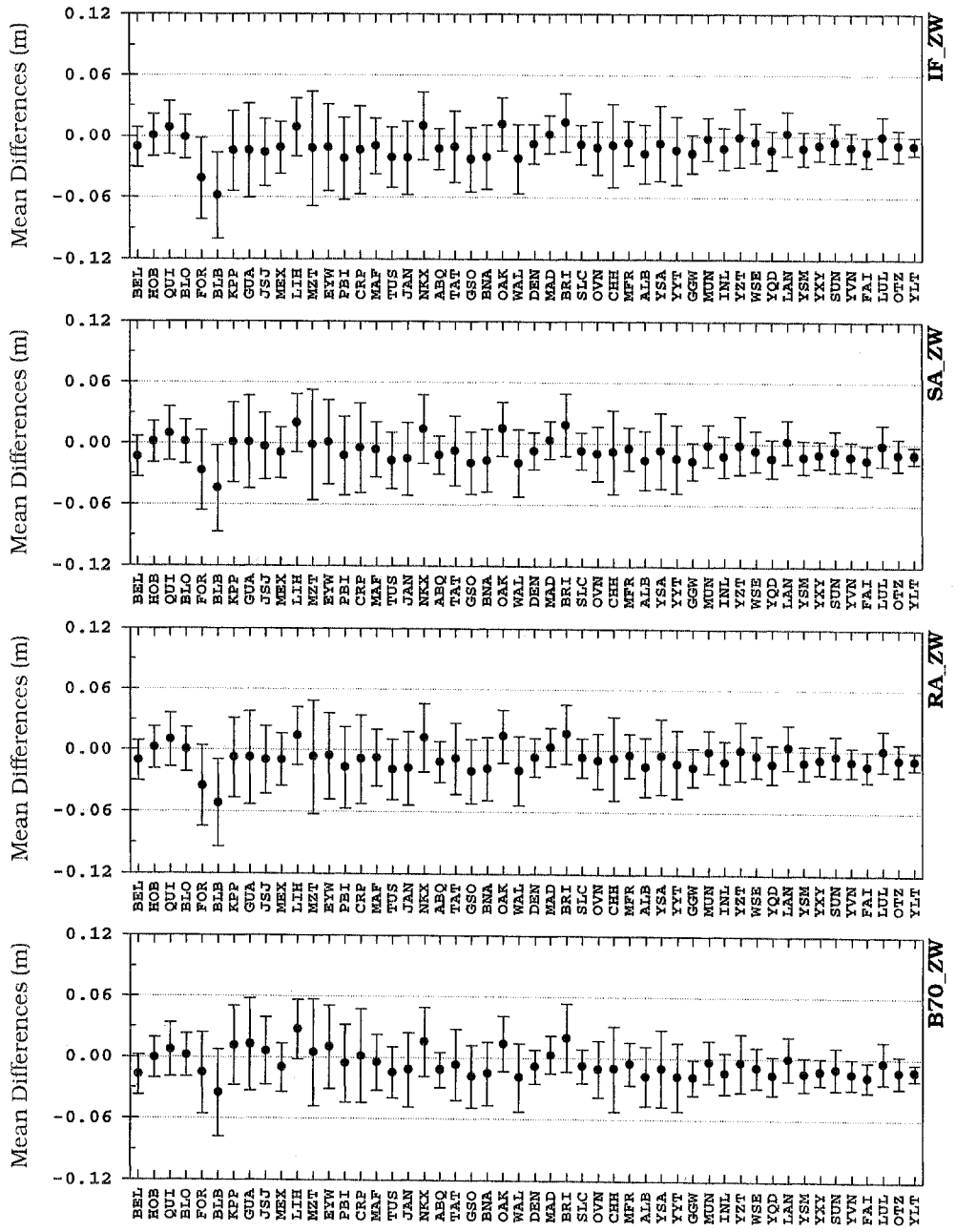
IF_ZW
SA_ZW
RA_ZW
B70_ZW
Mean Differences (m)
0.12
0.06
0.00
-0.06
-0.12
BEL HOB QUI BLO FOR BLB KPP GUA JSJ MEX LIH MZT EYW PBI CRP MAF TUS JAN NKX ABQ TAT GSO BNA OAK WAL DEN MAD BRI SLC OVN CHH MFR ALB YSA YYT GGW MUN INL YZT WSE YQD LAN YSM YXY SUN YVN FAI LUL OTZ YLT

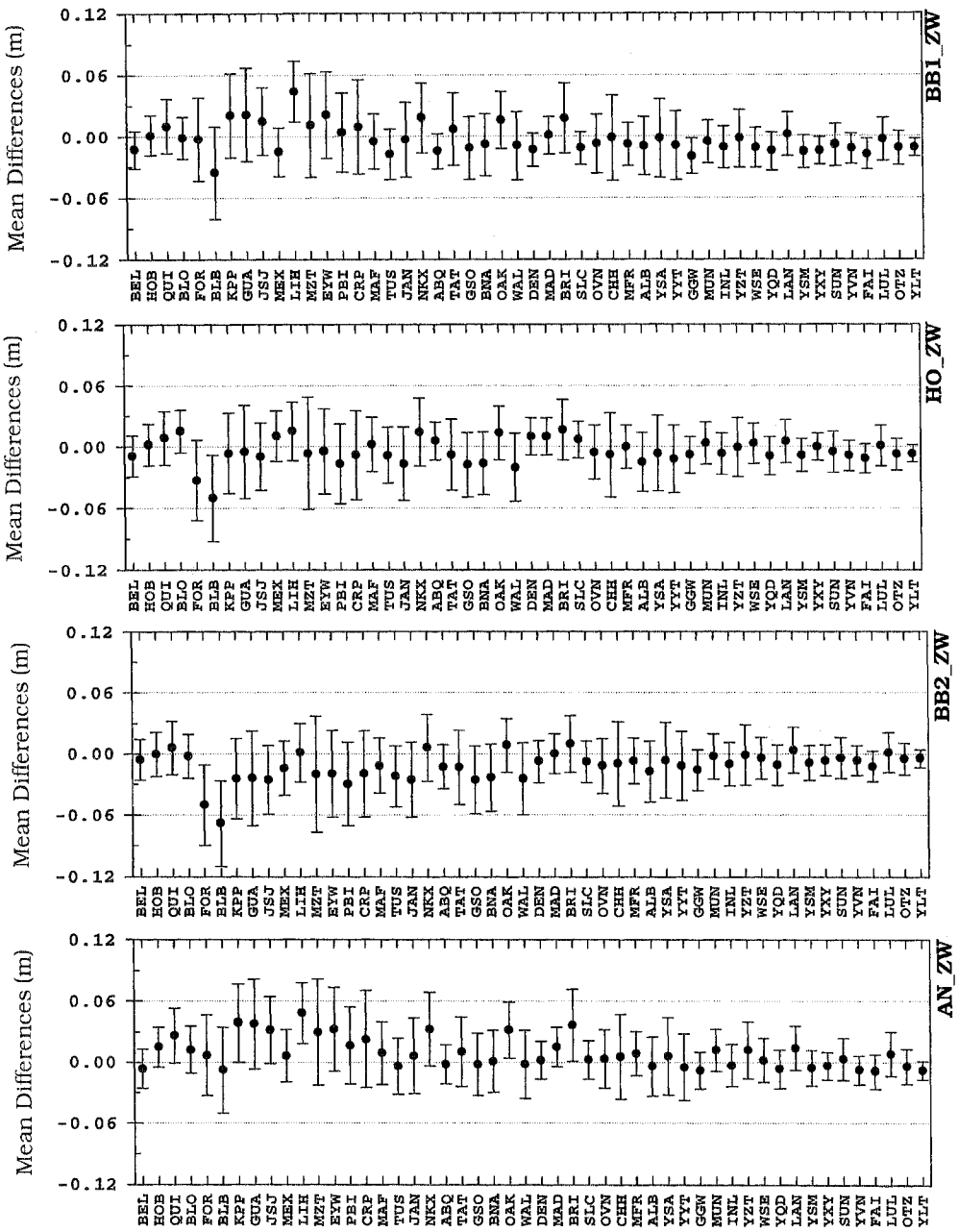
Mean Differences (m)
0.12
0.06
0.00
-0.06
-0.12
BB1_ZW
HO_ZW
BB2_ZW
AN_ZW
BEL HOB QUI BLO FOR BLB KPP GUA JSJ MEX LIH MZT EYW PBI CRP MAF TUS JAN NKX ABQ TAT GSO BNA OAK WAL DEN MAD BRI SLC OVN CHH MFR ALB YSA YYT GGW MUN INL YZT WSE YQD LAN YSM YXY SUN YVN FAI LUL OTZ YLT

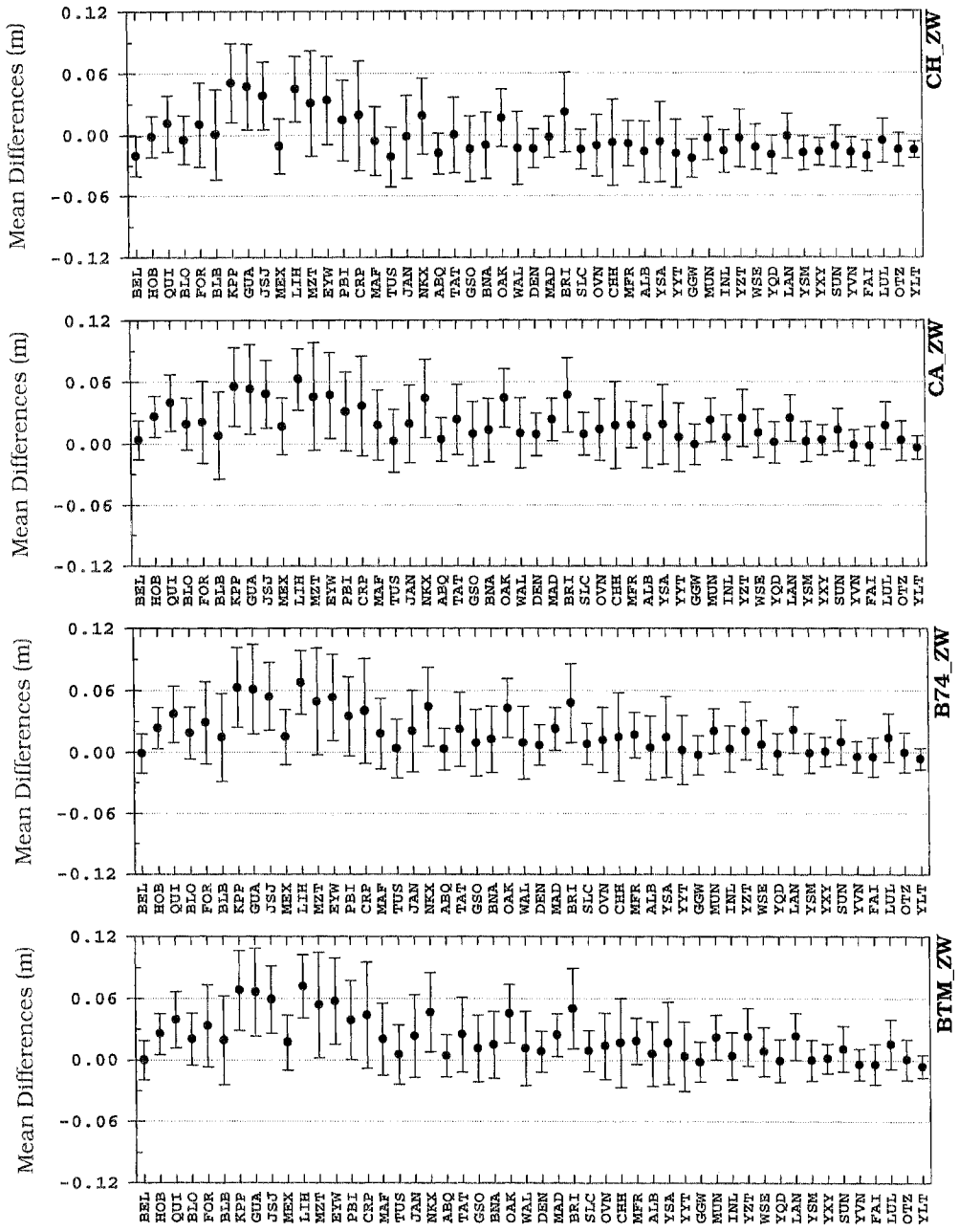
Mean Differences (m)
0.12
0.06
0.00
-0.06
-0.12
CH_ZW
CA_ZW
B74_ZW
BTM_ZW
BEL HOB QUI BLO FOR BLB KPP GUA JSJ MEX LIH MZT EYW PBI CRP MAF TUS JAN MKX ABQ TAT GSO BNA OAK WAL DEN MAD BRI SLC OVN CHH MFR ALB YSA YYT GGW MUN INL YZT WSE YQD LAN YSM YXY SUN YVN FAI LUL OTZ YLT

APPENDIX VIII

Zenith total delay model statistics

Annual mean bias and rms scatter (one-sigma level) of the differences with respect to ray tracing for different zenith total delay prediction models, for 50 radiosonde stations listed in Appendix III.

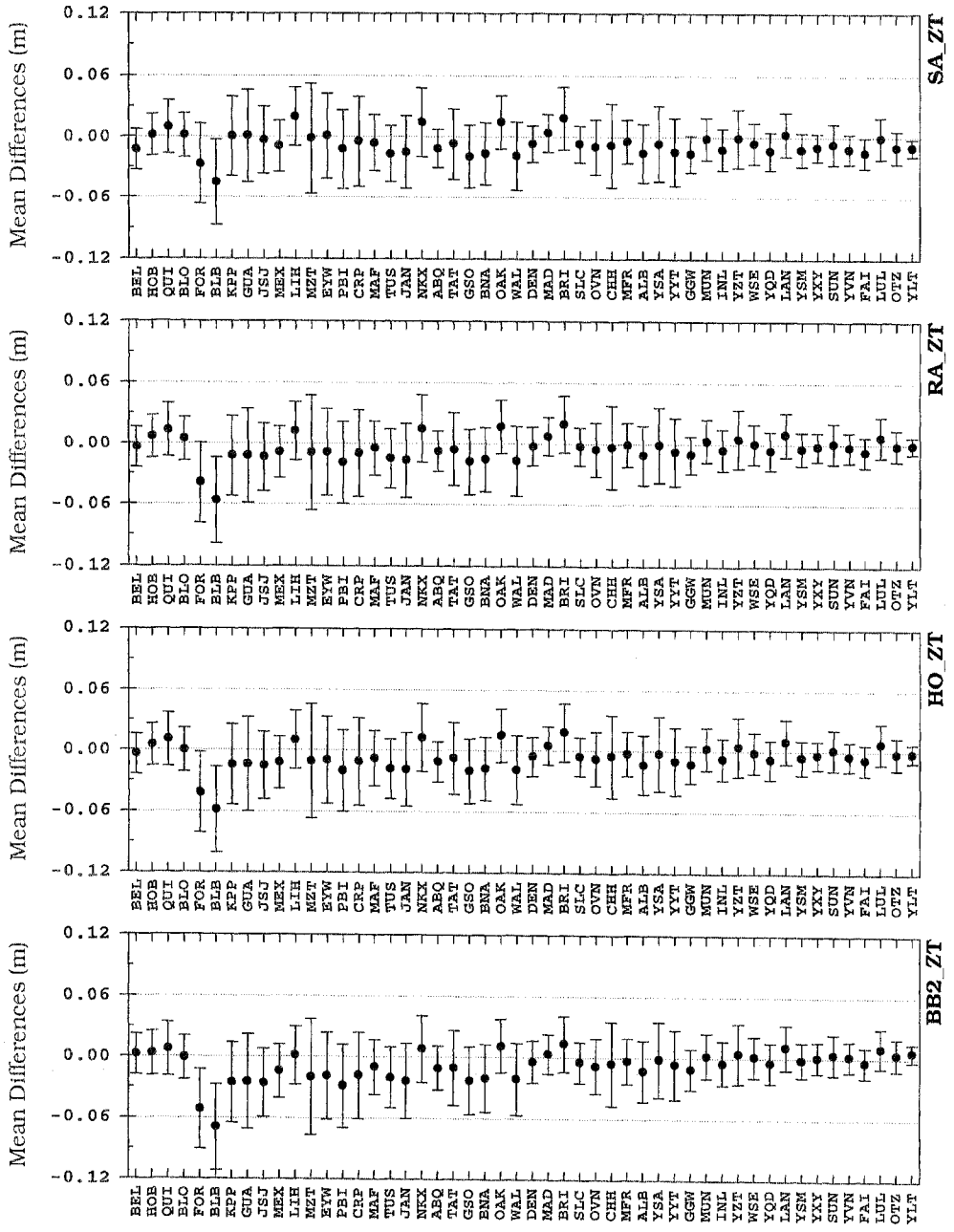
Mean Differences (m)
0.12
0.06
0.00
-0.06
-0.12
SA_ZT
RA_ZT
HO_ZT
BB2_ZT
BEL HOB QUI BLO FOR BLB KPP GUA JSJ MEX LIH MZT EYW PBI CRP MAF TUS JAN NKX ABQ TAT GSO BNA OAK WAL DEN MAD BRI SLC OVN CHH MFR ALB YSA YYT GGW MUN INL YZT WSE YQD LAN YSM YXY SUN YVN FAI LUL OTZ YLT

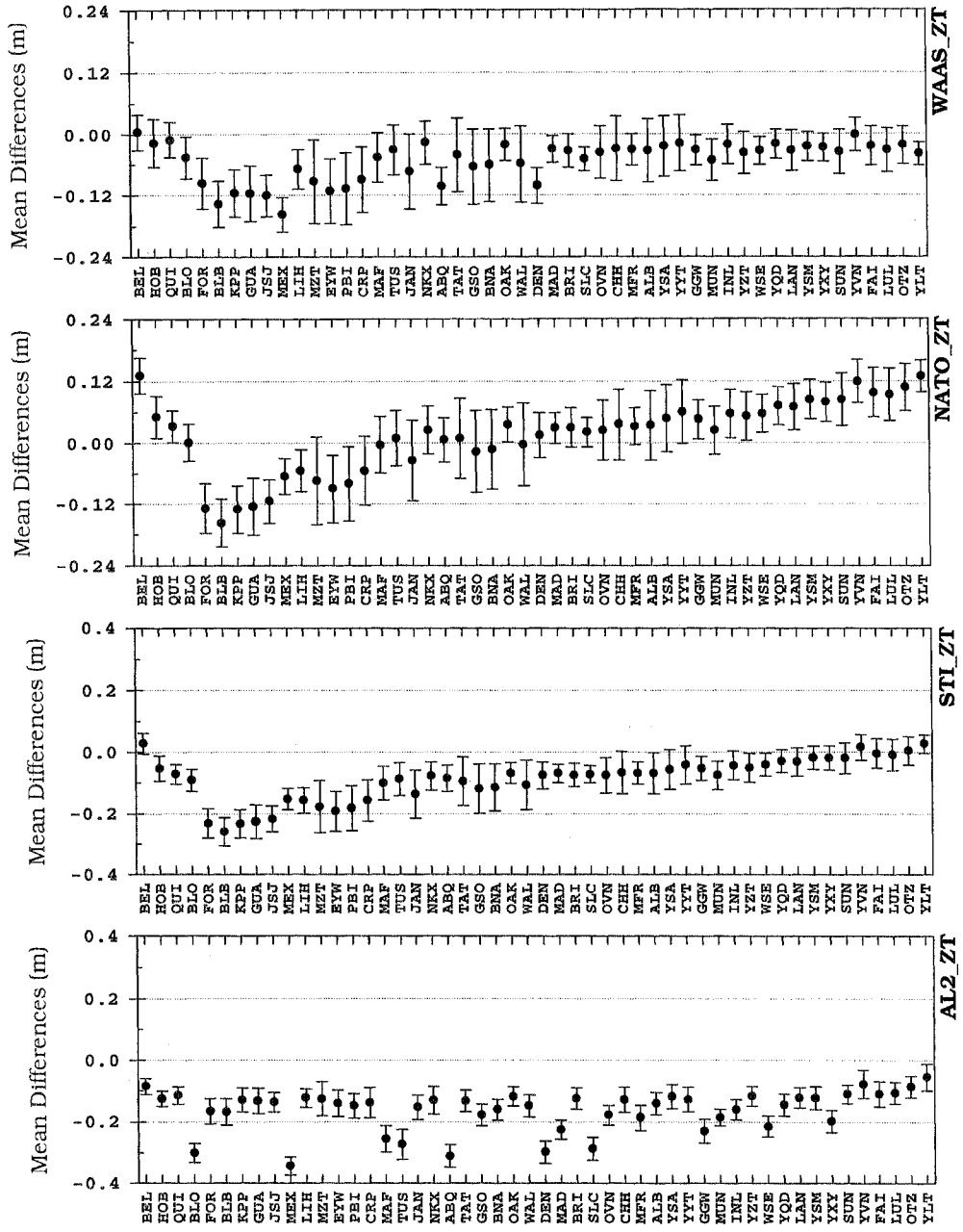
Mean Differences (m)
0.24
0.12
0.00
-0.12
-0.24
WAAS_ZT
NATO_ZT
0.4
0.2
0.0
-0.2
-0.4
STI_ZT
AL2_ZT
BEL HOB QUI BLO FOR BLB KPP GUA JSJ MEX LIH MZT EYW PBI CRP MAF TUS JAN NKX ABQ TAT GSO BNA OAK WAL DEN MAD BRI SLC OVN CHH MFR ALB YSA YYT GGW MUN INL YZT WSE YQD LAN YSM YXY SUN YVN FAI LUL OTZ YLT

APPENDIX IX

Hydrostatic mapping function statistics

Annual mean bias and rms scatter (one-sigma level) of the differences with respect to ray tracing for different hydrostatic mapping functions, for 50 radiosonde stations listed in Appendix III, and at different elevation angles.

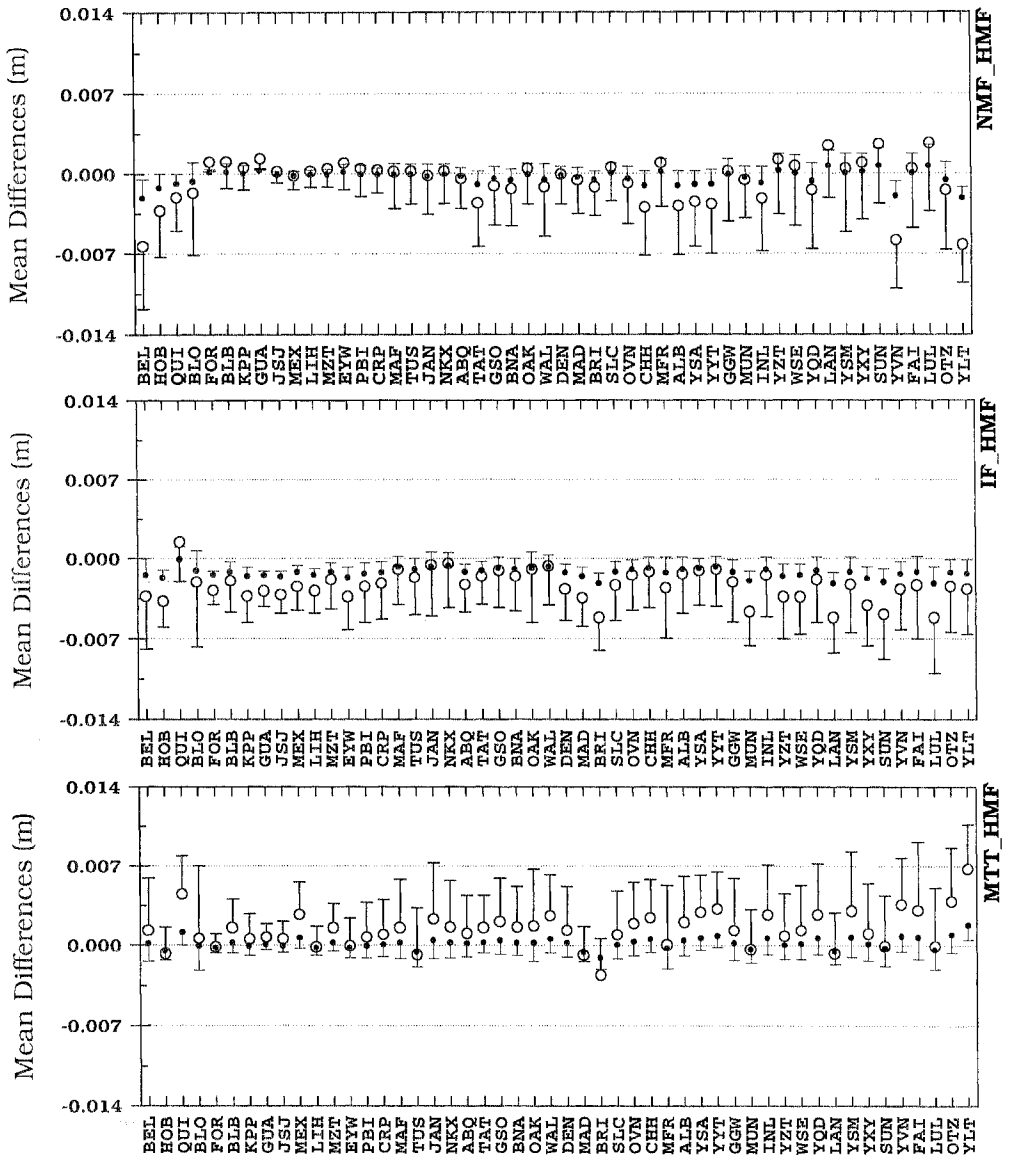

Appendix IXA – Annual mean bias and associated rms scatter for 15° (black dot) and 10° (open circle) elevation angles (continued).

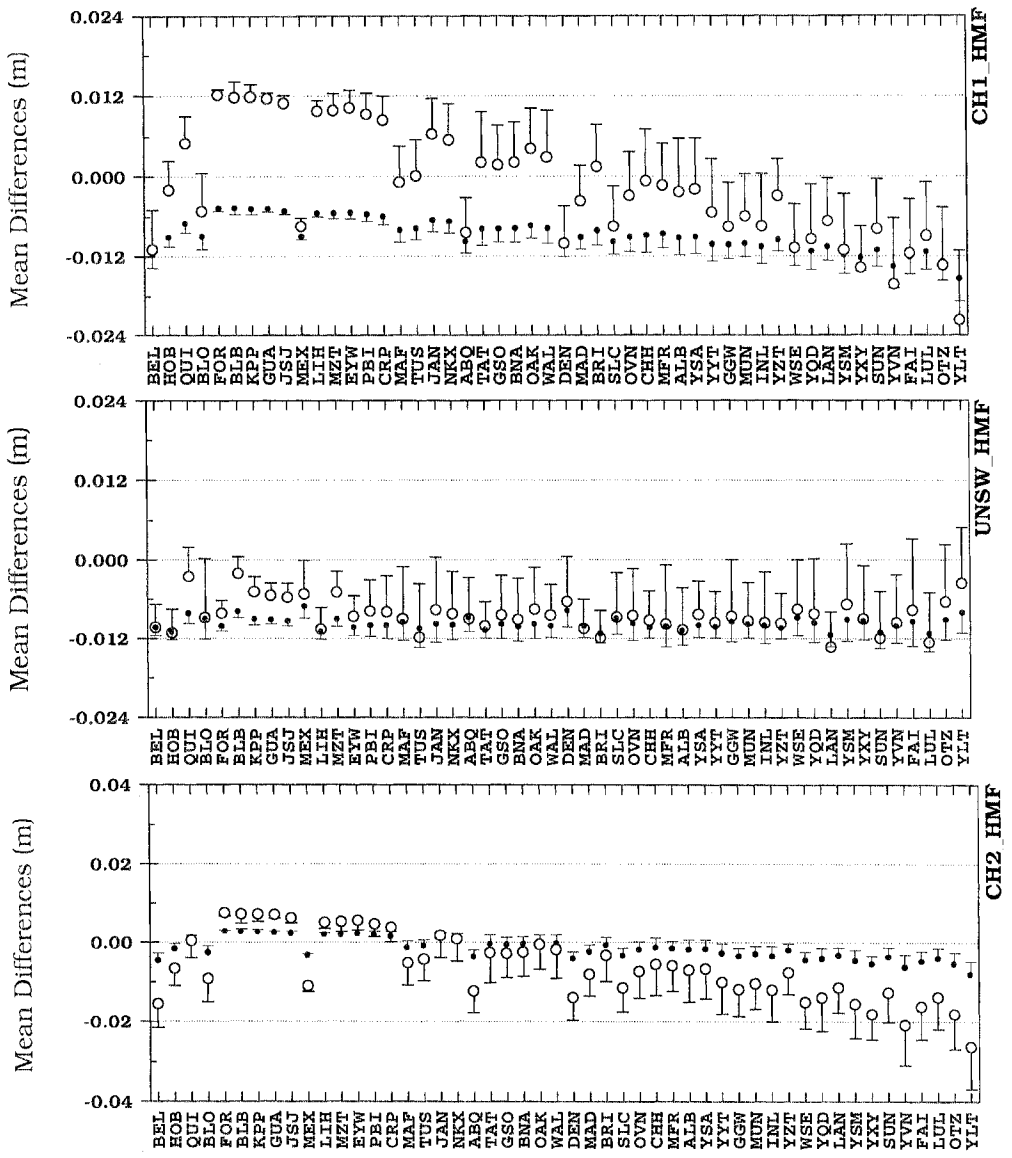

Appendix IXA – Annual mean bias and associated rms scatter for 15° (black dot) and 10° (open circle) elevation angles (continued).

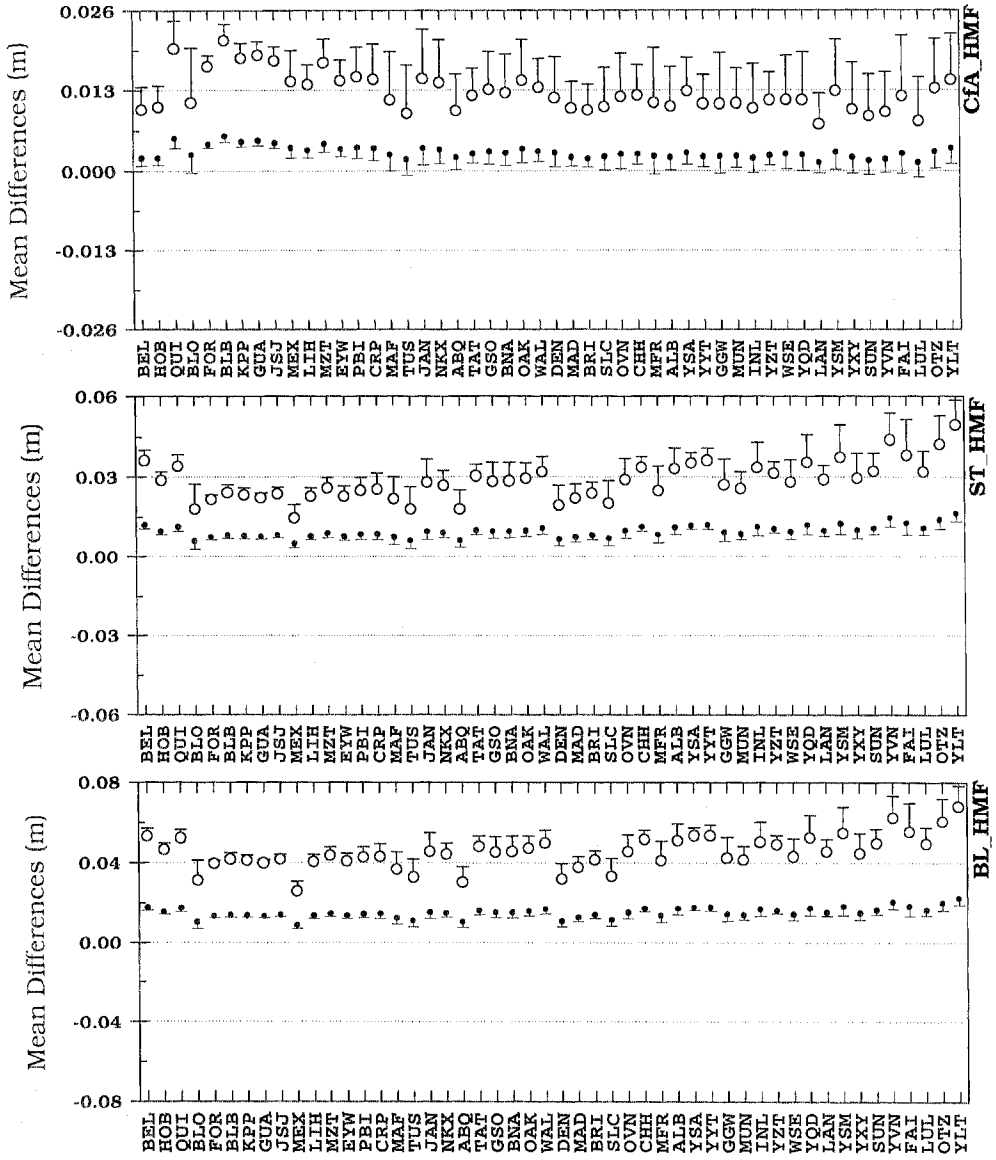

Appendix IXA – Annual mean bias and associated rms scatter for 15° (black dot) and 10° (open circle) elevation angles (continued).

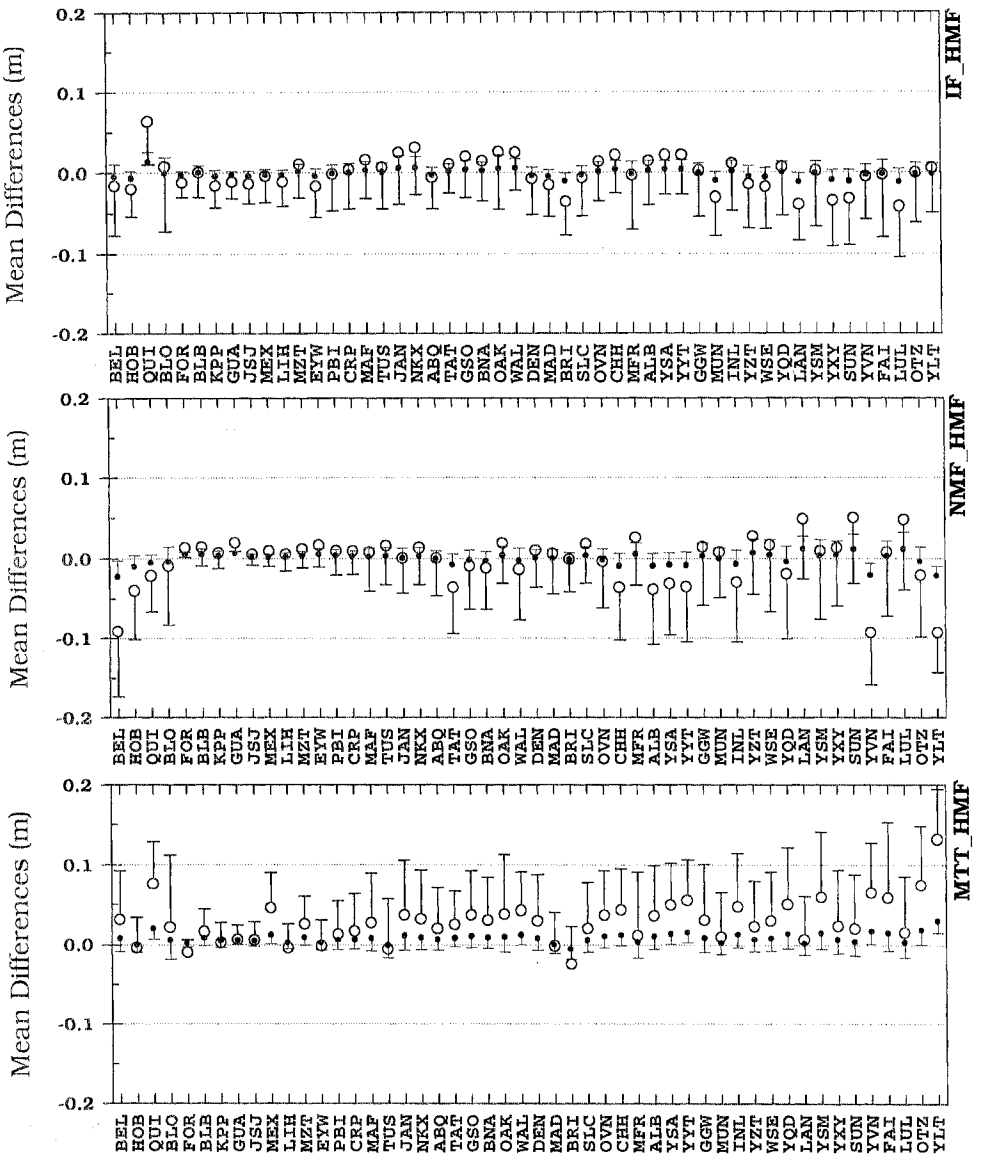

Appendix IXA – Annual mean bias and associated rms scatter for 15° (black dot) and 10° (open circle) elevation angles.

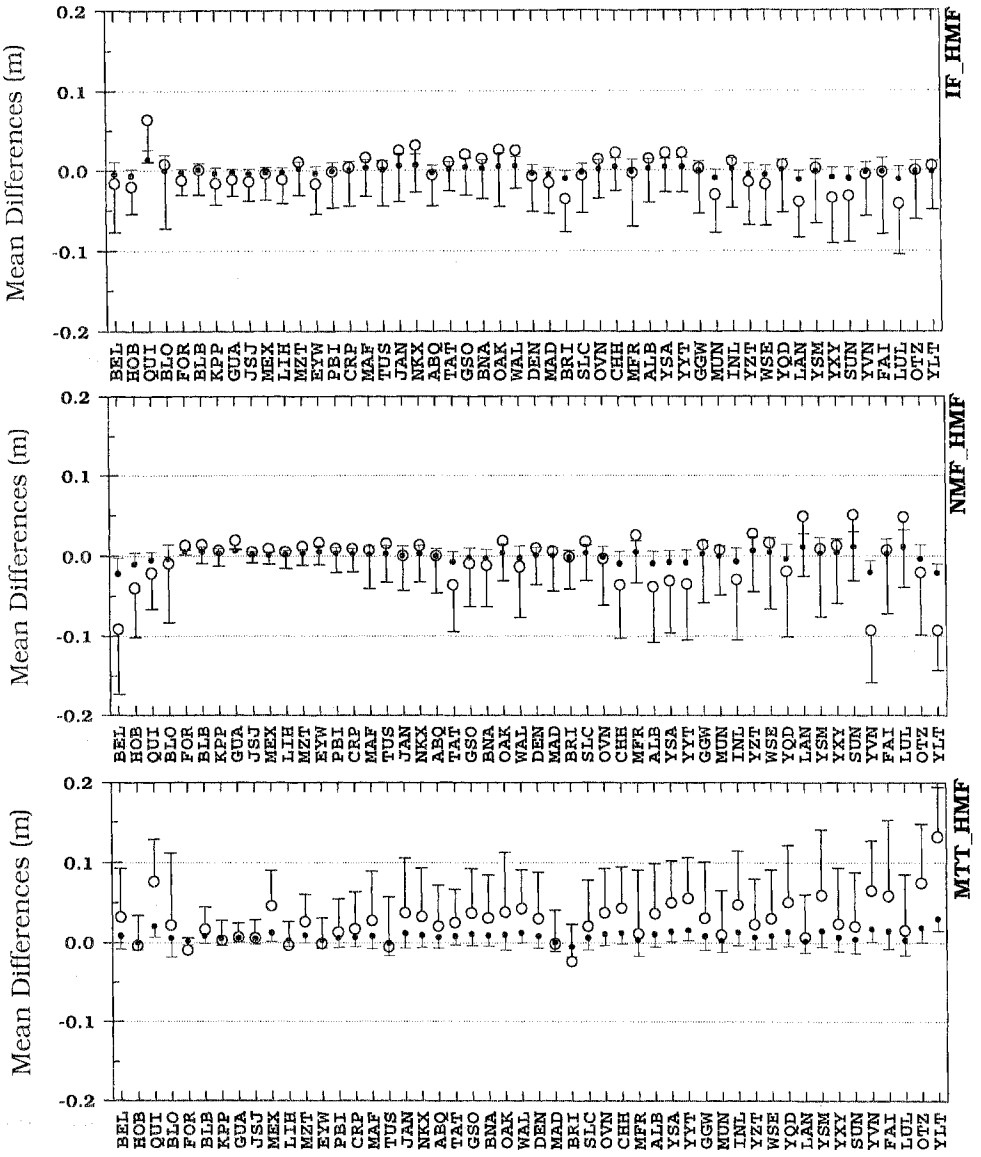

Appendix IXB – Annual mean bias and associated rms scatter for 6° (black dot) and 3° (open circle) elevation angles (continued).

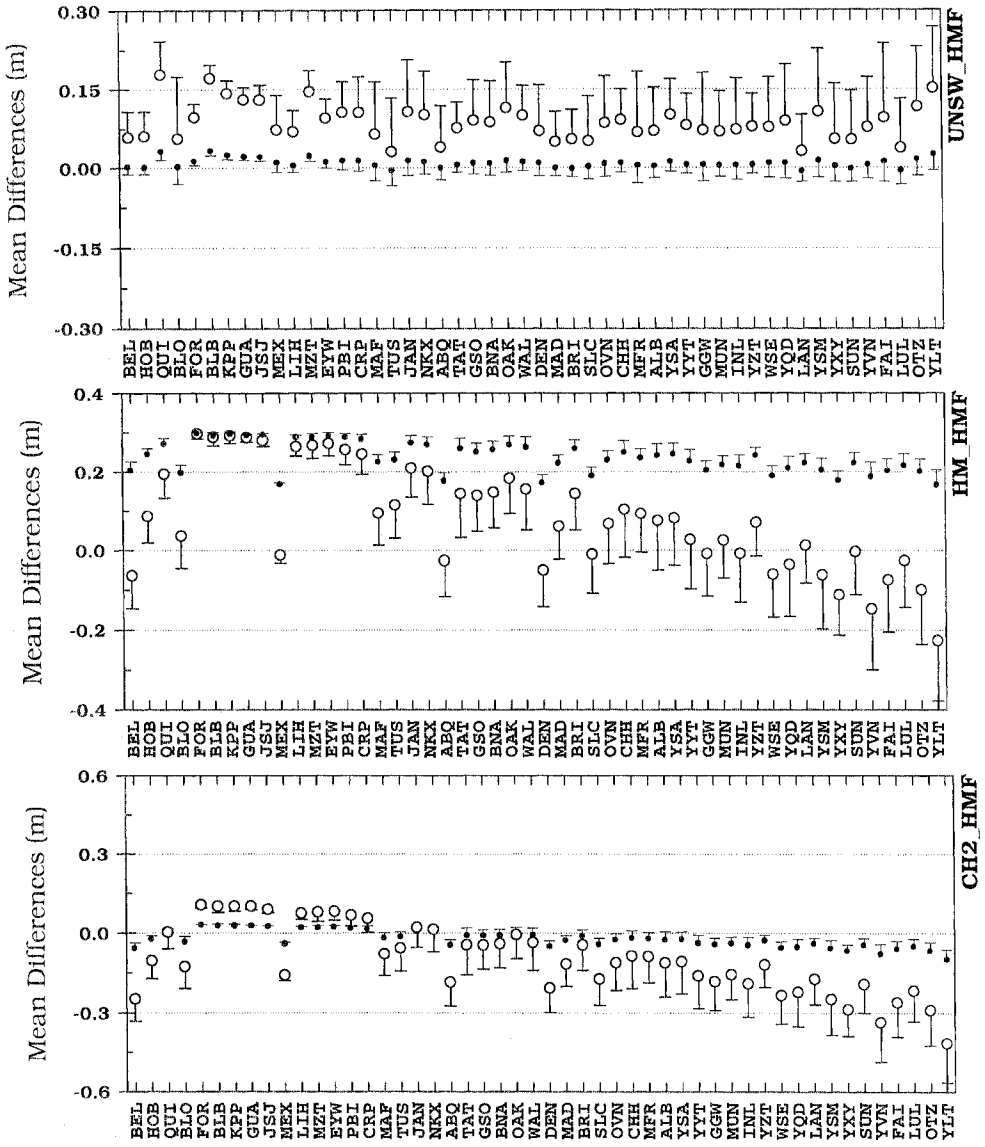

Appendix IXB – Annual mean bias and associated rms scatter for 6° (black dot) and 3° (open circle) elevation angles (continued).

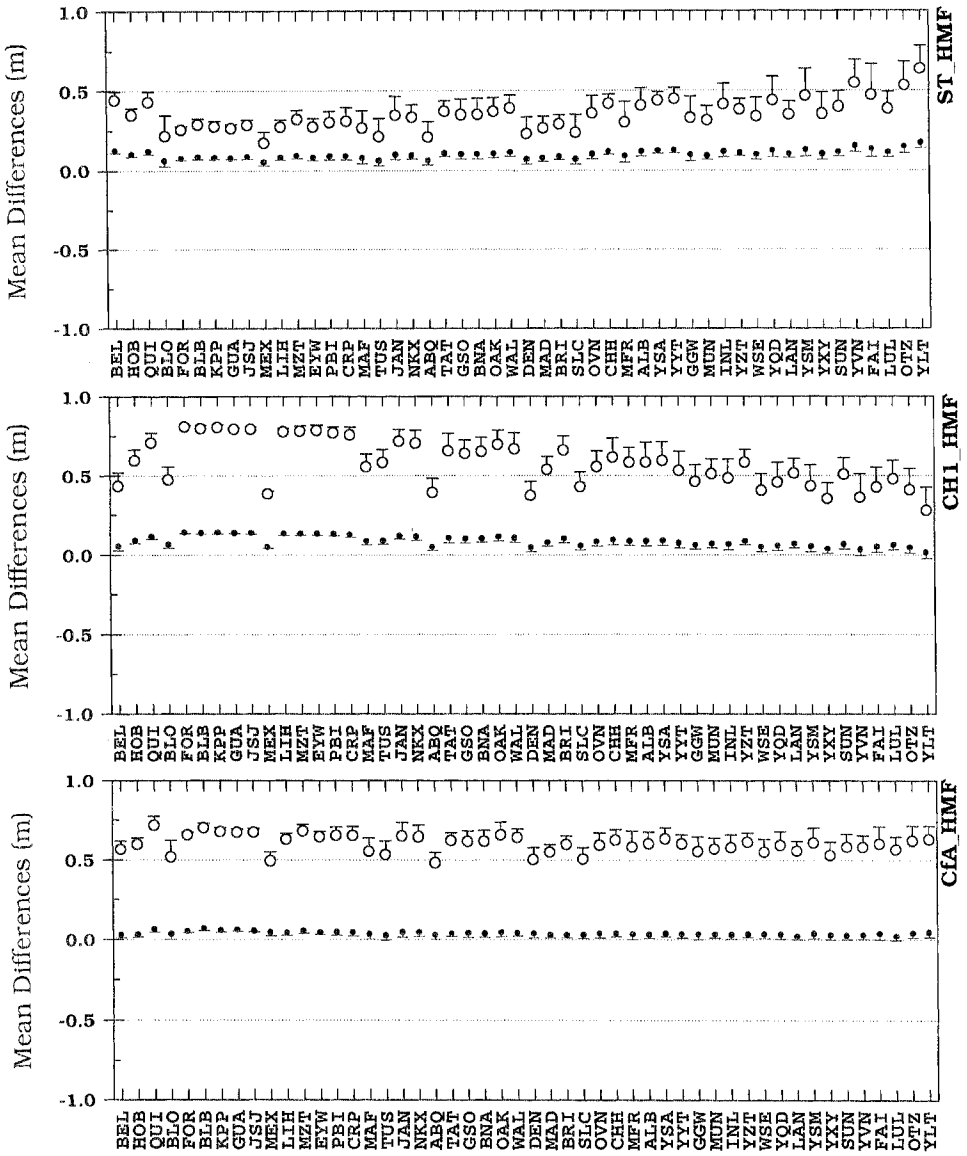

Appendix IXB – Annual mean bias and associated rms scatter for 6° (black dot) and 3° (open circle) elevation angles (continued).

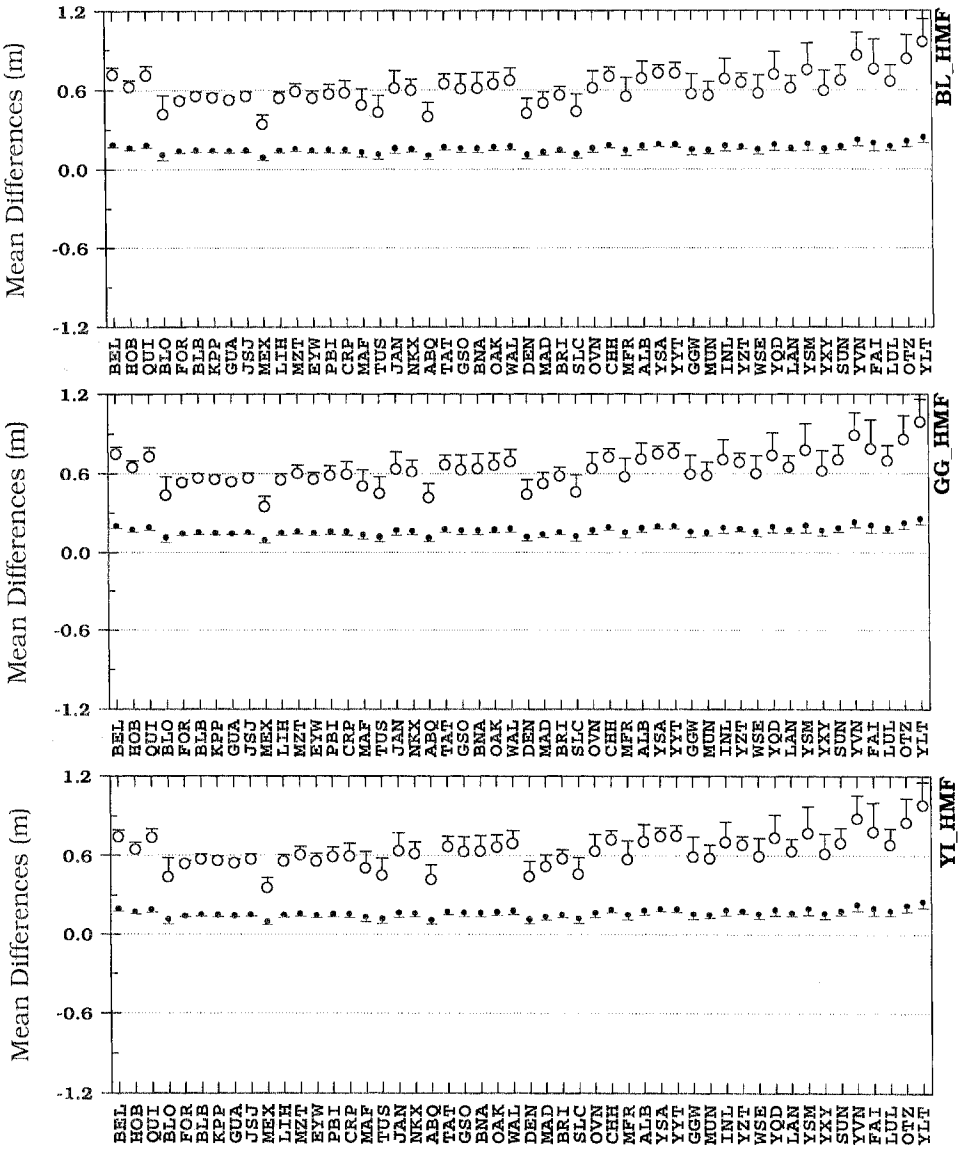

Appendix IXB – Annual mean bias and associated rms scatter for 6° (black dot) and 3° (open circle) elevation angles.

APPENDIX X

Non-hydrostatic mapping function statistics

Annual mean bias and rms scatter (one-sigma level) of the differences with respect to ray tracing for different non-hydrostatic mapping functions, for 50 radiosonde stations listed in Appendix III, and at different elevation angles.

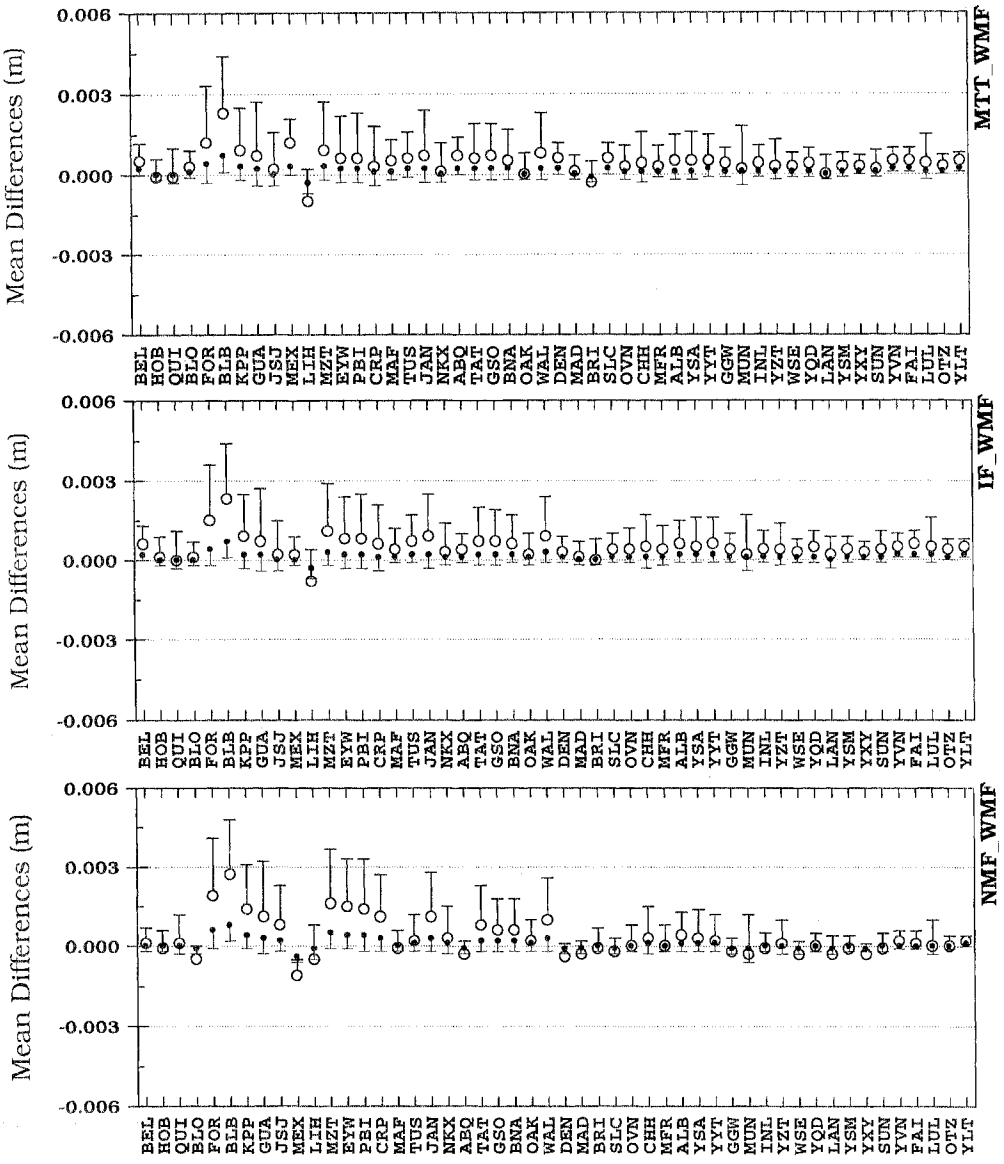

Appendix XA – Annual mean bias and associated rms scatter for 15° (black dot) and 10° (open circle) elevation angles (continued).

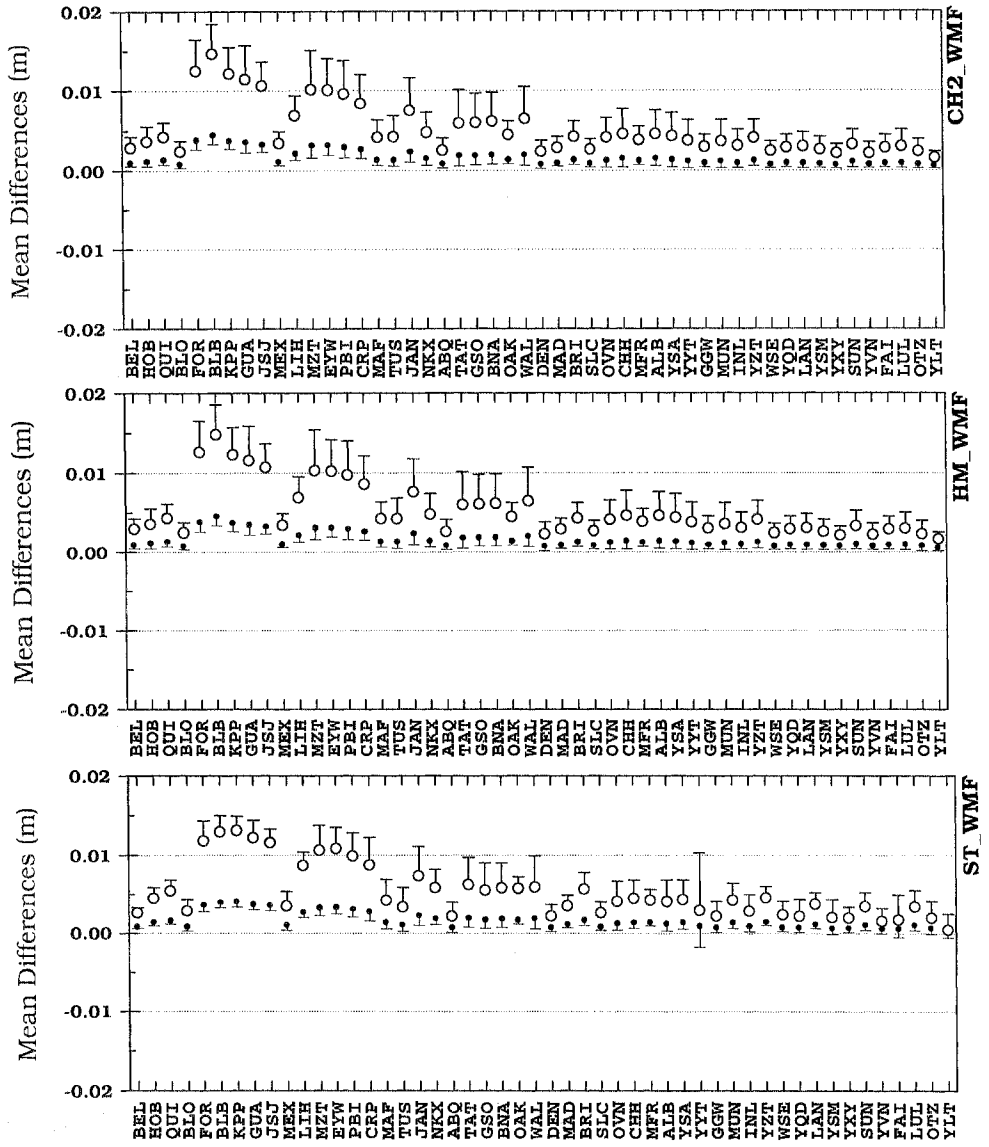

Appendix XA – Annual mean bias and associated rms scatter for 15° (black dot) and 10° (open circle) elevation angles (continued).

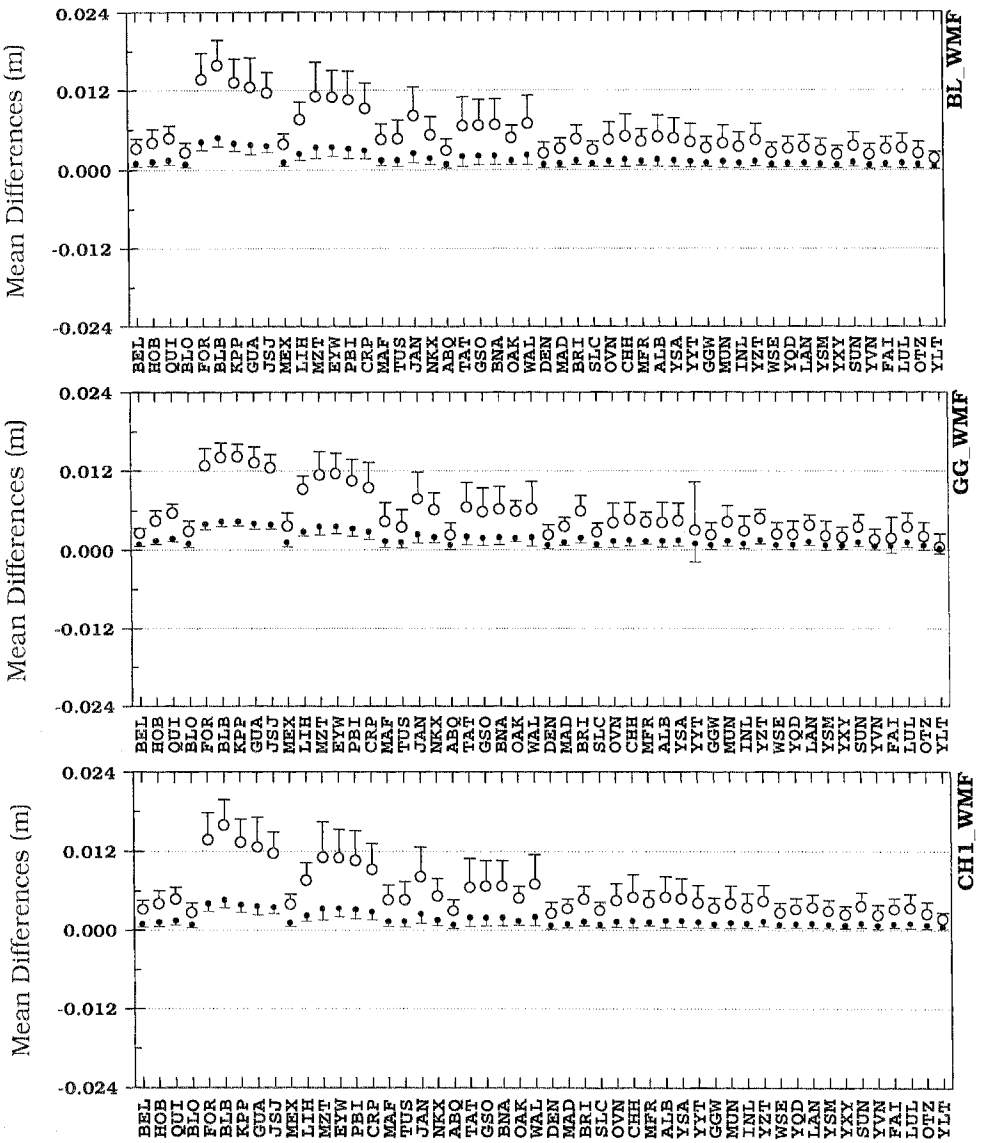

Appendix XA – Annual mean bias and associated rms scatter for 15° (black dot) and 10° (open circle) elevation angles (continued).

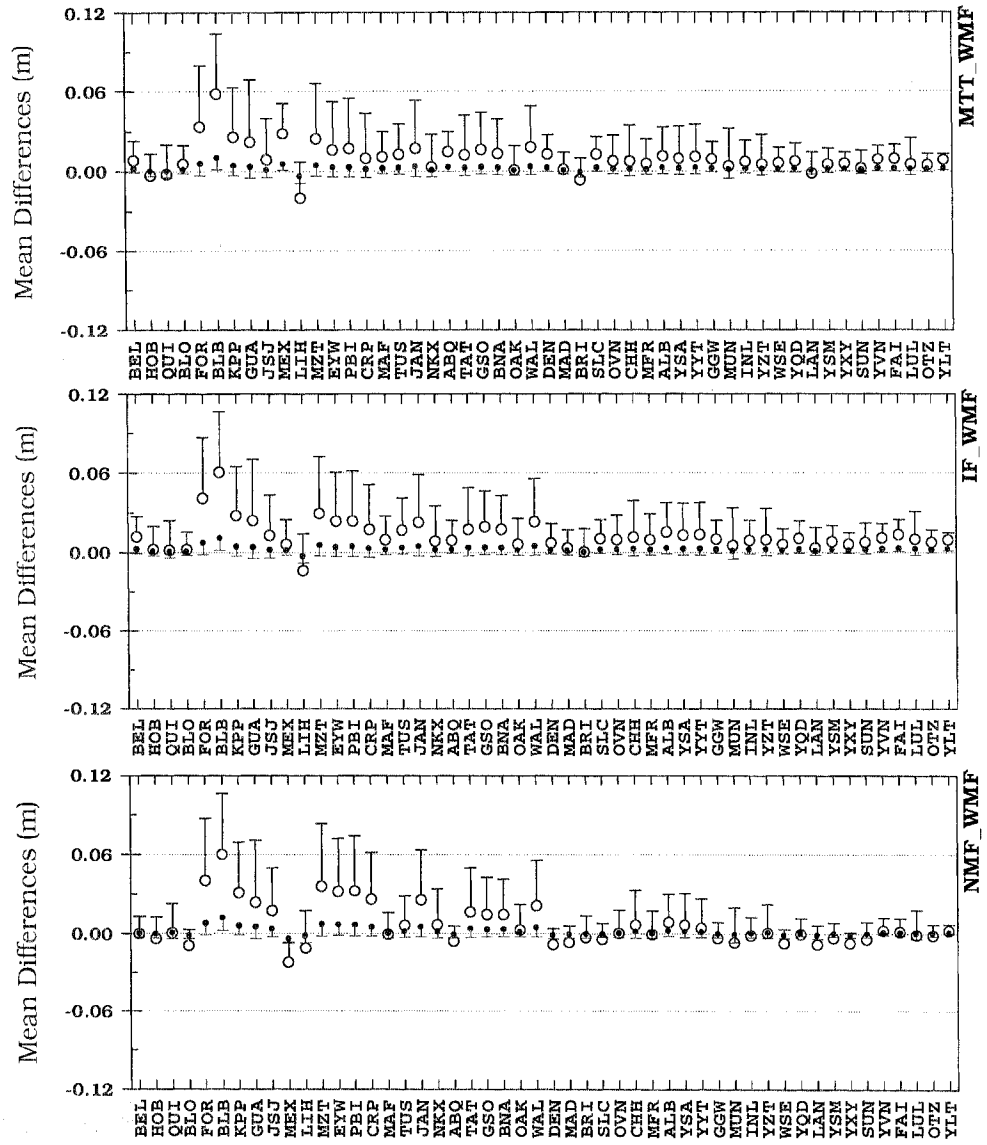

Appendix XA -- Annual mean bias and associated rms scatter for 15° (black dot) and 10° (open circle) elevation angles.

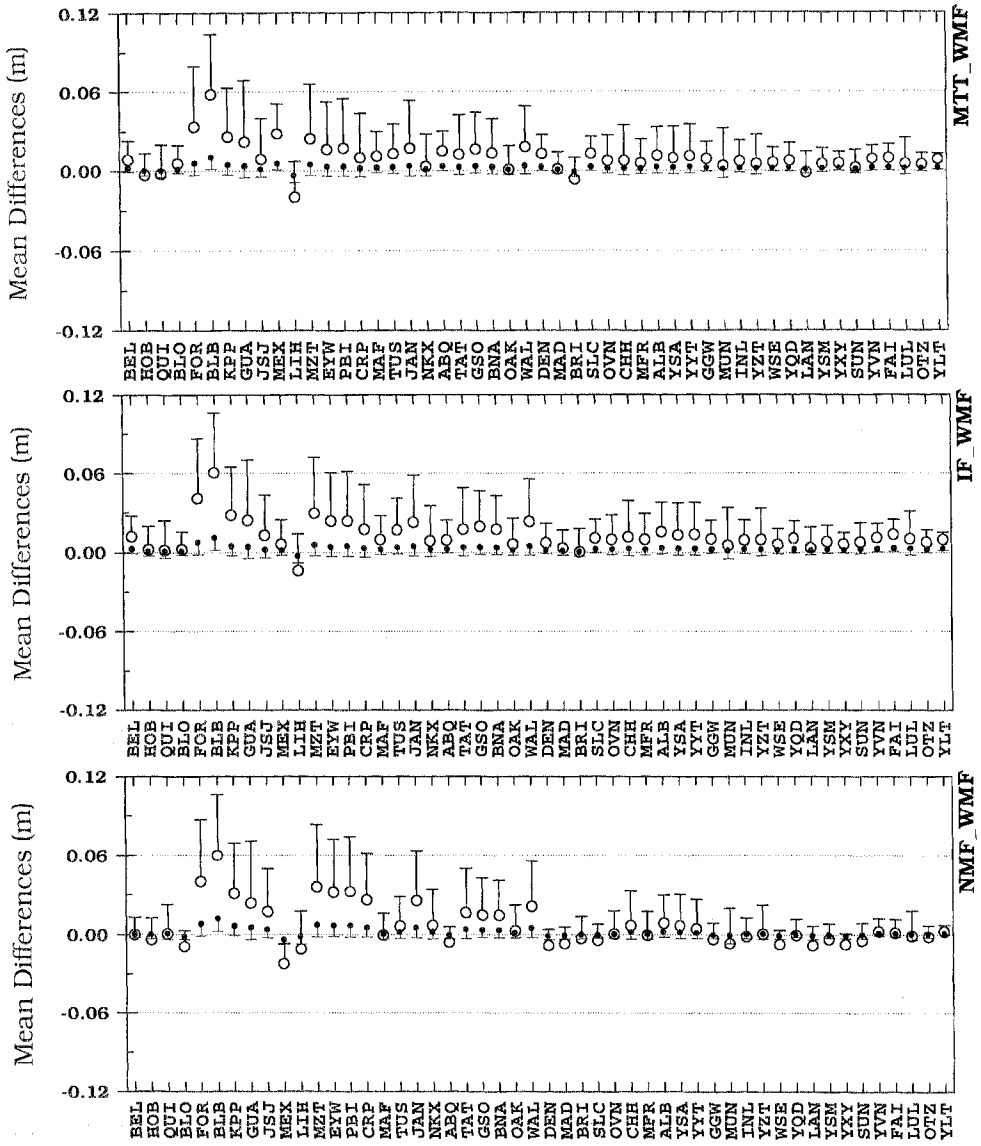

Appendix XB – Annual mean bias and associated rms scatter for 6° (black dot) and 3° (open circle) elevation angles (continued).

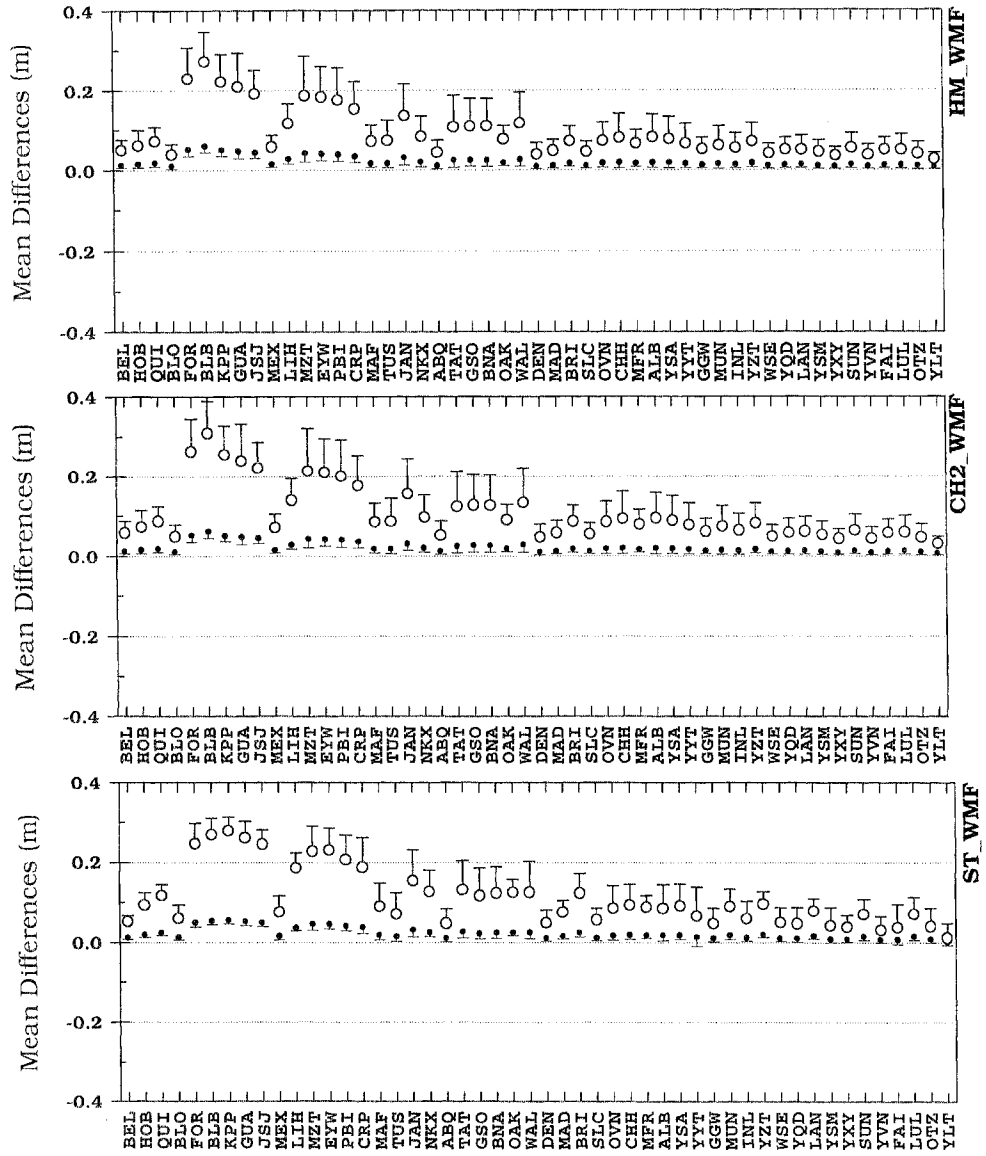

Appendix XB – Annual mean bias and associated rms scatter for 6° (black dot) and 3° (open circle) elevation angles (continued).

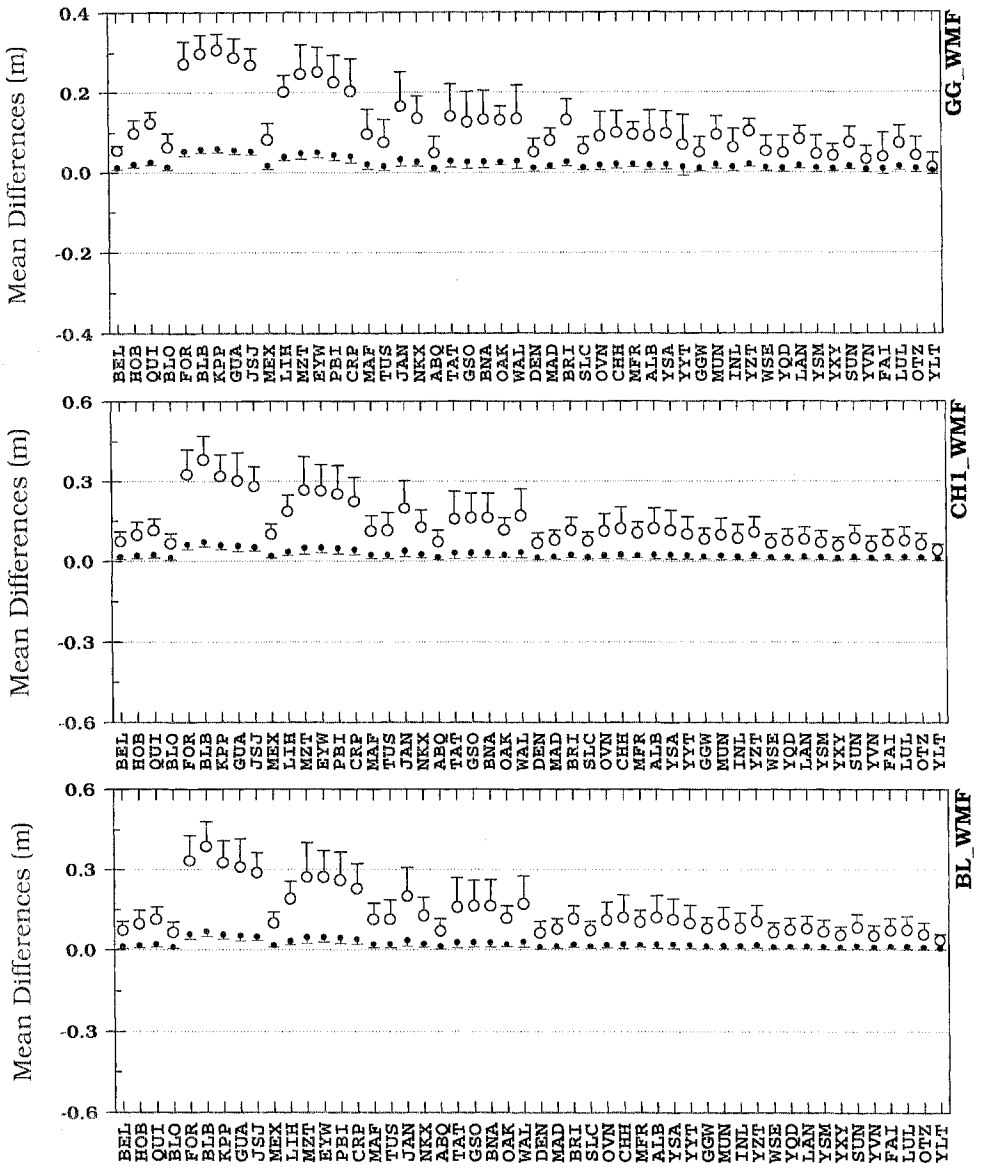

Appendix XB – Annual mean bias and associated rms scatter for 6° (black dot) and 3° (open circle) elevation angles (continued).

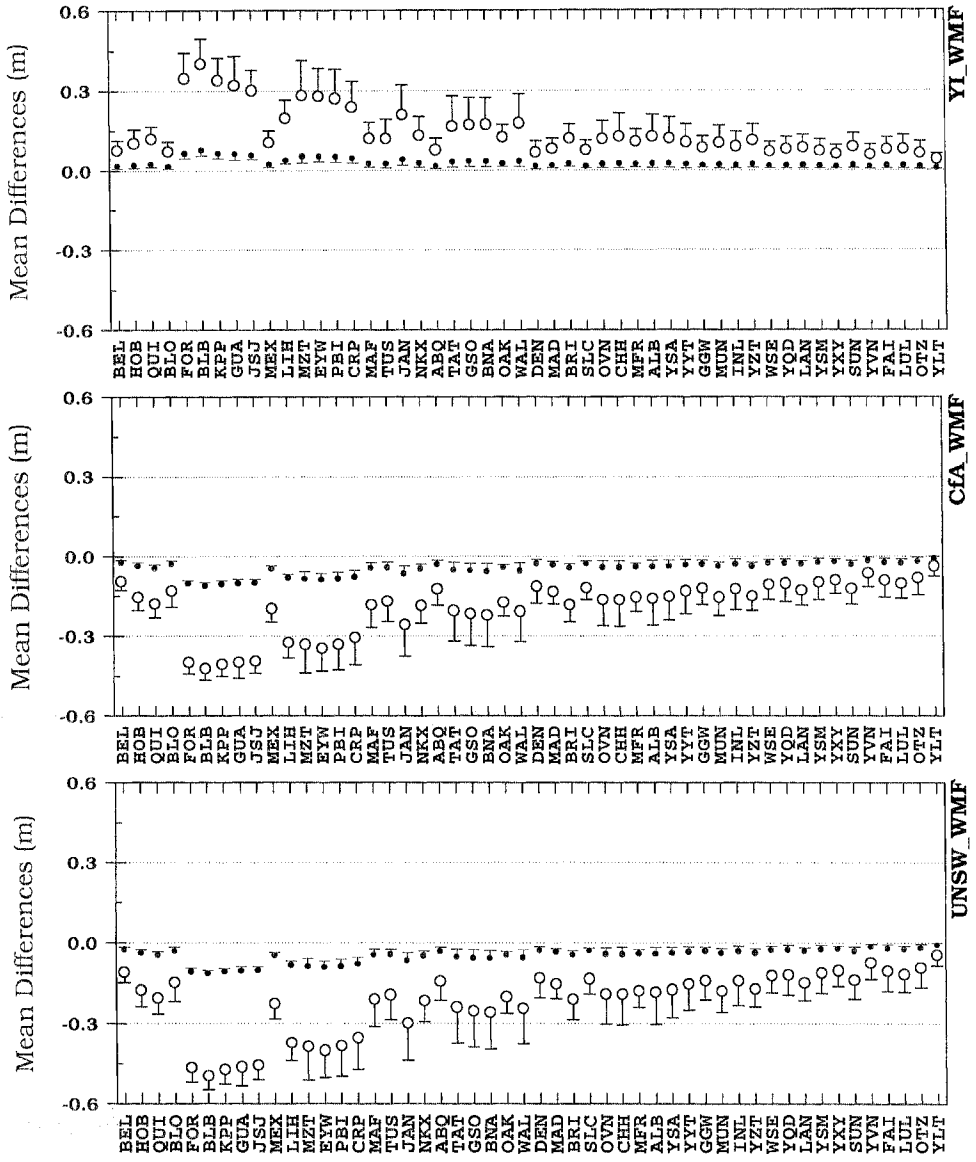

Appendix XB – Annual mean bias and associated rms scatter for 6° (black dot) and 3° (open circle) elevation angles.

APPENDIX XI

Total mapping function statistics

Annual mean bias and rms scatter (one-sigma level) of the differences with respect to ray tracing for different total mapping functions, for 50 radiosonde stations listed in Appendix III, and at different elevation angles.

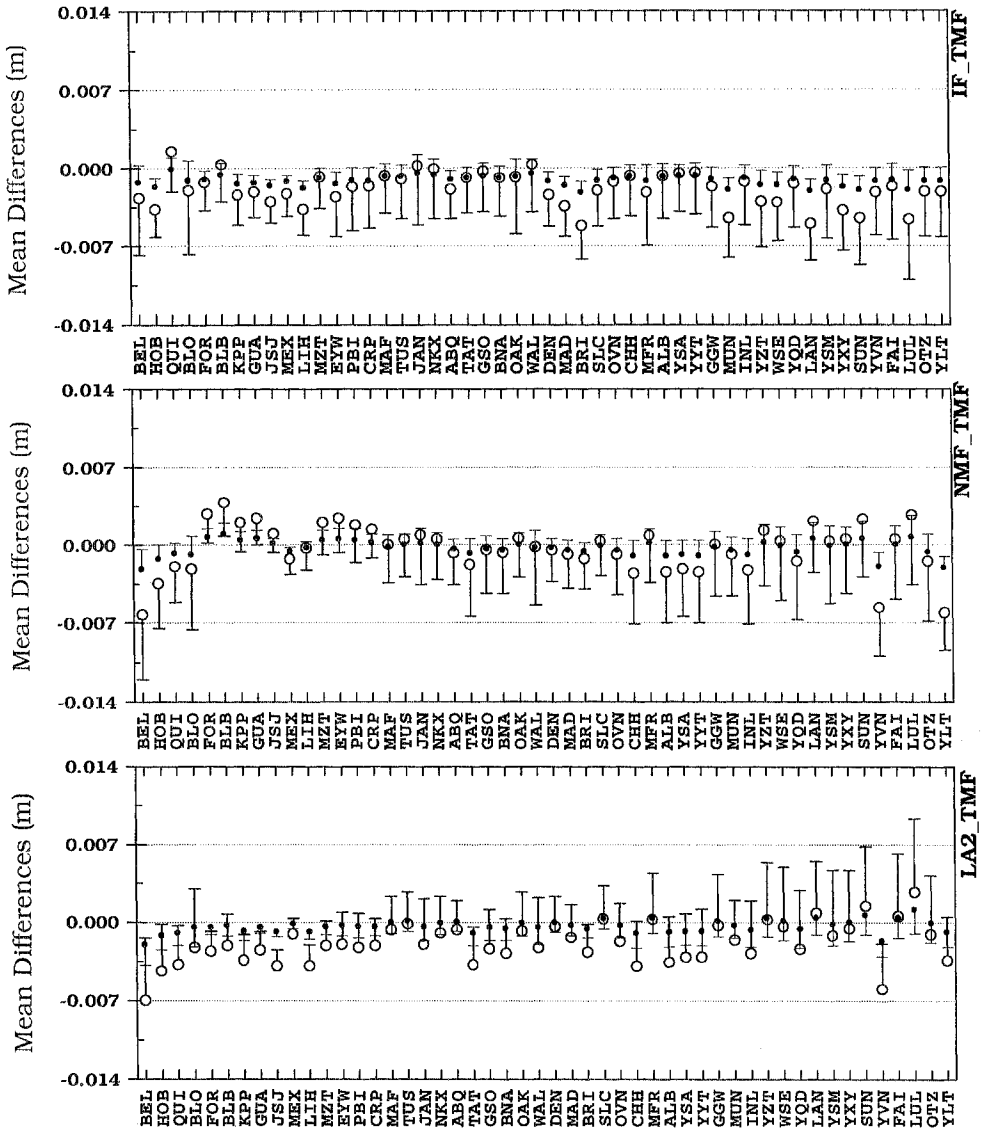

Appendix XIA – Annual mean bias and associated rms scatter for 15° (black dot) and 10° (open circle) elevation angles (continued).

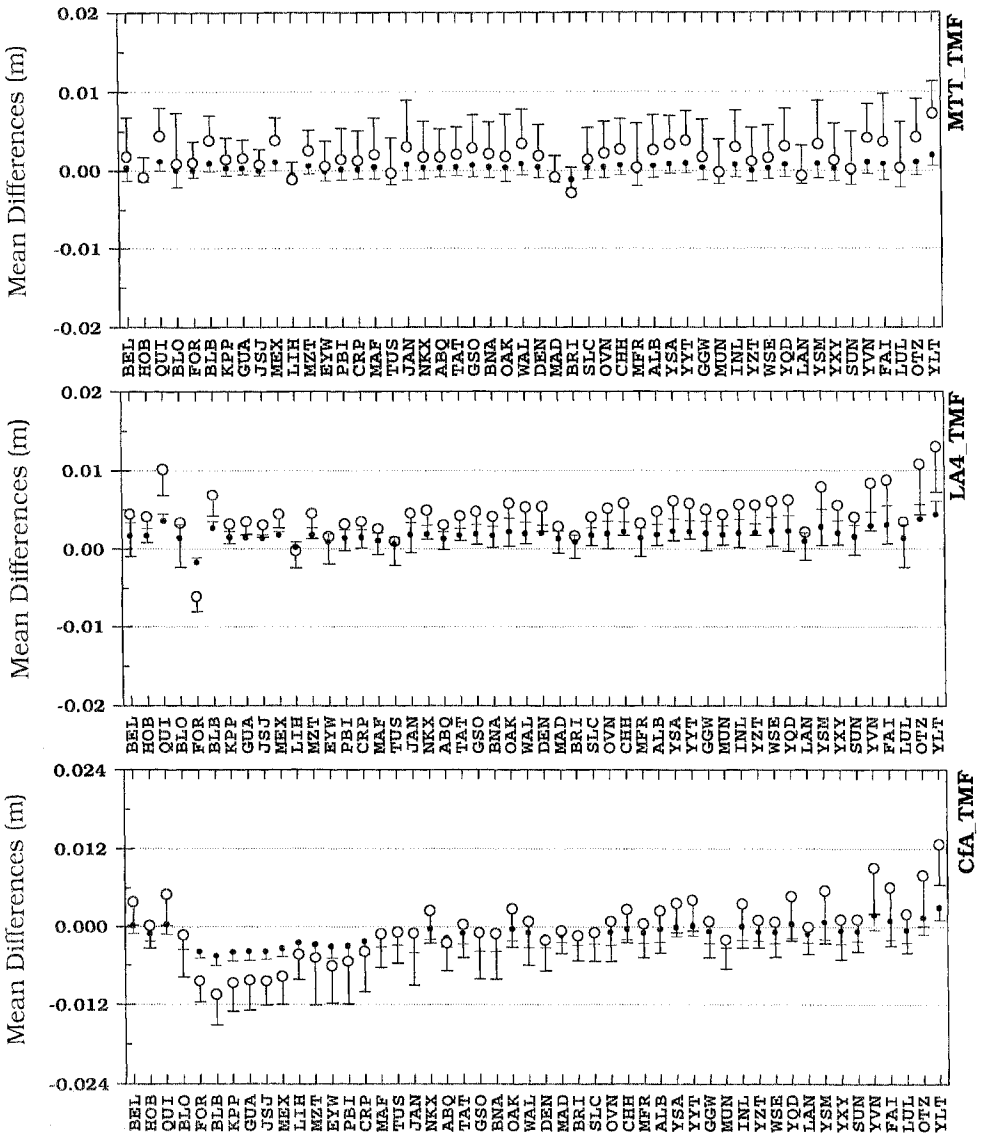

Appendix XIA – Annual mean bias and associated rms scatter for 15° (black dot) and 10° (open circle) elevation angles (continued).

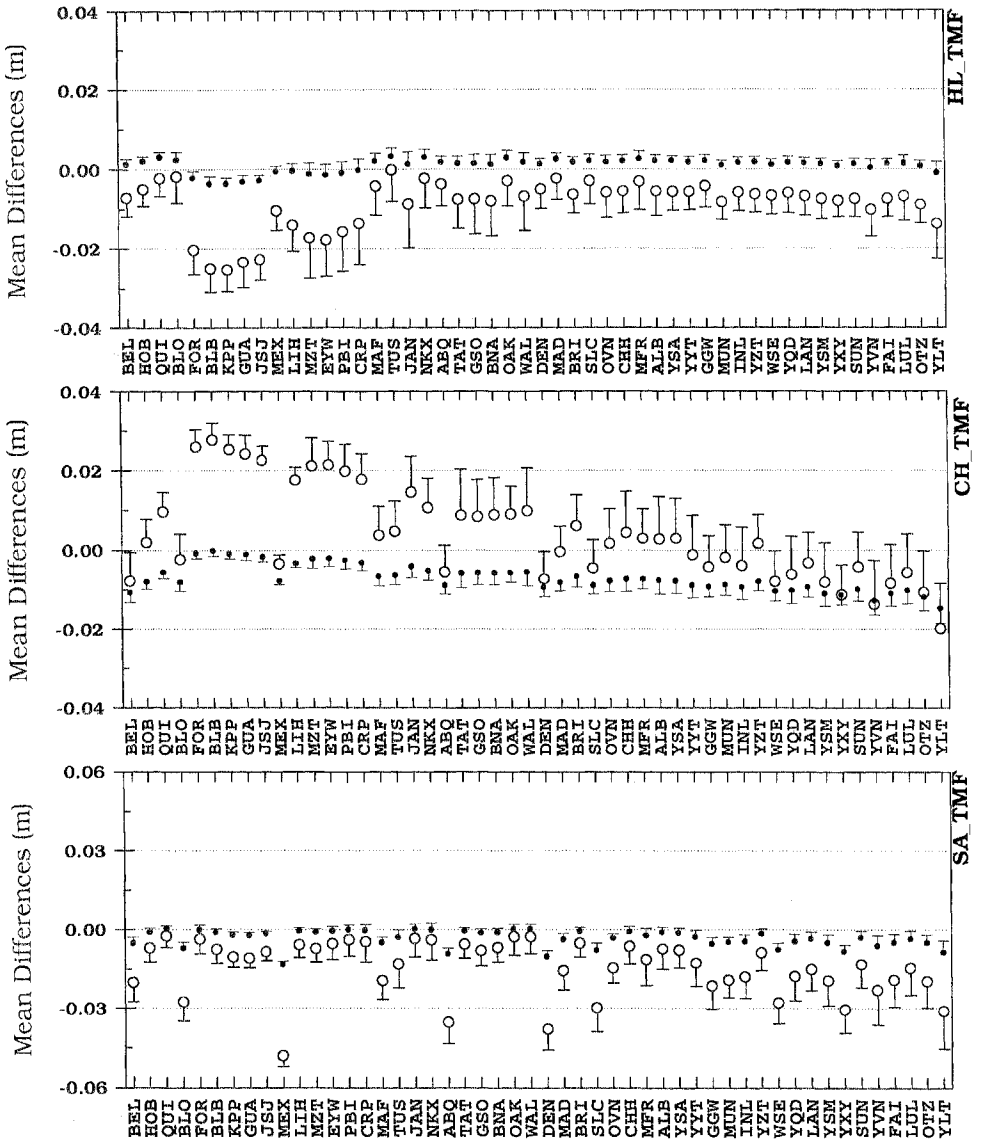

Appendix XIA – Annual mean bias and associated rms scatter for 15° (black dot) and 10° (open circle) elevation angles (continued).

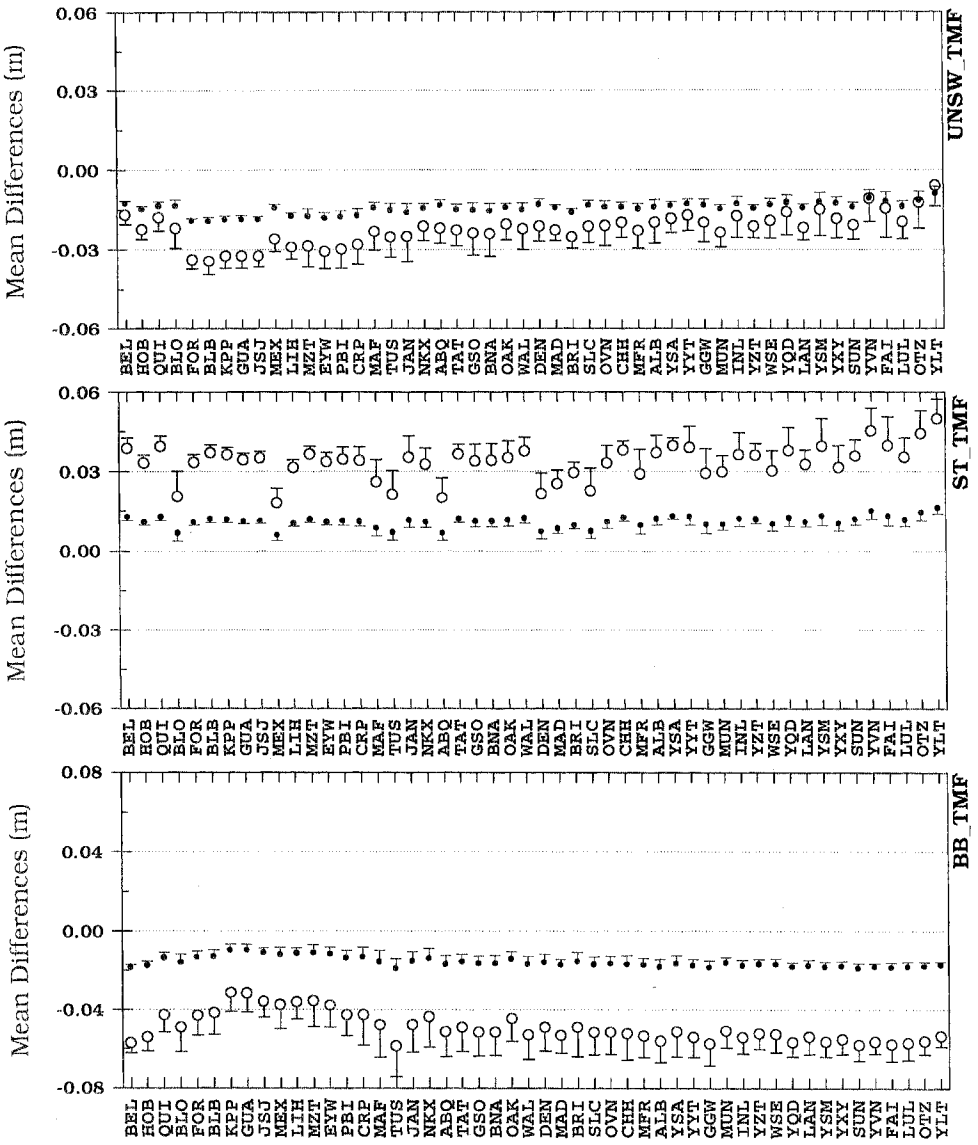

Appendix XIA – Annual mean bias and associated rms scatter for 15° (black dot) and 10° (open circle) elevation angles (continued).

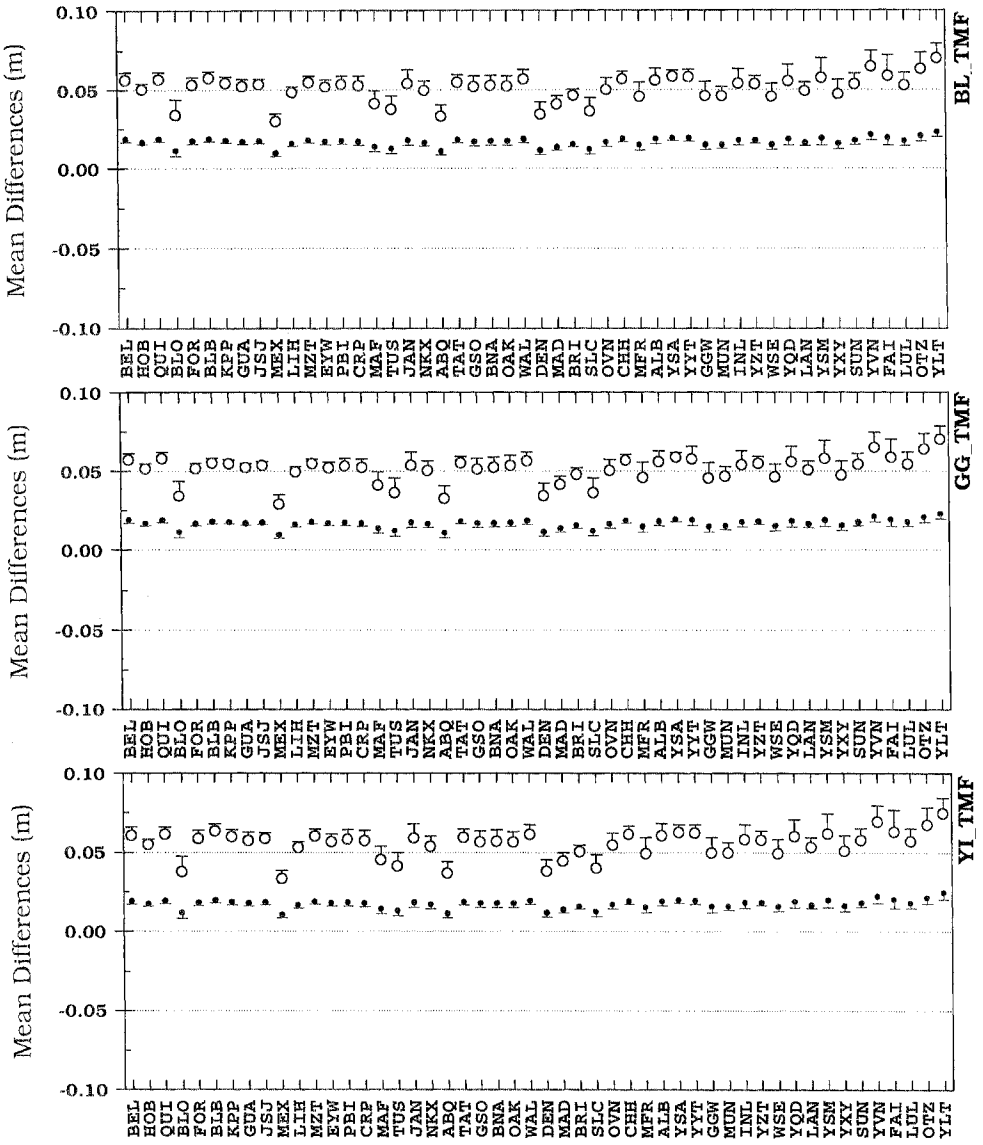

Appendix XIA – Annual mean bias and associated rms scatter for 15° (black dot) and 10° (open circle) elevation angles (continued).

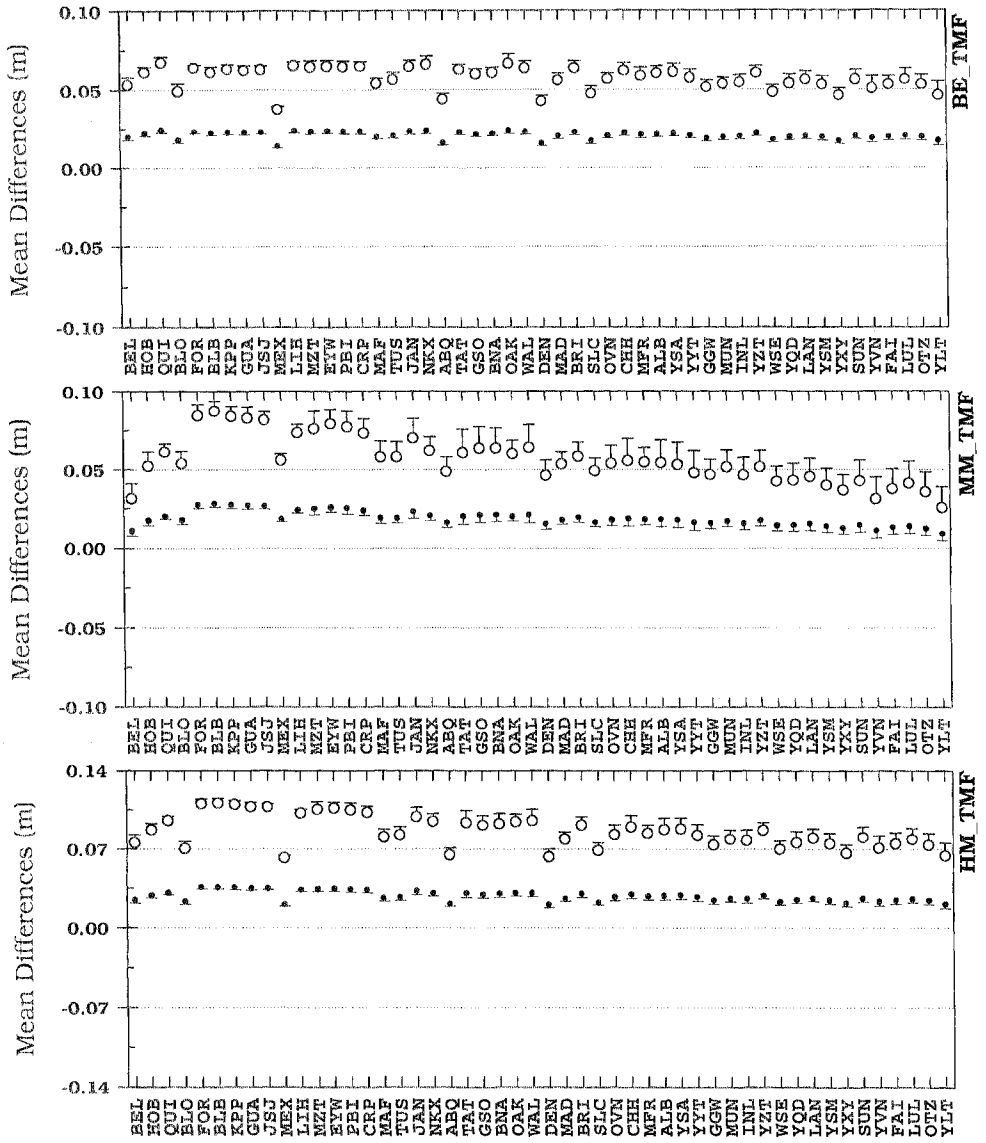

Appendix XIA – Annual mean bias and associated rms scatter for 15° (black dot) and 10° (open circle) elevation angles.

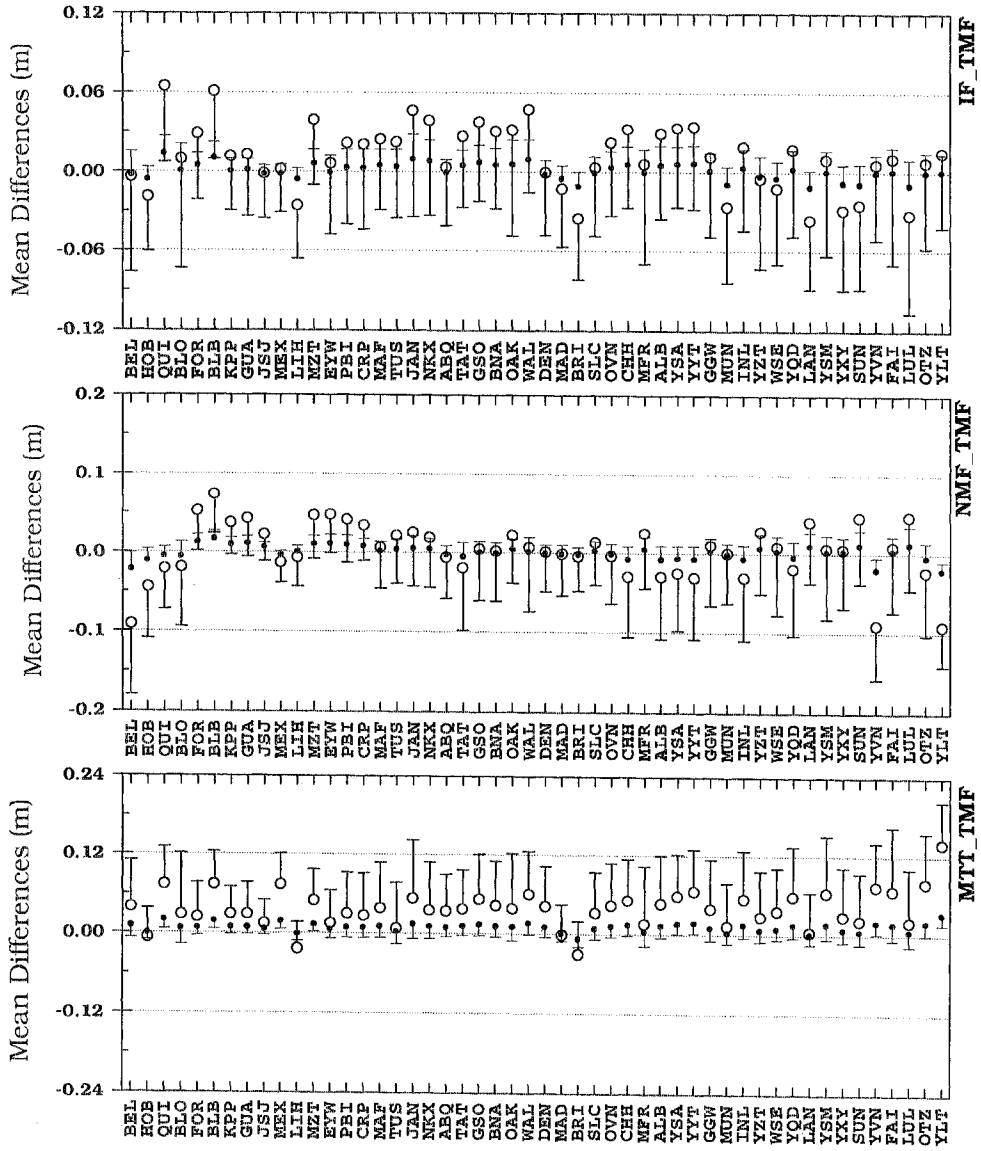

Appendix XIB – Annual mean bias and associated rms scatter for 6° (black dot) and 3° (open circle) elevation angles (continued).

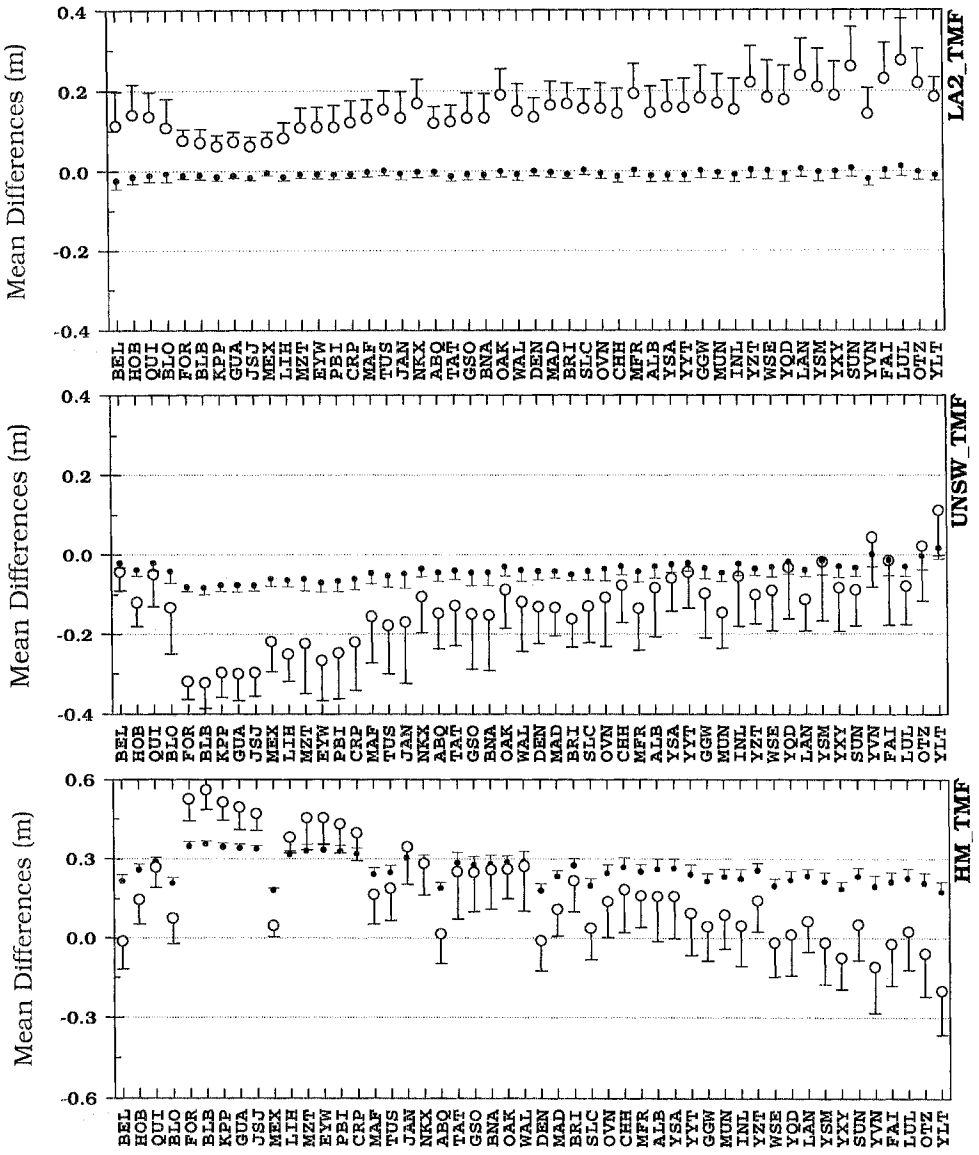

Appendix XIB – Annual mean bias and associated rms scatter for 6° (black dot) and 3° (open circle) elevation angles (continued).

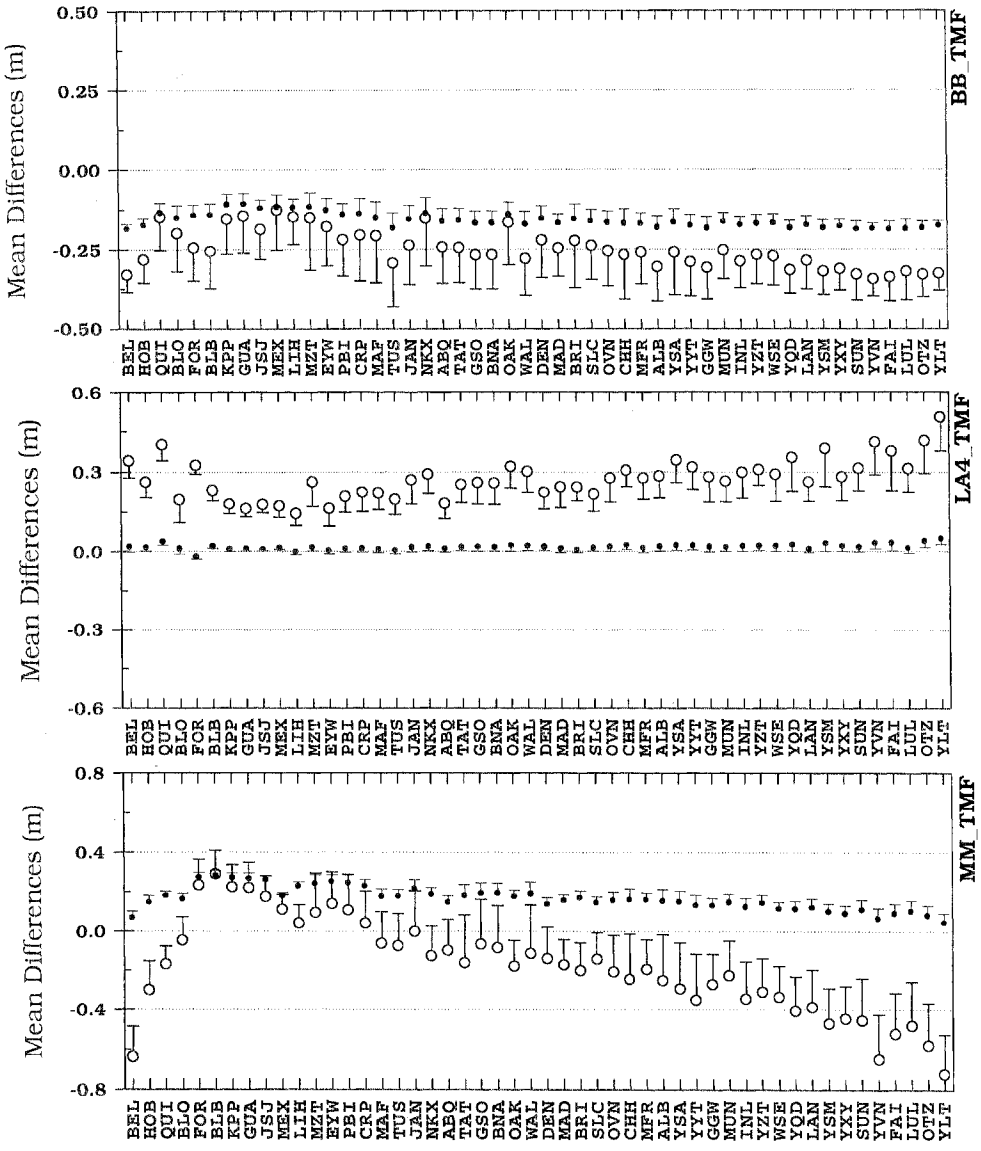

Appendix XIB – Annual mean bias and associated rms scatter for 6° (black dot) and 3° (open circle) elevation angles (continued).

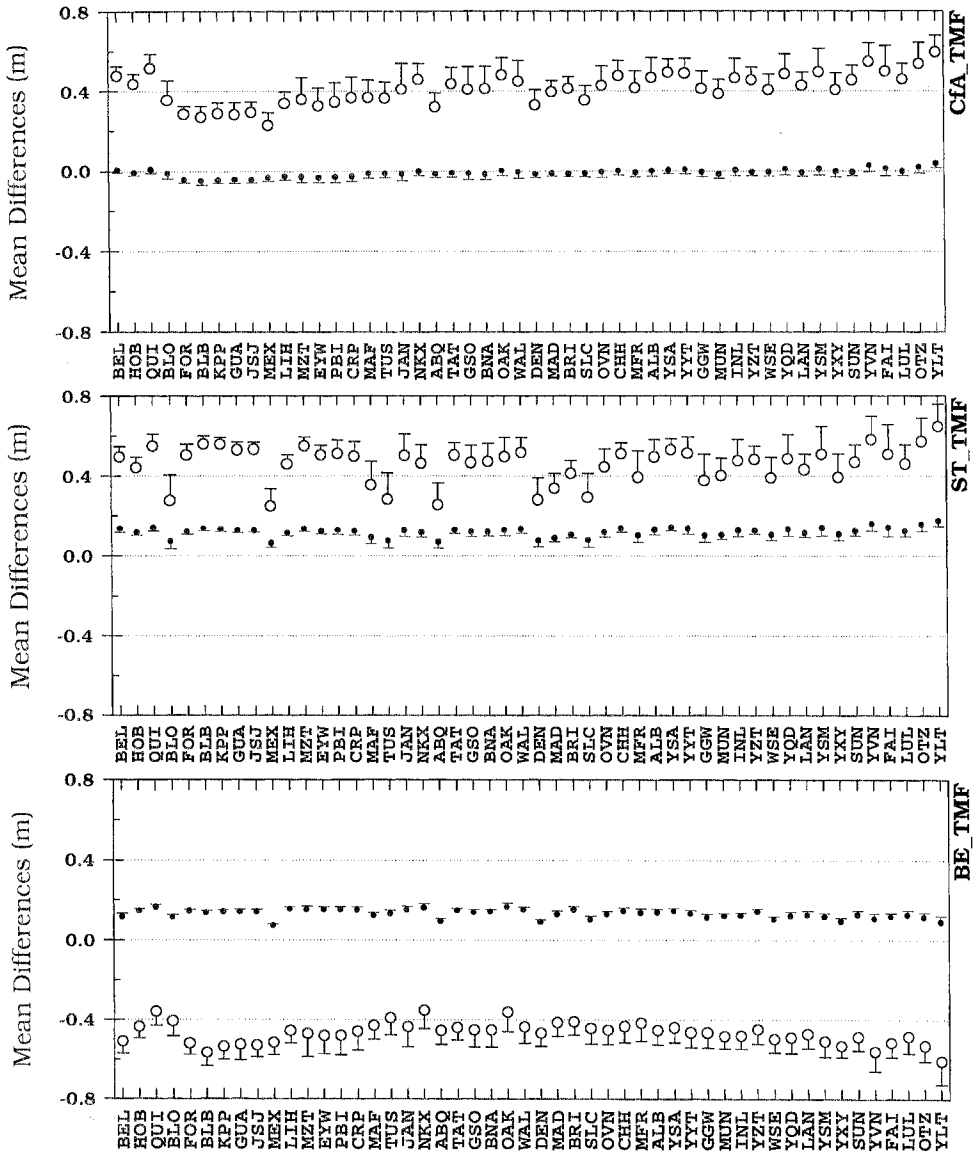

Appendix XIB -- Annual mean bias and associated rms scatter for 6° (black dot) and 3° (open circle) elevation angles (continued).

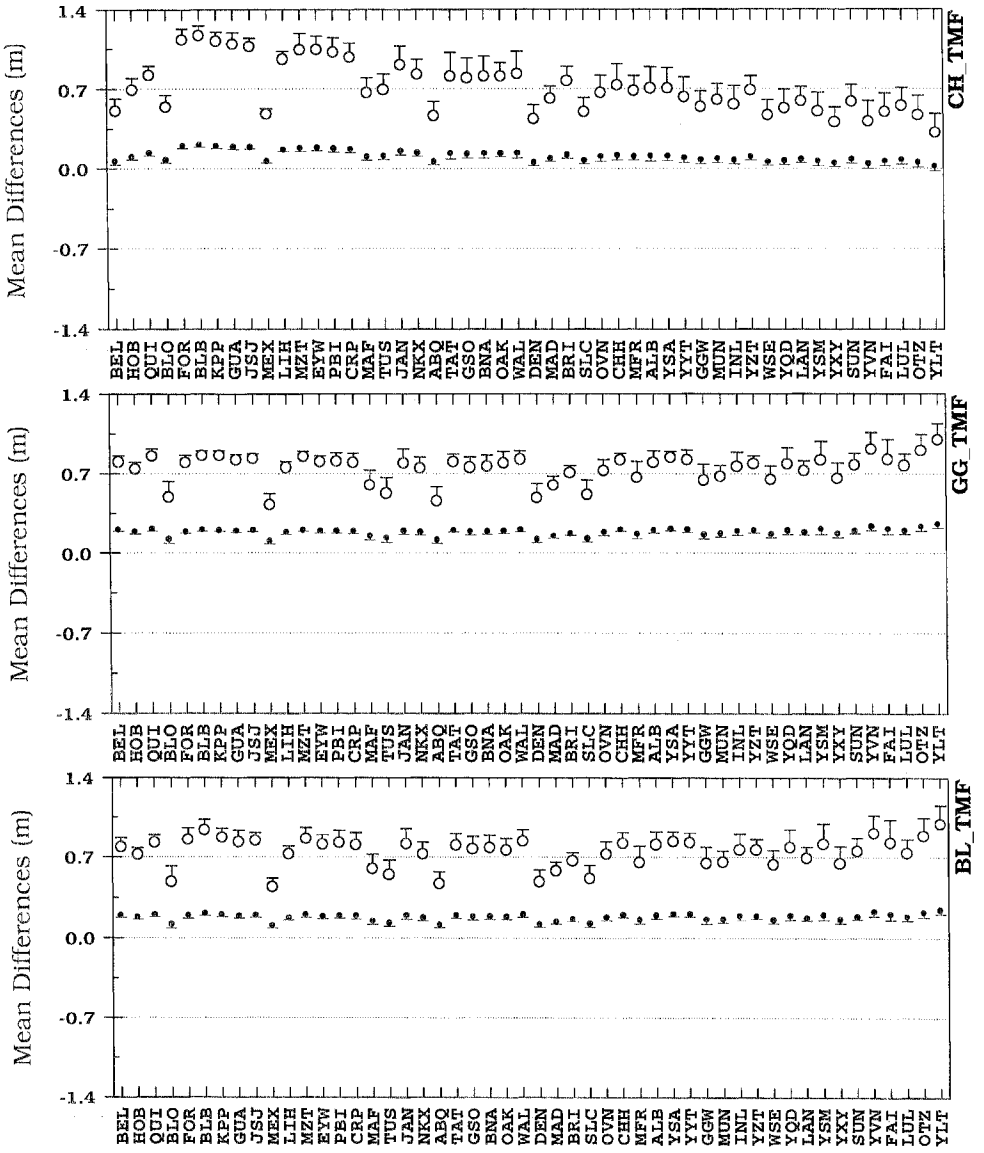

Appendix XIB – Annual mean bias and associated rms scatter for 6° (black dot) and 3° (open circle) elevation angles (continued).

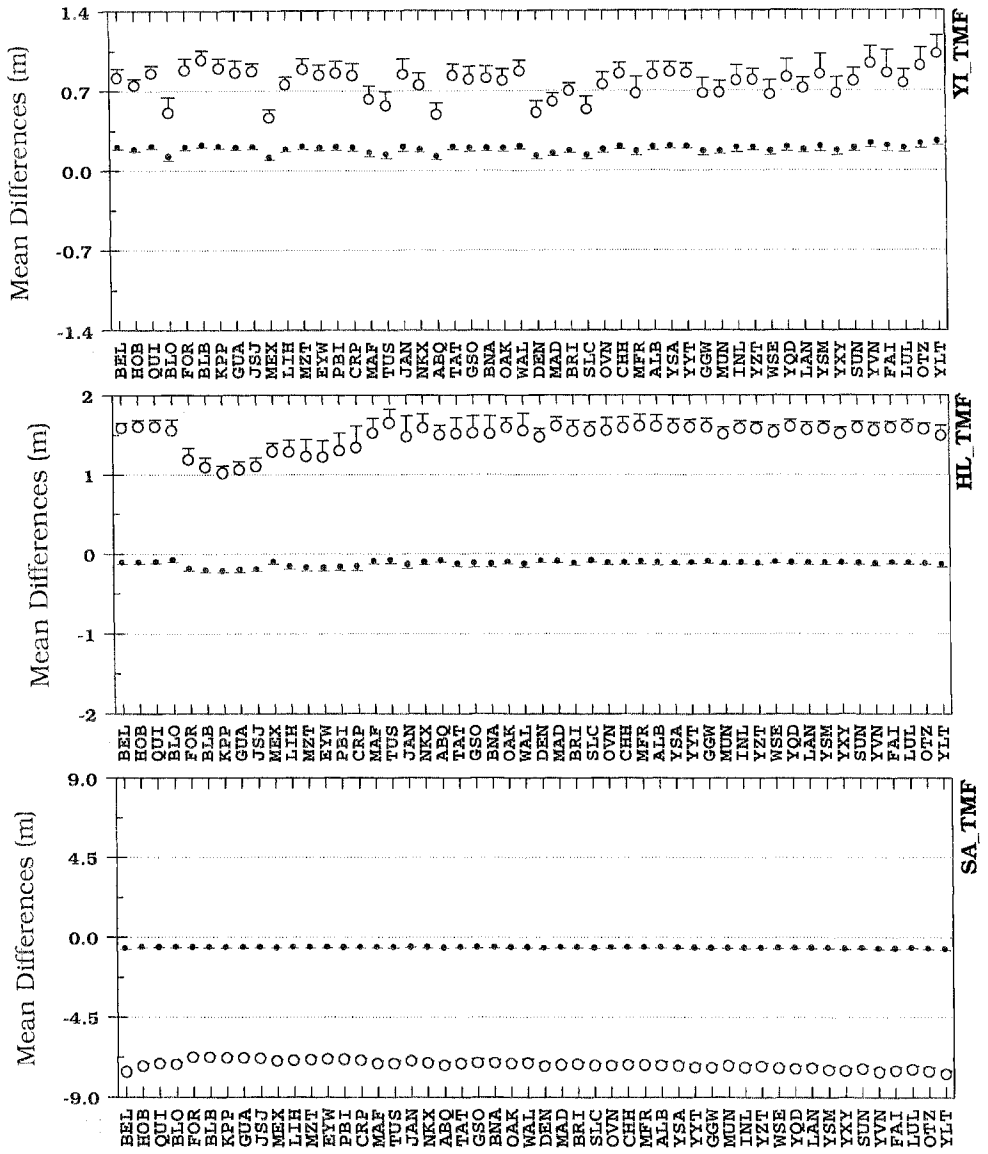

Appendix XIB – Annual mean bias and associated rms scatter for 6° (black dot) and 3° (open circle) elevation angles.

VITA

Candidate's Full Name: Virgílio de Brito Mendes

Place and Date of Birth: Seia, Portugal, 6th June 1958

Permanent Address: Praceta Armada das Índias, 6 - 3° D
2735 Cacém, Portugal

Schools Attended: Escola Secundária de Seia

Universities Attended: Faculdade de Ciências da Universidade de Lisboa
Diploma in Geographic Engineering (1987)

Publications and conference presentations:

Mendes, V.B. (1988). "Os erros nas efemérides dos satélites do Sistema de Posicionamento Global (GPS)." Revista do Instituto Geográfico e Cadastral, No. 8, pp. 1-6.

Mendes, V.B. (1989). "Perspectivas do Sistema de Posicionamento Global." Congresso 89, Ordem dos Engenheiros, October 9-13, Coimbra, Portugal.

Mendes, V.B. (1990). "Perturbações nas órbitas dos satélites do Sistema de Posicionamento Global." *Provas de Aptidão Pedagógica e Capacidade Científica*, Faculdade de Ciências da Universidade de Lisboa, Lisboa.

Mendes, V.B. (1990). "TRANSIT e GPS: dois conceitos no posicionamento por satélite". *Provas de Aptidão Pedagógica e Capacidade Científica*, Faculdade de Ciências da Universidade de Lisboa, Lisboa.

Mendes, V.B. (1992). "Posicionamento relativo de alta precisão com o Sistema de Posicionamento Global." *Revista do Instituto Geográfico e Cadastral*, No. 11, pp. 57-61.

Mendes, V.B. and R.B. Langley (1993). "Application of the Global Positioning System to the assessment of crustal deformation in the Charlevoix Seismic Zone." in Proceedings of ION GPS - 93, 6th International Technical Meeting of the Satellite Division of The Institute of Navigation, Salt Lake City, Utah, September 22 - 24, 1993; Vol. II, pp. 1205-1219.

Mendes, V.B. and R.B. Langley (1993). "Assessment of crustal deformation in the Charlevoix Seismic Zone using the Global Positioning System." International Association of Geodesy General Meeting, August 8-13, Beijing.

Mendes, V.B. and R.B. Langley (1994). "Modeling the tropospheric delay from meteorological surface measurements: comparison of models." American Geophysical Union Spring Meeting, Baltimore, MD, May 23-27 (Abstract: *EOS, Transactions of the American Geophysical Union*, Vol. 75, No. 16, p. 105).

Mendes, V.B. and R.B. Langley (1994). "A comprehensive analysis of mapping functions used in modelling tropospheric propagation delay in space geodetic data." *Proceedings of the International Symposium on Kinematic Systems in Geodesy, Geomatics and Navigation (KIS94)*, Banff, Canada, August 30 - September 2, pp. 87-98.

Mendes, V.B. and R.B. Langley (1995). "Modelling of the elevation dependence of the tropospheric delay: accuracy analysis of mapping functions." Paper presented at the 1995 International Earth Rotation Service (IERS) Workshop, May 10-12, Paris Observatory, Paris.

Mendes, V.B. and R.B. Langley (1995). "Zenith tropospheric delay determination using prediction models: accuracy analysis." *Cartografia e Cadastro*, Instituto Português de Cartografia e Cadastro, N° 2, pp. 41-47.

Mendes, V.B., J.P. Collins, and R.B. Langley (1995). "The effect of tropospheric propagation delay errors in airborne GPS precision positioning." in Proceedings of ION GPS - 95, 8th International Technical Meeting of the Satellite Division of The Institute of Navigation, 12-15 September, Palm Springs, CA, Vol. II, pp. 1681-1689.

Mendes, V.B. and R.B. Langley (1995). "Modeling the elevation angle dependence of the tropospheric delay in GPS-meteorology applications." Presented at the AGU Fall Meeting, 11-15 December, S. Francisco, CA. (Abstract: *EOS, Transactions of the American Geophysical Union*, Vol. 76, No. 46, p. F145).

Niell, A.E., A.J. Coster, F.S. Solheim, **V.B. Mendes**, P.C.P. Toor, and R.B. Langley (1995). "Comparison of the measurements of atmospheric water vapor by GPS, VLBI, WVR, and radiosondes during CONT95." Presented at the AGU Fall Meeting, 11-15 December, S. Francisco, CA (Abstract: *EOS, Transactions of the American Geophysical Union*, Vol. 76, No. 46, p. F146).

Pagarete, J.F., and **V.B. Mendes** (1996). "Application of the Global Positioning System to the determination of Crustal Deformation in the Lower Tagus Valley Area". Paper presented at the EGS XXI General Assembly, May 6-10, The Hague.

Pagarete, J., J.T. Pinto, **V.B. Mendes**, C. Antunes, and H. Ribeiro (1996). "The importance of classical geodetic observations for analyzing the geodynamic behaviour of the Açores archipelago." Paper presented at the Wegener Assembly, June 3-7, Vila Nova de Gaia, Portugal (accepted for publication at *Tectonophysics*).

Martins, J.A., J.F.P. Varela, **V.B. Mendes** e J. Pagarete (1996). "Geodesia de precisão com GPS: uma análise dos efeitos dos erros das órbitas e do atraso troposférico." *Cartografia e Cadastro*, Instituto Português de Cartografia e Cadastro, N° 4, pp. 39-45.

Coster, A.J., A.E. Niell, F.S. Solheim, **V.B. Mendes**, P.C. Toor, R.B. Langley, and C.A. Ruggles (1996). "The Westford water vapor experiment: use of GPS to determine total precipitable water vapor." in *Proceedings of the 52nd Annual Meeting of The Institute of Navigation*, 19-21 June, Cambridge, MA, pp. 529-538

Niell, A.E., A.J. Coster, F.S. Solheim, **V.B. Mendes**, P.C. Toor, R.B. Langley, and C.A. Ruggles (1996). "Measurement of water vapor by GPS, VLBI, WVR, and radiosonde." Presented at the Eleventh Working Meeting on European VLBI for Geodesy and Astrometry, August 24-25, Onsala, Sweden.

Coster, A.J., A.E. Niell, F.S. Solheim, **V.B. Mendes**, P.C. Toor, K.P. Buchmann, C.A. Ruggles, and R.B. Langley (1996). "Measurements of precipitable water vapor by GPS, radiosondes, and a microwave water vapor radiometer." Presented at ION GPS-96, 9th International Technical Meeting of the Satellite Division of the Institute of Navigation, 17-20 September, Kansas City, MI.

Martins, J.A., J.F.P. Varela, **V.B. Mendes** e J.A.C.F. Pagarete (1996). "Geodesia de precisão com GPS: uma análise dos efeitos dos erros das órbitas e do atraso troposférico." Cartografia e Cadastro, Instituto Português de Cartografia e Cadastro, N° 4, pp. 39-45.

S.B. Bisnath, **V.B. Mendes** and R.B. Langley (1997). "Effects of tropospheric mapping functions on space geodetic data." *Proceedings of the IGS Analysis Center Workshop*, Jet Propulsion Laboratory, Pasadena, CA, 12-14 March, in press.

Coster, A.J., A.E. Niell, F.S. Solheim, **V.B. Mendes**, P.C. Toor, and R.B. Langley (1997). "The effect of gradients in the GPS estimation of tropospheric water vapor." *Proceedings of The Institute of Navigation 53rd Annual Meeting*, Albuquerque, NM, U.S.A., 30 June - 1 July 1997; pp. 107-114.

Coster, A.J., A.E. Niell, F.S. Solheim, **V.B. Mendes**, P.C. Toor, R.B. Langley, and C.A. Upham (1998). "The Westford Water Vapor Experiment: Accuracy issues involving the use of GPS to measure total precipitable water vapor." *Proceedings of the 10th Symposium on Meteorological Observations and Instrumentation*, 78th Annual Meeting of the American Meteorological Society, Phoenix, AZ, 11-16 January. pp. J70-J75.

Guarda, C., M. Gonçalves, G. Prates, L. Santos, L. Sousa, **V.B. Mendes**, e J. Pagarete (1998). "Impacto da duração da sessão de observação no posicionamento relativo estático GPS." Presented at the 1ª Assembleia Luso-Espanhola de Geodesia e Geofísica, Aguadulce (Almería, Spain), 9-13 February.

Pagarete, J. e **V.B. Mendes** (1998). "Controlo das deformações da crusta no Vale Inferior do Tejo usando GPS." Presented at the 1ª Assembleia Luso-Espanhola de Geodesia e Geofísica, Aguadulce (Almería, Spain), 9-13 February.

Pagarete, J. and **V.B. Mendes** (1998). "Global Positioning System crustal deformation studies in the Lower Tagus Valley area from 1994 to 1997." Presented at the European Geophysical Society XXIII General Assembly, Nice, France, 20-24 April.

Niell, A.E., A.J. Coster, F.S. Solheim, **V.B. Mendes**, P.C. Toor, R.B. Langley, and C.A. Upham (1998). "Measurements of water vapor in the atmosphere: comparison of radiosonde, water vapor radiometer, GPS, and VLBI." Presented at the European Geophysical Society XXIII General Assembly, Nice, France, 20-24 April.

Mendes, V.B. and R.B. Langley (1998). "An analysis of high-accuracy tropospheric delay mapping functions." Presented at the European Geophysical Society XIII General Assembly, 20 - 24 April 1998, Nice, France (Submitted to *Physics and Chemistry of the Earth)*.

Mendes, V.B. and R.B. Langley (1998). "Optimization of tropospheric delay mapping function performance for high-precision geodetic applications." Proceedings of DORIS Days, 27 - 29 April 1998, Toulouse, France.

Mendes, V.B. and R.B. Langley (1998). "Tropospheric zenith delay prediction accuracy for airborne GPS high-precision positioning." *Proceedings of The Institute of Navigation 54th Annual Meeting*, Denver, CO, June 1 - 3; in press.